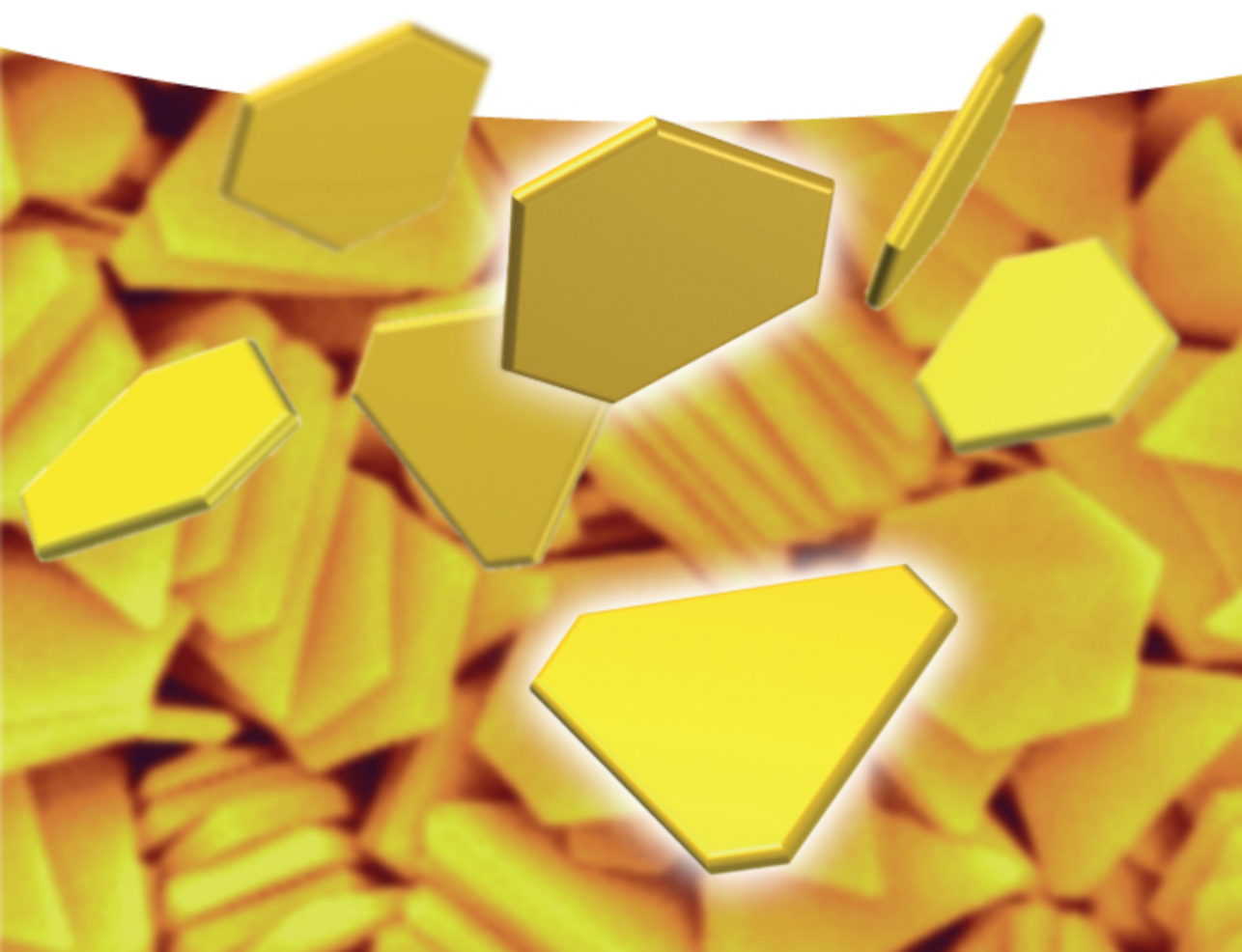Dieter Vollath

Nanoparticles – Nanocomposites – Nanomaterials

An Introduction for Beginners

Dieter Vollath

**Nanoparticles –
Nanocomposites –
Nanomaterials**

Related Titles

Manasreh, O.

Introduction to Nanomaterials and Devices

2012
Print ISBN: 978-0-470-92707-6

Wolf, E.L., Medikonda, M.

Understanding the Nanotechnology Revolution

2012
Print ISBN: 978-3-527-41109-2

Borisenko, V.E., Ossicini, S.

What is What in the Nanoworld

A Handbook on Nanoscience and Nanotechnology

3rd Edition
2012
Print ISBN: 978-3-527-41141-2

Schmid, G. (ed.)

Nanoparticles

From Theory to Application

2nd Edition
2010
Print ISBN: 978-3-527-32589-4

Cademartiri, L., Ozin, G.A.

Concepts of Nanochemistry

2009
Print ISBN: 978-3-527-32597-9

Wolf, E.L.

Quantum Nanoelectronics

An Introduction to Electronic Nanotechnology and Quantum Computing

2009
Print ISBN: 978-3-527-40749-1

Gubin, S.P. (ed)

Magnetic Nanoparticles

2009
Print ISBN: 978-3-527-40790-3

Poole, C.P., Owens, F.J.

Introduction to Nanotechnology

2003
Print ISBN: 978-0-471-07935-4

Dieter Vollath

Nanoparticles – Nanocomposites – Nanomaterials

An Introduction for Beginners

WILEY-VCH

Verlag GmbH & Co. KGaA

The Author

Prof. Dr. Dieter Vollath
NanoConsulting
Primelweg 3
76297 Stutensee
Germany

The coverpicture is based on a figure published in the article: Yun, Y.J., Park, G., Ah, C.S., Park, H.J., Yun, W.S., and Haa, D.H. (2005) Appl. Phys. Lett., 87, 233110–233113. With kind permission by The American Institute of Physics.

Contents

Preface

This book is really two books. It gives an introduction to the topics connected to nanoparticles, nanocomposites, and nanomaterials on a descriptive level. Wherever it seems appropriate, some topics are explained in more detail in separate boxes. It is not necessary to read these boxes; however, it may be interesting and helpful to the reader.

This textbook is intended for persons wanting an introduction into the new and exciting field of nanomaterials without having a formal education in science. It discusses the whole range from nanoparticles to nanocomposites and finally nanomaterials, explaining the scientific background and some of the most important applications. I want to provoke the reader's curiosity; he/she should feel invited to learn more about this topic, to apply nanomaterials and, may be, to go deeper into this fascinating topic.

This book is an excerpt from the course on nanomaterials for engineers that I give at the University of Technology in Graz, Austria and on the courses that NanoConsulting organizes for participants from industry and academia. This book is not written for scientists, so may be some physicists will feel unhappy about the simplifications that I made to explain complicated quantum mechanical issues.

I want to apologize for the selection of examples from the literature, as my selection of examples is, to some extent, unfair against those who discovered these new phenomena. Unfortunately, when a new phenomenon was described for the first time, the effect is only shown in principle. Later papers instead showed these phenomena very clearly. Therefore, the examples from later publications seemed more adequate for a textbook like this.

As the size of this book is limited, I had to make a selection of phenomena for presentation. Unavoidably, this selection is influenced by personal experience and preferences. I really apologize if a reader does not find information of interest for themselves or their company.

It is an obligation for me to thank my family, in particular my wife Renate, for her steady support during the time when I wrote this book and her enduring understanding for my passion for science. Furthermore, I have to thank Dr. Waltraud Wüst from Wiley-VCH for her steady cooperation.

Stutensee, June 2013   *Dieter Vollath*

1
Introduction

Everyone talks about nanomaterials. There are many publications, books and journals devoted to this topic. This is not surprising, as the economic importance is steadily increasing. Additionally, interested persons without specific education in one of these fields, have, at the moment, nearly no chance to understand this technology, its background and applications. This book fills this gap. It deals with the special phenomena found with nanomaterials and tries to give explanations, avoiding descriptions that are directed to specialists and need specialized education.

To get an idea about the actual size relations, think about a tennis ball, having a diameter of a little more than $6\,cm = 6 \times 10^{-2}\,m$ and compare it with a particle with diameter of $6\,nm = 6 \times 10^{-9}\,m$. The ratio of the diameters of these two objects is 10^7. An object 10^7 times larger than a tennis ball has a diameter of $600\,km$. This simple comparison makes clear: nanoparticles are really small.

The difficulty with nanomaterials arises from the fact that—in contrast to conventional materials—knowledge of material science is not sufficient; rather some knowledge of physics, chemistry, and materials science is necessary. Additionally, as many applications are in the fields of biology and medicine, some knowledge in these fields is necessary to understand these important applications. Figure 1.1 demonstrates that science and technology of nanomaterials are influenced by materials science, physics, chemistry, and for many, economically most important applications, also of biology and medicine.

The number of additional facts introduced to materials science is not that large, therefore, this new situation is not that complicated, as it may look to the observer from the outside. However, the industrial user of nanomaterials, as a developer of new products, has to accept that the new properties of nanomaterials demand deeper insight to the physics and chemistry of the materials. Furthermore, in conventional materials, the interface to biotechnology and medicine depends on the application. This is different in nanotechnology, as biological molecules, such as proteins or DNAs are building blocks, quite often also for applications outside of biology and medicine.

The first question to be answered is: What are nanomaterials? There are two definitions. One, the broadest, says: nanomaterials are materials with sizes of the individual building blocks below 100 nm at least in one dimension. This definition
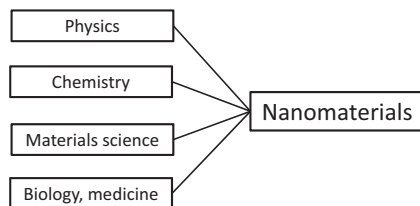
Figure 1.1 To understand and apply nanomaterials, besides knowledge on materials science, a basic understanding of physics and chemistry is necessary. As many applications are connected to biology and medicine; knowledge in these fields are also of advantage.
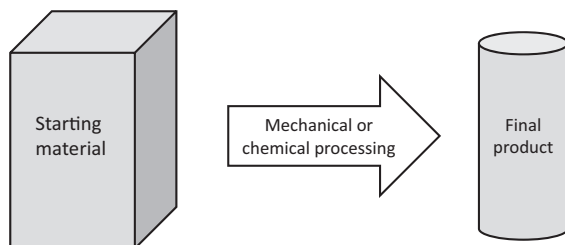
Figure 1.2 Conventional goods are produced by top-down processes, which start from bulk material. Using mechanical or chemical processes, the intended product is obtained.

is quite comfortable, as it does not require deeper thoughts about properties and applications. The second definition is more restrictive. It says that nanomaterials are ones with properties inherently depending on the small grain size. As nanomaterials usually are quite expensive, such a restrictive definition makes more sense.

The main difference between nanotechnology and conventional technologies is the "bottom-up" approach preferred in nanotechnology, whereas conventional technologies usually prefer the "top-down" approach. The difference between these two approaches is explained for example, using the example of powder production. In this context, chemical synthesis is typical of the "bottom-up" approach; whereas, crushing and milling are techniques that may be classified as "top-down" processes. Certainly, there are processes, which may be seen as "in between". A typical example is the defoliation of silicates or graphite to obtain graphene.

The expression "top-down" describes processes starting from large pieces of material to produce the intended structure by mechanical or chemical methods. As long as the structures are in a range of sizes accessible by mechanical tools or photolithographic processes, top-down processes have an unmatched flexibility in application. Figure 1.2 summarizes the basic features of top-down processes.

"Bottom-up" processes are, in general chemical processes starting from atoms or molecules as building blocks to produce nanoparticles, nanotubes or nanorods, thin films or layered structured. Using their dimensionality for classification, these
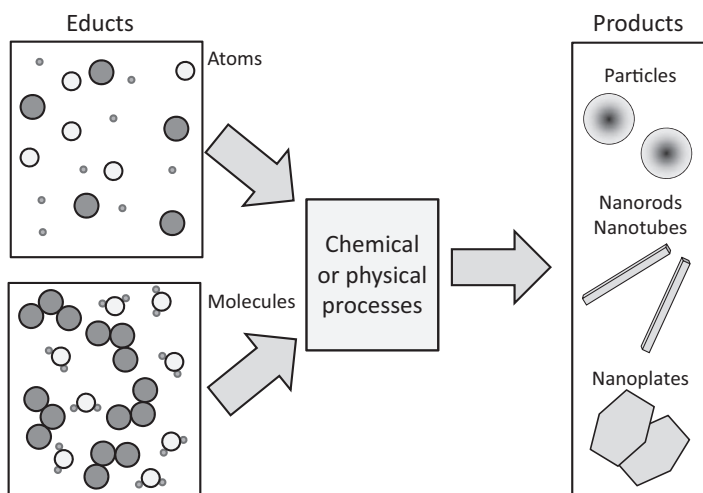
Figure 1.3 Chemical synthesis as bottom-up process. Bottom-up processes are characterized by the use of atoms or molecules as educts. Products are particles, nanotubes or nanorods, or layered structures.

features are also called zero-, one-, or two-dimensional nanostructures. This is graphically demonstrated in Figure 1.3. Bottom-up processes give tremendous freedom in the composition of the resulting products; however, the number of possible structures to be obtained is comparatively small. Ordered structures are obtained by processes that are supplemented by self-organization of individual particles. Often, top-down technologies are described as subtractive ones, in contrast to additive technologies describing bottom-up processes.

Figure 1.4 shows the size ranges of the different processes applied in nanotechnology. Certainly, there is a broad range of overlapping, between the top-down and bottom-up technologies. Most interesting, there are improved top-down technologies, such as electron beam or X-ray lithography entering the size range typical for nanotechnologies. These improved top-down technologies obtain increasing importance, for example, in highly integrated electronic devices.

For industrial applications, the most important question is the price of the product in relation to the properties. As far as the properties are comparable, in most cases, nanomaterials and products applying nanomaterials are significantly more expensive than conventional products. This becomes problematic in cases where the increase in price is more pronounced than the improvement of the properties due to the application of nanomaterials. Therefore, economically interesting applications of nanomaterials are found primarily in areas where properties that are out of reach for conventional materials are demanded. Provided this condition is fulfilled, the price is no longer that important. However, in cases where nanomaterials are in direct competition to well-established conventional technologies, the price is decisive. This fierce price competition is extremely difficult for a young and expensive technology and may lead sometimes to severe, financial
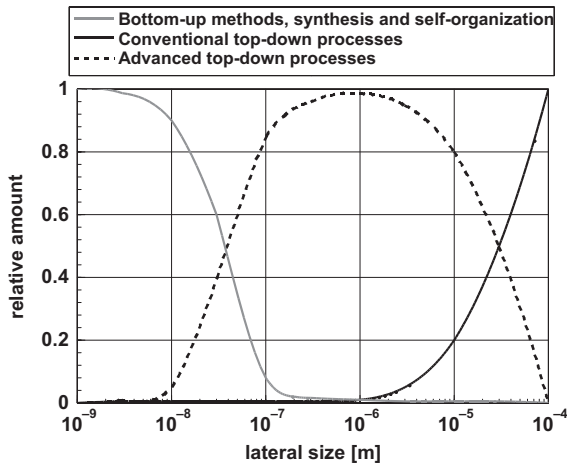
Figure 1.4 Estimated lateral limits of different structuring processes. The size range of bottom-up and conventional top-down processes is limited. New, advanced top-down processes expand the size range of conventional ones and enter the size range typical for bottom-up processes.

problems for newly founded companies. As a general rule one may say that in the case of nanomaterials one is rather selling "knowledge" than "tons".

Nanoparticles are neither new nor unnatural. In nature, for example, some birds and mammals apply magnetic nanoparticles for navigation, a sense called magnetoception. In plants the phenomenon of self-cleaning of leafs caused by nanoparticles at the surface, called the *Lotus* effect is well known and meanwhile technically exploited for self cleaning windows or porcelain ware for sanitary use (see Box 1.1). Man-made nanomaterials, in this case nanocomposites, have been known for more than 2500 years. The Sumerians already produced a red pigment to decorate their pottery. This pigment consisted of gold nanoparticles embedded in a glass matrix stabilized with tin oxide. In science, especially chemistry, suspensions of nanoparticles have been well known since the nineteenth century; however, at that time, this science was called colloid chemistry.

Box 1.1   The Lotus Effect

As an example of a macroscopically observable phenomenon caused by nanostructures, the *Lotus* effect will be explained. It is well known that the leaves of the *Lotus* plant are always clean. This is caused by the fact that the *lotus* leaf can not be moistened, it is hydrophobic, each drop of water flows immediately off the leaf, picking up any dust, which is, in general, hydrophilic.

The *Lotus* effect is caused by an apparent increase of the contact angle between water and a solid surface. The undisturbed situation is depicted in Figure 1.5.
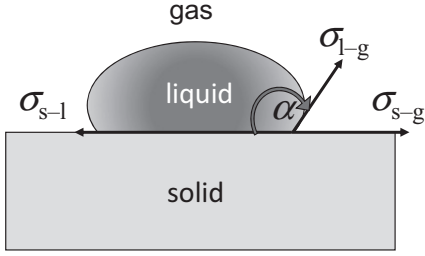
Figure 1.5 Equilibrium of surface stresses at a contact between a solid and a liquid.
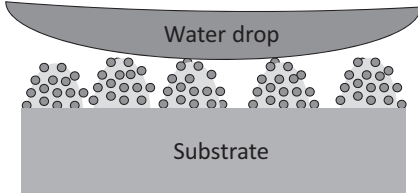
Figure 1.6 Contact situation in the case of the *Lotus* effect. Due to the corrugated surface, one has the impression of a huge contact angle α. However, looking at the points of contact of the individual particles, it is obvious that there is nothing special there, one finds the standard values.

The contact angle, in the case of a water/solid interface, at a maximum of 110° is a result of the equilibrium of the surface stresses.

$$\sigma_{s-g} - \sigma_{s-l} = \sigma_{l-g}\cos\alpha. \tag{1.1}$$

The quantities in Eq. (1.1), σ_{s-g} describe the surface stresses at the interface between the solid and the gas phase, σ_{s-l} the surface stress between the solid and the liquid phase, σ_{l-g} the one between liquid and the gas pas phase, and α is the contact angle. (To be mathematically exact, the surface stress is described by a vector in the tangential plane of the particle. However, for these simplified considerations, it is correct to work with the absolute values of these vectors.)

Assuming a corrugated surface with nanoparticles, as depicted in Figure 1.6, the situation conveys the impression of a larger contact angle. However, this is not correct, as the contact angle to each one of the nanoparticles has the correct value.

2
Nanoparticles – Nanocomposites

2.1
Nanoparticles

Nanoparticles may be classified as zero-dimensional, these are the nanoparticles per se, one-dimensional such as nanorods or nanotubes, and two-dimensional that are, in most cases, plates or stacks of plates. As a typical example of particles, Figure 2.1 displays an electron micrograph of zirconia (ZrO_2) powder, zero-dimensional objects.

The particles depicted in Figure 2.1 show a size of ca. 7 nm. It is important to mention that the particles are in a very narrow range of sizes. This may be important, as many properties of nanomaterials are size dependent. On the other hand, many applications do not need such sophisticated material or they just need a broad variation of properties. Therefore, in many cases, cheaper materials with broader particle size distribution, as is depicted in Figure 2.2a, are necessary or, at least, sufficient. The material depicted in this figure shows particles in the size range from 5 to more than 50 nm. Such materials are perfectly suited for applications as pigments, UV-absorbers, etc.

A further interesting class of particles may be described as clusters of extremely small particles. Typical examples of this type of materials are most of the amorphous silica particles, well known as "white soot", and amorphous Fe_2O_3 particles. Typically, particles of this type, as shown in Figure 2.2b, are applied as catalysts.

In producing bulk nanocomposites, the central problem is to obtain a perfect distribution of the particulate phase in the matrix. Processes based on mechanical blending or synthesizing the two phases separately and mixing during the step of particle formation, never lead to homogeneous products on the nanometer scale. Provided there are no preferences and the process of blending is random, the probability that two or more particles are touching each other and form a cluster is very high. Usually, in such a mixture, one wants to obtain a relatively high concentration of "active" particles, carrying the physical property of interest. Assuming, in the simplest case, particles of equal size, the probability p_n that a number of n particles with the volume concentration c are touching each other, is $p_n = c^n$. The consequences of this simple relation are severe: for example, assuming a concentration of 0.30, the probability of two touching particles is 0.09 and for
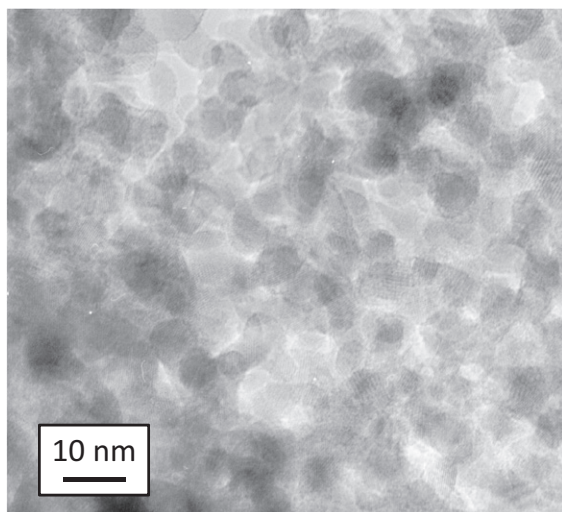
Figure 2.1 Electron micrograph of zirconia, ZrO_2 powder. A very narrow distribution of grain sizes is characteristic of this material. In many cases, this is predicated as important, because the properties of nanomaterials depend on the grain size [1].
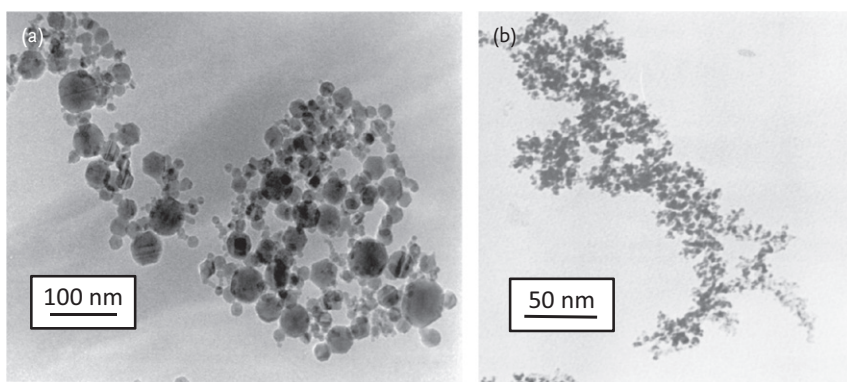
Figure 2.2 Two extremely different types of nanoparticulate Fe_2O_3 powder. (a) Industrially produced nanomaterial with broad particle size distribution, typically of application as pigments or UV-protection. Courtesy Nanophase, Nanophase Technologies Corporation, 1319 Marquette Drive, Romeoville, IL 60446. (b) Nanoparticulate powder consisting of clusters of amorphous particles with sizes around 3 nm. Catalysis is the most important field of application of this material with extremely high surface. Courtesy MACH I, Inc. 340 East Church Road, King of Prussia, PA 19406 USA.

three particles 0.027. Lastly, it is impossible to obtain the intended perfect distribution of two phases by blending. Further-reaching measures are necessary.

Except for properties related to grain boundaries, the special properties of nanomaterials are ones of single isolated particles that are altered or even lost in the case of interacting particles. Therefore, most of the basic considerations are related to isolated nanoparticles as the unavoidable interaction of two or more particles
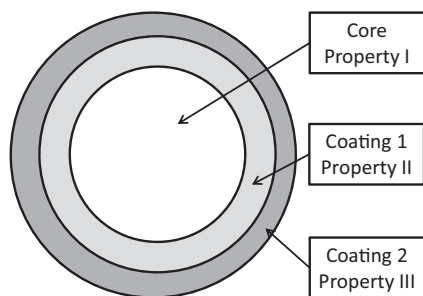
Figure 2.3 Typical design of a core–shell nanocomposite particle. The properties of the core and coating 1 are, in most cases, selected to the demand of the physics (e.g., magnetic and luminescence); the second coating is selected in view of the interaction with the surrounding medium (e.g., hydrophilic or hydrophobic) [2].

may change the properties significantly. Certainly, this is senseless in view of the technical applications.

The two problems described above and to exploit these very special properties of nanoparticles, composite particles of the core–shell type, with a second phase acting as distance holder were developed. The necessary distance depends on the phenomenon to be suppressed; it may be smaller, in the case of tunneling of electrons between particles, and is larger in the case of dipole–dipole interaction. Furthermore, such composite particles can be designed in a way to combine different "incompatible" properties, such as magnetism and luminescence. The typical design of these particles is depicted in Figure 2.3.

The core–shell composite design, as depicted in Figure 2.3 is typical for advanced applications, for example, in medicine or biotech. Such a core–shell nanocomposite consists of a core, carrying the property, which demand the largest volume, for example, magnetism. The property of Coating 1, is the case of a bifunctional particle, for example, luminescence. The outermost layer, Coating 2 in Figure 2.3 has to mediate with the surrounding medium. Therefore, in most cases, it is either hydrophilic or hydrophobic. In many medical applications, the outermost layer may consist of a protein or enzyme, which is characteristic for a specific type of cells.

Typical examples for coated particles are shown in Figures 2.4a–c. In Figure 2.4a, a ceramic core (ZrO_2), which is coated with a ceramic layer (Al_2O_3), an amorphous one, is displayed. In Figure 2.4b, the ceramic core (Fe_2O_3) is coated with a polymer (PMMA). This type of composite is often used as a special magnetic material. As a third variety, a ceramic particle (TiO_2) decorated with a metal (Pt) is displayed in Figure 2.4c. Coating of ceramic particles with thin metallic layers is, because of the relation in the surface energy, in most cases impossible. Instead of a coating, one obtains a decoration of the core with metallic clusters. This type of composite is often used as a catalyst.

Most interesting are the particles displayed in Figure 2.4a, as they show an important phenomenon, characteristic of nanomaterials. This figure shows three coated ceramic particles. The particle in the center of the figure originates from
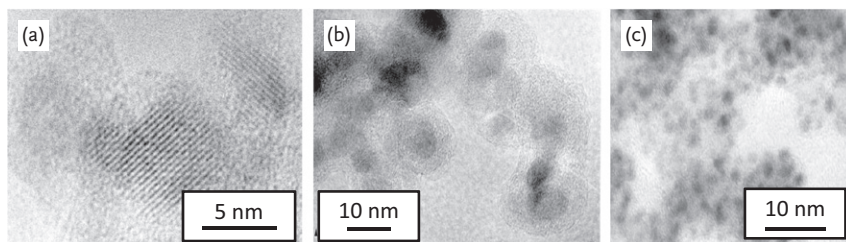
Figure 2.4 Three typical examples of nanocomposite particles. In (a), a crystallized ceramic core (ZrO_2) is coated with an amorphous ceramic layer (Al_2O_3). It is also possible (b) to coat a ceramic core (Fe_2O_3) with a polymer. Coating a ceramic core (TiO_2) with a thin metal (Pt) layer (c) is impossible because of the difference in the surface energies. In such a case, tiny metal clusters decorate the ceramic particles [1, 3]. (a, b: Reproduced with permission by Elsevier; c: Vollath, Szabó unpublished results.)
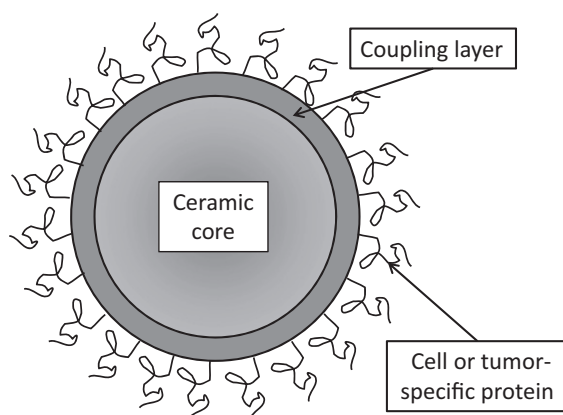
Figure 2.5 Nanocomposite particle for application in biology or medicine. The ceramic core may be magnetic, luminescent, or even bifunctional. The cell or tumor-specific proteins or enzyme at the surface, necessary for coupling of the particle at the intended type of cells, need a coupling layer as; in general, these molecules cannot be attached directly at the ceramic surface.

coagulation of two zirconia particles. As the process of coagulation was incomplete, there are concave regions of the zirconia core visible. During the coating process, these concave areas were filled with alumina; therefore, finally, the coated particle has only convex surfaces. This minimizes surface energy; an important principle acting in any type of nanomaterial.

As already mentioned above, multifunctional particles are widely used in biology and medicine. For this application, it is necessary to add proteins or other biological molecules, which are characteristic of cells, where the particle should attach at the surface of the particles. Biological molecules are attached at the particles only via specific types of molecules, accommodated in the outermost coupling layer [4]. The development of these coupling layers is one of the crucial points for this application. Figure 2.5 displays such a biologically functionalized particle. The

Dimensionality of the composites
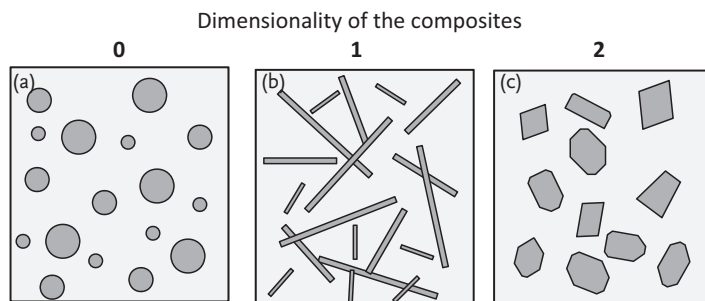
Figure 2.6 Three basic types of nanocomposites. (a) Composite consisting of zero-dimensional particles in a matrix. In the ideal case, the individual particles are not touching each other. (b) One-dimensional nanocomposite consisting of nanotubes or nanorods distributed in a second, in general, polymer matrix. (c) Two-dimensional nanocomposite consisting of platelets embedded in a second matrix.

ceramic core, usually, is either magnetic or luminescent, or multifunctional. In the design depicted in Figure 2.5, the coupling layer may consist of an appropriate polymer or a type of glucose; however, in many cases, hydroxylated silica is sufficient, too. At the surface of the coupling layer, the biological molecules, such as proteins or enzymes are attached.

Bulk nanocomposites – as described in this chapter – are composite materials with at least one phase exhibiting the special properties of a nanomaterial. In general, random arrangements of nanoparticles in the composite are assumed. Figure 2.6 displays the most important three different types of nanocomposites. The types differ in the dimensionality of the second phase. This phase may be zero-dimensional, isolated nanoparticles, one-dimensional, consisting of nanotubes or nanorods, or two-dimensional composites with platelets as second phase; one may also think of stacks of layers. In most cases, such composites are close to zero-dimensional ones. However, some of them with polymer matrix have existing mechanical and thermal properties; therefore, they are used primarily in the automotive industry. In particular, the latter ones will be discussed in detail in Chapter 11.

A typical electron micrograph of a nearly ideal nanocomposite, a distribution of zirconia (ZrO_2) nanoparticles in an alumina (Al_2O_3) matrix is displayed in Figure 2.7. This figure displays a micrograph of a sintered material. The starting material was alumina-coated zirconia powder. It is obvious that the particles remain separated. For products of this type, it is essential that there is no mutual solubility between the core and coating. After sintering of the powder, consisting of coated nanoparticles, the coating will form the matrix.

Looking at applications, one will find zero-dimensional composites of the type depicted in Figure 2.4a quite often in connection to magnetic materials. One- and two-dimensional nanocomposites are often found in applications where high mechanical strength is demanded. Looking at carbon nanotubes (one-dimensional)
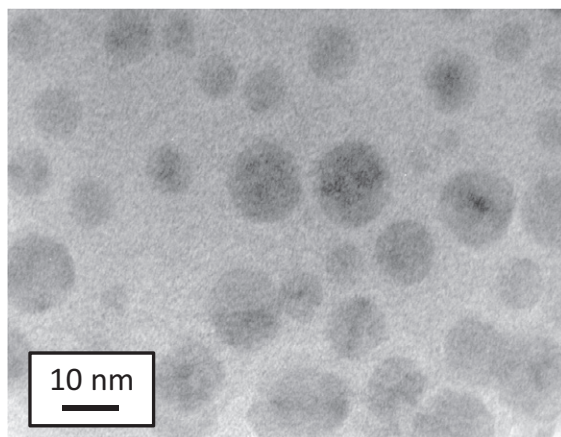
Figure 2.7 Transmission electron micrograph of a zero-dimensional nanocomposite. It depicts a composite zirconia particles embedded in an alumina matrix. The specimen was produced from zirconia particles coated with alumina. This micrograph was taken from an ion-beam-thinned sample. It is essential to realize that there is a high probability that particles are not touching each other, because they are lying in different planes [3]. (Reproduced with permission by Springer.)
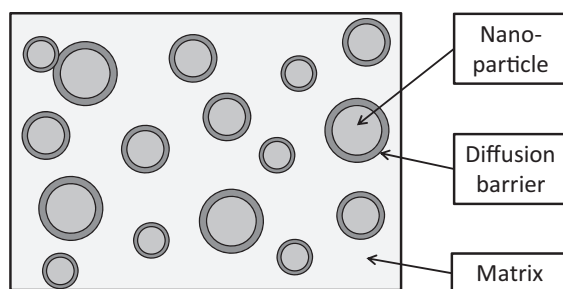
Figure 2.8 Zero-dimensional nanocomposite. To avoid dissolution in the matrix, the particles are coated with a diffusion barrier.

or graphene (two-dimensional) as a filler, a very important application is found in the field of optically transparent electrical conductors. Because of the large aspect ratio of these particles, electrical conductivity is obtained already with extremely small concentrations of these particles.

Practically, the composites, as depicted in Figures 2.4a,b exist primarily using a polymer matrix. In all the other cases, there is the possibility that there is a mutual solubility between the nanoparticles and the matrix. To avoid dissolution of the particles, often it is necessary to coat the particles with a diffusion barrier. This situation is depicted in Figure 2.8.

Figure 2.8 displays the oldest, man-made type of nanocomposite with more or less spherical nanoparticles. This composite is realized in the well-known gold-ruby glass. It consists of a glass matrix with gold nanoparticles as second phase.

However, as gold can be dissolved in the glass matrix, a diffusion barrier is necessary. In the case of gold-ruby glass the diffusion barrier consists of tin oxide. In colloid chemistry, this principle of stabilization is well known as "colloid stabilization". This material was produced for the first time by the Sumerians in the seventh century BC and re-invented by *Kunkel* in Leipzig in the seventeenth century. It is interesting to note that the composition used by the Sumerians was practically identical to the one reinvented by *Kunkel* and that is used nowadays.

Furthermore, the properties of a bulk solid made of coated nanoparticles may be adjusted gradually with the thickness of the coating. Depending on the requirements of the application, the coating material may be ceramic or polymer. Coating nanoparticles with a second and third layer leads to the following improvements:

- The distribution of the two phases is homogenous on a nanometer scale.

- The kernels are arranged in a well-defined distance. Therefore, the interaction of the particles is controlled.

- The kernel and one or more different coatings may have different properties. This allows the combination of properties in one particle that are never found together in nature. Additionally, by selecting a proper polymer for the outermost coating, it is possible to adjust the interaction with the surrounding medium.

- During densification, i.e. sintering, the growth of the kernels is thwarted, provided core and coating show no mutual solubility. An example for this is depicted in Figure 2.7.

These arguments demonstrate that the most advanced type of nanocomposites are coated nanoparticles. They allow not only the combination of different properties in one particle, but also in bulk materials.

In addition to the composites displayed in Figures 2.6 and 2.7, one observes nanocomposites with regular well-ordered structure, as displayed in Figure 2.9.

In general, self-organization processes in the case of spherical filler particles or mechanical stretching are appropriate mechanisms to create this type of composite, if the filler particles are one- or two-dimensional. Successful realization of self-organization processes, leading to structures as depicted in Figure 2.9a, requires particles nearly identical in size.

2.2
Elementary Consequences of Small Particle Size

2.2.1
Surface of Nanoparticles

The first and most important consequence of the small particle size is the huge surface area. To get an impression of the importance of this geometric

(a)

(b)
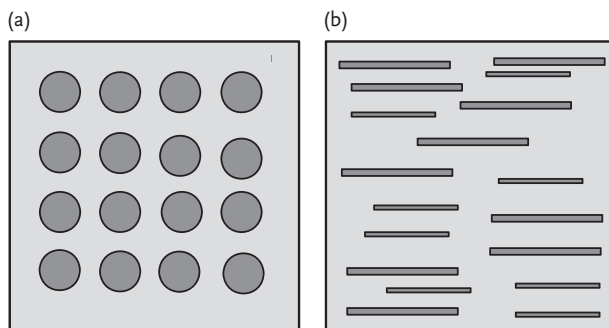
Figure 2.9 Typical examples of ordered nanocomposites. In the case of a zero-dimensional filler (a), it is necessary that the particles are more or less equal in size; whereas, in the case of one- or two-dimensional fillers, in general, the particles have different size; however, they are oriented in parallel.

variable of nanoparticles, the surface over volume ratio is discussed. Simple calculations show that the ratio surface / volume is inversely proportional to the diameter of the particle. Similar to the surface over volume ratio for one particle, in molar quantities, this ratio is inversely proportional to the particle diameter, too.

Box 2.1   Surface of Particles

Assuming spherical particles with the diameter d, the surface area a of one particle is given by

$$a = \pi d^2.$$

The volume v of this particle is

$$v = \frac{\pi}{6} d^3.$$

The surface/volume ratio R

$$R = \frac{a}{v} = \frac{6}{d}. \tag{2.1}$$

This ratio is inversely proportional to the particle size. The surface A per mol, a quantity important in thermodynamics, is

$$A = na = \frac{M}{\rho \dfrac{\pi d^3}{6}} \pi d^2 = \frac{6M}{\rho d}, \tag{2.2}$$

with n the number of particles per mol, M the molecular weight, and ρ the density of the particles.
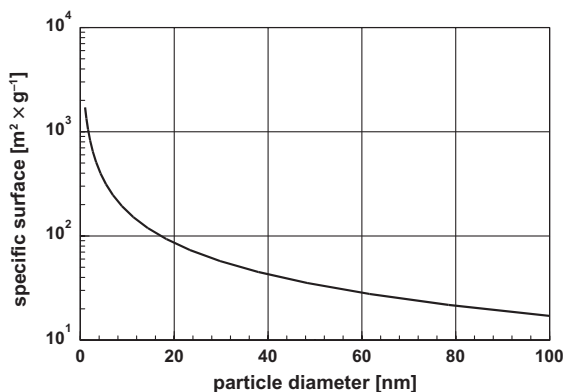
Figure 2.10 Theoretical dependency of the specific surface area of the particle diameter. Due to the agglomeration of the particles, experimentally these values are not realized.

To get an idea about the magnitudes of surfaces that may be expected in case of nanoparticles, Figure 2.10 displays the theoretical surface of one gram of a powder consisting of spherical particles with a density of $3.5 \times 10^3 \, \text{kg m}^{-3}$ (alumina).

In Figure 2.10, the surface is given in the non-SI unit $\text{m}^2 \, \text{g}^{-1}$. This unit is applied because this is the only unit that is generally accepted for the specific surface area. In general, the specific areas visible in Figure 2.10 are never realized experimentally. The reason for this discrepancy is found in the agglomeration of the particles. The influence of this phenomenon increases with decreasing particle diameter, as the influence of the *van der Waals* forces increases too. (*Van der Waals* forces are weak interactions between molecules or small particles having their origin in quantum dynamics. These forces are neither covalent nor based on electrostatic or dipolar interaction.) Experimentally, the largest values are measured with activated charcoal in the range of $2000 \, \text{m}^2 \, \text{g}^{-1}$ and finely dispersed amorphous silica with values up to $600 \, \text{m}^2 \, \text{g}^{-1}$.

The surface is such an important topic for nanoparticles that there is a full chapter devoted to surface and surface-related problems (see Chapter 3).

2.2.2
Thermal Phenomena

Each isolated object, in this case a nanoparticle, has a thermal energy, which is directly proportional to the temperature. Furthermore, each object tries to be in a state where the energy is a minimum. Generally, this is a stable state. Certainly, energetically speaking, there are other states with higher energy possible. The energy difference between the state of lowest energy and the next one may depend for example, on the mass of the particle. As the mass of the particle decreases with particle diameter, there is the possibility that, starting at a sufficiently high temperature, the thermal energy gets larger than the difference between the

two neighboring states. Now the system is no longer stable, and the system fluctuates.

Box 2.2 Thermal Instability

Thermal energy u_{th} of an isolated particle is given by

$$u_{\text{th}} = kT,$$

with k the *Boltzmann* constant and T the temperature.

Assuming an energy that depends on the volume of the particle $u(v)$. The system is no longer stable, it fluctuates, if the condition

$$u(v) \le kT \qquad (2.3)$$

is fulfilled.

A simple example: The energy necessary to lift a particle with the density ρ the elevation x.

$$u(v) = \rho v x.$$

This particle moves around thermally and jumps up to a height x, if the condition

$$\rho v x \le kT \quad \text{or} \quad T \ge \frac{\rho v}{k} x$$

is fulfilled.

Schematically, this situation is depicted in Figure 2.11.

Looking at thermal instabilities (fluctuations), one can design a simple example. One can ask for the size of a zirconia particle ($\rho = 5.6 \times 10^3\,\text{kg m}^{-3}$) that could be lifted at room temperature to a height equal to its diameter. The answer is somewhat surprising, the diameter of 1100 nm. If one asks, how high could a particle
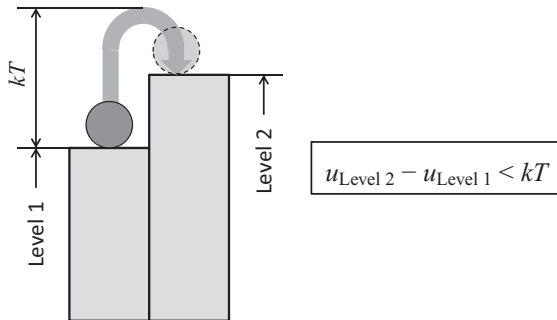
Figure 2.11 Schematic visualization of thermal fluctuation. In this case, the thermal energy is larger than the energy difference between level 1 and level 2.

of 5 nm diameter jump these simple calculations lead to a height of more than one meter. Certainly, these games with number do not have physical reality; however, they indicate that nanoparticles that are not fixed at a surface are moving around. Doing electron microscopy, this dynamic becomes reality. Provided the particles and the carbon film on the carrier mesh are clean, the particles of the specimen move around like ants on the carbon film. This makes electron microscopy difficult.

The thermal instability presented here, demonstrates a simple consequence of smallness; however, other physical properties may change significantly and this may lead to new properties. The most important phenomenon of this group, superparamagnetism, will be described in Chapter 8 on magnetic properties. Fluctuations are also observed in connection with phase transformation, for example, melting and crystallization of nanoparticles.

2.2.3
Diffusion Scaling Law

Diffusion is controlled by the two *Fick*'s laws. Solutions of these equations, important for nanotechnology, say that the squared mean diffusion path of the atoms is proportional to the time. In other words: Assuming the particle diameter as the diffusion path, doubling of the diameter leads to a four-fold time needed for diffusion.

Box 2.3   Scaling Law of Diffusion

Mathematically, diffusion is described by the two laws of *Fick,* a set of two partial differential equations. The solution, important for the considerations connected to nanoparticles says:

$$\langle x \rangle^2 \propto Dt. \tag{2.4}$$

The brackets $\langle \ \rangle$ stand for the mean value of an ensemble; the quantity x stands for the diffusion path; therefore, $\langle x \rangle^2$ is the mean square of the diffusion path, D is the diffusion coefficient and t the time. Generally, the diffusion coefficient depends exponentially on the temperature,

$$D \propto \exp\left(-\frac{q}{kT}\right), \tag{2.5}$$

which means that the diffusion will get faster with increasing temperature. The quantity q is the activation energy.

This scaling law for diffusion has dramatic consequences when applied to nanomaterials. As an example, the homogenization time necessary in the case of conventional and nanomaterials are compared. Conventional materials usually have grain sizes of around 10 µm. It is well known that at elevated temperatures,

these materials need homogenization times in the range of many hours. Looking at materials with grain sizes around 10 nm, which is 10^{-3} of the conventional grain size, according to the scaling law of diffusion Eq. (2.3) the time for homogenization is reduced by a factor of $\left(10^3\right)^2 = 10^6$. This means that the homogenization time of hours, for conventional materials, is reduced to milliseconds; for nanomaterials. Lastly, this says that homogenization is virtually instantaneous. This phenomenon is often called "instantaneous alloying". One may also say: Each thermally activated reaction will happen nearly instantaneously. Therefore, it is not possible to produce nonequilibrium systems of nanomaterials, well known for conventional materials, at elevated temperatures.

The possibility of nearly instantaneous diffusion through nanoparticles is exploited technically. The most important example is the gas sensor applying the variation in the electric conductivity due to changes in the stoichiometry of oxides. (The stoichiometry describes the ratio oxygen / metal.) Variations of stoichiometry are often observed in oxides of transition metals. Because of the small particle size, any change in the oxygen potential in the surrounding atmosphere changes the stoichiometry of the sensing particles immediately. In contrast to conventional gas sensors, the time response is now controlled by the gas diffusion through the narrow channels in between the nanoparticles. Figure 2.12 displays the general design of such a sensor.

Such a gas sensor is set up on a conductive substrate on a carrier plate. The surface of this conductive layer is covered completely with the oxide sensor nanoparticles. Transition-metal oxides, well suited for this purpose are example, TiO_2, SnO_2, Fe_2O_3. On the top of the oxide particle layer, the counterelectrode, a gas-permeable conductive layer is applied. Variations in the oxygen potential in the surrounding atmosphere changes the stoichiometry of the oxide, and, therefore, the electrical conductivity. This process is reversible.
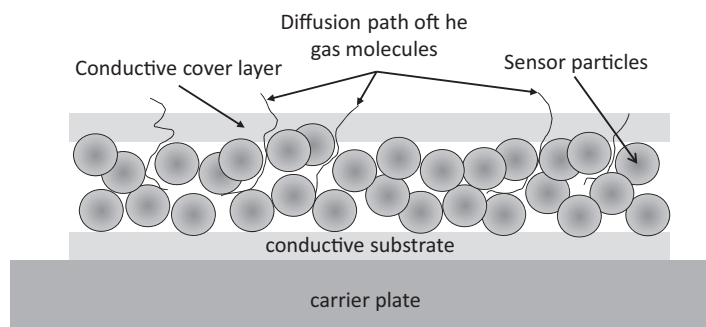
Figure 2.12 General layout of a gas sensor based on nanoparticles. This gas sensor consists of a layer of sensing nanoparticles, in most cases SnO_2, placed on a conductive substrate. The whole system is covered with a gas-permeable electrode. The diffusion within the nanosized grains is no longer time controlling, it is rather the diffusion in the open-pore network in-between the grains.
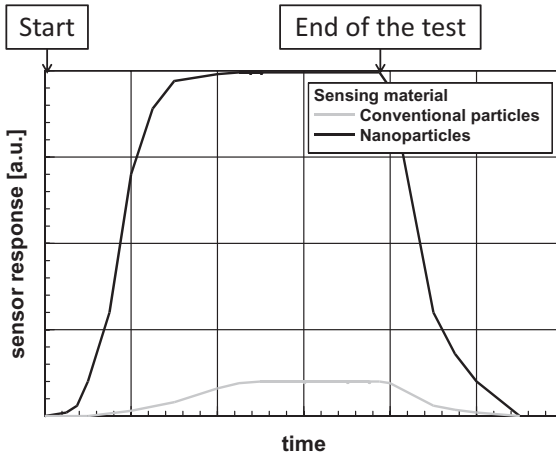
Figure 2.13

Figure 2.13 Comparison of the sensor response between a sensor using conventional particles and one applying nanoparticles.
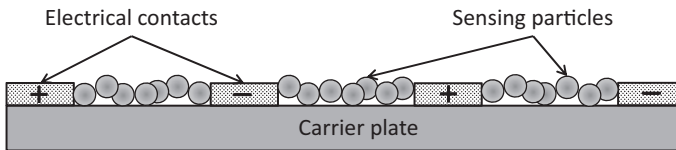
Figure 2.14

Figure 2.14 Alternative design of a gas sensor using nanoparticles. In this design, the electrodes are fixed on a carrier plate (in the figure, the electrodes are marked by "+" or "−", symbolizing electrical connectors for DC). Compared with the design depicted in Figure 2.12, this design has the advantage that it is possible to assemble many of these sensors on one chip.

Figure 2.13 displays schematically a comparison of the response of a sensor made of conventional material with grains in the micrometer size range and a sensor using nanomaterials.

Analyzing Figure 2.13, one realizes that the response of the sensor using nanoparticles is faster and the signal is better. Having the diffusion scaling law in mind, Eq. (2.4), one expects an even faster response. In a sensor using nanoparticles, as depicted in Figure 2.13, the time constant depends primarily on the diffusion of the gas molecules in the open-pore network and through the conducting cover layer.

Figure 2.14 displays a further design for gas sensors using particulate oxides as the detector; Figure 2.15 displays the topview of such a sensor. This design avoids the response-delaying conductive surface layer, however, the electric path through the sensing particles is significantly longer. With respect to fabrication, this type of sensor is more economical, as the carrier plate with electrical leads

Electrical connections   Sensor layer   Electrodes
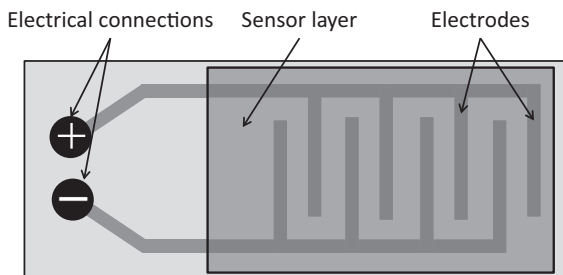
Figure 2.15 Top view of a gas sensor of the design depicted in Figure 2.13. The crucial advantage of this design is the fact that the carrier plate with the electrical leads can be produced independently in large quantities.

can be produced in large quantities independently of the sensor material. The layer with the sensing properties is producible either by sputtering or by wet chemical methods.

The design depicted in Figures 2.13 and 2.14 is thus more progressed as it can be miniaturized, a fact that allows the integration of many of these sensor elements on a chip. This has two major advantages: (i) By averaging of many signals, the noise can be reduced significantly; therefore, the measured signal is more reliable, and (ii) the whole sensor chip can be coated with a diffusion layer, for example, made of silica or alumina, of varying thickness and heated in a way that each sensing element is at a different temperature. Depending on the molecular size the time response of the different elements depends on the thickness of the surface coating and the temperature of the individual element. After empirical calibration, such a design is able to give, besides the oxygen potential (this is the thermodynamic quantity, which is, in technical applications, mathematically converted to concentrations), information on the gas species, too.

References

1 Vollath, D., and Szabó, D.V. (2002) *Innovative Processing of Films and Nanocrystalline Powders* (ed. K.-L. Choi), Imperial College Press, pp. 219–225.

2 Vollath, D. (2010) *Adv. Mater.*, **22**, 4410–4415.

3 Vollath, D., and Szabó, D.V. (1999) *J. Nanoparticle Res.*, **1**, 235–242.

4 Niemeyer, C.M. (2001) *Angew. Chem. Int. Ed.*, **40**, 4128–4158.

3
Surfaces in Nanomaterials

3.1
General Considerations

The surface forms a sharp interface between a particle and the surrounding atmosphere or between a precipitated phase and the parent phase. In mathematics, the surface of a body, for example, a sphere or a polyhedron, is clearly defined. As already mentioned in Chapter 2, in a sphere, the ratio surface over volume is indirectly proportional to the diameter. This is different in the case of a real, physically existing material. In this case, one has to distinguish between free surfaces in the case of particulate materials and grain boundaries in bulk material. As nanoparticles are small, they have large surfaces. However, what is a surface of a real solid? The answer must not be restricted to the geometrical surface. Looking at a solid and its behavior, one has to take note of the surface-influenced volume. A simplified model assumes a layer with a thickness δ at the surface. Depending on the property in question, this thickness is found experimentally in the range between 0.5 and 1 nm.

Box 3.1   Physical Surface of Particles

Assuming a sphere with the diameter d and a layer with the thickness δ, which is influenced by the surface. In this case the volume of this shell is

$$v_{\text{shell}} = \frac{\pi}{6}d^3 - \frac{\pi}{6}(d-\delta)^3 = \frac{\pi}{6}\left[d^3 - (d-2\delta)^3\right], \tag{3.1}$$

Now a dimensionless volume ratio R^* is defined as:

$$R^* = \frac{v_{\text{shell}}}{v_{\text{sphere}}} = \frac{\frac{\pi}{6}\left[d^3 - (d-2\delta)^3\right]}{\frac{\pi}{6}d^3} = 1 - \left(\frac{d-2\delta}{d}\right)^3. \tag{3.2}$$

This ratio approaches one if $d \approx 2\delta$.

Figure 3.1 depicts the ratio of the surface-influenced volume over the total volume of the particle. For reasons of simplicity, the shape of the particles was assumed to be spherical.

Scrutinizing this graph, one realizes that in case of a 5-nm particle, 49% or 78%, respectively, of the volume belongs to the surface-influenced volume. In the case of smaller particles, the relative amount of material influenced by surface phenomena is significantly larger. There are applications where this has severe consequences. For example, in a first approximation the magnetic moment at saturation and the susceptibility depend primarily on the part of the particles, which is not influenced by the surface; hence, magnetic nanoparticles exhibit only low values for these parameters (see Chapter 8). Lastly, the considerations, valid for free nanoparticles, may be adapted for nanocrystalline bulk materials; one has just to replace the term "free surface" by grain boundaries. Schematically, this situation is depicted in Figure 3.2. It is interesting to note that the atoms located
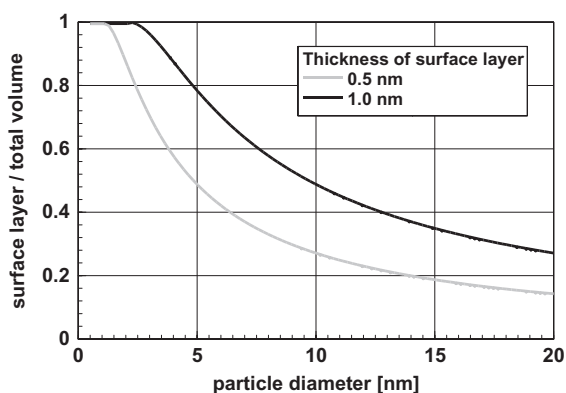
Figure 3.1 Ratio of the surface shell volume over the total volume of the particle. The thickness of the surface layer was selected to be 0.5 or 1.0 nm.
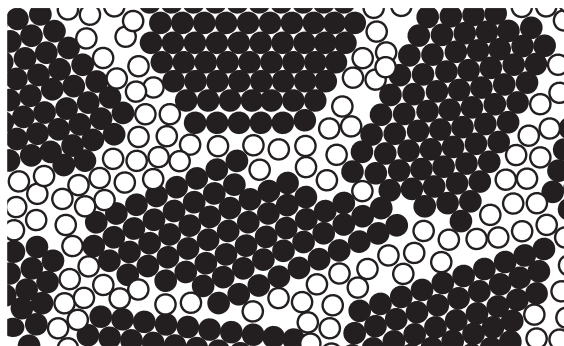
Figure 3.2 Nanocrystalline material. The full circles represent atoms in the crystallized phase, whereas the open circles represent atoms at the grain boundary.

in the grain boundaries are highly mobile; sometimes this behavior is called "liquid-like".

Surfaces and grain boundaries are connected to surface energy. The surface energy is proportional to the surface. In this context, as the surface of the particle, the geometrical value is used.

Box 3.2   Surface Energy of Particles

One particle with a geometrical surface $a = \pi d^2$ and a specific surface energy γ has a surface energy of

$$u_{\text{surface}} = a\gamma. \qquad (3.3)$$

With respect to thermodynamic considerations, the surface energy per mol is needed.

The number of particles per mol $N = \dfrac{M}{\rho v}$ and the volume of one particle is $v = \dfrac{\pi}{6} d^3$.

(M is the molar weight, d is the particle diameter, ρ is the density of the material). One obtains for the surface energy per mol

$$U_{\text{surface}} = N\gamma a = \frac{M}{\rho v}\gamma a = \frac{M}{\rho}\frac{6}{\pi d^3}\gamma \pi d^2 = \gamma 6 \frac{M}{\rho}\frac{1}{d}. \qquad (3.4)$$

Equation (3.4) shows that the surface energy per mol is indirectly proportional to the particle diameter.

Please note: Quantities related to one particle are printed in lower case letters and quantities valid for one mol in capital letters.

It is important to realize that the surface energy per mol is inversely proportional to the particle diameter; this means that the surface energy increases drastically when the particle size gets very small. In cases related to very small particles, this has dramatic consequences.

3.2
Surface Energy

A model to explain the origin of surface energy starts with an infinitely extended solid. As a next step, the production of a particle by dividing this large chunk of material into small particles is assumed. To do this, the bonds between neighboring atoms are separated. (Within this introductory text, the word atom is used equally for atoms, ions and molecules.) Now, between each two atoms in the
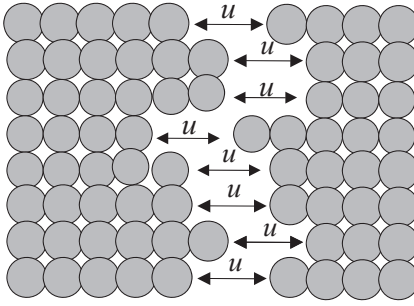
Figure 3.3 Creating new surfaces, for example, by breaking a larger part into smaller pieces requires the energy *u* for each bond to be broken.
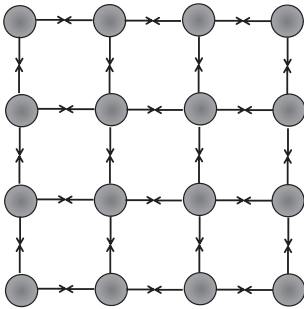
Figure 3.4 Forces acting between atoms at lattice positions. Because of the reduced number of neighbors, the atoms at the surface are pulled in the direction to the interior of the particle. However, this does not lead to a pressure comparable with a hydrostatic pressure, rather, it leads to a stress in the surface, the surface stress. For the estimation of thermal effects, for example, during coagulation of two particles, the sum value of the surface energy of both particles, Eq. (3.6), is the ruling one.

lattice, the energy of bonding, *u* is needed to break the bonds. This is demonstrated in Figure 3.3.

Therefore, to break a larger part of material into smaller pieces, each bond between two neighboring atoms must be broken. After breaking, two new surfaces emerge. Hence, on both sides, for each atom at the new surface, half of the binding energy is stored at the surface. In the interior of a particle, the atoms are in a mechanical equilibrium of binding forces, fixing them at their lattice positions. Arrows mark these forces in Figure 3.4. It is obvious that atoms at the surface have lost bonds at the outside. Because of the reduced number of neighbors, at each atom at the surface, a force acts perpendicular to the surface. At a plane surface (to be mathematically exact: the surface of a plane infinite half-space),

against any intuition, this does not lead to a hydrostatic pressure in the material, rather to a stress in the surface plane. Consequently, the surface stress deforming the surface results in the surface stretching. In a spherical particle of limited size, the situation is different. Caused by the curvature, in connection with the surface stress, a hydrostatic pressure, comparable with one stemming from a gas or a liquid at the outside, in the particle comes into action. This allows modeling of the surfaces of particles as a skin made of elastic material. Consequently, the rubber skin model of the surface was developed.

Box 3.3   Origin of Surface Energy

Breaking a chunk of material into two parts forms two surfaces, with n broken bonds. The binding energy u per atom is split to both sides. Hence, for breaking, the energy

$$u_{\text{break}} = n\frac{u}{2}.$$

The specific energy to break the bonds is

$$\gamma_0 = N^*\frac{u}{2}, \tag{3.5}$$

where N^* is the number of broken bonds per square meter. Due to the uncompensated bonds at the surface, a force f perpendicular to the surface emerges. If a is the area occupied by one atom, the resulting surface stress is

$$\sigma = \frac{f}{a}.$$

The stress σ leads to a surface stretch ε_s, assumed constant in any direction of the tangent plane of the particle, of the surface, (To be mathematically exact, σ and ε_s are vectors in the tangential plane of the surface. For reasons of simplicity, they are replaced by their absolute values. In the context of these considerations, this does not make any difference.) leading to the contribution γ_s to the surface energy.

$$\gamma = \gamma_0 + \gamma_s. \tag{3.6}$$

The contribution γ_0 exists only in the case of solids; for liquids $\gamma_0 = 0$ is valid.
   The pressure p caused by surface stress σ is given by

$$p = 4\frac{\sigma}{d}. \tag{3.7}$$

For more details see [1].

Even when the situation at the surface can be described by quite plausible physical and exact mathematical models, the experimental situation is very poor. Usually, it is impossible to discriminate between the total surface energy and the surface stress. Therefore, it is necessary to use the values published for the surface energy for all applications. From the considerations above it is clear that the determination of the surface energy by measuring the interface stress is not sufficient. These methods deliver only the surface stress, whereas calorimetric measurements, e.g. connected to grain growth, result in a value for the surface energy. Lastly, only these values are useful for thermodynamic considerations.

In the case of anisotropic lattices, the relations are more complex since there are directional bonds. The surface energy of these materials depends on the direction; hence, to minimize surface energy, these materials crystallize in rods or platelets. Furthermore, surface-active substances can influence the surface energy. Technically, this fact is used for the production of one- or two-dimensional particles such as needles or plates.

In the case of small particles, the surface energy dominates the behavior. Whenever possible, particles that are touching each other will coagulate with a temperature flash. Figure 3.5 displays a graph showing the temperature flash occurring as a consequence of the coagulation of two spherical particles of equal size. For reasons of simplicity, it is assumed the resulting particle is spherical too. Furthermore, as material, zirconia particles with a density $\rho = 5.6 \times 10^3 \, \mathrm{kg \, m^{-3}}$, a surface energy $\gamma = 1 \, \mathrm{J \, mol^{-1}}$, and a heat capacity $C_\mathrm{p} = 56.2 \, \mathrm{J \, mol^{-1} \, K^{-1}} \triangleq 781 \, \mathrm{J \, kg^{-1}}$ was selected. (For reasons of simplicity, the materials data are those of conventional materials; the value for the surface energy is a rough approximation. According to more recent results, this value may be too low.) From Figure 3.5 one learns that, in the case of small particles, the temperature flash may be in the range of a few hundred Kelvin. Considering more recent values of the surface energy, which are a few times higher, the temperature flash may further increase by a few hundred *Kelvin*.
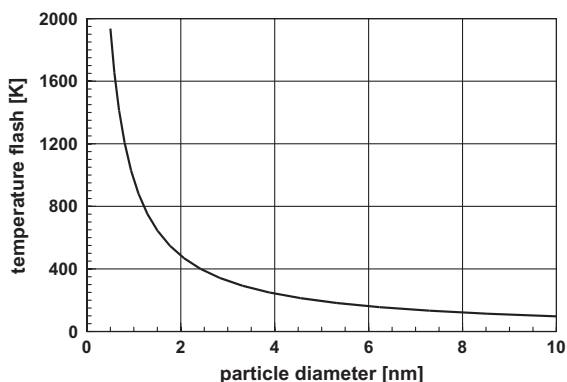

Figure 3.5 Temperature flash occurring as a consequence of the adiabatic coagulation of two spherical zirconia particles of equal size.

Box 3.4 Temperature Flash Caused by Particle Coagulation

During coagulation of two particles with the diameter d, the surface $a_{resulting}$ of the new particle with the diameter $d_{resulting}$ is smaller than the sum of the surfaces $a_{starting}$ of two starting particles.

$$a_{starting} = 2\left(\pi d^2\right) \quad \text{and} \quad a_{resulting} = \pi d_{resulting}^2$$

$$v_{resulting} = 2v_{starting} \Rightarrow \frac{\pi}{6} d_{resulting}^3 = 2\frac{\pi}{6} d^3 \Rightarrow d_{resulting} = 2^{\frac{1}{3}} d.$$

This leads to an excess of surface energy

$$\Delta u = \gamma \Delta a = \gamma (2\pi d^2 - \pi d_{resulting}^2) = \gamma \pi d^2 \left(2 - 2^{\frac{2}{3}}\right) \Rightarrow \Delta U = N\Delta u.$$

The system contains $N = \dfrac{M}{\rho v_{start}}$ particles per mol and the increase of the temperature ΔT in an adiabatic system is: (ρ is the density, C_p is the heat capacity, M is the molecular weight)

$$\Delta T = \frac{\Delta U}{C_p} = \frac{N\Delta u}{C_p} = \frac{M}{\rho v_{start}} \frac{\Delta u}{C_p} = \frac{M}{\rho} \frac{6}{\pi d^3} \gamma \pi d^2 \left(2 - 2^{\frac{2}{3}}\right) = \frac{M}{C_p \rho} 6\gamma \left(2 - 2^{\frac{2}{3}}\right)\frac{1}{d}.$$

$$(3.8)$$

Lastly, one has to realize that the temperature flash makes coagulation possible at all, as the increased temperature increases the mobility of the atoms. The significant decrease of the temperature flash with increasing particle size explains the occurrence of odd-shaped particles in the size range above 3 or 4 nm. This is not pure theory. The process of coagulation can be observed in the electron microscope, too. Figure 3.6 displays a series of excellent electron micrographs displaying the process of coagulation of two gold particles. The series starts with two particles; one is in an orientation where lattice fringes are visible. These particles are moving around on the surface of the carbon specimen carrier. This movement changes the relative orientation of the particle lattice to the electron beam and; therefore, the lattice fringes. When, by chance, the particles touch each other, the particles rotate until their orientation is equal. Now coagulation starts; the larger particle swallows the smaller one. This process needs a significant thermal mobility of the atoms, to some extent, the necessary thermal energy is provided from the reduction of the surface.

The temperature flash occurring due to coagulation has a severe influence on the particle formation during synthesis. Lastly, the consequence is that, using a random process; it is nearly impossible to obtain very small particles, provided one does not take special measures to thwart coagulation. This will be discussed in Chapter 4 in great detail.
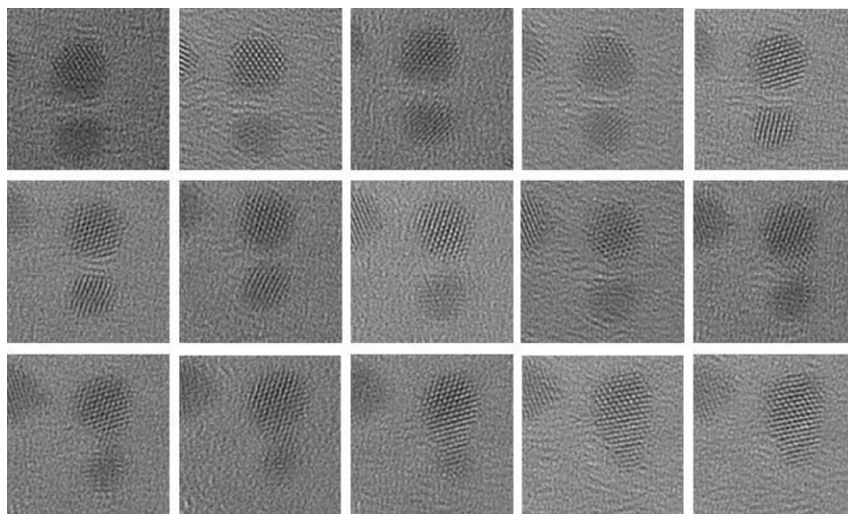
Figure 3.6 A series of electron micrographs depicting the coagulation of two gold particles. The orientation of the lattice fringes changes from frame to frame, indicating the movement of the particles. During coagulation, a grain boundary is not formed; rather, the orientation of the two particles is aligned. With progression of the time, the resulting particle becomes more and more rounded (Ascencio, J., Univ. Nacional Autonoma de Mexico, private communication, 2008).

To demonstrate the relative amount and importance of surface energy, Figure 3.7 displays for zirconia as an example, the free enthalpy of formation, ΔG_{ZrO_2} the free enthalpy for the transformation monoclinic–tetragonal $\Delta G_{monoc.-tetr.}$ in comparison to the surface energy, and the difference of the surface energy caused by the transformation from the monoclinic to the tetragonal phase. Again, for the surface energy a value of $1 \, J \, m^{-2}$ was used.

In Figure 3.7 one sees that for particles smaller than 2 nm the surface energy is comparable to the energy of formation. The free enthalpy of the monoclinic–tetragonal transformation is significantly smaller than the surface energy. However, in the latter case one has to look only at the surface change during this phase transformation. The small difference of the surface caused by the volume change of roughly 4% during phase transformation leads to a change of the surface energy, which is comparable to the free enthalpy of transformation. It is obvious that the particle size influences the phase transformation significantly (see also Chapter 7).

Looking at isolated particles, one has to take note of the hydrostatic pressure caused by surface stress in the particles (see Box 3.3). (The surface-induced hydrostatic pressure is also why free water drops are spherical.) This hydrostatic pressure p is a function of the curvature and the surface stress; and most importantly, in the case of a spherical particle, it is inversely proportional to the particle diameter. Figure 3.8 depicts the hydrostatic pressure caused by surface energy within
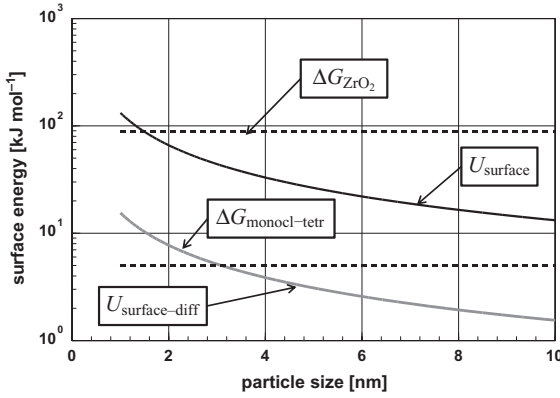
Figure 3.7 Surface energy of zirconia particles as a function of grain size. For comparison, the free enthalpy of formation ΔG_{ZrO_2} and the free enthalpy of the monoclinic–tetragonal phase transformation $\Delta G_{monoc.\text{-}tetr.}$; and, additionally, the difference of the surface energy between the monoclinic and the tetragonal phase (as volume difference a value of 4% was used) is plotted.
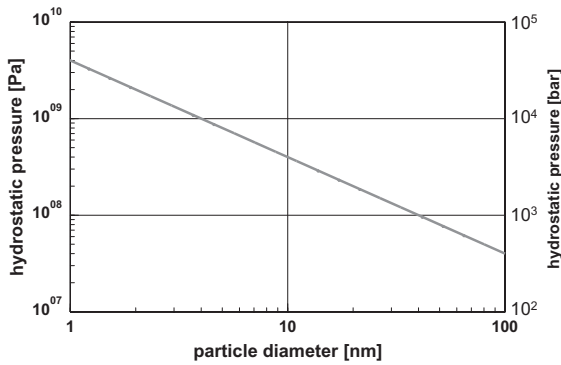
Figure 3.8 Hydrostatic pressure in nanoparticles as a function of the particle diameter. The surface stress σ was assumed as $1\,N\,m^{-1}$.

a nanoparticle. For the surface stress, a value of $1\,N\,m \triangleq 1\,J\,m^{-2}$ was selected. As values for the surface energy and surface stress are poorly known for ceramic materials, this value is often selected.

The hydrostatic pressure in a spherical particle with a diameter of $5\,nm$ and a surface energy of $1\,N\,m^{-1}$ is, according to Figure 3.8, $4 \times 10^8\,Pa \triangleq 4 \times 10^3\,bar$. This is a very high value. Hence, phase transformations connected to a volume change, which are pressure sensitive, depending on the external pressure, are significantly influenced. Therefore, particle size influences phase transformations. This topic will be discussed in Chapter 7.
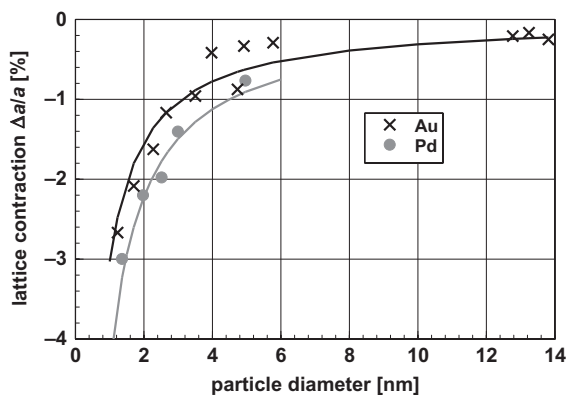
Figure 3.9 Experimental values for the lattice constant of gold [2] and palladium [3] nanoparticles. Due to the deformation due to the hydrostatic pressure originated by the surface tension, decreasing lattice parameters are observed with decreasing particle size.

One may expect that the hydrostatic pressure, caused by the surface stress deforms the particle. In fact, this phenomenon leads, in the case of metallic nanoparticles, to particle contraction. However, this contraction is so small that is can be determined only by high-precision X-ray lattice constant measurements. In the case of ceramic particles, this reduction is, generally, superimposed by phenomena leading to lattice expansion.

Considering the experimental difficulty determining lattice constants with high precision in the case of small particles, this phenomenon is well documented. Figure 3.9 displays, as examples, the lattice constants of gold [2] and palladium [3] as a function of the particle diameter. In both cases, a significant reduction of the lattice constant was observed.

Particles of ceramic oxides behave differently. Figure 3.10 depicts the dependency of the unit cell volume of γ-Fe_2O_3 as function of the particle size [4]. It is important to realize that, in contrast to metals, the lattice expands with decreasing particle size. This phenomenon is explained by a change in the lattice structure at the surface with decreasing particle size. The starting point for the explanation is the observation that, in most cases, the cations at the surface of an oxide are terminated by oxygen ions or other anions, such as $(OH)^-$. Therefore, the surface of an oxide is covered with ions, all bearing negative electrical charges. These negative charges repel each other; hence, the lattice expands [5].

3.3
Vapor Pressure of Small Particles

From the *Clausius–Clapeyron* law, Lord *Kelvin* derived an equation for the vapor pressure of a curved surface as a function of the curvature radius. In connection to particulate matter, this equation connects the vapor pressure of a free surface
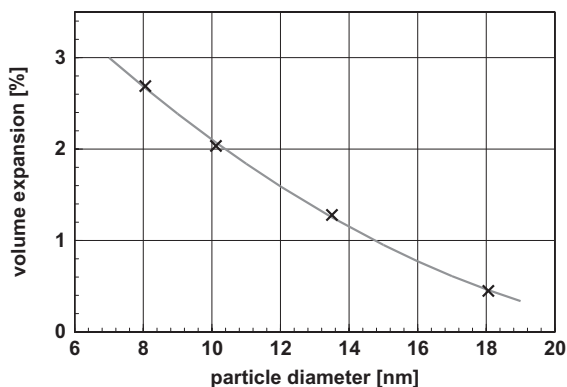
Figure 3.10 Volume expansion of γ-Fe_2O_3 nanoparticles [4] as a function of the particle size. In contrast to metallic particles, in oxides one observes a volume dilation with decreasing particle size. This is a consequence of electrostatic repulsion due to the termination of metal cations by anions with electric charges of equal sign at the surface.

with surface energy and particle size. In view of the interpretation of experimental results, it is of importance that the *Kelvin* equation is valid for convex and concave surfaces. Mathematically, in the case of a convex surface, the curvature (=inverse radius of the largest inscribed sphere with the same tangent plane as the surface in question) is positive, whereas, in the other case, the concave surface, the curvature is negative.

Box 3.5   Vapor Pressure of a Curved Surface

The *Kelvin* equation (also called the *Thomson* equation) connects the vapor pressure with surface energy and particle size

$$\ln\left(\frac{p}{p_\infty}\right) = \frac{4\gamma}{d}\frac{V_m}{RT} \Rightarrow p = p_\infty \exp\left(\frac{4\gamma}{d}\frac{V_m}{RT}\right), \qquad (3.9)$$

where p_∞ is the vapor pressure over a flat plane, V_m is the molar volume, which is the volume of one mol, R is the gas constant, T is the temperature.

At constant temperature, the vapor pressure over a curved surface shows the proportionality

$$p \propto \exp\left(\frac{1}{d}\right). \qquad (3.10)$$

The *Kelvin* equation says that, in equilibrium, the vapor pressure of a particle with the diameter d increases exponentially with decreasing diameter.

Equation(3.9) is valid for surfaces with positive (convex) and negative (concave) curvature, which is defined as the inverse value of the radius of a sphere with the same tangent plane.
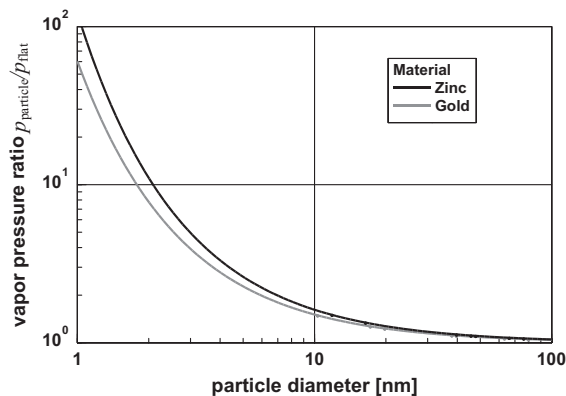
Figure 3.11 Vapor pressure ratio of the vapor pressure p of nanosized droplets related to the one of a flat plane p_∞ at constant temperature, the melting point ($\gamma_{Au} = 1.13\,\mathrm{J\,m^{-2}}$, $\gamma_{Zn} = 0.77\,\mathrm{J\,m^{-2}}$ [6, 7]). Please note the drastic increase at small particle sizes.

Figure 3.11 displays a graph showing the vapor pressure of small spherical particles using zinc and gold as examples. As a temperature, the melting point was selected.

The graph in Figure 3.11 displays the ratio of the vapor pressure for nanosized droplets at the melting point of the bulk material over the vapor pressure of a flat surface. Even when the properties of these two metals are very different, the ratio of the vapor pressures does not differ that much. It is important to see the severe increase of the vapor pressure over droplets with sizes in the range of one nanometer. The significant increase of the vapor pressure for small particles has important technical consequences:

- Synthesis in the gas phase at elevated temperature: Analyzing the formation of particles, it is obvious that the nuclei must have a minimum size to avoid evaporation before they have the chance to grow by condensation of further material. Hence, in nature, heterogeneous nucleation is preferred over homogeneous nucleation, as the probability for homogenous nucleation is low, because for particle sizes close to zero, the vapor pressure is extremely high. Therefore, in the case of gas-phase reactions, it is easier to produce small particles of materials with low vapor pressure as compared to ones with high vapor pressure. Lastly, this is why it is not that difficult to synthesize small particles for materials with extreme low vapor pressure, for example, the refractory oxides such as ZrO_2, HfO_2, etc.

- A further consequence is related to particle shape. For nanoparticles consisting of a material with low vapor pressure, there is a higher chance to obtain facetted particles, whereas nanoparticles of materials with higher vapor pressure crystallize in a more spherical shape. As a typical example, the gold articles depicted in Figure 3.6 are rounded; whereas the ceria (CeO_2) particles shown in Figure 3.12 are facetted.
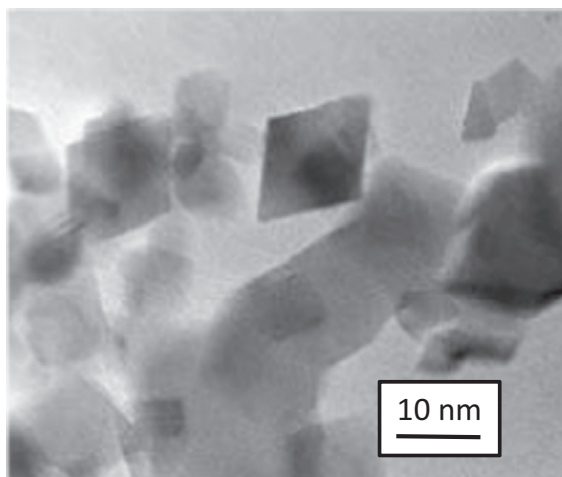
Figure 3.12 Faceted ceria, CeO_2 nanoparticles. In high-temperature processes, the formation of facets connected to sharp edges is possible only in the case of low vapor pressure of the material. Courtesy Nanophase Technologies Corporation, USA.

Certainly, the formation of particle shapes is not monocausal. There are more phenomena influencing the shape of particles. It is well known that different crystallographic planes have different surface energies, for example, in cubic systems, the planes forming a cube have the lowest surface energy. Additionally, in the case of oxides, the termination changes the surface energy of different crystallographic planes differently. Both phenomena may give a tendency for the formation of facetted particles. However, experimentally, small particles, especially metallic ones, are usually spherical or close to a sphere. This finding is compatible with the relationships for the vapor pressure, which increases with the curvature. In most cases, sharp edges or tips are energetically not favorable; they are removed by evaporation and condensation processes. These processes will not be dominant in material with an extremely low vapor pressure; therefore sometimes the particles are facetted, even when they are produced at high temperatures (see Figure 3.12).

- Sintering is selected as the third example. To understand the processes of evaporation and condensation connected to sintering process, Figure 3.13 displays the ratio of the vapor pressures as a function of the inverse curvature for zinc nanoparticles at the melting point.

It is remarkable that outside of the size range of nanoparticles, this ratio is close to one, whereas for small particles or narrow wedges , between two grains, this value is extreme large (convex surface), respectively, small (concave surface). The difference in vapor pressure between ranges with positive and negative curvature is the most important driving force during the first stages of sintering; it causes the formation of sintering necks. The details, with respect to sintering, are depicted in Figure 3.14.
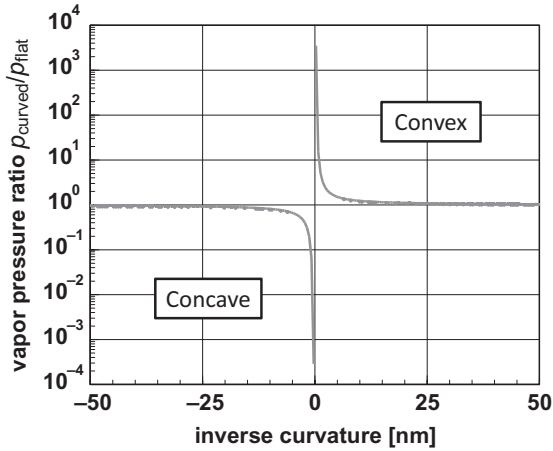
Figure 3.13 Vapor pressure ratio of the vapor pressure *p* of a curved plane over that of a flat plane p_∞ for zinc. A positive curvature is related to convex surfaces, negative curvature to concave surfaces.
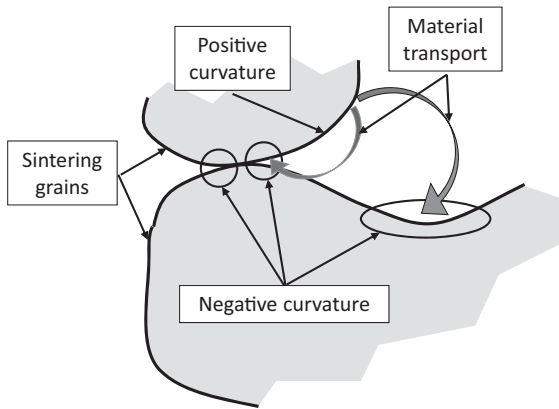
Figure 3.14 Material transport by evaporation and condensation during sintering. The material is transported from ranges with positive curvature to ranges with negative curvature.

To understand the material transport by evaporation and condensation during sintering, one has to realize that the curvature is positive at the particle surface. At the point of contact of two particles, the curvature is negative. For negative curvature, the vapor pressure is very small. Therefore, bodies consisting of pressed nanoparticles start sintering very rapidly, as small particles have a high vapor pressure. The evaporated material is deposited at the points of contact of two particles and other areas, where the curvature is negative. In total, this type of material transport by evaporation and condensation leads, in the case of nanoparticles, to an early start of the sintering process at comparatively low temperatures.
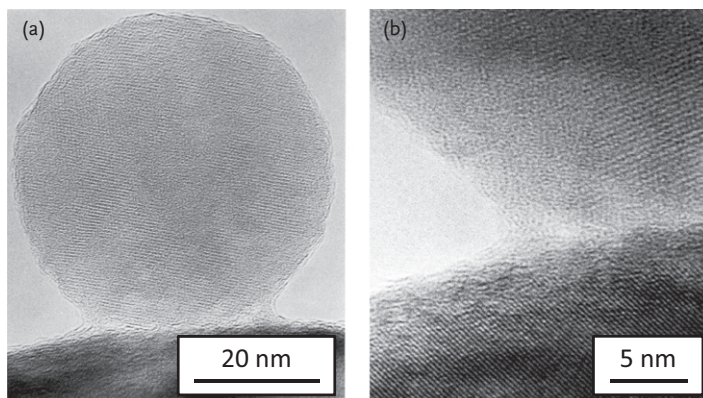
Figure 3.15 Two sintering alumina particles. As a consequence of the curvature dependent vapor pressure, material evaporates at the positively curved surfaces of the particles, and condenses in the neck between the two particles, where the curvature is negative. (Reproduced with permission by Springer.)

This process can be proven experimentally. The situation sketched in Figure 3.14, is nearly repeated in the micrograph displayed in Figure 3.15, displaying an example of such a sintering neck between two alumina particles.

In the electron micrographs in Figure 3.15, one sees clearly the material that was transported by evaporation and condensation processes to the contact point of the two particles. Furthermore, it is well visible that both particles are crystallized, recognizable by the striations within the grains (lattice fringes). It is interesting to see that the material deposited in the sintering neck is not crystallized, therefore, lattice fringes are not visible.

3.4
Hypothetical Nanomotors Driven by Surface Energy

There are experiments applying energy exchange during coagulation or the dependency of the surface energy of anisotropic materials on the orientation for technical use.

A prominent example is the proposal of Regan *et al.* for a nanomotor based on coagulation processes [8, 9]. The basic idea of a "motor" based on coagulation is relatively simple. It applies the migration of metallic atoms in an electric field at the surface of carbon nanotubes [10]. Because of its low melting point, this device is realized with indium as the metal to be transported. This led to the idea of a relaxation oscillator, as sketched in Figure 3.16. On a carbon nanotube, which is connected to a direct current, DC source, two droplets of indium are placed in close proximity. After switching the electrical current on, indium is transported by electromigration from one droplet to the next. As a result, on the carbon nanotube, one droplet shrinks and the other grows. When this process comes to the
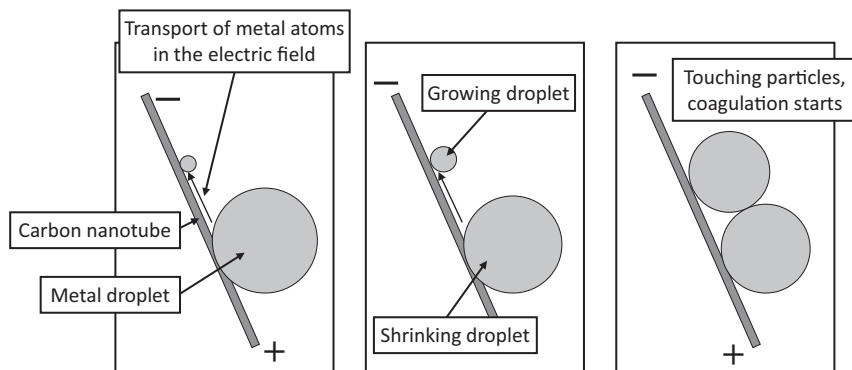
Figure 3.16 Nanomotor based on coagulation of metal droplets by surface energy [8, 9]. The device consists of a multiwall carbon nanotube and two droplets of liquid metal, that is, indium. With an electric field across the nanotube, metal atoms are transported from the larger droplet to the smaller one. Therefore, the larger droplet shrinks and the smaller one grows until both drops are touching. At this moment, the droplets coagulate and the process starts again with the material transport from the large drop to a point, where a new drop can be formed.
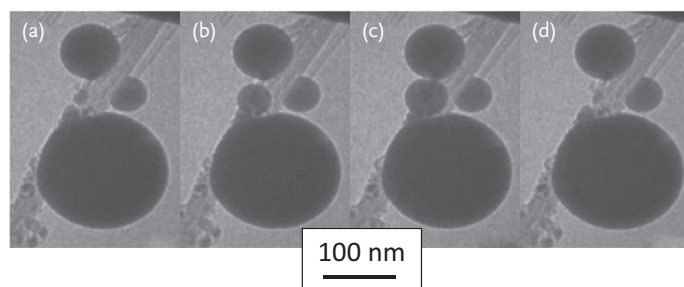
Figure 3.17 Oscillating system driven by surface energy and electrical current [8]. These electron micrographs of a nanomotor display the sequence of droplet growing (micrographs a, b, and c) and after coagulation (micrograph d). Indium atoms are transported by electromigration at the surface of a carbon nanotube [9]. (Reproduced by permission of Springer.)

point where the two droplets touch each other, they coagulate. The coagulation process concentrates the material of both drops in the larger drop. After coagulation, the continuing material transport leads again to the formation of the smaller second droplet, which is nucleated at a discontinuity at the surface of the nanotube. If there are no evaporation losses, this setup oscillates as long as it is connected to a DC source.

It was possible to visualize this process in an electron microscope. A series of figures displaying this process is presented in Figure 3.17.

In Figure 3.17, the carbon nanotube, the droplets and, most importantly, the growth of the smaller particle at the expense of the larger one can be seen easily
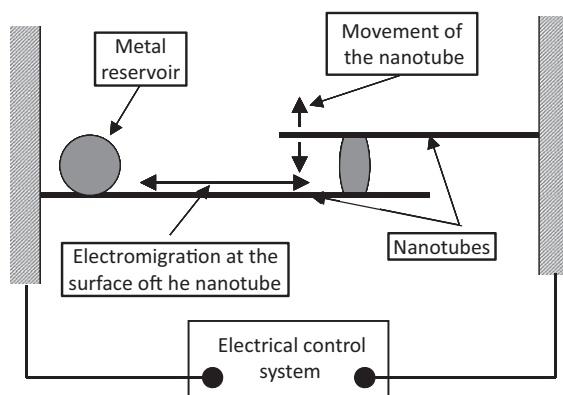
Figure 3.18 Principle of a nanomotor based on electromigration at the surface of a nanotube and the anisotropy of surface energy of a noncubic metal according to Regan *et al.* [10]. Metal atoms are transported from and to a metal reservoir.

The metal extension bar changes its length, because, due to the anisotropy of the surface energy, metal atoms are added or removed only at the planes directly adjacent to the carbon nanotubes.

in the series of electron micrographs from Figure 3.16a–c. Figure 3.17d depicts the arrangement after coagulation; now, the process may start again. The time for complete coagulation was estimated to be in the range of 200 ps.

A further nanomotor, presented by the same group applies the difference of the surface energy of a material crystallizing in an anisotropic structure. As the metal to be transported, again indium, crystallizing in a tetragonal structure, was selected. As in the previous example, the indium atoms are transported at the surface of a carbon nanotube. Figure 3.18 displays the principle of this device.

The device consists of two nanotubes connected with a small indium bar, the extension bar, and, a metal reservoir. Again, the material is transported by electromigration. Indium crystallizes tetragonally, an anisotropic structure. The indium crystal grows anisotropically and if additional indium is transported to the bar, it elongates. Therefore, the nanotubes are bent. Changing the direction of the electric current leads to transport in the opposite direction. The indium bar reduces its length. By an external source of electrical current, the movement of the nanotubes is controlled. Changing the direction of the current changes the direction of the movement. This behavior is displayed in Figure 3.19. The voltage connected to the system controls the speed of the movement; within a limited range, the speed is proportional to the voltage. A typical value for the speed is ca. $1 \, nm \, s^{-1}$ for extension and shrinking, respectively. If the voltage is low, the speed is reduced significantly, because the transport is activated thermally and, in this case, the electrical *Joule* heating is not sufficient. In addition, the maximum speed is limited by *Joule* heating as the temperature of the system must not exceed the melting point of the metal.
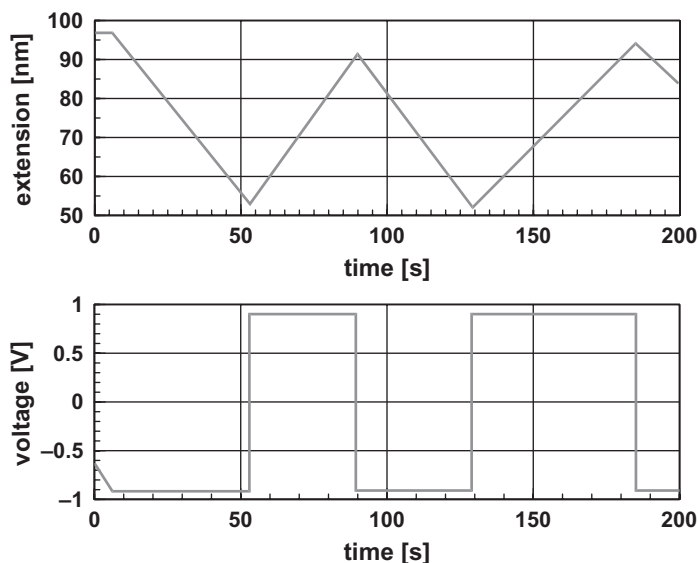
Figure 3.19 Extension and voltage of a nanomotor designed according to Figure 3.18 [10]. Within a limited range, the extension rate is controllable by the applied voltage.

References

1 Fischer, F.D., Waitz, T., Vollath, D., Simha, K. (2008) *Prog. Mater. Sci.*, **53**, 481–527.

2 Mays, C.W., Vermaak, J.S., and Kuhlmann-Wilsdorf, D. (1968) *Surf. Sci.*, **12**, 134–137.

3 Lamber, R., Wetjen, S., and Jaeger, I. (1995) *Phys. Rev. B*, **51**, 10968–10971.

4 Ayyub, P., Multani, M., Barma, M., Palkar, V.R., and Vijayaraghavan, R. (1988) *J. Phys. C*, **21**, 2229–2245.

5 Ayyub, P., Palkar, V.R., Chattopadhyay, S., and Multani, M. (1995) *Phys. Rev.*, **51**, 6135–6138.

6 Miedema, A.R., and Boom, R. (1978) *Z. Metallkde.*, **69**, 183–190.

7 Miedema, A.R. (1978) *Z. Metallkde.*, **69**, 287–292.

8 Regan, B.C., Aloni, S., Jensen, K., Ritchie, R.O., and Zettl, A. (2005) *Nano Lett.*, **5**, 1730–1733.

9 Regan, B.C., Aloni, S., Jensen, K., and Zettl, A. (2005) *Appl. Phys. Lett.*, **86**, 123119. 1–3.

10 Regan, B.C., Aloni, S., Ritchie, R.O., Dahmen, U., and Zettl, A. (2004) *Nature*, **428**, 924–927.

4
Gas-Phase Synthesis of Nanoparticles

4.1
Fundamental Considerations

The first nanoparticles were synthesized using gas-phase processes. Significantly earlier, colloid chemistry was used to synthesize nanoparticles in suspensions (=colloids); however, separating of the particles from the liquid is difficult; the colloidal particles form agglomerates.

In gas-phase processes, a vapor of the material condenses in a gas phase forming small particles. These particles may be isolated particles or agglomerates.

Box 4.1   Processes of Particle Formation

An environment containing a gas and atoms or molecules that can condensate in a low concentration is assumed. These are the assumptions for a random process (*Poisson* process) forming particles. Generally, particle formation is described by four major steps:

- **Nucleation**. A nucleus is the smallest stable unit. Usually, it consists of at least three atoms or molecules. Such nuclei are formed if three atoms collide coincidently. This nucleus acts as a core for further

- **condensation** of atoms or molecules at the surface of the nucleus. Therefore, the nucleus grows and forms a cluster and later a particle. Condensation is a random process ruled by the dynamics of the gas species. Colliding cluster or small particles may coagulate. During

- **coagulation** by exchange of surface energy, a new, larger particle is formed. Having reached a certain size, the difference of surface energy will be so small that further coagulation of particles is impossible. Now the process of

- **agglomeration** starts. Agglomerates consist of two or more individual particles. Often, one distinguishes soft and hard agglomerates. Soft agglomerates are bound by *van der Waals* bonds; hard agglomerates are sintered. If at all, only soft agglomerates can be separated.

In most cases, it is nearly impossible to separate the particles from agglomerates. If at all, only soft agglomerates can be separated. High temperatures during synthesis promote the formation of hard agglomerates. Therefore, after synthesis and particle formation, it is necessary to reduce the temperature in a quenching step as fast as possible. This reduces the probability for agglomeration and the formation of hard agglomerates.

The processes of condensation and coagulation are random ones; this leads to a relatively broad distribution of particle sizes. Generally, experiments deliver particle-size distributions with a long tail on the side of the large particles. The theory of random process says that these size distributions are described by *Poisson* distributions. However, as this distribution function is, mathematically, quite uncomfortable to handle, generally, it is approximated with sufficient precision by the log-normal distribution. There are possibilities to bias the process of particle formation, and, therefore, the particle-size distribution, by quenching or charging the particles electrically.

Box 4.2   Distribution Functions for Particle-Size Distributions

The *Poisson* distribution, which is characteristic of random processes with small probability, is described by the equation

$$p_\mu(n) = \frac{\mu^n}{n!} \exp(-\mu) \text{ with } \mu \in \mathbb{R} \text{ and } n \in \mathbb{N}. \tag{4.1}$$

The quantity μ stands for the mean value, which is in this distribution equal to the variance (=squared standard deviation, σ). n is an integer number, which stands for the size of the particles. For larger values of n, $n!$ and μ^n are huge numbers, which may create problems for calculation. Therefore, in general, the *Poisson* distribution is approximated by the log-normal distribution,

$$p(x) = \frac{1}{\sigma x (2\pi)^{0.5}} \exp\left[-\frac{(\ln x - \mu)^2}{2\sigma^2} \right]. \tag{4.2}$$

In Eq. (4.2), μ stands for the mean value and σ for the variance.

Figure 4.1 displays a graph depicting a *Poisson* distribution and a fit of this distribution using a log-normal distribution. Taking into account that experimental data of particle-size distributions are usually afflicted with significant scatter in the range of small probabilities, the quality of this fit is sufficient.
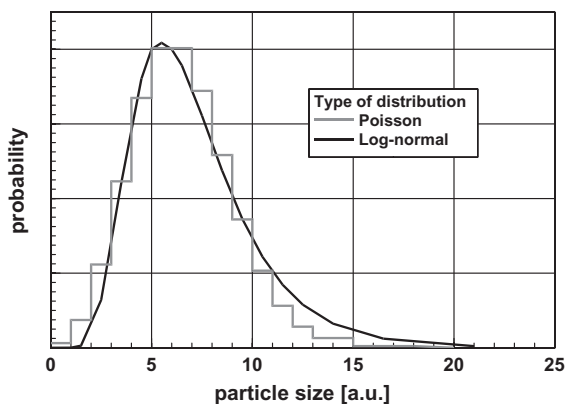
Figure 4.1 Fit of a *Poisson* distribution with a log-normal distribution.

To understand the probability of the collision of particles with different diameters, it is necessary to estimate the probability to find two particles during a short time interval in the same volume element. The size of this volume element is assumed to be equal to the volume passed by the particles within this time interval. The probability to find this volume element at a special location within a given volume, for example, of the experimental arrangement, is the quotient of these two volumes. To find the probability for collision of two particles, one has to calculate the probability that the volume passed by these two particles is found in the time interval at the same spot. This combined probability is the product of the two probabilities for the two particles under consideration. This estimation process is valid if the particles are significantly smaller than the free path length of these particles in their surrounding gas atmosphere. In fact, the calculations show that this presumption is fulfilled in any experimental situation that may be used for gas-phase synthesis.

Box 4.3   Collision Probability of Two Particles

To understand the size-dependent probability of condensation and coagulation, it is necessary to analyze the geometry of the collision of two particles with the diameters d_1 and d_2. For these estimations, it is necessary that the particles are smaller than the mean free path lengh of the particles in the gas, a presumption that is fulfilled for nanoparticles, in nearly all ranges of gas pressures applied for synthesis.

The geometry assumed for the collision of two particles is depicted in Figure 4.2.

A particle with the mass m and a mean velocity c

$$c = 2\left(\frac{2kT}{\pi m}\right)^{0.5} \tag{4.3}$$
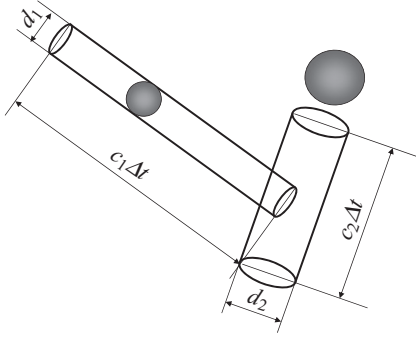
Figure 4.2 Geometrical model to estimate the probability of the collision of two particles with diameters d_1 and d_2. The lines give the limitation of the cylinders circumscribing the trajectories of the particles.

passes the volume v of the cylinder in the short time interval Δt:

$$v = \frac{\pi}{4} d^2 c \Delta t = \frac{\pi}{4} d^2 2 \left(\frac{2kT}{\pi m} \right)^{0.5} \Delta t = \frac{\pi}{4} d^2 2 \left(\frac{2kT}{\pi \rho \frac{\pi}{6} d^3} \right)^{0.5} \Delta t = \left(\frac{3kT}{\rho} d \right)^{0.5} \Delta t$$

(4.4)

(ρ is the density of the particle).

To obtain the collision probability of two particles with the diameters d_1 and d_2, it is necessary to estimate the probability p_1 to find, for example, the particle with the number 1 in a well-defined volume element.

$$p_1 = \frac{v_1}{V_{\text{total}}}$$

(4.5)

(V_{total} is the volume of the device under consideration). To find the particles with the numbers 1 and 2 in the time interval Δt in the same volume element is given by the product:

$$p_{1-2} = p_1 p_2.$$

(4.6)

To relate the probability for collision with the particle diameters one obtains

$$p_{1-2} = \frac{1}{V_{\text{total}}} \left(\frac{3kT}{\rho} d_1 \right)^{0.5} \Delta t \frac{1}{V_{\text{total}}} \left(\frac{3kT}{\rho} d_2 \right)^{0.5} \Delta t = \text{const} (d_1 d_2)^{0.5} T.$$

(4.7)

Equation (4.7) shows that, at constant temperature, the probability for the collision of two particles is proportional to the square root of the product of the two diameters.

Therefore, one may call this parameter, depending only on the geometry of the particles, "collision parameter". Furthermore, Eq. (4.7) shows that the collision probability increases linearly with temperature. Hence, if particle growth by coagulation should be minimized, one has to reduce the temperature as far as possible.

Figure 4.3 Collision parameter as a function of the particle diameter for particles with three different diameters.

As mentioned above, having estimated the probability to find one particle in a certain volume element of an experimental device, the probability to find two particles in the same volume element is the product of these two probabilities. Based on this combined probability, it is 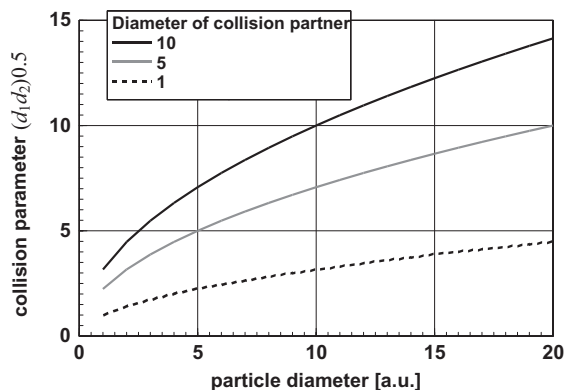possible to derive a "collision parameter" that gives information on the tendency of the collision probability as a function of the two particle diameters. The probability for the collision of two particles is linearly proportional to the temperature and the collision parameter, based on the geometry of the particles, which is proportional to the square root of the product of the diameters of the collision partners. With respect to optimizing the process of gas-phase synthesis, the collision probability of two particles gives important hints on how to obtain small particles: (i) The temperature has to be kept as low as possible and (ii) the growth of particles by coagulation must be avoided as far as possible. This conclusion supports the use of a quenching step.

Figure 4.3 depicts this collision parameter as function of particles diameter with collision partners of different size.

On analyzing Figure 4.3, one realizes, as expected intuitively, that the collision parameter increases with the particle diameter. This steeper increase of the collision parameter for larger particles makes it impossible to obtain a product within a narrow range of particle sizes. As a result, larger particles grow faster than the smaller ones, in particular, the collision probability of large particles with large ones increases, leading to an extension of the particle-size distribution into the direction of the larger ones. As a consequence, particle-size distribution functions of particles produced by a process of random collisions are always nonsymmetric functions with a long tail on the side of the large particles. Figure 4.4 displays a typical particle-size distribution for zirconia particles, produced by the inert-gas condensation technique, determined by evaluation of electron micrographs [1].

The size distribution depicted in Figure 4.4 displays the characteristic asymmetric size distribution, which is typical for products synthesized by random processes. Size distributions of this kind are usually fitted with a log-normal
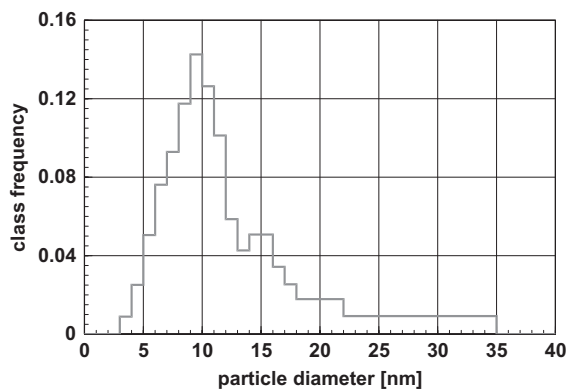
Figure 4.4 Size distribution for a zirconia, ZrO$_2$, powder synthesized by the inert-gas condensation technique. The asymmetric particle-size distribution with a long tail towards large particle sizes is typical for products made by random processes. This type of size distributions is, generally, fitted with the log-normal distribution function [1].
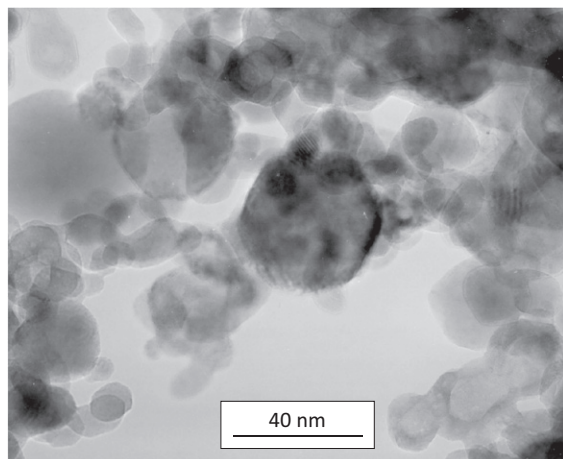
Figure 4.5 Electron micrograph of titania powder with broad particle-size distribution as is obtained by purely random synthesis processes. In this micrograph, the particle size ranges from 5 nm to 50 nm. (Vollath, D., and Sickafus, K.E., Los Alamos Natoinal Laboratory, USA (1992) unpublished results.)

distribution. Two points need special attention: There were no particles with sizes below 3 nm detected and there is a long tail towards larger particle sizes. Both features are characteristic for particles produced by a purely random process. As an aid for visual perception, Figure 4.5 displays an electron micrograph of titania powder with a broad particle-size distribution. In this product, the particle sizes range from 5 to 50 nm. Lastly, the message provided by Figure 4.5 is the same as that of Figure 4.4: there is a broad distribution of particle size containing a few with large diameter.

To obtain a narrower particle-size distribution and, what is more important, to avoid the formation of a few large particles, it is necessary to influence the process of particle formation in a way that the simple collision parameter, which increases with increasing particle size is altered. In contrast, one would prefer a system in which the collision parameter decreases with increasing particle size. Two of the technical possibilities to influence particle coagulation and obtain this goal were already mentioned: (i) Decreasing the temperature, a measure that reduces the collision probability in general; however, it is not size sensitive. (ii) Quenching immediately after the first particles were formed with a cold gas; indeed, this process step reduces the number of large particles, and (iii) electrical charging of the particles. The effect of this latter measure will now be discussed.

To reduce the probability of coagulation, one can think of loading the particles with electric charges of equal sign, as electrical charges of equal sign repel each other. Electrical charges of spherical particles are proportional to the particle diameter. This is an experimentally and theoretically well-proven fact. The repelling force between two particles carrying electric charges of equal sign is directly proportional to the product of the electrical charges. Lastly, this leads to a modification of the collision parameter, which is for charged particles the inverse to that of neutral particles, it is indirectly proportional to the square root of the product of the particle diameters. The temperature dependence remains unchanged as linear. Figure 4.6 displays the collision parameter as a function of the particle diameter for three different particle sizes.

The consequence of particle charging on the "collision parameter" is visible in Figure 4.6, where the collision parameter is plotted versus particle diameter for collision partners with different sizes. In contrast to neutral particles (Figure 4.3),

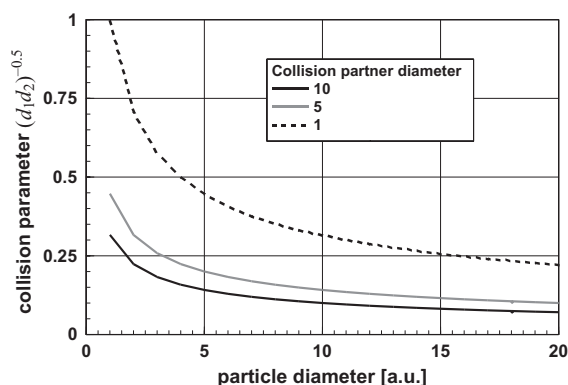**Figure 4.6** Collision parameter of particles carrying electrical charges of equal sign. The collision parameter is plotted versus the particle size. The size of the collision partner is the parameter for the curves. The decreasing collision parameter with increasing particle size limits particle growth during synthesis. The electrical charge of the particles is proportional to the particle diameter.

where the collision parameter increases with increasing particle size, calculated values for electrically charged particles (Figure 4.6) show a continuous decrease of the collision parameter with increasing size of the collision partners. Figure 4.6 demonstrates that charging the particles limits the size of the particles. The long tail on the side of the large particles in the size distribution may be avoided, as the collision probability of large particles is significantly reduced. The experimental results confirm these considerations.

How is it possible to exploit the advantages of a synthesis process with charged particles? As will be demonstrated later, the best possibilities are found using plasma processes. As the next possibility, one may think of charging by thermal electron emission. This seems to be promising, as the radius of nanoparticles is small and the processing temperature high. However, such a thermal charging process does not give a high percentage of electrically charged particles. It can be shown theoretically that a partial ionization of the particles does not lead to the intended effect. Therefore, it is not surprising that this phenomenon was never observed experimentally.

Box 4.4 Electrical Charges of Small Particles

To analyze the coagulation behavior of charged particles, first it is necessary to calculate the electrical charges of the particles. To do this, electrically charged particles are treated as spherical capacitors. The capacitance C of a sphere is equal to the diameter, $C = d$, carrying the electrical charge $Q = VC$. (V . . . electric potential) The assumption that all particles are charged to the same potential, $V = \dfrac{Q}{C} = \dfrac{Q}{d} = \text{const}$ leads to the important relationship describing the dependency of the electrical charge of the diameter:

$$Q = VC = Vd. \tag{4.8}$$

Small particles carry fewer electric charges than larger ones. This relationship is experimentally well proven in aerosol physics [2]. Taking the quantized nature of electrical charges into account, one has, according to Zieman *et al.* [2], to rewrite Eq. (4.8)

$$\begin{aligned} d \leq d_0 &\Rightarrow Q = Q_0 \\ d > d_0 &\Rightarrow Q = Q_0 + \kappa(d - d_0) \end{aligned} \tag{4.9}$$

(d_0 is the limiting diameter, Q_0 is the electrical charge of the smallest particles, κ is the constant factor, which is not necessarily an integer number, as only mean values over many particles are considered. This smears the quantization of the electric charge).

Box 4.5   Collision of Electrically Charged Particles

Two particles with diameters d_1 and d_2 at a distance r carrying electric charges Q_1 and Q_2 of equal sign repel each other with the force F:

$$F = \frac{Q_1 Q_2}{r^2} = \frac{\kappa_2}{r^2} \frac{1}{d_1 d_2}. \tag{4.10}$$

This force results in an deceleration $\dfrac{Q_1 Q_2}{mr^2}$ reducing speed and changing the direction of the path of the particles. This reduces the collision volume passed in the time interval Δt. To a first approximation, the reduction of the collision volume is given by the factor $\dfrac{1}{Q_1 Q_2} \propto \dfrac{1}{d_1 d_2}$. Inserting this factor into Eq. (4.7) leads to the following modified collision parameter:

$$p_{1-2} = p_1 p_2 = \text{const}\, T (d_1 d_2)^{0.5} \frac{1}{d_1 d_2} = \text{const}\, T (d_1 d_2)^{-0.5}. \tag{4.11}$$

As a consequence of the introduction of a repulsion term, Eq. (4.11) now describes a reduced collision probability with increasing particle size. This limits particle growth by coagulation and agglomeration, especially for large particles, as the probability for collision gets smaller with increasing particle size. The temperature dependence remains unchanged as linear. The collision parameter for charged $(d_1 d_2)^{-0.5}$ particle is inversely to that for neutral particles.

4.2
Inert-Gas Condensation Process

Historically most important, the first process for synthesizing nanoparticles in the gas phase is the inert-gas condensation process (also called evaporation and condensation process) [3], applying thermal evaporation of a metal within a vacuum chamber filled with a small amount of inert gas. To produce metal particles, for example, gold nanoparticles, gold is evaporated in a boat at sufficiently high temperature. The atoms of the gold vapor emanated from the boat are thermalized and lose energy by collisions with the atoms of the inert gas. Collisions of gold atoms with others lead to nucleation and subsequently to particle formation. The particles formed in the gas phase move by thermophoresis (this process is also called thermodiffusion) to a cold finger, where they are collected. Figure 4.7 displays the general layout of such equipment.

At the end of a production cycle, the metal particles are carefully scraped from the cold finger. If necessary, this design allows further processing of the product without breaking the extremely pure conditions. To obtain oxides, before scraping the powder from the cold finger, minor amounts of oxygen are introduced into
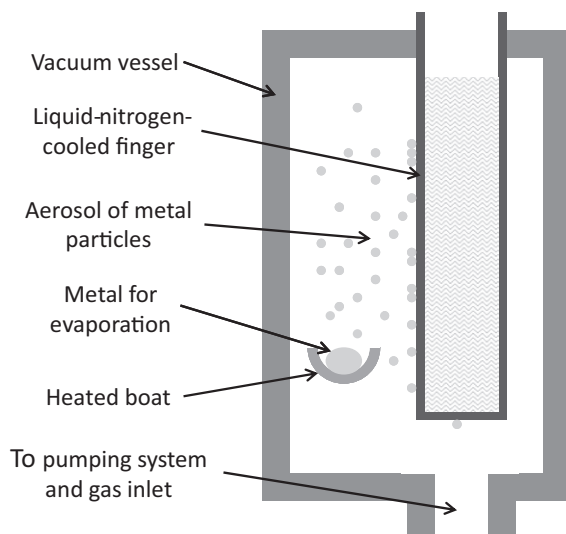
Vacuum vessel

Liquid-nitrogen-
cooled finger

Aerosol of metal
particles

Metal for
evaporation

Heated boat

To pumping system
and gas inlet

Figure 4.7 Typical setup for synthesis using the inert-gas condensation process. In a vacuum vessel, filled, at reduced pressure, with an inert gas, a metal is evaporated. In the gas atmosphere, the metal vapor is thermalized. The metal atoms lose thermal energy by collision with the inert gas atoms, and form nanoparticles. In a temperature gradient, the product moves to a liquid-nitrogen-cooled finger by thermophoresis and is collected from the surface of the cold finger.

the system to oxidize the metal powder slowly. Careful oxidation is essential, as otherwise the product is overheated and sintered. As the formation of the particles is a purely random process, typically, the inert-gas evaporation process leads to a product with broad particle-size distribution; an example is given in Figure 4.4.

4.3
Physical and Chemical Vapor Synthesis Processes

The basic principle of the inert-gas condensation process led to many variants. These systems differ in how the metal is introduced into the system and evaporated. Technical upscaling of the inert-gas condensation process needs elements to limit particle size growth to avoid the formation of the long tail of the size distribution function on the side of the large particles. There are two possible measures to control particle size and particle-size distribution: (i) Reduction of the residence time of the particles in the reaction zone and (ii) quenching, rapid cooling of the particles after leaving the reaction zone. Both measures disrupt the originally diffusion-controlled process. To bring these measures into action, it is necessary to replace the transport by thermal diffusion by transport using a carrier
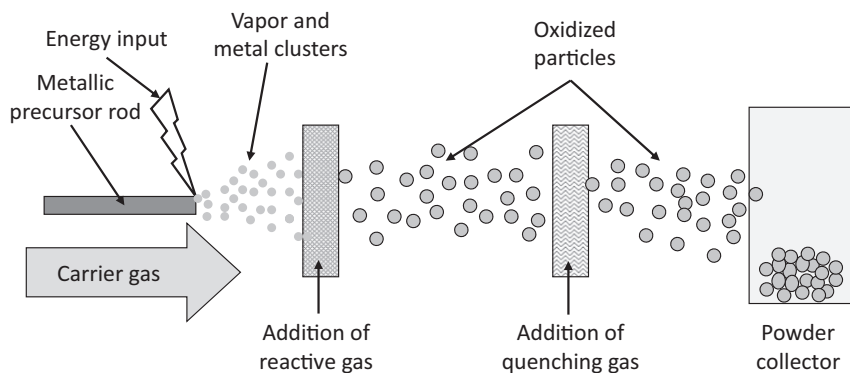
Figure 4.8 Setup for physical vapor synthesis of oxide nanoparticles. The metallic precursor is evaporated, for example, by an electric arc and transported by an inert carrier gas to the reaction zone, where the metal particles are oxidized. Particle growth and agglomeration are limited in the final quenching step.
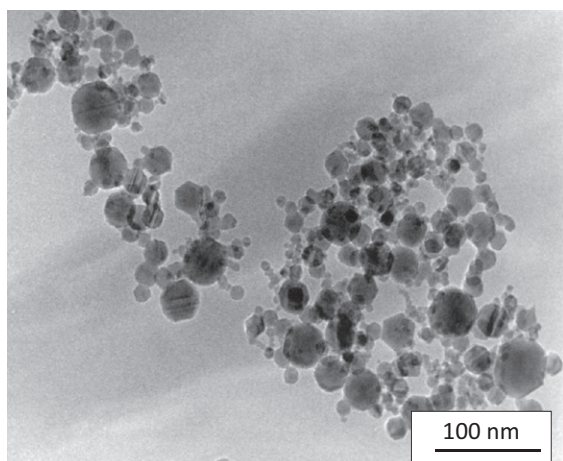
Figure 4.9 Fe_2O_3 powder produced in a device, similar to the one sketched in Figure 4.8. The broad particle-size distribution, in this example from 5 to 50 nm, is characteristic of this type of products.

(Courtesy Nanophase Technologies Corporation, 1319 Marquette Drive, Romeoville, IL 60446, USA. http://www.nanophase.com.)

gas. As heat source for mass production, an electrical arc, an electron beam, or a laser have many advantages and are quite often applied. Figure 4.8 displays the layout of such a system.

A typical industrial product, Fe_2O_3, stemming from a process similar to the one depicted in Figure 4.8 is displayed in Figure 4.9. It shows the characteristic,

relatively broad particle-size distribution, which is typical for unbiased random processes.

Besides pure metals, as rods or powders, volatile compounds are used as precursor, too. In many instances, this is of economical advantage. Using these modifications, this process for synthesis is called "chemical vapor synthesis". Generally, it applies a tubular furnace with temperatures up to 1500 K as a source of heat. A carrier gas, argon or nitrogen, transports the evaporated precursor through the hot reaction zone. As precursor, one uses chlorides, carbonyls, or metalorganic compounds. The final selection depends on the properties, availability, and price of these compounds. Additionally, it is important to note that these precursors lead to typical reaction products in the off-gas and may leave some traces behind that could be dissolved in the matrix of the particles or adsorbed at the particle's surface. This may be severely disturbing as, for example, chlorine or hydrochloric acid reacts with high probability with organic materials applied for functionalizing the surface of the particles.

Box 4.6   Chemical Reactions to Synthesize Oxides

To obtain the metal oxide MeO_y, starting from a chloride, a typical reaction is:

$$MeCl_x + \frac{y}{2}O_2 \Rightarrow MeO_y + \frac{x}{2}Cl_2. \tag{4.12}$$

Generally, this reaction is carried out at a temperature in the range from 1200 to 1500 K. To reduce the reaction temperature water is added:

$$MeCl_x + \frac{x}{2}H_2O + \frac{2y-x}{2}O_2 \Rightarrow MeO_y + xHCl. \tag{4.13}$$
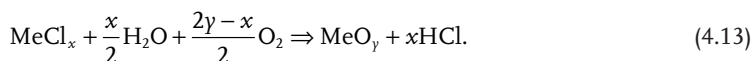
In many cases, the advantage of reduced reaction temperature is compensated by the huge disadvantage of getting highly corrosive hydrochloric acid, HCl as a byproduct in the system. If available, the use of carbonyls is recommended; for example, the synthesis of Fe_2O_3:

$$2Fe(CO)_5 + \frac{13}{2}O_2 \Rightarrow Fe_2O_3 + 10CO_2. \tag{4.14}$$
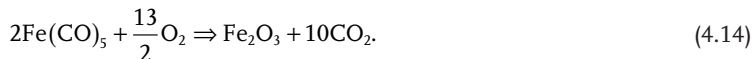
For most of the carbonyls, carbonyl chlorides, or nitrosyl carbonyls, this process works in a temperatures window between 600 and 800 K.

To replace chlorides, carbonyls, or metalorganic compounds are often used as precursors. In most cases, this allows reduction of the operating temperature of the tubular furnace for the reaction from ca. 1500 K down to approximately 650 K, with the consequence of significant energy savings. Avoiding chlorides avoids the

problematic, chlorine-containing compounds in the off-gas and saves energy. However, there are also a series of severe disadvantages. Problematic may be not only the high price but also the difficult handling. Handling is difficult, because most of the carbonyls are highly toxic and of limited stability in open air. This is valid also for some of the organic precursors, which are quite often self-igniting. As organic precursor compounds one preferably applies metal alkoxides and acetyl acetonates. Particularly for metals of the groups II, IIa, and the rare-earth elements, these are the most important precursors. The application of precursors, reacting at relatively low temperatures, gives freedom in the intended powder morphology, as the selected temperature influences the powder morphology. Low temperatures lead to extreme fine fluffy, often glassy powders, whereas the products crystallize with higher probability at increased reaction temperature. A typical example for such a product, glassy Fe_2O_3 with quite uniform particle size in the range of ca. 3 nm, synthesized at low temperature, is depicted in Figure 4.10.

Besides for oxides, the chemical vapor synthesis process is well suited for the synthesis of carbides and nitrides, too; even when the chemical stability of these compounds, as compared to oxides, is significantly lower.

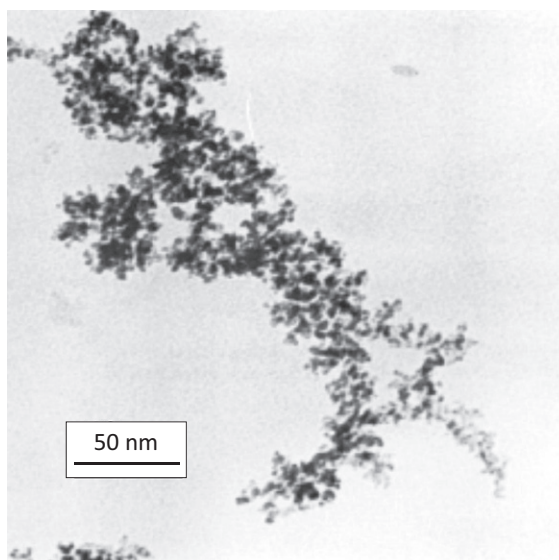**Figure 4.10** Fe_2O_3 powder synthesized by decomposition of $Fe(CO)_5$ and subsequent oxidation. (Courtesy of MACH I Inc, King of Prussia, USA.) This amorphous product consists of fractal agglomerates with a primary particle size of 3 nm. This high surface product has excellent catalytic properties.

Box 4.7   Synthesis of Carbides and Nitrides

Because of their sensitivity against oxidation, it is more difficult to synthesize nanoparticulate carbides or nitrides. A typical, often applied reaction for SiC synthesis is

$$(CH_3)_3 ClSi \Rightarrow SiC + 2CH_4 + HCl. \tag{4.15}$$

Even though this reaction equation looks straightforward, this reaction is difficult to handle, as inappropriate selection of the reaction temperature leads to the formation of elemental silicon particles and soot.

To synthesize nitrides, nitrogen is used as reaction and carrier gas. However, chlorides are more stable than the nitrides, therefore, it is necessary to add hydrogen to shift the equilibrium to the side of the formation of the nitride and hydrochloric acid.

$$MeCl_n + \frac{m}{2}N_2 + \frac{n}{2}H_2 \Rightarrow MeN_m + nHCl. \tag{4.16}$$

Instead of hydrogen, one may also add ammonia to the carrier gas:

$$MeCl_n + \frac{m}{2}NH_3 \Rightarrow MeN_m + nHCl + \frac{3m-n}{n}H_2. \tag{4.17}$$
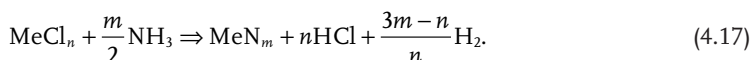
Generally, the addition of ammonia instead of hydrogen reduces the reaction temperature; however, there is the disadvantage of the formation of NH_4Cl as a byproduct.

4.4
Laser-Ablation Process

Instead of a tubular furnace or an electric arc, pulsed lasers are often applied as the source of energy.

The "laser-ablation technique" has the advantage of allowing not only the application of metals, but also the use of oxides, even mixed targets are possible, for the synthesis of nanoparticles. From the basic idea, this makes particle synthesis extremely universal in application. Figure 4.11 displays a typical design of a production unit applying the laser-ablation process.

A laser-ablation system for powder production, generally, consists of the pulsed high-power laser together with the optical focusing system and the feeding device for the precursor. For the production of larger quantities, rotating targets and automatic wire feeding systems were developed.

High-power laser pulses are focused onto the surface of the precursor target to evaporate material. Depending on the thermal conductivity, at the focus point, the target is heated to temperatures high enough to evaporate the material. Because
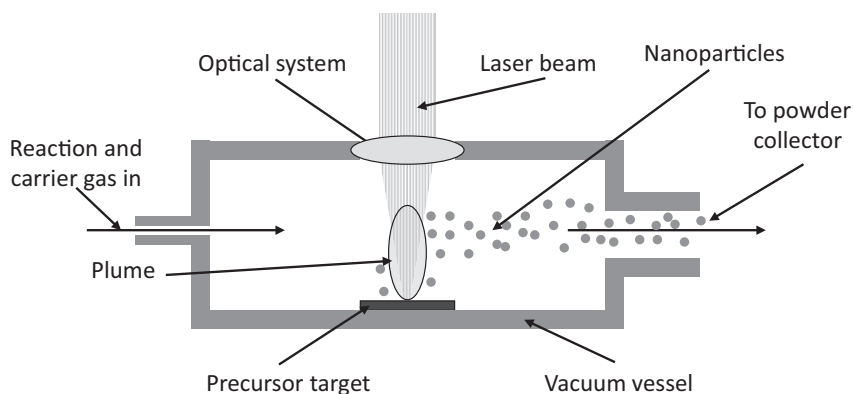
Figure 4.11 Schematic drawing of the experimental setup for nanoparticle synthesis applying laser ablation. The pulsed laser beam is focused at the surface of the precursor target that may be a metal or an oxide. The high-intensity laser beam causes a plume, a supersonic jet of evaporated material, which is ejected perpendicular to the target surface, expanding into the gas space above the target. The particles formed by condensation in the plume are transported with the carrier gas to the powder collector.

of the fast evaporation in the high-power laser pulse, even the stoichiometry of a complex mixed target may be preserved in the vapor phase. During the pulse, a plume, a supersonic jet of evaporated material, is ejected perpendicular to the surface into the surrounding gas and expands adiabatically. Immediately after the laser pulse, the temperature in the plume reaches values of a few thousand *Kelvin* [4]. During the adiabatic expansion of the plume, the temperature decreases and particles are formed. The continuous stream of carrier gas transports the particles to the powder collector. The carrier gas may also contain reactive gas components; to obtain oxides, oxygen, for carbides methane, CH_4, and for nitrides ammonia, NH_3, is added. Due to the supersaturation in the vapor caused by decreasing temperature within the plume, formation of particles occurs. The duration of the supersaturated conditions is limited by the adiabatic expansion of the plume; therefore, the gas pressure in the reaction vessel plays a crucial role in particle nucleation and particle growth. At low gas pressure, the plume expands very rapidly. Therefore, the concentration of reactive species in the plume decreases very rapidly, a process limiting particle growth. At higher gas pressure, the supersaturation is higher. The higher the supersaturation, the smaller the size of the nuclei required for condensation. This leads to a large number of nuclei and, and as consequence, to smaller particle sizes. This simplified description of the complex processes in the plume is well supported by experimental results. As an example, Figure 4.12 displays the dependency of Co_3O_4 particle size on the gas pressure [5]. This figure shows small particles are formed at low and at higher gas pressure, in an intermediate range the particles are largest.
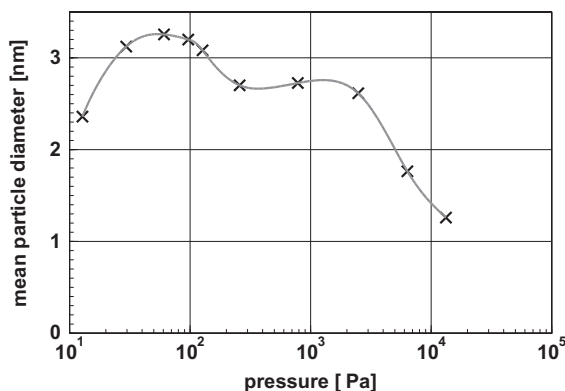
Figure 4.12 Production of nanoparticles using the laser-ablation process. The figure shows the influence of the gas pressure in the reaction chamber on the mean particle size of the reaction product, Co_3O_4 [5].

As the energy source, often frequency-converted Nd-YAG or excimer lasers with pulse durations in the nanosecond range are applied. The interaction of these nanosecond pulses leads, especially at the surface of good thermal conductors, prior to evaporation to the formation of a pool of melted material. In the case of targets with complex composition, this may lead to a composition of the powder that differs from that in the precursor. The application of a picosecond laser avoids this problem. During such a short high-power laser pulse, the material evaporates instantaneously; therefore, melting at the surface is impossible.

A general problem of the laser-ablation process is the high concentration of evaporated material in the plume. Insufficiently fast expansion leads to the formation of agglomerates, a phenomenon that is often observed. These agglomerates are, in most cases, fractal- or web-like. The formation of agglomerates is not intended. Therefore, a huge effort went into the direction of synthesizing individualized particles using this process. A typical example of a successful approach was published by Wang *et al.* [6]. As a precursor for iron oxide, γ-Fe_2O_3, a wire of pure iron was used. These authors used, atypically, a YAG laser with a wavelength of 1064 nm with a pulse width of 0.3–20 ms. The particle-size distribution of this product, as depicted in Figure 4.13, was in the range from 5 to 55 nm, only a minor amount of material was found in the size range from 50 to 90 nm.

The particle-size distribution displayed in Figure 4.13 is a nonsymmetric distribution function, which is typical of a random process of particle formation. This figure demonstrates the inherent high potential of the laser-ablation process into the direction of nonagglomerated materials. This is of some importance, as the laser-ablation process has very few special requirements for the precursor.
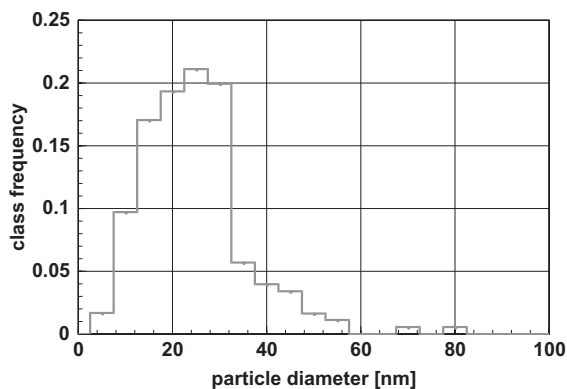
Figure 4.13 γ-Fe_2O_3 powder synthesized by the laser-ablation process. The particle diameter distribution of the product is nonsymmetric, typical of synthesis methods based on purely random processes [7].

4.5
Plasma Processes

4.5.1
Microwave Plasma Processes

Gas-phase synthesis processes, if unbiased, favor the coagulation of the larger particles (see Box 4.4). Chemical and physical vapor synthesis processes and, to some extent, the laser-ablation process are purely random processes. These processes allow manipulation of particle size and size distribution by altering the concentration of active species in the gas, the residence time in the reaction zone, temperature, and by quenching the carrier gas after leaving the reaction zone. Fundamentally different is the agglomeration behavior in the case of particles carrying electrical charges of equal sign (see Box 4.5). In this case, the probability collision of large particles is reduced. These conditions may be reached in the case of plasma processes, especially the microwave plasma process. Therefore, the probability for coagulation and agglomeration is significantly reduced, as the collision parameter decreases with increasing particle size. The present author developed a microwave plasma process operating at reduced gas pressure for synthesis of nanoparticles exploiting the benefits of charged particles, allowing high production rates of unagglomerated particles and narrow particle-size distribution, features that are contradictions with respect to the classical processes of gas-phase synthesis. In a plasma, one finds free electrons, ions, dissociated gas and precursor molecules in addition to neutral gas species. Interaction with an electrical field is possible only with charged species. The oscillating electrical field of the microwaves transfers energy primarily to the electrons, because the energy transfer to
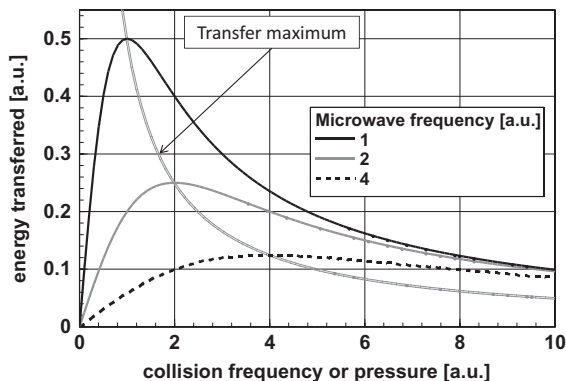
Figure 4.14 Energy transferred in a microwave plasma to an electrically charged particle as a function of the collision frequency and the microwave frequency. The maximum energy is transferred when the collision frequency is equal to the microwave frequency; additionally, the course of the maximum of the energy transfer is indicated.

charged particles is inversely proportional to the mass of the charged particles. The amount of energy transferred depends not at least on the free path length of the electrons, which depends on the gas pressure. This leads to a function exhibiting a maximum of the energy transfer. The maximum of this energy transfer function is found under conditions where the microwave frequency and collision frequency are equal. Figure 4.14 displays this function for three different frequencies of the microwaves as a function of the collision frequency, which is proportional to the gas pressure. Additionally, the course of the maximum of the energy transfer is plotted. It is remarkable that this function decreases with increasing collision frequency.

Box 4.8   Energy Transfer in a Microwave Plasma

In an oscillating electrical field with the frequency f, the energy U transferred to a particle with the electric charge Q and the mass m is given by.

$$U \propto \frac{Q}{mf^2}. \tag{4.18}$$

As the mass of the electrons is a few thousand times smaller than the mass of the ions, the energy is transferred primarily to the electrons, and not to the heavy ions. Equation (4.18) is valid for one charged particle in an oscillating electrical field. In a plasma, the free electrons interact with ions, dissociated gas and precursor molecules, and neutral gas species. Therefore, collisions between charged and uncharged particles limit the mean free path of the

charged particles accelerated in the electric field. Hence, the collision frequency z must be considered [8]

$$U \propto \frac{Q}{m} \frac{z}{f^2 + z^2}.$$ (4.19)

Equation (4.17) does not alter the mass relationship of the energy transfer; rather, it describes the reduction of the energy transferred to the charged particles due to the collisions with neutral species. Furthermore, this function has a maximum for the energy transfer at $f = z$. For $f < z$ the energy transfer increases, for $f > z$ the energy transfer decreases with increasing gas pressure. The collision frequency z in the plasma is, to a first approximation, proportional to the gas pressure. The free path length λ of the electrons limits the maximum energy U_{max} transferred in an electric field with the field strength E:

$$U_{max} = Q\lambda E.$$ (4.20)

As the strength of the electric field in a resonant microwave cavity is in the range of a few $10^6\,V\,m^{-1} \triangleq 10^4\,V\,cm^{-1}$, the energy transferred to an electron, may be, depending on the gas pressure, up to a range of kiloelectron volts.

The energy transfer in an electric field is a function of the microwave power, gas pressure and energy input. These are powerful parameters to adjust the conditions for synthesis, and are optimized for the desired chemical reactions and the product.

In the range of gas pressures usually applied for microwave plasma synthesis, the mean free path length for free electrons may be in the range from 10^{-3} to $10^{-2}\,m$ leading to an energy of the electrons in the range from a few hundred eV to more than one keV. The energy transferred to the ions is, at a maximum, close to $100\,meV$, which is significantly above the thermal mean value, too. Increasing the gas pressure leads to a decrease of the mean free path length of the electrons. As a consequence, the energy uptake in the electrical field is reduced. This has a number of consequences: In the low-pressure regime, the energy of the electrons is high enough to ionize the particles; the particles carry positive charges. Even when in this range electrons and positively charged ions coexist, the probability for recombination of the positively charged particles with highly energetic electrons is small. In the high-pressure regime, the energy of the electrons is low; the electrons are unable to ionize the particles, the electrons rather attach at the surface of the particles; the particles obtain negative electrical charges. In both regimes, the particles repel each other. In between these two ranges there is a broad range where the particles carrying positive or negative charges are found; particles carrying electrical charges of different sign attract each other. This leads to additional agglomeration of particles of any size. In this range of operating conditions, products with narrow size distribution are obtained only in cases of extreme short residence times in the reaction zone and efficient quenching processes after the reaction zone.

Figure 4.15 displays the energy transferred to the particles by the electrical field again; however, on a logarithmic scale for the collision frequency. The three ranges with the different signs of the electrical of the particle charges are indicated.

The design of a microwave plasma system for nanoparticle synthesis, working in the low-pressure regime, is displayed in Figure 4.16.
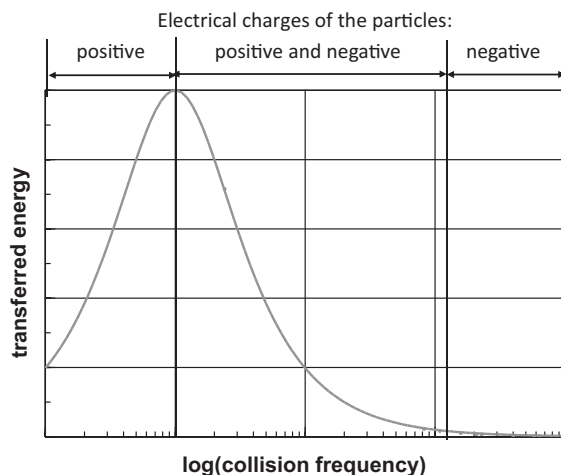

Figure 4.15 Energy transferred in an oscillating electric field to charged particles as a function of the collision frequency, which may be seen to be equivalent to the gas pressure. In this graph, the ranges with different particle charges are indicated. It is important to note that in physical reality these ranges are not clearly limited; in fact, to some extent, they are overlapping.
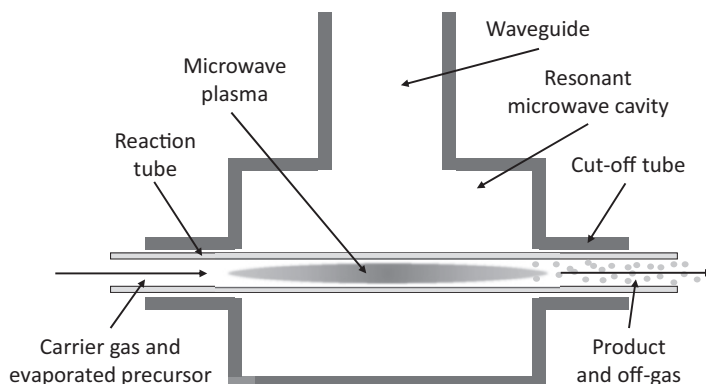

Figure 4.16 Design of a microwave system working in a pressure range that ensures positively charged particles. A carrier gas also containing the reaction gas transports an evaporated precursor into the plasma zone. The reaction product, nanoparticles, is collected after the reaction zone. Microwaves are coupled into the device with the waveguide.

To avoid parasitic absorption of the incoming microwaves the central reaction tube is made of pure silica glass, which passes through a resonant microwave cavity, connected via a waveguide to the microwave generator and the tuning system [9]. Concentrically to the reaction tube, at each end of the cavity there is a cut-off tube. This is a safety feature, as it attenuates microwaves and avoids leakage into the environment. The plasma, the zone where the particles are synthesized, burns at the intersection of the reaction tube and the microwave cavity. The evaporated precursor is introduced into the system via a stream consisting of carrier and reaction gases. The gas flow is selected to keep the residence time of the particles in the reaction as short as possible; in most cases, a residence time in the range of less than 10 ms is selected. Depending on the intended product, the temperature is selected in a range from 400 to 800 K. Such low reaction temperatures are possible, because in contrast to a chemical vapor synthesis in a tubular furnace, the mechanism of the formation of the nanoparticles in the microwave plasma is different, as the reactants are ionized and dissociated. Looking at the price for the devices, in most cases it is advised to select the so-called "kitchen frequency" of 2.45 GHz for the power supply. In special cases, primarily connected to large-scale production, a frequency of 0.915 GHz is applied.

As proof that the above-discussed ideas can be realized in experimental reality, Figure 4.17 displays the particle-size distribution of a ZrO_2 powder, synthesized in a low-pressure microwave plasma system, with a mean particle size around 3 nm. This size distribution was determined by particle mass spectrometry.

Analyzing the particle-size distribution function depicted in Figure 4.17, one realizes besides the extreme small mean particle size that the distribution is, as expected, extremely narrow and asymmetric. Certainly, there are a few large particles in the system, indicating that the particles grew by a process of random collisions.
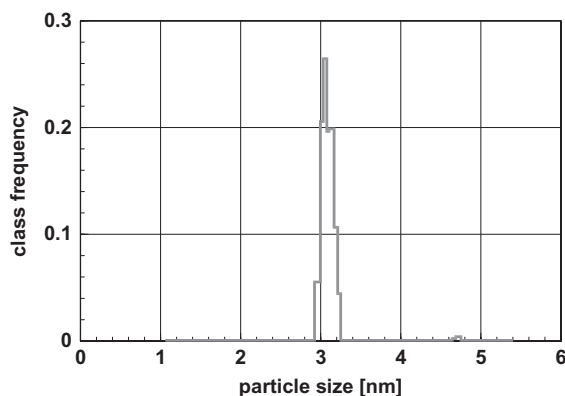

Figure 4.17 Particle-size distribution of zirconia powder synthesized at low gas pressure using the microwave plasma process. This size distribution was measured during synthesis, online, with a particle size spectrometer. (Roth, P., University of Duisburg, Germany) private communication.

In general, the chemical reactions are the same as in a conventional furnace, just at lower temperature. The lower temperatures are possible, because the reactive species are ionized or dissociated in the plasma. Therefore, there is no activation energy needed to initiate the chemical reactions. However, one must be careful that the reaction or the reaction products are not neutralizing the electric charges of the particles.

Box 4.9   Temperature in a Microwave Plasma

The definition of a temperature in a plasma environment is not straightforward, as in terms of thermodynamics, a plasma is a nonequilibrium system. This is caused by the fact that electrical energy is transferred only to charged species and also for charged species the energy transfer depends on the mass of the charged particles (Eq. 4.17). The largest amount of energy is deposited at electrons, the species with the lowest mass, as the energy transfer is indirectly proportional to the mass of the charged particles. To the neutral particles in the electrical field no energy will be transferred. As temperature and energy are just connected just by a constant factor ($u = kT$), these two quantities are to some extent equivalent. Therefore, the electrons carry the highest temperature and the neutral particles (e.g., carrier gas atoms) the lowest. Temperature measurements makes sense only directly after the plasma zone, leading to an averaged temperature. The temperature in an AC or DC plasma is found to be in the range up to 10^4 K. In low-pressure microwave plasma processes the temperature can be adjusted in the range from 400 to 1200 K.

Box 4.10   Plasma Reaction in the Presence of Water

In general, in a microwave plasma, chemical reactions are, more or less, the same as in thermal systems; however, because of dissociation and ionization of the reactive components at lower temperature. Thermal activation of the reactions is not necessary. In selecting chemical reactions, it is necessary to avoid side reactions, which may shift particle formation into an unintended direction. This problem should be clarified with the following example in connection with the synthesis of oxides using chloride precursors: To reduce the reaction temperature, it is of advantage to add water to the reaction gas:
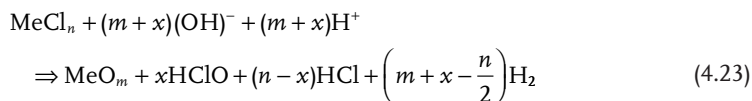
$$MeCl_x + \frac{x}{2}H_2O + \frac{2y-x}{2}O_2 \Rightarrow MeO_y + xHCl. \tag{4.21}$$
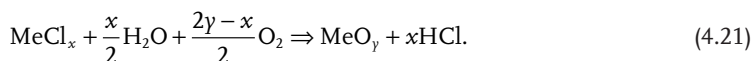
In a plasma environment, the water will dissociate:

$$H_2O \Rightarrow H^+ + (OH)^-. \tag{4.22}$$

This leads to the following side reactions:

Side reaction I:

$$MeCl_n + (m + x)(OH)^- + (m + x)H^+$$

$$\Rightarrow MeO_m + xHClO + (n - x)HCl + \left(m + x - \frac{n}{2}\right)H_2 \qquad (4.23)$$

Side condition: $x \ll n$.

Assuming positively charged particles, one observes

Side reaction II:

$$H_2O \Rightarrow H^+ + (OH)^- \text{ particle}^{n+} + n(OH)^- \Rightarrow (\text{particle}^{n+} + n(OH)^-)^{\text{neutral}}. \qquad (4.24)$$
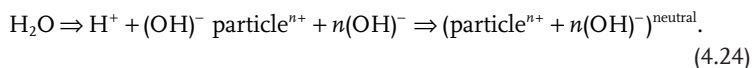
This side reaction leads to a neutralization of the particles, which now carry a hydroxide layer at the surface. As a result, the repulsion mechanism is no longer active; the particles grow similarly as in the previously discussed chemical vapor synthesis process. See also Figure 4.18.

In the case of negatively charged particles, a similar neutralization reaction using the protons occurs.
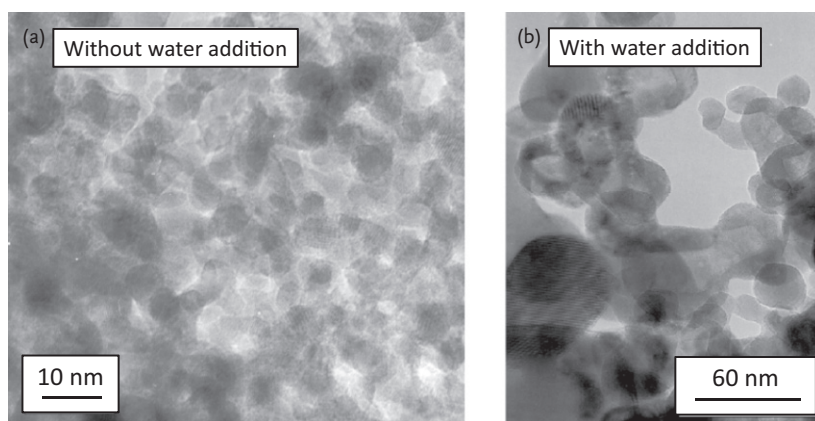

Figure 4.18 Zirconia, ZrO_2, powders synthesized by the microwave plasma process from $ZrCl_4$ at low pressure with and without water addition [10]. (a) Water-free conditions. The size-limiting effect of particle charging during synthesis was active. (b) Water added to the reaction gas. The size-limiting effect of electrical particle charging was lost, as the positively charged particles are neutralized by the $(OH)^-$ radicals originated from water dissociation. (Reproduced with permission by Springer.)

An example where the reaction products of an unintended side reaction leads to particle growth is shown in Figure 4.18. In this case, water was added to the reaction gas. By dissociation of the water $(OH)^-$ ions were formed that neutralized the positively charged particles. For comparison, this figure displays the same material, synthesized under the same experimental conditions; however, produced

with and without water addition. This product shows small particles within a narrow size distribution. The zirconia specimen, displayed in the micrograph, produced without addition of water excel with a grain size around 8 nm with a very narrow size distribution, whereas the material produced with water additions is characterized by a broad distribution of particle sizes in the range from 10 to 50 nm. This dramatic difference between these two batches of the same material clearly proves the validity of this model.

As long as the product is not an electrical conductor, nearly every material can be produced with an arrangement as depicted in Figure 4.16. A typical example of a further product, ZrN, is displayed in Figure 4.19. This material was synthesized using $ZrCl_4$ as precursor and a mixture of N_2 and NH_3 as carrier and reaction gas [11]. As this figure demonstrates, the nitrides also take advantage of the electrical charges of equal sign, the particles are small (less than 10 nm) and show a narrow particle-size distribution.

Figure 4.15 shows that there is a second range, where particles, carrying electrical charges of one sign, negative charges. Such a system, powered with a radiofrequency, RF, generator was described by Buss [12] und later by Matsui [13]. The design of their system is depicted in Figure 4.20.

The system depicted in Figure 4.20 works with a pulsed plasma, burning between two permeable electrodes. In the axis of the reaction tube, a steady flow of carrier gas mixed with evaporated precursor flows. As long as the RF is "on", the particles are kept in the reaction zone and grow. In the "off" cycle, the particles are blown out from the reaction zone and collected outside of the reaction zone. The operating conditions, gas pressure and RF frequency are selected in such a way that the energy of the electrons is in the range of 3 eV. Electrons in this energy range tend to attach at the surface of the particles; they are not ionizing; therefore, the particles carry negative charges. As the particles carry unipolar electrical
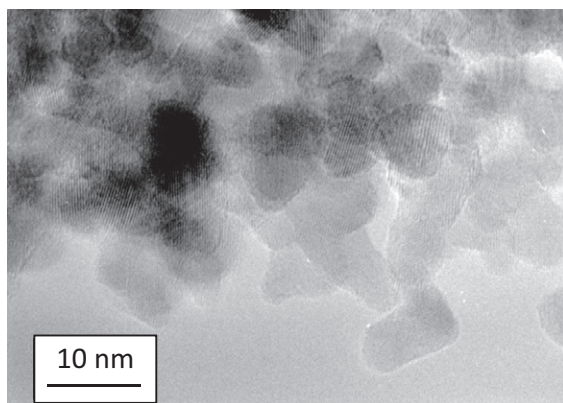

10 nm

Figure 4.19 Zirconium nitride, ZrN particles made of $ZrCl_4$ as precursor and a mixture of N_2 and NH_3 as carrier and reaction gas, in a microwave plasma. The lattice fringes visible within some of the particles indicate they are well-crystallized material [11]. (Reproduced by permission of Elsevier.)
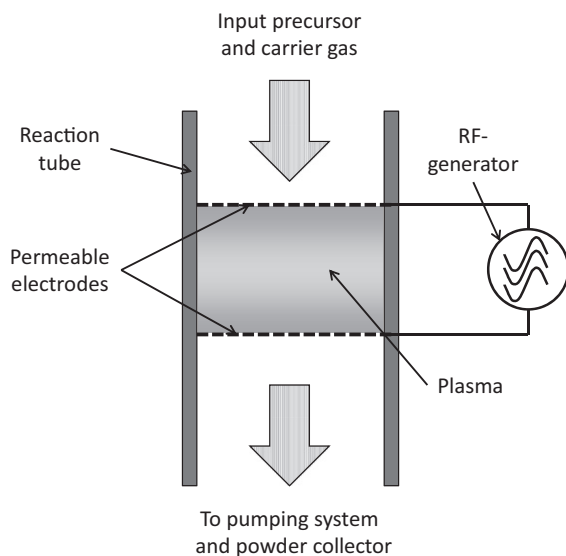
Figure 4.20 System for synthesis of nanoparticles working with operating conditions where all particles carry negative charges. In this design, the radio-frequency, RF, field is in-between two permeable electrodes, where the plasma burns. As long as the RF is "on", and, therefore, the plasma burns, the particles are kept between the electrodes and grow [12, 13].

charges, the resulting products excel with quite a narrow particle-size distribution. An essential advantage of this design is the ability to adjust the particle size by the pulse length of the RF. Figure 4.21 displays the dependency of the particle size as a function of the RF pulse length.

Figure 4.22 shows an electron micrograph of a typical product, in this case hard magnetic FePt particles. The particles were placed on a holey carbon film. As expected, the particles depicted in Figure 4.22 are very uniform in size.

4.5.2
RF and DC Plasma Processes

Plasma processes working with direct current, DC, or radio-frequency, RF sources for the energy supply are high-temperature processes. Therefore, the quenching step, directly following the plasma synthesis is of essential importance. Additionally, in most cases, argon is used as carrier gas. As argon is, looking at industrial scales, quite expensive, process gas recycling is of economic importance. Furthermore, one has to distinguish two basic design varieties: Processes using electrodes, in most cases powered with direct current, DC, or alternating current, AC, and electrodeless designs powered with radio-frequency, RF, generators. In general, independent of the power supply, these considerations lead to a process design,
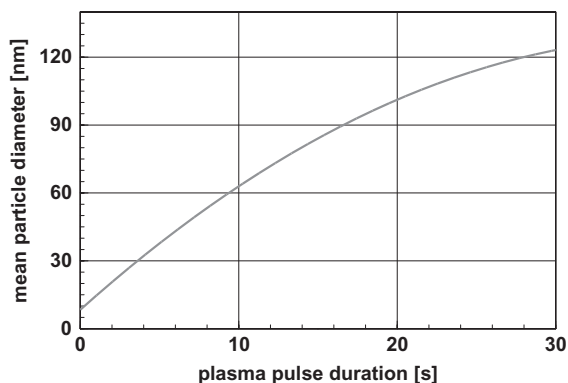
Figure 4.21 Dependency of the size of FePt particles on the duration of the radio-frequency, RF, pulse in an equipment according to Figure 4.20 [13].
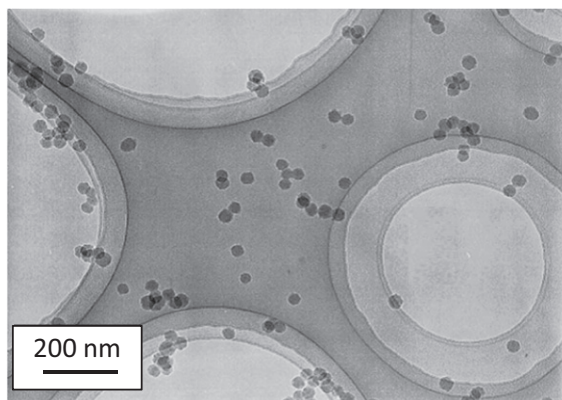

Figure 4.22 Hard magnetic FePt particles synthesized in a plasma system according to Figure 4.20. The very narrow distribution of particle sizes, visible in the electron micrograph, is remarkable [13]. (Reproduced by permission of Springer.)

as is depicted in Figure 4.23. Figure 4.24 displays two designs for plasma processes using electrodes.

For processes depicted in Figure 4.24, the precursor is either gaseous or a powder blown with a carrier gas into the plasma flame. Even when this type of process is used for the production of large quantities, it must be stated that the quality is, with respect to the very special requirements for most of the applications of nanoparticles, very poor. In this respect, the electrodeless RF processes are significantly more successful. Such devices are, in the meantime available industrially as turnkey products. Figure 4.25 displays such a design.

The advantage of a design according to Figure 4.25 is the extended residence time of the precursor in the plasma. This is important in cases where the reaction
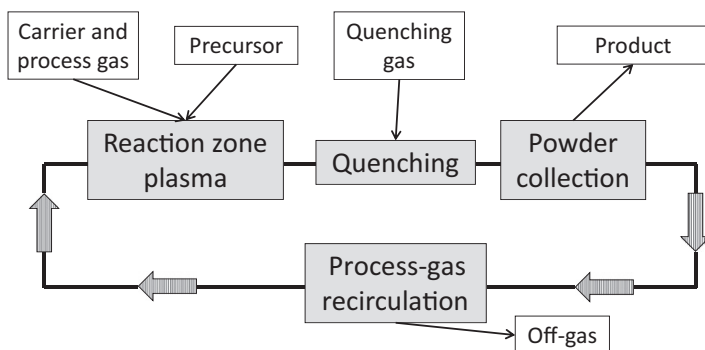
Figure 4.23 Process schema for high-temperature plasma processes. To obtain top-quality products, the design of the quenching step is of essential importance. For economic reasons, process gas recycling is necessary.
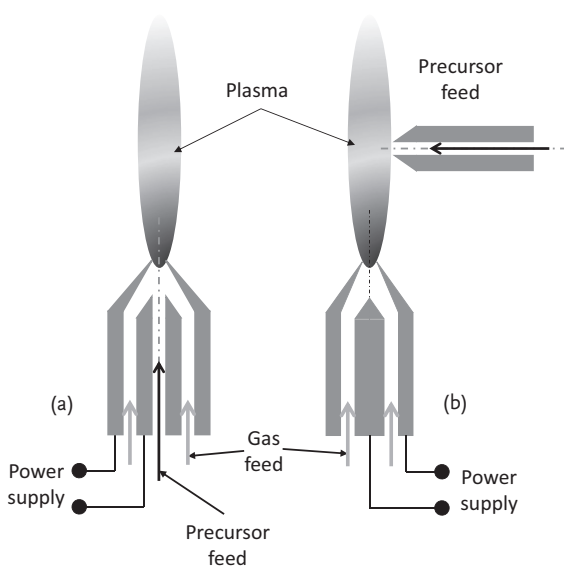

Figure 4.24 Two basic designs for plasma processes applying electrodes. The two designs differ in the feed of the precursor; either coaxial into the plasma burner (a) or the precursor is blown perpendicular into the plasma flame (b). Such systems are powered either by DC or AC sources.

rate of particle formation is low. The capacity of such systems reaches from grams to kilograms per hour. A typical example of a product of such an industrial equipment is shown in Figure 4.26, displaying GeO powder with a surprisingly narrow particle-size distribution. Additionally, this figure documents the importance of and the opportunities to influence the particle size of the product. In these micrographs, the influence of the quenching conditions is clearly visible. Obviously,
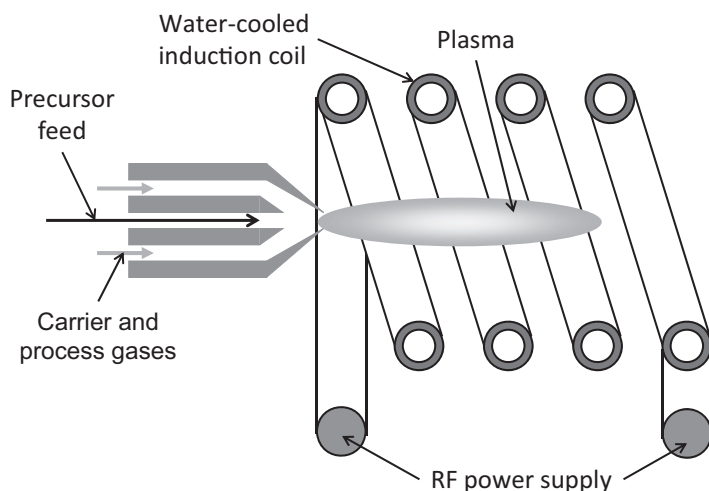
Figure 4.25 Design of an electrodeless radio frequency, RF plasma system. In this design, the precursor is blown, together with the process gas, axially into the system.
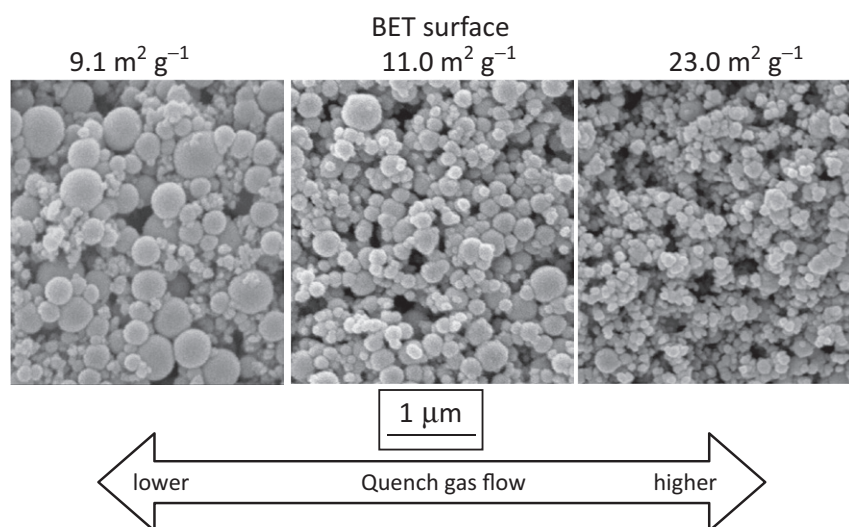
Figure 4.26 GeO nanopowder produced using an industrial, electrodeless RF system. These three micrographs verify the significant influence of the quenching conditions on the particle size of the final product. As a measure for the particle size, the specific surface is given. (Courtesy of Tekna Plasma Systems Inc., Sherbrooke, Québec, J1L 2T9, Canada).

quenching influences the mean particle size and the width of the size distribution. In this example, as a measure for the particle size, the specific surface area in square meters per gram is given. Highly optimized industrial systems produce nanopowders of good quality with particle sizes of less than 100 nm. Possible products are metals, oxides, carbides, and nitrides. Except for oxides and precious metals, powders of these products may be highly pyrophoric; therefore, it is strongly recommended to handle these products in an inert gas atmosphere, if possible within glove boxes.

4.6
Flame Processes

Since prehistoric times, in China, carbon black has been produced by flame processes, as pigments for inks. The flame aerosol process is the oldest of all processes to produce nanoparticulate powders in our time. This technology, or one of its many variants, is applied to produce thousands of metric tons of carbon black, fumed silica, and titania, TiO_2 pigments. Lastly, it is the only process applicable for mass production in the kiloton range. Even though this process is well established and widely applied in industry, the basis principles are not completely understood. This is not least because these processes have been working for decades; therefore, for a long time, there was no need for basic studies, which are difficult and expensive, because particle formation takes place at extremely high temperatures in very short times. With the trend to apply this process also for high value added products, the situation has changed significantly.

The aerosol flame process has a long history and broad application; therefore, with respect to new materials, many highly specific variants, leading to particles with different morphology, size, and crystallinity were developed. Important reviews on flame aerosol processes were published by Pratsinis [14] and Wooldrige [15].

In the simplest case, a flame reactor is set up as shown in Figures 4.27a,b. Basically, a flame reactor consists of a primary flame that is fueled with hydrogen, methane or another hydrocarbon fuel. As far as possible, the selection of a gaseous precursor is advised. Such a precursor may be, for example, to synthesize silica, SiO_2, silane, SiH_4 or silicon tetrachloride, $SiCl_4$. Generally, the gaseous fuel comes premixed with oxygen or air in the burner. In general, the design of the burner follows one of the two principles depicted in Figure 4.27: Figure 4.27a displays the most conventional system, where the precursor, if necessary diluted with a carrier gas, is blown from the side into the flame. The dilution of the precursor with a carrier gas is also applied to adjust the particle size of the product.

The design displayed in Figure 4.27b is more advanced. Characteristic of this design are the many small primary flames surrounding the secondary flame, where the precursor reacts with the excess oxygen forming a secondary flame, where the reaction for particle formation occurs.
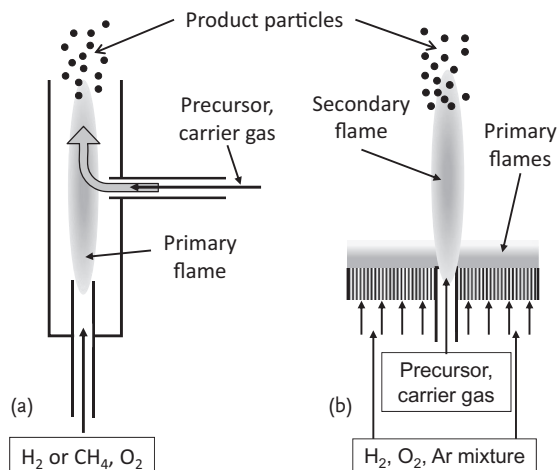
Figure 4.27 Typical arrangements for flame synthesis of nanoparticles. (a) In this design, the vaporized precursor is introduced from the side into the primary flame for reaction. (b) A field of primary flames surrounds a secondary flame, in which the powder is produced.
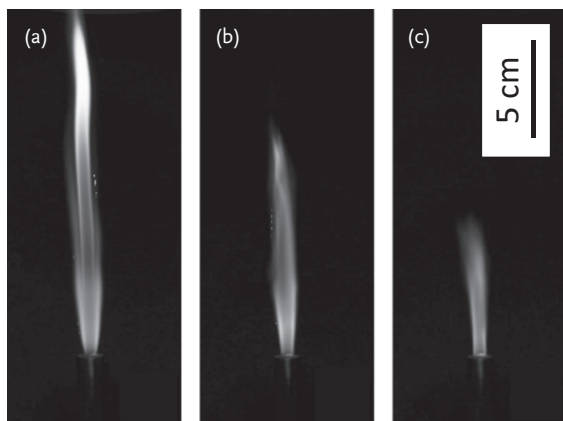
Figure 4.28 Appearance of flames with methane as fuel and hexamethyl disiloxane, $C_6H_{18}OSi_2$ as a precursor for silica. The amount of oxygen increased from (a) over (b) to (c). The flame with the lowest oxygen content was unstable, fluctuated. With increasing oxygen content, the flame burns more stably and the temperature increases [16]. (Reproduced by permission of Elsevier.)

Reproducible results of the synthesis process are obtained only under conditions where the flame is absolutely stable. A critical ingredient for a stable flame is the correct amount of oxygen. Figure 4.28 displays the appearance of the flame with different additions of oxygen to the fuel, methane, CH_4. This example displays the flame in the case of silica synthesis, where hexamethyl disiloxane, $C_6H_{18}OSi_2$ was used as precursor.

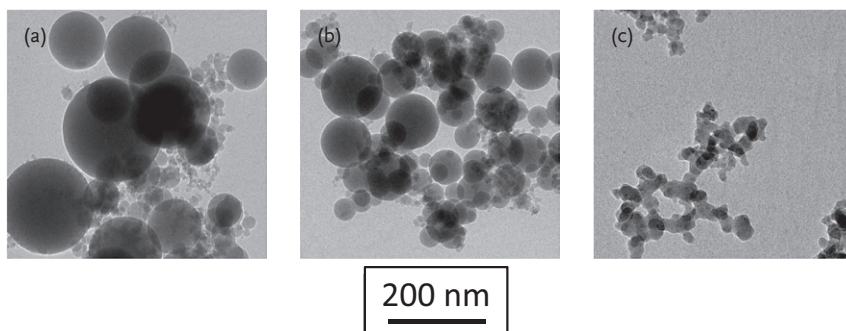**Figure 4.29** Electron micrographs of silica powders produced with varying oxygen content in the flame under otherwise constant conditions. The conditions for synthesis are identical to those given in Figure 4.28 [16]. (a) Oxygen addition 2.5 l min^{-1}. This product consists of nonagglomerated particles, however, with a broad distribution of particle sizes. (b) Oxygen addition 8.5 l min^{-1}. Similar as in Figure 4.29a, in this product the particles are not agglomerated. Even when the distribution of particle sizes remained broad, the size of the largest particles is reduced. (c) Oxygen addition 25 l min^{-1}. In contrast to the products depicted in Figures 4.29a,b, this product forms fractal agglomerates. The size of the particles is smallest and quite uniform. (Reproduced by permission from Elsevier.)

In Figure 4.28 the oxygen content in the flame increased from Figure 4.28a to 4.28b. At low oxygen flow rates, the flame is instable and fluctuating. With increasing oxygen addition the flame is more stable and hotter. The oxygen content in the flame influences the average particle size; this is visible in Figures 4.29a–c. In these electron micrographs, the oxygen content in the flame increased from Figures 4.29a–c, similar as in the case of the flames depicted in Figures 4.28a–c.

The oxygen content of the gas supplying the flame has a significant influence on the morphology of the powder, too. This has two reasons: Under otherwise constant conditions, with increasing addition of oxygen to the flame, the temperature in the flame increases. Additionally, the flow rate increases and, as shown in Figure 4.28, the flame gets shorter. Therefore, the residence time of the powder particles in the flame shortens. This is the reason for the decreasing particle size with increasing oxygen addition, as is visible in the micrographs depicted in Figure 4.29.

There have been many attempts to reduce the tendency of the flame processes to deliver agglomerated particles of small size. In this case, the phenomena work in opposite directions: High oxygen content in the gas results in high temperatures, leading to small particles; however, they are agglomerated. How to modify the process to reduce this problem? One way out of this problem may be found in the fact that one needs high temperatures to obtain small particles; at these temperatures a significant fraction of the particles will show thermal ionization. (For good reasons, flames are often called "thin plasmas".) This gives the possibility to influence the process of particle formation and agglomeration using external

electrical fields. Figure 4.30 displays two experimental assemblies to study these possibilities.

As mentioned above, at high temperature, one expects thermal emission of electrons from the particles. However, as these electrons only have thermal energy in the range of less than 1 eV, therefore, they can also attach at the surface of the particles. Hence, one may expect positively and negatively charged particles. Figure 4.31 displays a proof of this assumption. The figure displays a flame
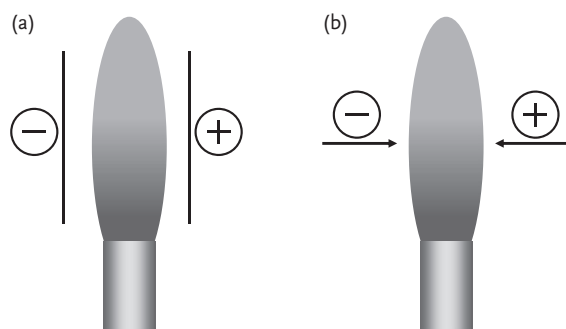

(a)   (b)

Figure 4.30 Experimental arrangement to influence flame synthesis with an external electrical field. The two possibilities depicted are an electrical field in-between two plate electrodes (a) and in-between two needle-shaped electrodes (b). In the latter case, electron emission from the needles is possible.
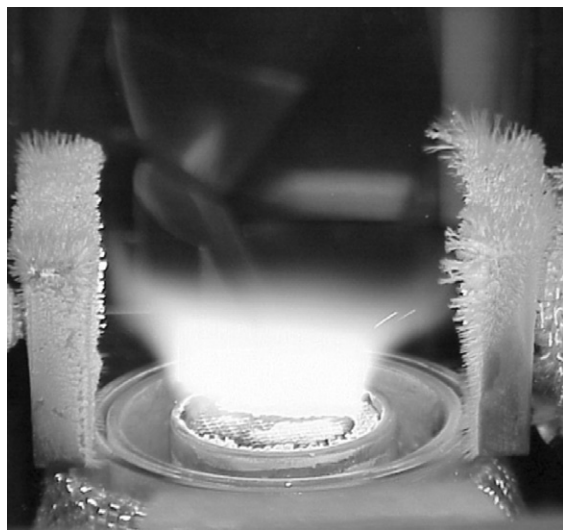

Figure 4.31 Flame in-between plate electrodes with an electrical field of 2 kV cm^{-1}. According to the different signs of the electrical charges, the flame is split up by the electric field. The synthesized particles, titania, were, according to the sign of their electrical charges, attracted by the electrode plates and deposited [17]. (Reproduced by permission from Elsevier.)

in-between two plate electrodes. The field strength was $2\,kV\,cm^{-1}$. One sees that both electrodes are covered with particles. This indicates that the particles carry, as assumed, electrical charges of both sign.

In the arrangement using plate electrodes (Figures 4.30a and 4.31), due to their electrical charges, the particles are pulled out of the flame. Therefore, the time for growing and, most importantly, for agglomeration is reduced. This improves the chance to obtain unagglomerated products with small particles. A different mechanism, however, also with encouraging results is observed in the experimental setup depicted in Figure 4.30b. At the tips of the needle electrodes, one observes corona discharge. These electrons move across the flame. Because of their high energy, these electrons ionize the particles, now all of them carry negative electrical charges. These negatively charged particles, repelling each other, move to the positive electrode and are collected. As result, one may expect that the particle size of the product decreases with increasing field strength between the needle electrodes. These ideas were perfectly proved. Figure 4.32 displays the mean particle size of titania produced from the chloride in a flame as a function of the electrical field strength synthesized in both arrangements depicted in Figure 4.30.

The graph in Figure 4.32 clearly demonstrates the effect of a transversal electrical field. In the case of plate electrodes, the reduction of the particle size starts already at relatively low electrical field strength and this reduction continues further with increasing field strength. This is different with needle electrodes. In this design, the size reduction starts at significantly higher electrical fields. Obviously, the system needs a minimum field strength until electron emission starts. After the onset of electron emission, the reduction of the particle size is continued with further increase of the electrical field strength. Figure 4.31 demonstrates that there is a more or less equal number of positively and negatively charged particles
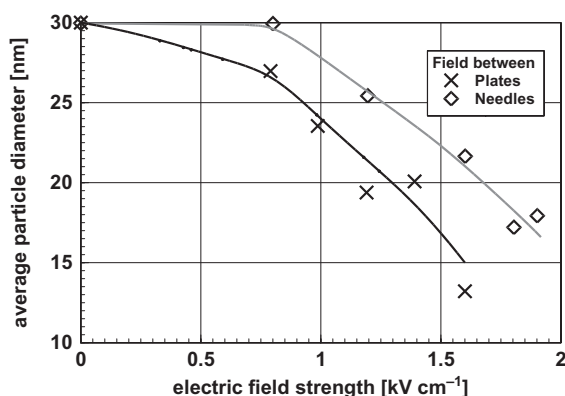
Figure 4.32 Average particle size of TiO_2 ex $TiCl_4$ synthesized in a methane–oxygen flame as a function of the transversal electrical field. The different influence of the two experimental arrangements is clearly visible. It is essential to realize that, in the case of needle electrodes, the field influence starts at higher electrical fields. This is, because the system needs an electrical-field strength, where corona discharge starts [17, 18].

in the system. The design using needle electrodes will come to its full efficiency at field strengths where the electron emission is so high that all particles that carried a positive charge in the flame are negatively charged.

There is a broad variation of different designs for flame synthesis. An important variation applies a liquid fuel, having the advantage that the precursor can be dissolved in the liquid fuel Typical examples are a solution of water-free chlorides in, for example, acetonitrile, CH_3CN or solutions of acetylacetonates, for example, $(C_5H_8O_2)_3Al$ in appropriate organic solvents. An important criterion in selecting organic liquid fuels the avoidance of soot formation, which is often observed in the case of benzene, C_6H_6. On the other hand, mixtures of benzene with ethanol have been applied successfully, too.

4.7
Synthesis of Coated Particles

Many applications of nanoparticles and nanomaterials need nanocomposites. The required nanocomposites may be either multifunctional particles or bulk materials. In the case of multifunctional particles, one selects materials with different properties for the core and the coating of the particles. Looking at bulk nanocomposites, in most cases it is necessary to obtain optimal properties such that the particles are not touching. Both requirements can be fulfilled only with coated particles. A series of possible applications were already explained in Chapter 2. To synthesize coated particles, the process must fulfill a series of requirements. Most important is the demand that the particles must not touch each other; otherwise, one coats clusters of particles and not particles. Furthermore, in many instances, the coating consists of organic compounds. Therefore, the temperature must be so low that these compounds are not altered or even destroyed. The first process succeeding in synthesizing coated nanoparticles and, until now, the only gas-phase process fulfilling these challenges is the microwave plasma process [19, 20]. Figure 4.33 displays such an equipment, which is lastly a doubling of the design as presented in Figure 4.16.

The microwave plasma device to synthesize ceramically coated ceramic nanoparticles consists essentially of two microwave plasma devices working consecutively. It is important to ensure that the distance between these reactors is as small as possible; otherwise, too large a number of the particles produced in the first step will lose their positive electrical charge stemming from the synthesis process. The risk of losing the positive charges is relatively high, as, to maintain electrical neutrality, there are, also outside of the plasma zone, free electrons with low energy in the system. This increases the risk of agglomeration. Losing the electrical charges of the particles can be minimized by using conditions with a long free path length of the particles to reduce the probability of collisions. At each collision, a free electron will lose energy in the range of 10 to 15 eV. Assuming an energy of the free electron of approximately 1 keV, there are, at maximum, 100 collisions allowed. Electrons with low energy will neutralize the particles and attach at the
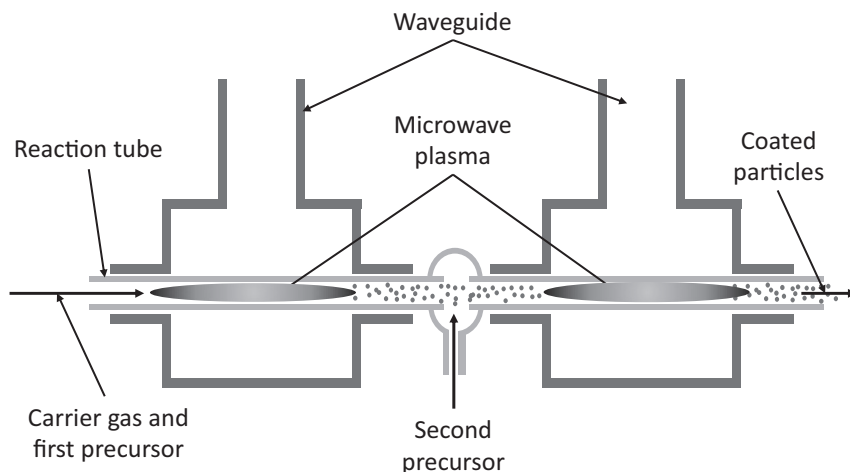
Figure 4.33 Microwave plasma device for synthesizing ceramic-coated ceramic nanoparticles in a microwave plasma according to Vollath [19, 20]. This was the first design of gas-phase processes allowing the production of significant quantities of coated nanoparticles.
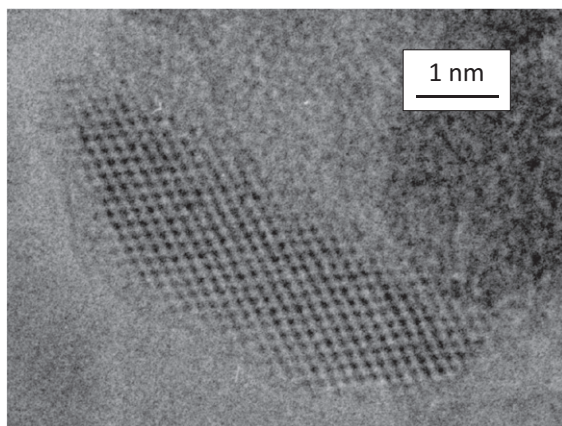

Figure 4.34 Zirconia, ZrO_2 particle coated with a second ceramic material, alumina, Al_2O_3. This material was produced with the microwave plasma device, depicted in Figure 4.33. The zirconia core is perfectly crystallized, as is indicated by the lattice fringes. The alumina coating is amorphous; therefore, it shows no structure [19, 20]. (Reproduced with permission by Elsevier.)

surface. As the movement of the electrons is random in all directions, it is quite difficult to estimate the maximum allowed distance between the two reaction zones.

A typical example of such a product is depicted in Figure 4.34. This figure shows a zirconia particle coated with alumina. The electron micrograph shows crystallized zirconia, which is documented by the lattice fringes, and amorphous alumina,
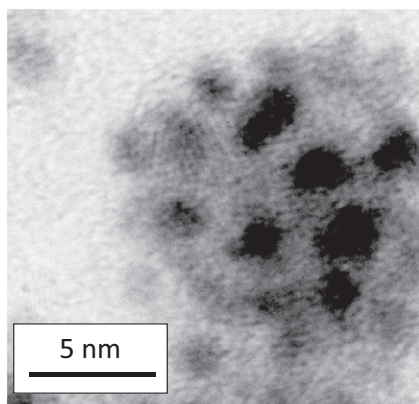
5 nm

Figure 4.35 Ceramic particle, titania, TiO_2 decorated with metallic clusters (the dark spots), platinum, synthesized using the two-stage microwave plasma process, as depicted in Figure 4.33. At the surface of ceramic particles, metals form clusters and not a continuous layer. Not until the metal layer gets quite thick (after the metal clusters touch each other) is a continuous coating possible. (Vollath, D., and Szabó, D.V. (2000), Forschungszentrum Karlsruhe, unpublished results.)

showing no lattice fringes at all. (Under the conditions of microwave plasma synthesis, alumina, similar to silica, is never crystallized.) From the nonspherical shape of the zirconia particle one may guess that this particle is a result of the coagulation of two particles.

Certainly, one could think of coating ceramic particles with metals, for example, platinum. For application as catalysts, this would save expensive material. However, it is impossible to realize this idea. Because of the relations of the surface energy, this type of coating is impossible, the metal is deposited as clusters, a phenomenon that is very helpful in looking at applications as catalysts. Figure 4.35 displays such a particle decorated with metallic clusters. In this case, the ceramic core consisted of titania and the metallic clusters of platinum. For the synthesis of this composite, the precursors were titanium chloride, $TiCl_3$ and platinum carbonyl chloride, $Pt(CO)_2Cl_2$.

As already mentioned in the motivation for the development of coated particles, ceramic particles coated with an organic material are of great importance, especially, as by appropriate selection of the constituents, the design of multifunctional particles such particles becomes possible. This may be coating with a polymer as the distance holder in bulk bodies or functional organic molecule, for example, luminescent ones. In selecting the operating conditions and the organic molecules, the temperature and the oxidizing atmosphere must be taken into account. In particular, coating of oxide particles with organic molecules is, with very few exceptions, only possible with the microwave plasma process. Figure 4.36 displays the setup for synthesis of polymer coated nanoparticles.
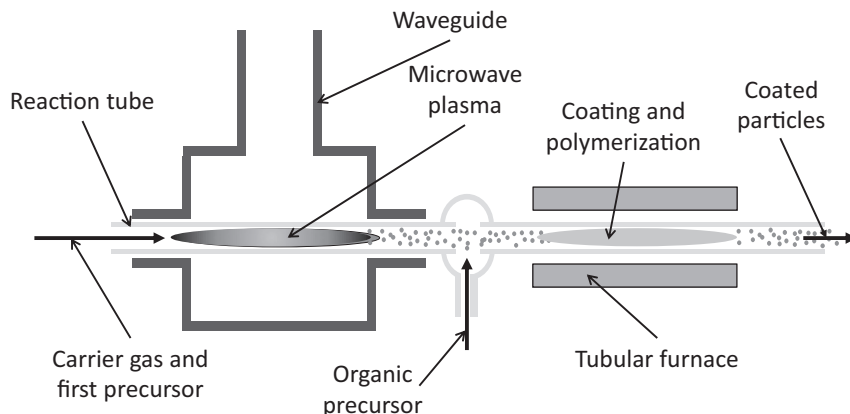
Figure 4.36 Experimental setup for the synthesis of polymer coated ceramic nanoparticles according to Vollath *et al.* [21]. The system consists of a microwave plasma reactor, where the ceramic particles are produced, and subsequently a reaction zone in a tubular furnace, where the coating occurs.

To coat, for example, oxide particles with a polymer first, the particles are synthesized in the microwave plasma region. After the cut-off tube, the organic precursor is added. To obtain a polymer, the corresponding monomer or easily evaporating oligomer is added. The temperature in the system is selected in a way that the condensation of these organic precursor molecules at the surface of the nanoparticle is possible. To obtain the correct temperature and to avoid particle losses by thermophoresis, the condensation zone is heated by a tubular furnace or another heating system. Provided the compounds are selected properly, under the influence of temperature und the UV radiation from the microwave plasma, the monomer at the surface of the nanoparticles starts to polymerize. Additionally, in many cases, the organic compounds react with the oxide particle forming one huge molecule consisting of the particle and the polymer coating. This changes the properties of the particles and the polymer molecules dramatically. As these new giant molecules have, for example, new optical properties, the interaction between oxide nanoparticles and PMMA at the surface is explained in Chapter 9. As an example, Figure 4.37 displays an iron oxide particle coated with PMMA.

The coated particle displayed in Figure 4.37 consists of a core of maghemite, $\gamma\text{-Fe}_2\text{O}_3$, and a PMMA coating. In this example, the ceramic core has a diameter of 6–7 nm; whereas the thickness of the coating is between 3 and 4 nm. The device, as depicted in Figure 4.36, may be setup with more than one stage for coating. This allows a first coating, for example, with a luminescent material and a second polymer layer for protection [10]. This leads to multifunctional particles [22]; details of this class of nanocomposites are explained in Chapters 2 and 9.
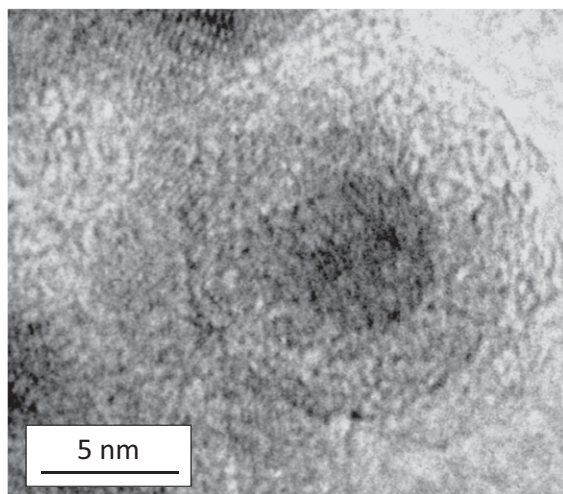
5 nm

Figure 4.37 Iron-oxide nanoparticle coated with PMMA. This composite was produced in a setup according to Figure 4.36. The dark core is the iron-oxide kernel [21]. (Reproduced with permission by Elsevier.)

References

1 Nitsche, R., Rodewald, M., Skandan, G., Fuessl, H., and Hahn, H. (1996) *Nanostruct. Mater.*, **7**, 535–546.

2 Ziemann, P.J., Kittelson, D.B., and McMurry, P.H. (1996) *J. Aerosol Sci.*, **27**, 587–606.

3 Kimoto, K. (1953) *J. Phys. Soc. Jpn.*, **8**, 762.

4 Puretzky, A.A., Geohegan, D.B., Fan, X., and Pennycook, S.J. (2000) *Appl. Phys.*, **A70**, 153–160.

5 Li, Q., Sasaki, T., and Koshizaki, N. (1999) *Appl. Phys.*, **A69**, 115–118.

6 Wang, Z., Liu, Y., and Zeng, X. (2006) *Powder Technol.*, **161**, 65–68.

7 Li, S., and El-Shall M. S. M., (1998) *Appl. Surf. Sci.*, **127–129**, 330–338.

8 MacDonald, A. D. (1966) *Microwave Breakdown in Gases*, John Wiley & Sons, Inc., New York.

9 Vollath, D., and Sickafus, K.E. (1992) *Nanostruct. Mater.*, **1**, 427–438.

10 Vollath, D., and Szabó, D.V. (2006) *J. Nanopart. Res.*, **8**, 417–418.

11 Vollath, D., and Sickafus, K.E. (1993) *Nanostruct. Mater.*, **2**, 451–456.

12 Buss, R.J. (1997) RF-plasma Synthesis of Nanosize Silicon Carbide and Nitride, DOE Report, Sandia Laboratories, SAND97-0039.

13 Matsui, I. (2006) *J. Nanopart. Res.*, **8**, 429–443.

14 Pratsinis, S. (1998) *Prog. Energy Combust. Sci.*, **24**, 197–219.

15 Wooldrige, M.S. (1998) *Prog. Energy Combust. Sci.*, **24**, 63–87.

16 Mueller, R., Kammler, H.K., Pratsinis, S.E., Vital, A., Beaucage, G., and Burtscher, P. (2004) *Powder Technol.*, **140**, 40–48.

17 Kammler, H.K., Pratsinis, S.E., Morrison, P.W., Jr., and Hemmerling, B. (2002) *Combust. Flame*, **128**, 369–381.

18 Pratsinis, S.E. (1998) *Prog. Energy Combust. Sci.*, **24**, 197–219.

19 Vollath, D., and Szabó, D.V. (1994) *Nanostruct. Mater.*, **4**, 927–938.

20 Vollath, D., and Szabó, D.V. (1999) *J. Nanopart. Res.*, **1**, 235–242.

21 Vollath, D., Szabó, D.V., and Fuchs, J. (1999) *Nanostruct. Mater.*, **12**, 433–438.

22 Vollath, D. (2010) *Adv. Mater.*, **22**, 4410–4415.

5
One- and Two-Dimensional Nanoparticles

5.1
Basic Considerations

One and two-dimensional nanoparticles, generally called nanotubes and nanorods for the one-dimensional ones and nanoplates, the two-dimensional ones, are often observed. These entities are interesting both from the standpoint of science and for economic reasons, as these particles have a broad range of applications in many fields of technology. Within this group there is a very special type of particle, the fullerenes; fullerenes based on carbon or other inorganic compounds. As per definition, fullerenes are zero-dimensional particles, as they are simply spherical entities; however, their geometry and the formation is understood only in connection to the related nanotubes or nanoplates.

One expects the shape of nanoparticles to represent a minimum of surface energy. Therefore, in most cases, nanoparticles are spherical in shape, at least facetted particles, which are close to a sphere. To understand the reason for nonspherical nanoparticles, one has to look at the crystalline structure and to the method for synthesizing.

The surface energy depends on the crystallographic plane. For example, in cubic structure, the planes describing a cube have the lowest surface energy. The discussion is most important in noncubic systems. Depending on the surface energy of the different planes, noncubic substances may have a tendency to crystallize in rods or plates. If the surface energy is modified by surface-active substances, also in the case of cubic structures, rods or plates are obtainable. Therefore, it is possible to produce rods of gold, even when gold crystallizes in a cubic structure.

The dependency of the surface energy on the crystallographic plane has consequences on the shape of nanoparticles: Assuming a prism with a quadratic base with an edge length a, and a height c one obtains a rod-like prism in the case that the surface energy of the base plane is large compared to that of the side plane. In the other case, one obtains a plate-like prism. The ratio of the sides of a tetragonal prism is equal to the ratio of the surface energies. This is the rule for the formation of nanorods or nanoplates that can be derived from thermodynamics.

Box 5.1   Shape of Noncubic-Shaped Particles

Surface energy is the reason for nonspherical nanostructures in case of aniso-tropic (noncubic) crystal structures. As an example, assuming a tetragonal body with the sides a, c, and the surface energies γ_a and γ_c. The surface energy of such a prism is u_{surf}:

$$u_{\mathrm{surf}} = 4\gamma_a ac + 2\gamma_c a^2. \tag{5.1}$$

The ratio $\dfrac{a}{c}$ of this prism is obtained under the presumption of a constant volume v

$$v = a^2 c \Rightarrow c = \frac{v}{a^2} \Rightarrow u_{\mathrm{surf}} = 4\gamma_a \frac{v}{a} + 2\gamma_c a^2.$$

The minimum of surface energy is calculated by

$$\frac{\partial u_{\mathrm{surf}}}{\partial a} = -4\gamma_a \frac{v}{a^2} + 4\gamma_c a = -4\gamma_a c + 4\gamma_c a = 0,$$

leading to the important relation

$$\frac{\gamma_a}{\gamma_c} = \frac{a}{c}. \tag{5.2}$$

Equation (5.2) says: The ratio of the sides of a tetragonal prism is equal to the ratio of the surface energies. This is the thermodynamic reason for the formation of nanorods or nanoplates. As in cubic structures $\gamma_a = \gamma_c$ is valid, Eq. (5.2) leads to $a = c$, a cube. For hexagonal structures, the same derivation is possible.

The same mechanism is valid on combining two prisms. Two rod-like prisms will combine in a way to extend the length, the second prism will not attach at the side. In the other case, it is just the opposite: The second platelet will attach at the side. This is depicted in Figure 5.1. Combinations leading to a minimum of surface energy are those indicated as (a) and (d). The combinations (b) and (c) are energetically not favorable, and they will be avoided. One can establish the rule: Agglomerates of nanorods reduce their surface energy by increasing their aspect ratio and in the case of nanoplates, surface energy is reduced by decreasing the aspect ratio. In both cases, the tendency of formng a rod or a plate is enhanced.

It is important to mention that the mechanism described above is valid for "clean" surfaces only, these are surfaces that are not modified by contaminants or functionalization. By proper selection of surface-active molecules, it is possible to grow rods or even plates from isotropic materials. In this context it must be mentioned that even from gold, a cubic material, nanorods and nanoplates are well known. The interest on these specially shaped nanoparticles is promoted by many interesting physical properties connected to these structures.
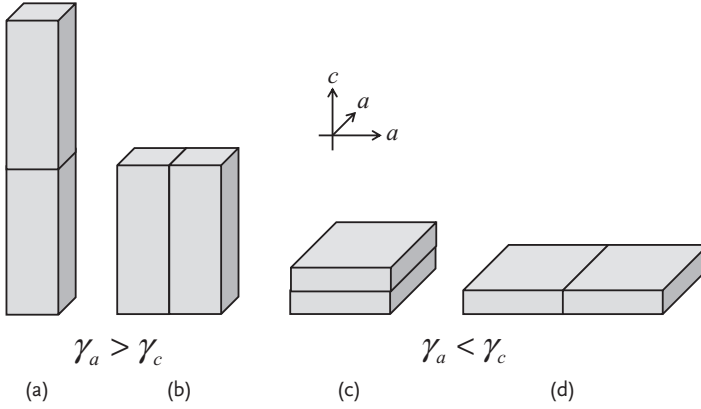
Figure 5.1 Combination of prisms with different surface energy. To minimize surface energy, combinations of two prisms will occur in the way as indicated as (a) and (d). The two other combinations (b) and (c) lead to higher surface energy; therefore, they do not occur.

Box 5.2   Formation of Rods and Plates

The configuration (a) shown in Figure 5.1 has a surface energy of

$$u_{\text{surf}-\text{A}} = 8\gamma_a ac + 2\gamma_c a^2 \tag{5.3}$$

and the arrangement indicated as (b)

$$u_{\text{surf}-\text{B}} = 6\gamma_a ac + 4\gamma_c a^2. \tag{5.4}$$

Comparing formulae (5.3) and (5.4) and keeping in mind $a < c$ one can compare the surface energies of the arrangements (a) and (b); this leads to

$$8\gamma_a ac + 2\gamma_c a^2 < 6\gamma_a ac + 4\gamma_c a^2 \Rightarrow \frac{\gamma_a}{\gamma_c}\frac{c}{a} < 1$$

or

$$\frac{\gamma_a}{\gamma_c} < \frac{a}{c}. \tag{5.5a}$$

Equation (5.5a) is equivalent to Eq. (5.2). For the configurations (c) and (d) one obtains analogously:

$$\frac{\gamma_a}{\gamma_c} > \frac{a}{c}. \tag{5.5b}$$

Agglomeration of particles of a compound fulfilling condition (5.5a) will grow as rods, those fulfilling the condition (5.5b) as platelets.
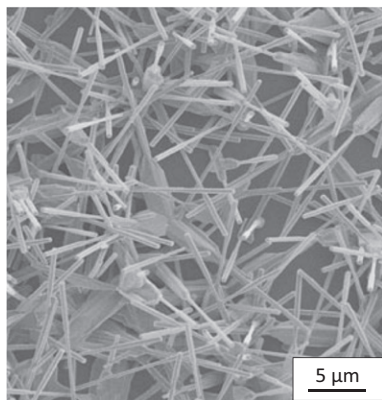
Figure 5.2 Secondary electron micrograph of ZnO nanorods [1]. At one end, most of these nanorods show a bulge, which is typical for a synthesis via a gas-phase route. (Reproduced with permission of Springer.)
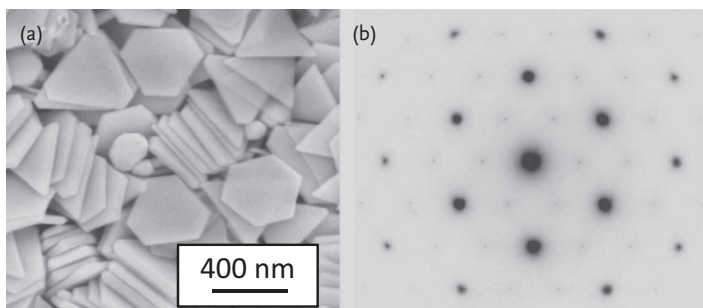

Figure 5.3 Gold platelets. This special hexagonal shape was obtained by the addition of poly vinyl pyrrolidone to the solution used for precipitation [2]. Fig. 1a,b. (a) Electron micrograph of the gold platelets. The size of these hexagonal platelets is around 400 nm; the thickness is in the range from 25 to 60 nm. (b) Electron diffraction pattern of one gold platelet as depicted in Figure 5.3a. The hexagonal symmetry of the diffraction pattern shows that the electron beam was perpendicular to the faces of a platelet; which were (111) planes at the surface. (Reproduced with permission by The American Institute of Physics.)

An example of a rod-like structure is depicted in Figure 5.2. These ZnO rods with a length of the around 15 μnm and a diameter in the range from 120 to 140 nm are clearly separated. Because of their excellent luminescence properties in the UV, ZnO nanoparticles and nanorods are of scientific and economic interest. (According to the definitions of nanomaterials, these rods with linear dimen-

sions beyond 100 nm are, strictly speaking, no longer a nanomaterial. However, as this micrograph is so perfect, it was selected for illustration purposes.) At one end of most of the particles a bulb is visible, this is a structure element indicating a synthesis process via the gas phase.

By attaching surface-active molecules, it is possible to alter the surface energy. This technology makes it possible to synthesize even nanoplates of gold, as is depicted in Figure 5.3 [2]. The size of these platelets is around 400 nm; the thickness varies in the range from 25 to 60 nm. The shape of all platelets is hexagonal, this indicated that the nanoplates have single orientation with (111) plane at the surface. In the cubic system, the (111) plane has hexagonal symmetry. This is perfectly visible in the electron diffraction pattern in Figure 5.3b. In this case, the surface active molecules added during synthesis led to plates, the application of other organic agents may also lead to the formation of nanorods. The nanoplates displayed in Figure 5.3a are nearly atomically flat. Such gold platelets are applied in nanotechnology for manufacturing of small devices.

Altering the habit of nanoparticles is possible not only with metals, but also with ceramic materials. Such an example is displayed in Figure 5.5. Again a material, $CuFe_2O_4$.crystallizing in a cubic structure (spinel structure) was forced by surface-active substances to crystallize as platelets, again with the (111) plane at the top. The magnetic properties of materials depend strongly on the anisotropy of the particles; therefore, to obtain very special properties one adjusts the shape of the particle during synthesis. Adding different amounts of surface-active molecules changes the shape from a plate to a rod [3].

Box 5.3   Miller Indices to Describe Crystallographic Planes and Orientation

The *Miller* indices, a notation system applied to characterize planes and directions in a crystallographic lattice, are, in the simplest case, explained in a cubic lattice. Figure 5.4 shows a cubic cell and six different lattice planes indicated in gray and the associated *Miller* indices.

The *Miller* indices of a lattice plane are the reciprocal values of the intercept of the lattice planes with the axes of the coordinate system. The reciprocal intercept in the x-direction is denoted with h, in the y-direction with k, and in the z-direction with l. The coordinate system is normalized; it achieves the value 1 at the lattice constant a; therefore, *Miller* indices are always integers. *Miller* indices of planes are written in round brackets (hkl). The minus sign is denoted above the index, for example, $(11\bar{2})$. The set of all planes with equivalent symmetry is denoted in curved brackets $\{hkl\}$. Crystallographic directions (lattice vectors) are written in square brackets, they designate a direction in the lattice from the origin to a point. Important: The vector $[hkl]$ is perpendicular to the plane (hkl). The set of all lattice vectors perpendicular to the set of lattice planes $\{hkl\}$ is written in arrow brackets $\langle hkl \rangle$.
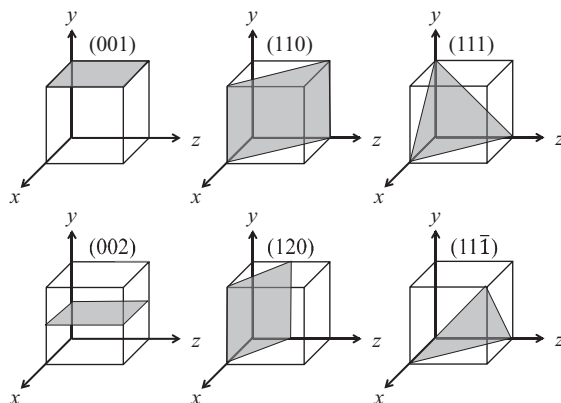
Figure 5.4 Six cubes, within each one a lattice plane is plotted together with the *Miller* indices.
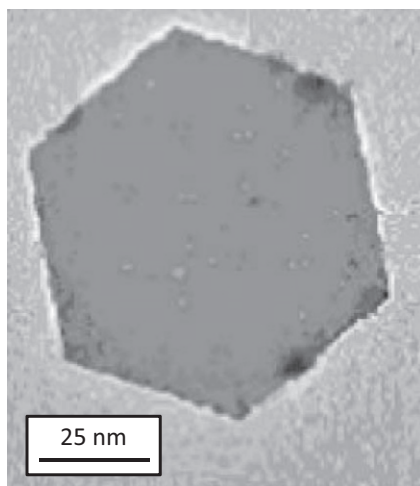

Figure 5.5 Electron micrograph of a $CuFe_2O_4$ platelet with the (111) plane at the top surface. The hexagonal shape deviates from the expected cubic one. It is obtained by adding surfactants to the solution to precipitate the ferrite [3]. (Reproduced with permission by Elsevier.)

Studying the electron micrographs in Figures 5.3a and 5.5, one observes extremely smooth surfaces. This is not surprising, as any imperfection of the faces enlarges the surface and, therefore, the surface energy increases.

One- and two-dimensional features, such as nanotubes and nanoplates, are often related to materials crystallizing in layered structures. Typical examples are BN, WS_2, MoS_2, WSe_2, $MoSe_2$, and, most important, carbon as graphite. In most cases, these are structures, where the layers are held together with *van der Waals*
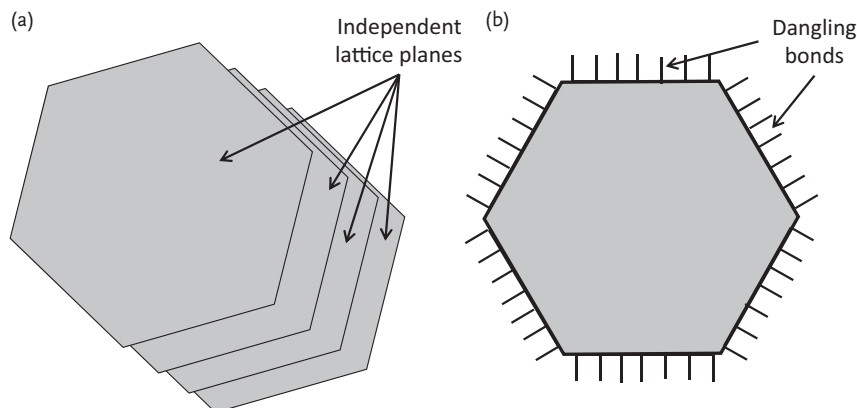
(a)

Independent
lattice planes

(b)

Dangling
bonds

Figure 5.6 Layout of a particle that crystallizes in a layered structure. (a) Setup of such a particle. (b) One layer of a particle as depicted in Figure 5.6a. The dangling bonds at the circumference; indicated by short lines, of the layer are not saturated. These dangling bonds require additional energy. Therefore, there is a strong tendency to saturate these dangling bonds.

forces. An exception are layered silicates, mica, which are based on electrostatic attraction between the layers and alkaline ions positioned in-between the layers. Within the layers, the ions are bonded covalently. The general appearance of particles crystallizing in layered structures is depicted in Figure 5.6. Such a crystal consists of a stack of independent layers. Depending on the bonding in-between the layers, the layers can be delaminated (singularized) by means of chemical or physical methods.

Looking at the boundary of a singularized plate, as depicted in Figure 5.6b, one realizes unsaturated bonds, "dangling bonds". The dangling bonds contribute to the total energy of the crystal. This contribution is negligible in the case of conventional particles; however, significant for nanoparticles. Therefore, there is a tendency to saturate these bonds. Nature has developed a number of methods to reduce the excess energy caused by the dangling bonds. The simplest way is just to add charge-compensating ions at the circumference of a layer. The next possibility, which is of extreme interest in connection to nanotechnology, is rolling up these layers to form a tube, nanotubes or fullerenes. (This important possibility will be discussed in a special section.) In the case of synthesis, such planes, respectively particles, with dangling bonds may touch each other. Also, this process may lead to a saturation of the bonds. A typical example of such a reaction product consisting of three tungsten disulphide, WS_2 particles is shown in Figure 5.7.

A further, very interesting possibility to obtain nanotubes is one-dimensional crystallization; however, the number of compounds showing one-dimensional crystallization is quite small. The most important class of one-dimensional crystallizing compounds are allophanes, a special class of silicates. Allophanes are short-range-ordered aluminosilicates existing in a broad range of compositions,
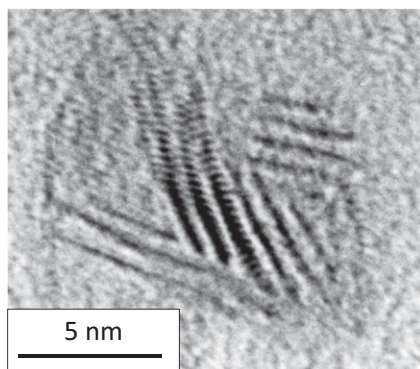
Figure 5.7 Three tungsten disulfide WS₂ nanoparticles, each one consisting only of a few lattice planes, bonded together to saturate dangling bonds at the circumference (Szabo, D.V., and Vollath, D., KIT, Germany, unpublished results (1998).)

following the chemical formula $Al_2O_3 \cdot (SiO_2)_x \cdot (H_2O)_y$, with $1.3 < x < 2$ and $2.5 < y < 3$. Generally, allophanes crystallize in hollow spherules with diameters in the range between 3 and 5 nm. Under special conditions of synthesis and depending on the composition, one obtains tubes with a diameter in the range from 2 to 5 nm. The diameter of the tubes can be adjusted by the relative aluminum content. Additionally, some of the aluminum may be exchanged by iron ions with the same valency. This substitution influences the diameter and color of the tubes.

Comparing the three possibilities of producing one- and two-dimensional nanostructures, those related to layered compounds are, with respect to technical applications, the most important ones.

Box 5.4 Imogolite, a One-Dimensional Silicate

An important compound in the group of one-dimensional silicates is imogolite, $(Al_2O_3) \cdot (SiO_2)_x \cdot 2.5(H_2O)$. Imogolite tubes with this composition have an inside diameter around 1 nm and outside diameters of ca. 2 nm; both can be adjusted by the silicon / aluminum ratio. Figure 5.8 displays the atomic arrangement in a cross section of such an imogolite tube.

This structure of imogolite is characterized by aluminum, silicon, oxygen, and $(OH)^-$ ions arranged in rings. The $(OH)^-$ ions at the surface allow addition of ("functionalize") organic molecules.

As shown in Figure 5.9, imogolite can be synthesized in long fibers.

Figure 5.9 displays wet-chemically synthesized imogolite fiber, which are in a diameter range from 5 to 30 nm [5]. The length of the tubes is in the microm-
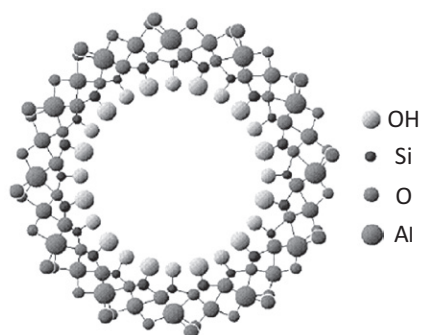
Figure 5.8 Atomic arrangement in an imogolite fiber with inside diameters of 1 nm and outside diameters of 2 nm. The diameter of the tubes can be adjusted by changing the silicon/aluminum ratio [4]. (Reproduced with permission by The Korean Chemical Society.)
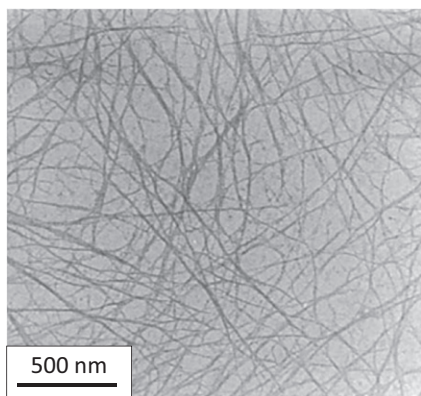

500 nm

Figure 5.9 Bundle of imogolite fibers. (Koenderink *et al.* [5]) The fibers with diameters in the range from 5 to 30 nm are arranged in a bundle. The length of these fibers may be up to a few micrometers. (Reproduced with permission by Elsevier.)

eter range. The surface area of imogolite is experimentally determined in the range of $1000 \pm 100 \, \text{m}^2 \text{g}^{-1}$. The *Mohs* hardness in the range from 2 to 3 is quite low. Even when the length of the fibers suggests the application as a filler in a composite with polymer matrix, the relatively low strength of these fibers keeps the advantage of such composites limited.

5.2
Vibrations of Nanorods and Nanotubes – Scaling Law for Vibrations

It is well known and part of everyone's daily experience that the frequency of vibrations increases with increasing length of a rod. This context is experienced for example, in the case of music instruments. Now, one may ask, what are the consequences if the dimensions go into the range of a few nanometers. This is the question about vibration frequencies of nanorods and nanotubes. It is well known that the resonance frequency of a rod, fixed on one end is, under the assumption of constant aspect ratio (the ratio length over diameter) of a cylindrical rod is indirectly proportional to the length of the rod.

Box 5.5   Resonance Frequency of a Rod Fixed on One End

The frequency of the basic bending vibration mode ν_1 of a cylindrical rod, fixed at one end, is given by (Todt, M., (2012) Vienna University of Technology, Austria, private communication.)

$$\nu_1 = \frac{\pi}{32} \frac{d}{l^2} \left(\frac{E}{\rho} \right)^{\frac{1}{2}} = \frac{\pi}{32} \alpha \frac{1}{l} \left(\frac{E}{\rho} \right)^{\frac{1}{2}}. \tag{5.6}$$

The quantity d stands for the diameter, l for the length, E for the Young's modulus, and ρ for the density of the material. Vibrations of such a rod are not harmonic, which means that the frequencies of the higher modes are not integer multiples of the basic frequency ν_1.

Considering vibrations of nanorods and nanotubes, one should take note of the influence of the dimensions on the *Young*'s modulus, which controls the frequency, too. In most cases, this influence is not known; therefore, one uses the bulk data. An exception are carbon nanotubes, a material with an extremely high *Young*'s modulus. Table 5.1 shows the influence of different sizes, macroscopic and on the nanoscale on the vibration frequency of a cylindrical rod with different dimensions assuming a constant aspect ratio.

Table 5.1   Estimation of the basic frequencies for bending vibrations of a cylindrical rod with an aspect ration of 10 of different size consisting of iron or carbon nanotube.

Length of the rod (m)	Frequency for iron (Hz)	Frequency for carbon nanotubes (Hz)
0.1	520	–
10^{-8}	5.2×10^9	2.2×10^{10}

For these calculations, iron ($E = 2.11\,\text{GPa}$, $\rho = 7.8 \times 10^3\,\text{kg\,m}^{-3}$) as material and an aspect ratio of ten are assumed. For a rough estimation, Eq. (5.6), given in Box 5.5, was also used to estimate the basic vibration mode of a carbon nanotube ($E \approx 1000\,\text{GPa}$, $\rho \approx 2 \times 10^3\,\text{kg\,m}^{-3}$).

Analyzing Table 5.1, one realizes that a 10-nm nanorod vibrates in a frequency range that is far from those that are in technical use. Vibrations of nanorods have been used to determine the mass of single molecules, sitting on the surface, by measuring the frequency shift. Such a device is able to act as a kind of balance for single molecules or atoms [6, 7].

5.3
Nanostructures Related to Compounds with Layered Structures

5.3.1
Carbon- and Boron-Nitride-Based Nanoparticles

Certainly, the most important group of objects are based on carbon. Except for the binding in the lattice influencing the physical properties, which does not have any influence on the geometry of the particles, nearly everything discussed in connection with carbon is valid for boron nitride, too. To understand carbon nanotubes, fullerenes, and graphene, it is necessary to look first at the binding and the geometry of the lattice. Figure 5.10 displays the structure of graphite, which is the basis to understand the following discussions.

As displayed in Figure 5.10, graphite crystallizes in a hexagonal structure. In this structure, each carbon atom is bond covalently to its three neighbors. Carbon has four valence electrons; however, in a graphene plane it has only three
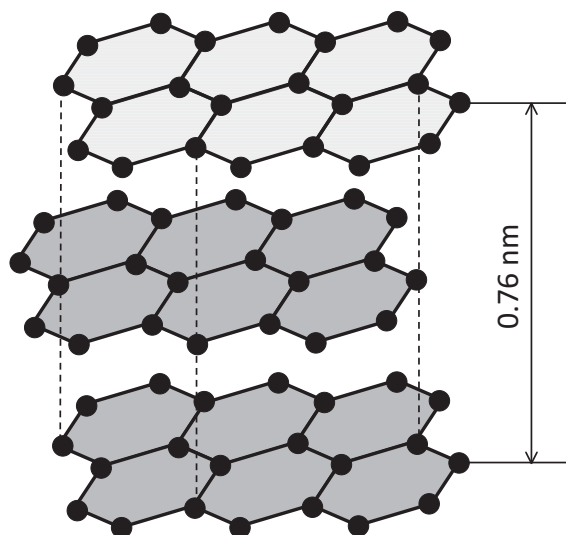

Figure 5.10 Structure of graphite. (The structure of boron nitride is identical.) Each one of these layers, called graphene, is independent. There are no electrostatic forces in-between the layers.

neighbors. Therefore, one double bond is necessary. In other words: three of the four valences of carbon are saturated. The fourth electron remains unbound; it is delocalized, which means it can move freely across the graphene sheets. As these fourth electrons are mobile, graphite shows electric conductivity within the layers. Perpendicular to the layers, graphite is an electrical insulator. The fourth unbound electron is also usable for functionalization. In this context, an interesting example is graphane, where each of the carbon atoms is associated with a hydrogen atom. This is different for boron nitride. As in boron nitride all valences are saturated, there are no free electrons. Boron nitride is an insulator. (As will be shown in Chapter 10, it is, strictly speaking, a wide-gap semiconductor.) Figure 5.11 displays one layer of the structure of these compounds together with the bindings.

Within the layers depicted in Figures 5.11a,b, there are covalent bonds; in-between the layers are weak *van der Waals* bonds. This allows cleaving layers of monocrystalline material by chemical or mechanical methods. In organic chemistry these hexagonal structures are well known in aromatic compounds, deriva-
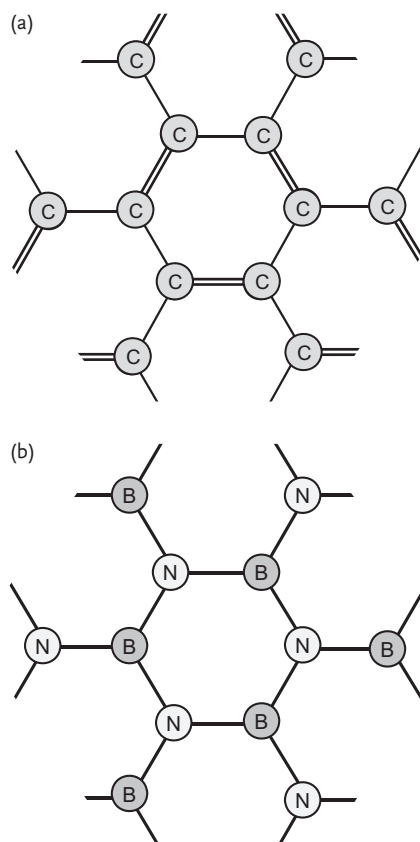

Figure 5.11 Structure and bindings of graphene (a) and boron nitride (b). It is important to realize that, in contrast to graphene, boron nitride has no double bonds.
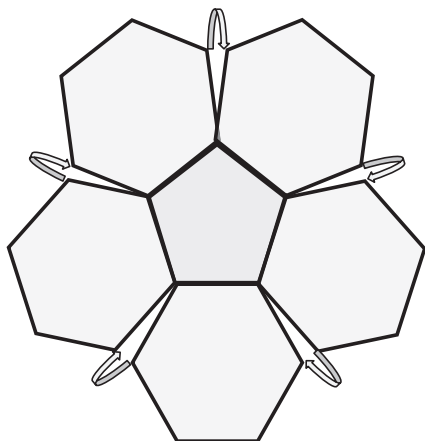
Figure 5.12 Effect of a pentagon in a hexagonal structure. Closing of the structure is possible only by bulging. This is the elementary requirement for the formation of three-dimensional structures, such as fullerenes.

tives of benzene. Therefore, graphene is often termed as infinitely extended two-dimensional aromatic compound.

Certainly, like in any other crystal, graphene is also prone to lattice defects. Among other possibilities, it is possible that a pentagon or a heptagon replaces a hexagon. In particular, the formation of pentagons is most important, as this defect enables the formation of three-dimensional objects, the fullerenes. Figure 5.12 demonstrates the bulging of the structure around a pentagon. This phenomenon makes the formation of three-dimensional structures, such as fullerenes, possible. If graphene can be called a two-dimensional aromatic compound, fullerenes are three-dimensional aromatics.

Combining a larger number of structures, as shown in Figure 5.12, leads to spherical shapes, polyhedra, consisting of pentagons and hexagons. *Euler* was the first to predict the existence of such polyhedra.

The most common fullerene, and the first one identified by Kroto and coworkers [8], consists of 60 carbon atoms, C_{60}. This molecule is set up of twelve pentagons and twenty hexagons. The next larger fullerene consists of 70 carbon atoms, C_{70}. Figure 5.13 displays these two fullerenes.

Besides C_{60} and C_{70}, many other fullerenes exist. Furthermore, fullerenes can form nested particles, "fullerene in an fullerene", like a "Russian Doll". These nested fullerenes are called onion crystals. Besides C_{60}, the most important further fullerenes are C_{70}, C_{76}, C_{78} und C_{84}. As C_{60} looks like a soccer ball, C_{60} is often called a "soccer ball molecule". Fullerene molecules are quite stable; however, like in graphene, each carbon atom has only three neighbors. Therefore, there are free valences, which may be used for functionalization, for example, it is possible to attach metal atoms or other molecules at the surface. In view of applications, this is of great importance.
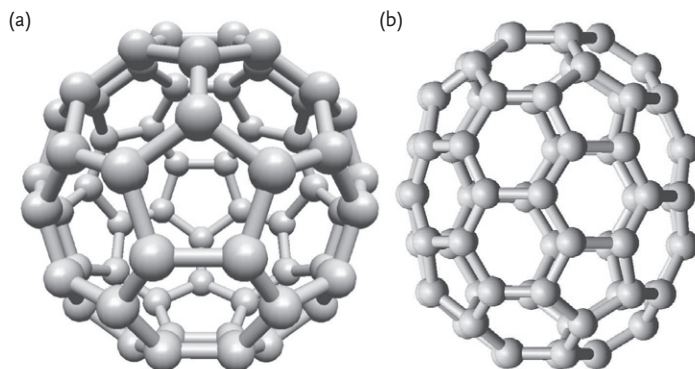
(a)

(b)

Figure 5.13 The fullerenes C_{60} (a) and C_{70} (b). The hexagons and pentagons the constitutive elements of fullerenes are readily visible (Reproduced with permission, http://www.jcrystal.com/steffenweber/pb/swpb2. pdf). The diameter of a C_{60} molecule is 0.7 nm. Certainly, C_{60} is larger than C_{70}, only for reasons of displaying, they are equal in size.

Box 5.6   Fullerenes

Polyhedra forming fullerenes are a subgroup of *Archimedea*n polyhedra, which consist of regular polygons, with identical vertices and identical arrangements of polygons around each polygon with a constant number of edges at each vertice. According to *Euler*, the number of vertices N, (in this case, identical with the number of carbon atoms) of these polyhedrons consisting of hexagons and pentagons follow the formula: $N = 2i$ with $i \geq 12$ and $i \in \mathbb{N}$ Therefore, the smallest fullerene should consist of 24 carbon atoms. All experimentally verified fullerenes consist of twelve pentagons and different numbers of hexagons. The stability of a fullerene particle is maximal, in the case that the pentagons are surrounded by hexagons only. Stable fullerenes consisting of less that 60 carbon atoms were never found. The fullerene C_{60} is thus of special interest, as it is the most symmetric molecule known. One can perform 120 symmetry operations, (rotations around an axis, reflections in a plane) mapping the molecule onto itself.

The smallest, however, unstable fullerene, experimentally found, is C_{20}. It is set up of pentagons only and, therefore, it is not a polyhedron following the *Euler* formula.

Fullerenes exist not only as single-wall objects but as multiwall objects, "onion crystals", too. However, the number of layers is limited. There is experimental evidence that multiwall fullerenes collapse. If the number of shells is too large the pressure in the center of such an onion particle becomes so high that the graphite-like structure of the multiwall fullerene transforms into the diamond structure [9].

From the explanations above, it is evident that forming a tube can reduce the energy stored in a graphene layer, too. From simple geometrical considerations, (think of the different possibilities of forming a tube from a sheet of paper) one realizes different possibilities of rolling up a sheet of graphene. Interestingly, the properties, especially electrical properties, depend strongly on the angle of coiling. Similar to the case of fullerenes, carbon nanotubes can exist in concentric multilayers, multiwall nanotubes, too. Figure 5.14 displays these two possibilities.

Most of the production processes deliver primarily multiwall nanotubes; generally, single-wall nanotubes are the exception. As for the discussion of nanotubes, there remain a series of dangling bonds at each end. Therefore, they have to be closed; closing is performed by an endcap, which is similar to a moiety of a fullerene. Figure 5.15 displays an electron micrograph of a multiwall nanotube and its endcaps. The contrast at the caps is, compared to the body of the nanotubes,
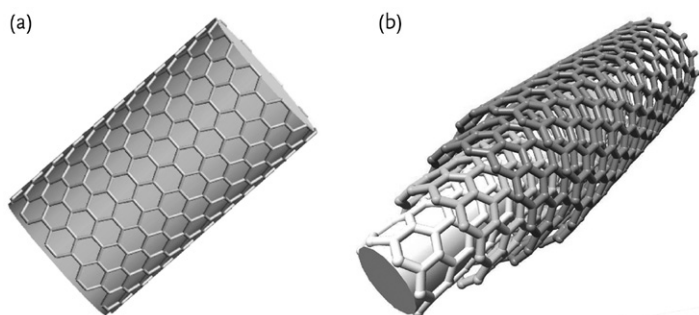
(a) (b)

Figure 5.14 Models of carbon nanotubes. A single-wall nanotube of the armchair type with the chirality vector (10,10) (a). The diameter of this tube is 1.35 nm (Reproduced with permission, http://www.jcrystal.com/ steffenweber/pb/swpb1.pdf). The multiwalled carbon nanotube of the zig-zag type depicted in (b) has the chirality vectors (see Box 5.6) [7,0], [10,0], [13,0] and [16,0]. The outer diameter is 1.25 nm.
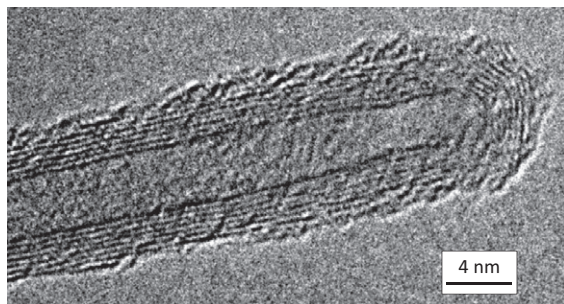

4 nm

Figure 5.15 Multiwall carbon nanotube with endcaps (Ritschel, M., and Leonhardt, A. (2007), IFE Dresden, Germany, unpublished results. http://www.ifw-dresden.de/institutes/iff/ research/Carbon/CNT/ferromagnetic-filled-cnts-by-cvd).

significantly reduced; therefore, electron microscopy of these endcaps is very difficult.

There are many applications exploiting the electrical conductivity and the high mechanical strength. The unique combination of small diameter and mechanical stiffness make carbon nanotubes ideal tips for scanning force or scanning tunnel microscopes. Furthermore, carbon nanotubes are applied in polymer-bond composites of high strength.

Box 5.7   Geometry of Graphene and Carbon Nanotubes

Graphene layers are described using a coordinate system with the unit vectors $\vec{e}_1$ and $\vec{e}_{2_1}$. In Figure 5.16, a section of a graphene layer is displayed, for some points the coordinates in this system are given. Nanotubes are described with a chirality vector

$$\vec{c} = n\vec{e}_1 + m\vec{e}_2, \quad n, m \in \mathbb{N} \tag{5.7}$$

that describes the length of the coordinates in the directions $\vec{e}_1$ and $\vec{e}_{2_1}$. Any vector in this system can serve as a chirality vector. To describe carbon nanotubes the convention $0 \leq m \leq n$ was adopted. The tube axis is perpendicular to the chirality vector. There are two chirality vectors, the "zig-zag line" $\vec{c} = (n,0)$ and the armchair line $\vec{c} = (n,n)$ describing special arrangements of the carbon atoms.
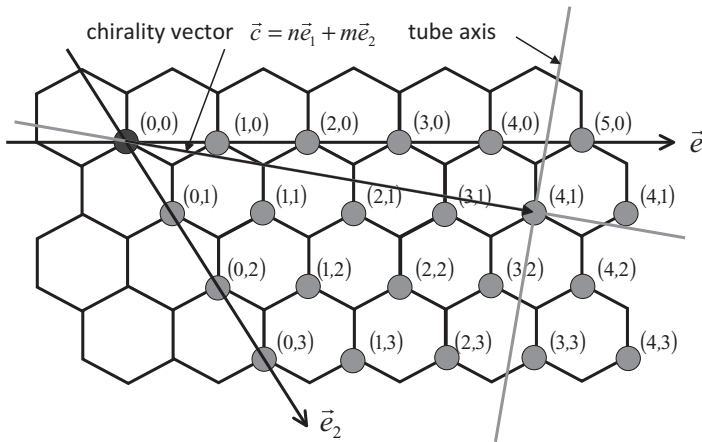

Figure 5.16   Description of the atom positions in a graphene sheet using a coordinate system with the unit vectors $\vec{e}_1$ and $\vec{e}_2$. In this graph, the directions of the unit vectors $\vec{e}_1$ and $\vec{e}_2$ are indicated; additionally, for some of the vertices the values of the coordinates are given.

Properties of Carbon Nanotubes Depending on Chirality

Chirality determines the properties of carbon nanotubes. Knowing the chirality vector, it is possible to calculate the diameter d of a nanotube, which is given by,

$$d = \frac{\sqrt{3}}{\pi} a_{C-C} \left(n^2 + m^2 + nm \right)^{0.5} = 0.0783 \left(n^2 + m^2 + nm \right)^{0.5} \, [\text{nm}]. \qquad (5.8)$$

The quantity $a_{C-C} = 0.14 \, \text{nm}$ is the distance between two neighboring carbon atoms. Experimentally, single-wall carbon nanotubes are found with diameters in the range from 1.2 to 1.4 nm. Multiwall nanotubes with significantly larger diameter were found. The chiral angle, the angle between the $\vec{e}_1$ axis and the chirality vector $\vec{c}$ is given by

$$\delta = \arctan \left[\sqrt{3} \, \frac{m}{2n + m} \right]. \qquad (5.9)$$

The chiral angle for the armchair line is 30°, the one for the zig-zag line is 0°. Carbon nanotubes show metallic electrical conductivity, iff the chirality vector fulfills the condition

$$\frac{2n + m}{3} = q, q \in \mathbb{N}. \qquad (5.10)$$

In the graphene coordinate system displayed in Figure 5.17 these vertices are indicated with darker dots.
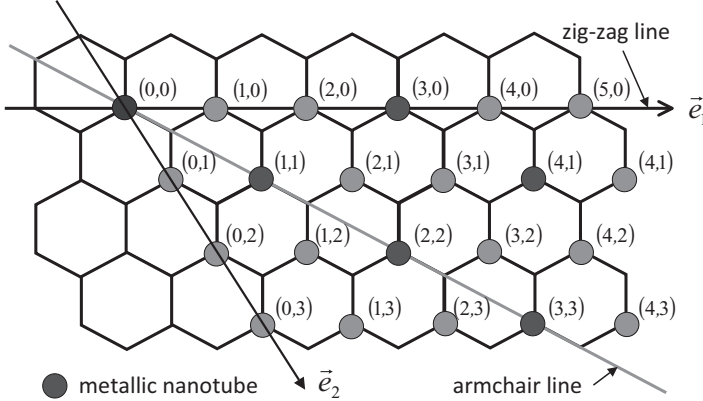

Figure 5.17 Coordinate system of graphene. The vertices connected to metallic electrical conductivity are indicated with dark dots. Additionally, the chirality vectors of the zig-zag line and the armchair line are indicated.
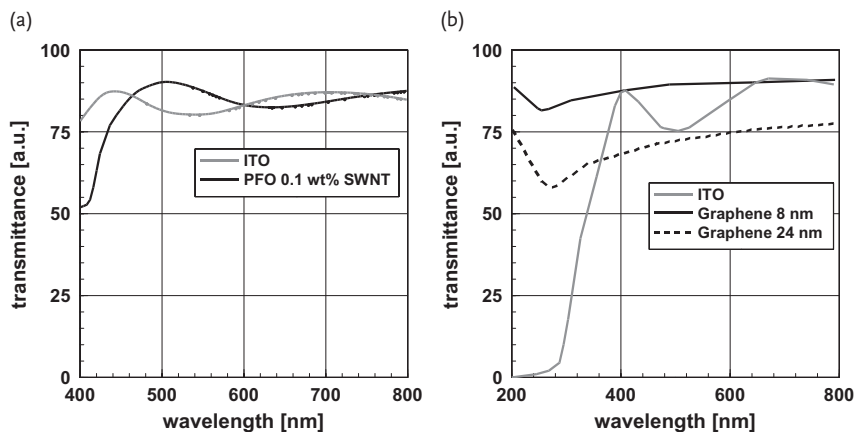
(a)

(b)

Figure 5.18 Optical transmittance of a polymer–carbon nanotube composite (a) and graphene with different thickness [10] (b). Both compared to ITO, the standard material for optically transparent electrical conductors. [11].

Carbon nanotubes and graphene are widely discussed, because there are many potential high value added applications. These applications are either connected to the high strength of these materials or to their electrical and optical properties. In the following, a typical application exploiting the electrical properties is described. For electronic displays, needed everywhere in the modern world, from computer displays to TV sets or smart phones, one needs optically transparent electrical conductors. Nowadays, one applies ITO, a solid solution of two oxides, consisting of roughly 90 wt% In_2O_3 and 10 wt% SnO_2. ITO has a few severe disadvantages, it is brittle, so it is not well suited for flexible substrates and, it is not printable, ITO conductors are prepared by high-vacuum sputtering. In contrast, electrically conductive nanocomposites consisting of a polymer and carbon nanotubes or graphene should not exhibit these disadvantages. Therefore, one has to look at the properties of these new materials. Figure 5.18 displays the optical transmittance of an electrical conductive polymer–carbon nanotube composite and graphene with different thickness, both compared to ITO.

In Figure 5.18a, the optical transmittance of a nanocomposite consisting of 0.1 wt.% carbon nanotubes (single-walled) and PFO [poly(2,7 − 9,9 − (di(oxy − 2,5,8 − trioxadecane))fluorene)] as polymer. The optical transmission of PFO with 0.1 wt.% single-wall nanotubes and that of ITO, show, except for the wavelength range below ca. 450 nm, no significant differences. The reduction in optical transmission in the blue regime of the optical spectrum is caused by the polymer. The optical transmission of graphene layers is, as depicted in Figure 5.18b, excellent, too. At least in the range of the visible part of the optical spectrum, graphene shows very good transmittance and no wavelength-dependent local depression, as is found in the case of ITO around 500 nm. Analyzing the two graphs in Figure 5.18, one realizes that, at least from the standpoint of the optical properties, there are no disadvantages of the new materials as compared to ITO.

Box 5.8   Synthesis of Singularized Graphene Layers

In a graphene sheet, each carbon atom has two single and one double bond. The latter is available for functionalization. However, it is also useable to produce graphene sheets from graphite. *Geim*, the first researcher working with graphene in depth, pointed out that any line with a black pencil produces a large quantity of graphene sheets [12]. Certainly, this method is not usable in a laboratory to obtain well-defined specimens. Generally, graphene is produced by a sequence of oxidation and reduction processes. (Oxydation is here meant in its most general sense: Giving away electrons, reciprocally for reduction.) In the simplest case, one immerses graphite in a solution of formic acid. These small molecules, attach at the weak points, the double bonds, and oxidize the carbon layers, forming graphene oxide,. This expands the distance between the layers in a first step.

This expanded lattice of the now modified graphite will be defoliated in a second step: The graphene layers, carrying formic acid molecules are treated with an alkaline solution for defoliation and followed by a reduction step, e.g., using hydrazine. As a result, one obtains graphene layers suspended in a liquid. Certainly, thermal reduction is also possible. Oxidation can also be performed using sulfuric or nitric acid.

A review on graphene synthesis is given by Choi *et al.* [13].

5.3.2
Nanotubes, Nanorods, and Nanoplates from Materials other than Carbon

Sulfides, selenides and some oxides of molybdenum and tungsten crystallize in layered structures. In contrast to graphite and boron nitride, the compounds are set up of bundles of layeres and not by layers with the thickness of one atom. Typically, these compounds have a sequence of layers as depicted in Figure 5.19.

It is important to realize that, within the triple packages, there is very stable covalent bonding. In-between these packages, the binding is very weak, it is of the
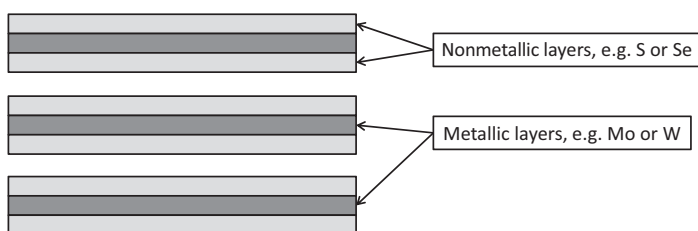

Figure 5.19   Simplified structural model of a layered structure. The bonding between the layers containing the metallic atoms and those with the nonmetals is of the covalent type. In-between the packages there is a *van der Waals* bonding.
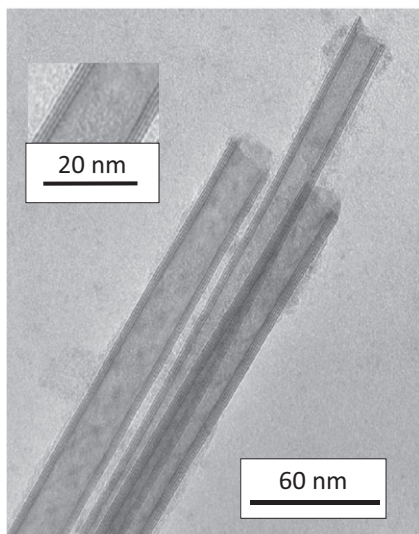
Figure 5.20 Three multiwall WS$_2$ nanotubes with diameters in the range from 15–20 nm (Tenne, R. private communication 2012, http://www.weizmann.ac.il/ICS/booklet/20/pdf/reshef_tenne.pdf). The insert in larger magnification displays one of the tubes with four walls.

van der Waals type. As in graphite, the packages can be shifted against each other. This loose binding in-between the packages is why these compounds are usable as solid-state lubricants.

It is now a generally accepted knowledge that all compounds crystallizing in layered structures form nanotubes and fullerene-like structures. Tenne and co-workers [14] synthesized the first noncarbon nanotubes consisting of MoS$_2$ and WS$_2$. Following these findings, such structures were observed with the selenides of molybdenum and tungsten [15]. Figure 5.20 displays four nanotubes of tungsten sulfide, WS$_2$. It is readily visible that these are multiwall tubes. The insert with higher magnification tells that these tubes have four walls. It is important to point out that that the lines showing the walls represent the tungsten atoms. Because of the large difference in the atomic number, the sulfur atoms are invisible. (The contrast in the electron microscope is proportional to the square of the atomic number; therefore, these micrographs show better contrast as compared to that of carbon nanotubes.).

As a second example, confirming the rule that any compound crystallizing in layered structure can form tubes and balls, is shown in Figure 5.21. This figure depicts a ZrSe$_2$ particle crystallized as an "onion" [16]. The multiwall fullerene depicted in Figure 5.21 is very symmetric, it is close to a ball. However, even when it is difficult to understand in terms of surface energy and stresses, spherical geometry is not necessary for such a multiwall fullerene. Such an example, a MoS$_2$ multiwall fullerene, is shown in Figure 5.22.
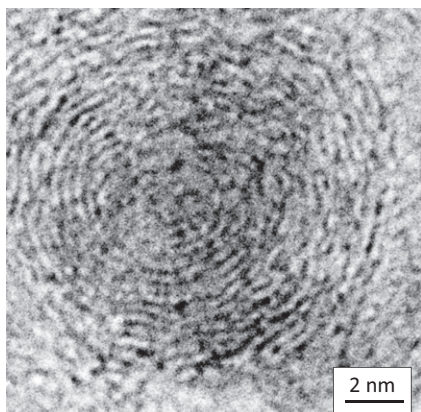
Figure 5.21 ZrSe$_2$ onion crystal, "a noncarbon multiwall fullerene." [16]. (Reproduced with permission by Elsevier.)
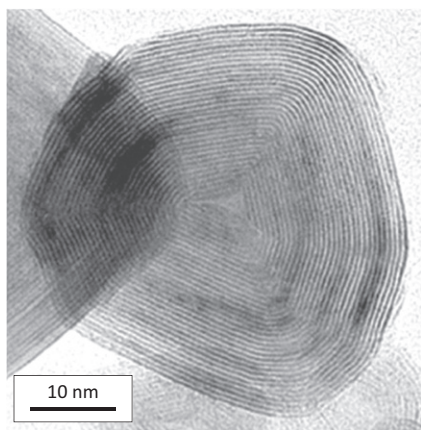

Figure 5.22 MoS$_2$ multiwall fullerene particle. The nonspherical geometry is, with respect to surface energy and stresses, difficult to understand. (Tenne, R., (2012) Weizmann Institute, Israel; private communication.)

The compounds MoS$_2$ and WS$_2$ are well known as solid-state lubricants. Conventionally, especially MoS$_2$ powder is widely used as solid lubricant, because the different layers bond by *van der Waals* forces glide easily on each other. Furthermore, these platelets act as distance holders between the two metal surfaces and eliminate direct contact, this minimizes metal wear. This is of special importance in the case of extreme loads, where oils and greases, used as lubricants,

are squeezed out. During application, the dangling bonds of the platelets react with the metal surfaces and, therefore, these particles lose their properties as lubricants.

The fullerene-like structures of MoS_2 and WS_2 have a high potential as solid-state lubricants; however, they act differently: As they have no open bonds at the circumference, the particles cannot react with the surface of the metal. This extends the lifetime of these lubricants. Also, the mechanism of reducing friction is different: The fullerene-like particles act like balls in a ball bearing [17]. Figure 5.23 compares the tribological behavior of the base grease with that of this grease using additions of MoS_2 platelets and fullerene-like particles. It is clearly visible that the addition of MoS_2 reduces friction. Furthermore, it is obvious that the addition of fullerene-like particles prevents the increase of the friction coefficient up to significantly higher loads as compared to the platelet addition. These experimental results vindicate the statement that fullerene-like MoS_2 and WS_2 particles improve the friction behavior significantly as compared to the platelet shaped material. Figure 5.24 displays in a large scale industrially produced MoS_2 fullerene-like particles.

Comparable improvements as in the case of sliding contact bearings are observed using WS_2 particles as an additive to metal-working fluids applied for high-precision machining, such as drilling or lathing. The advantage in such an application is twofold: Due to reduced friction, the applied forces and the temperature increase are reduced. In the case of high-precision parts with narrow tolerances, controlled temperature is essential to obtain the intended dimensions. Due to the reduced temperature, the amount of metal-working fluid needed is reduced and the lifetime of the cutting tools is extended.
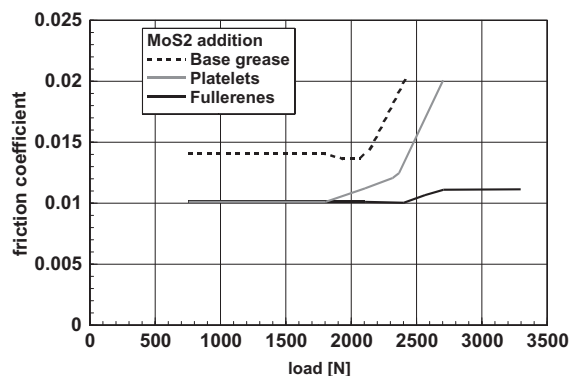

Figure 5.23 Influence of MoS_2 addition to the friction coefficient of a grease. It is important to realize that the addition of MoS_2 reduces friction. This phenomenon is more pronounced in the case of the fullerene-like particles (Tenne, R., Weizmann Institute, Israel, private communication 2012.).
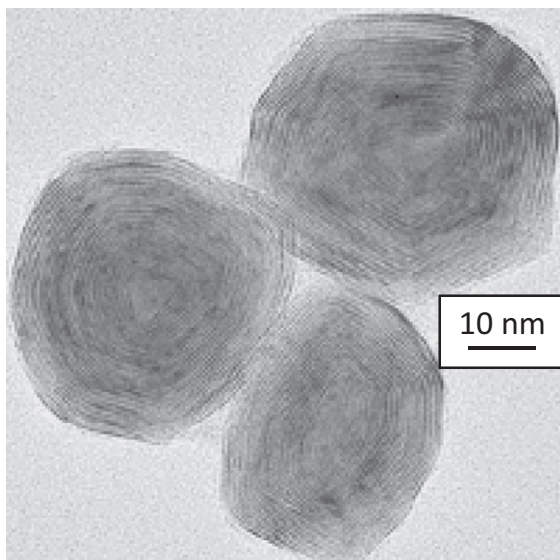
Figure 5.24 Industrially produced in large scale fullerene-like MoS$_2$ particles intended as friction-minimizing additive to oil or grease (Tenne, R., Weizmann Institute, Israel, private communication 2012.).

5.3.3
Polymer Composites Filled with Defoliated Phyllosilicates

Phyllosilicates are natural silicates with layered structure. Depending on the composition, these silicates are the minerals montmorillonite, hectorite, or saponite. In contrast to the layered structures discussed previously, electrostatic and not *van der Waals* forces hold the different layers of these minerals together. These minerals consist of negatively charged silicate layers, consisting of silicate tetrahedra and aluminum or magnesium and some lithium in various quantities. Within these layers, the bonds are covalent. These layers are approximately 1 nm thick. The distance between two layers is 0.2 nm. In-between these negatively charged layers are positively charged alkaline ions, in most cases sodium ions. Therefore, by electrostatic forces, these ions hold the layered system together. The lateral size of these platelets is in the range of a few hundred nanometers. To produce high-strength composites with a polymer matrix, these silicates need to be defoliated, which means that the individual layers are separated.

The process of defoliating is explained in Figure 5.25. Starting material are layered silicates (phyllosilicate).

To defoliate stacks of layered silicates, the cations in-between the layers are, in a first step, substituted by positively charged organic molecules. This leads to a swelling of the particle; the distance between the silicate layers increases to
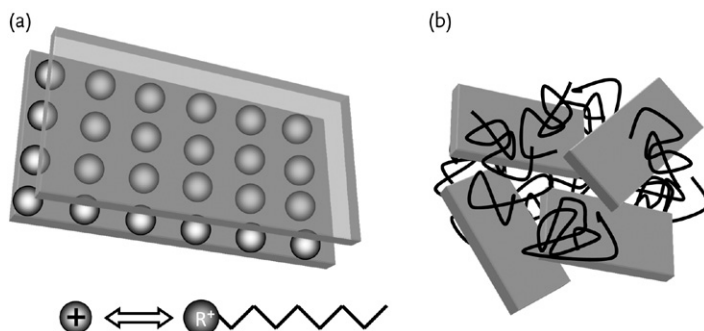
(a)

(b)

Figure 5.25 Defoliating of layered silicates to produce nanocomposites. (a) A layered silicate consists of negatively charged silicate layers bonded together with positives charged alkaline ions. The upper layer is drawn transparent. To start defoliating, the alkaline ions are exchanged with organic molecules carrying equal charge. (b) After exchanging the alkaline ions by equally charged organic molecules, the crystal defoliates. The individualized layers are now embedded in the polymer matrix.

values in the range between 2 and 3 nm. In the further progress of the process, defoliating of the crystal, as depicted in Figure 5.25b, occurs. Besides natural layered silicates, synthetic pure synthetic layered silicates, such as hydrotalcite, are in use. In contrast to the natural one, some synthetic phyllosilicates may also carry positive charges on the platelets and the negative ones on the intercalated ions.

Figures 5.26a,b show electron micrographs of such composites in different states of defoliation. These electron micrographs prove that the process explained above is a good description of the actual mechanism.

Figure 5.26a displays an electron micrograph of a composite material consisting of polypropylene as matrix material with additions of 4 wt% montmorillonite [18]. This micrograph shows, besides some already defoliated sheets, a montmorillonite particle that has just started to defoliate, on both ends the particle has opened. Furthermore, some of the defoliated plates consist of two or three sheets. The length of the sheets may be around 150 nm. Figure 5.26b shows primarily defoliated sheets. This specimen consisted of 5.6 wt% montmorillonite in a polystyrene matrix [19]. Besides the nearly perfect defoliation, the individual sheets seem to be more or less oriented in parallel. In the specimen depicted in Figure 5.26a, the size if the individual sheets is in the range of 150 nm, whereas it is nearly impossible to estimate their size in Figure 5.26b, perhaps the size is in the range of a few hundred nanometers.

5.3.4
Synthesis of Nanotubes, Nanorods, and Fullerenes

In small quantities, carbon nanotubes and fullerenes are always found in soot. Larger quantities of these materials are obtained by electric arcs between carbon
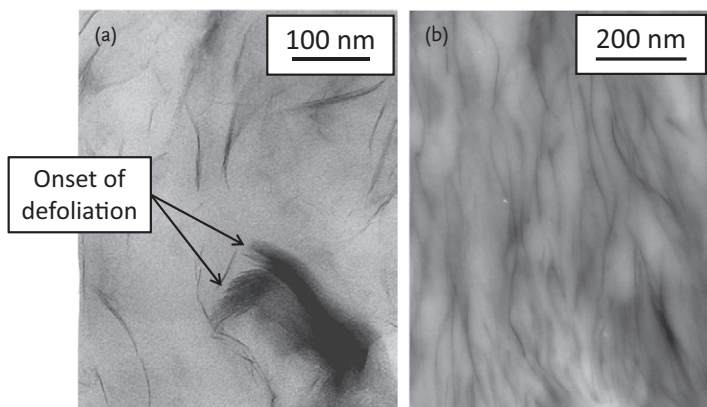
Figure 5.26 Two typical composites consisting of a layered silicate in a polymer matrix. (a) Composite with 4 wt% montmorillonite as ceramic phase in a polypropylene matrix [18]. (Reproduced with permission of The American Chemical Society.) The orientation of the defoliated layers is random. There is one particle where the onset of the defoliation process is visible. (b) Nearly completely defoliated composite consisting of 5.6 wt% montmorillonite in a polystyrene matrix. The defoliated layers are aligned almost parallel [19]. (Reproduced with permission by Elsevier.)
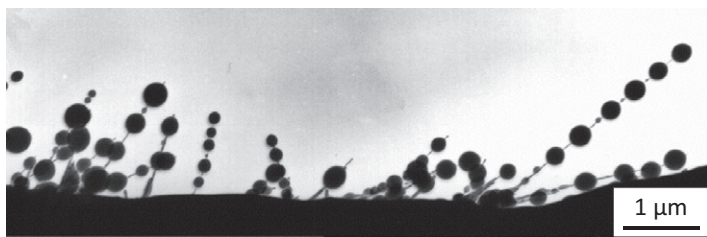
Figure 5.27 Carbon nanotubes produced in an electric arc, which arc melted the graphite. In this micrograph, at the surface of the nanotubes, there are residues of melted carbon as droplets. The outside of these droplets is glassy, as they had cooled faster than the interior. In the interior of the carbon droplets there was sufficient time for crystallization as nanotubes, which in the sequence of crystallization left the droplets (With permission by de Heer, W. http://www.gatech.edu/news-room/release.php?id=516).

electrodes. Furthermore, carbon nanotubes and fullerenes are obtained by laser-ablation processes. In all cases, the yield can be improved significantly by adding catalysts. As catalyst, one quite often applies iron, nickel, and alloys of these metals, perhaps with some yttrium added. Depending on the composition of the catalyst, the composition of the product may be shifted in one or the other direction.

Nanotube formation at high temperature, above 5000 K, seems to go via a liquid phase. This may be seen in the electron micrograph depicted in Figure 5.27. In this electron micrograph, one realizes frozen droplets on carbon nanotubes. As
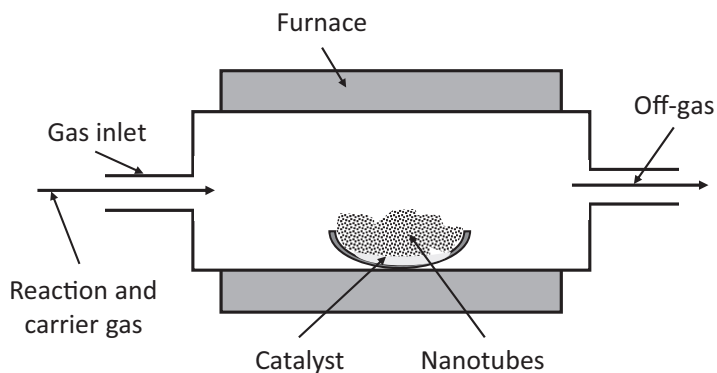
Figure 5.28 Arrangement with a tubular furnace to synthesize carbon nanotubes. The applied temperature is around 1300 K. As catalyst iron, nickel, and alloys of these metals, perhaps with some yttrium added, are in use.

the mechanism for the formation of these aggregates, one assumes that the carbon droplets are freezing very fast, forming a glassy surface layer. Within the droplets, the liquid carbon gets supercooled and starts to crystallize. The crystallizing nanotubes, growing from the liquid layer at the cathode, drag along small droplets of supercooled carbon. As a result, which supports this mechanism, one observes, besides the glassy droplets, a thin amorphous layer at the surface of the carbon nanotube.

The high-temperature processes to obtain carbon nanotubes and fullerenes always produce large amounts of soot. The soot is removed by careful oxidation in the temperature range between 1000 and 1100 K, as residue, one obtains carbon nanotubes, because soot is more susceptible to oxidation as compared to the intended product.

Besides the high-temperature process using an electric arc, carbon nanotubes are also obtained at more moderate temperatures for example, in a tubular furnace at temperatures around 1300 K. Certainly, these methods also require appropriate catalysts. Figure 5.28 displays such an arrangement. As mentioned above, as catalyst, iron, nickel, and alloys of these metals, perhaps with some yttrium added, are in use.

Similar arrangements are applied to produce nanotubes and fullerene-like particles of the sulfides of molybdenum and tungsten. For these processes, the following precursors and catalysts are applied:

- Carbon nanotubes: As reaction gas, a mixture of methane, CH_4 and hydrogen, H_2, generally diluted with argon, are in use. As catalyst: iron, nickel, and alloys of these metals, for example, with molybdenum or yttrium.

- MoS_2 or WS_2 nanotubes and fullerene-like structures: The carbonyls or the oxides as precursors for the metals and H_2S, as educt providing sulfur, diluted with argon, nitrogen, and hydrogen.
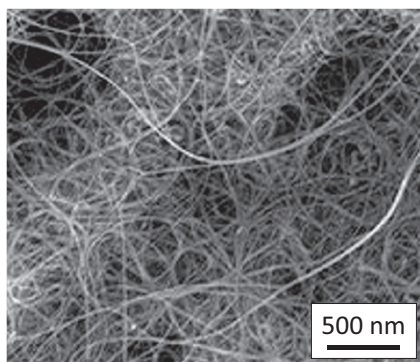
500 nm

Figure 5.29 Carbon nanotubes synthesized in a tubular furnace as shown in Figure 5.26 at a temperature around 1300 K. CH$_4$ was used as carbon precursor and iron as catalyst. (Ritschel, M., Leonhardt, A., (2007) IFE Dresden, Germany; private communication.)

- GaN nanorods: Ga-dimethyl amide (Ga$_2$[N(CH$_3$)$_2$]$_6$) as gallium source. Iron, applied as catalyst is provided as iron carbonyl, Fe(C$_5$H$_5$)$_2$ vapor. The reaction is performed in a nitrogen–ammonia gas mixture.

Looking at nanotubes, typically, the reaction product looks like a disordered ball of wool. As an example, Figure 5.29 displays carbon nanotubes synthesized with methane as precursor and an iron-containing catalyst. The diameter of the nanotubes is adjusted by selection of the catalyst.

To produce arrays of carbon nanotubes, as are needed, for example, for electron field emission displays, tiny droplets of a catalyst are arranged on a substrate either by printing or by a vapor process. After producing these substrates, the following process is similar to that described above, with just one difference: Now, the carbon nanotubes grow perpendicularly to the substrate. This process is, in a simplified manner, depicted in Figure 5.30.

The formation of the one-dimensional nanoparticle, nanotube or nanorod is connected to a process of dissociation, dissolution, and precipitation at the surface of the catalyst. First, the gaseous precursor is dissociated by reaction with the catalyst and partly dissolved. Here, one realizes a first criterion for the selection of the catalyst: It must be able to dissolve the material for the intended nanoparticle. After exceeding the maximal solubility, precipitation starts. The precipitation takes place as nanorods or nanotubes. This one-dimensional object will continue growing as long as the precursor is supplied. For example, looking at the synthesis of carbon nanotubes using methane, CH$_4$, as precursor, one observes dissociation of the methane at the surface of the iron catalyst particle. The released carbon dissolves in the catalyst particle and precipitates after exceeding the solubility limit. This precipitation is the intended carbon nanotube. The length of this nanotube is controlled by the supply of the precursor. As diffusion processes are significantly faster and solubilities are higher in liquids as compared to solids, the catalyst
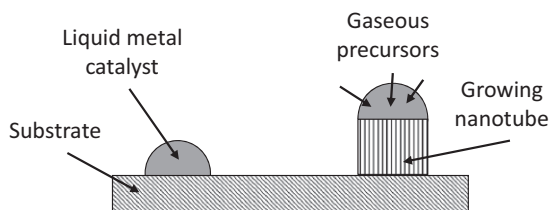
Figure 5.30 Synthesis of nanotubes or nanorods using a catalyst droplet sitting on a substrate. The gaseous precursor reacts with the catalyst and becomes partly dissolved. The quantity of the precursor beyond the solubility limit precipitates at the surface of the substrate. As a consequence, the catalyst droplet is lifted and the process continues. As long as the precursor is supplied, the one-dimensional precipitate will grow.
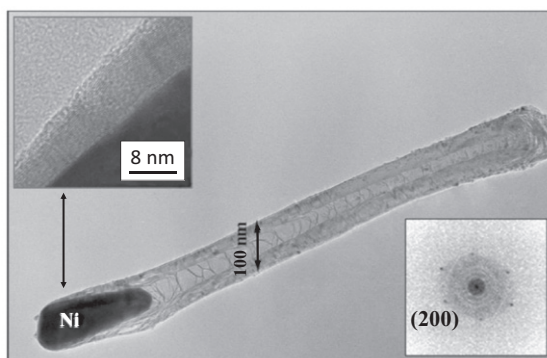

Figure 5.31 Experimental proof of the synthesis process as depicted in Figure 5.30. Multiwall carbon nanotube with the residues of a nickel catalyst droplet on one tip [20]. The insert above left displays the wall in higher magnification, making the different layers visible. The insert on the lower part shows an electron diffraction pattern representing the hexagonal structure of graphene, the constitutive element of carbon nanotubes. (Reproduced with permission by John Wiley & Sons.)

particles should be liquid. To avoid too high temperatures, the application of eutectic systems is recommended.

The description of the operation principle is not pure imagination, hard experimental proof exists. Figure 5.31 displays a multiwall carbon nanotube with the residues of a nickel catalyst droplet on one end [20]. This figure contains two inserts, one displaying the wall in higher magnification, making the different layers visible. The other one, an electron diffraction pattern represents the hexagonal structure of graphene, the constitutive element of carbon nanotubes.

It was mentioned above that the one-dimensional nanoparticles grow as long as the supply of the precursor continues. This statement needs a caveat; it is valid
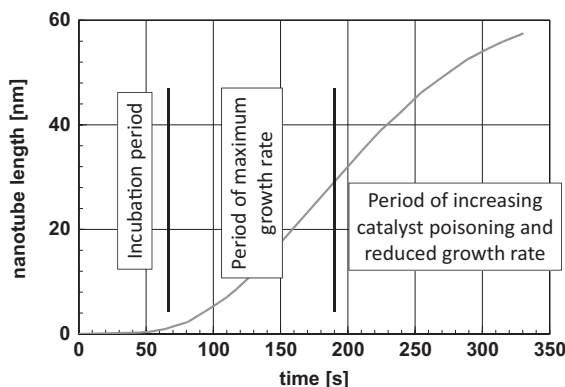
Figure 5.32 Graph showing the length of a growing carbon nanotube as a function of time [21]. This graph shows clearly the incubation period, where, primarily, the catalyst particle, in this case nickel, gets saturated with carbon from the gaseous precursor, ethyne. After a period of fast growth, the catalyst gets poisoned and, therefore, the growth rate is reduced.

as long as the catalyst is not poisoned. Poisoning of the catalyst may have its cause in gaseous impurities in the system. This slow down, which will potentially lead to a complete halt of the growth, is demonstrated in Figure 5.32 [21]. In this figure, the length of a growing carbon nanotube is plotted versus time. The experiment, background of this graph, was performed at a temperature of 920 K; ethyne, C_2H_2, was used as precursor and metallic nickel as catalyst. This graph shows three characteristic ranges: First, there is an incubation period with no or very slow growth. Within this period, the process is characterized by the saturation of the catalyst particle with carbon. After saturation of the catalyst with carbon and nucleation of the nanotube, the length growth starts. Now the process enters the range of maximum growth rate. With time, the growth rate decreases, the catalyst becomes poisoned. Poisoning of the catalyst may happen either by impurities stemming from the gas atmosphere, or, as in this case, by covering the surface of the catalyst with strongly bonded carbon atoms, a process that reduces the active surface. Analyzing Figures 5.30 and 5.31 makes it clear that the diameter of the one-dimensional product depends essentially on the size of the catalyst particle.

An even more striking proof of the mechanism of the formation of nanorods, as depicted in Figure 5.30, which is generally valid, is the series of electron micrographs showing the temporal development of a germanium nanorod as it is displayed in Figure 5.33 [22].

The series of electron micrographs showing a growing germanium nanorod together with a catalyst particle of gold, depicted in Figure 5.33 was taken *in situ*. The temperature was in the range between 1000 and 1200 K. As precursor, GeI_2 was selected, which is gaseous at the selected reaction temperature. The micrographs show clearly the gold particle at the beginning of the process. As first step,
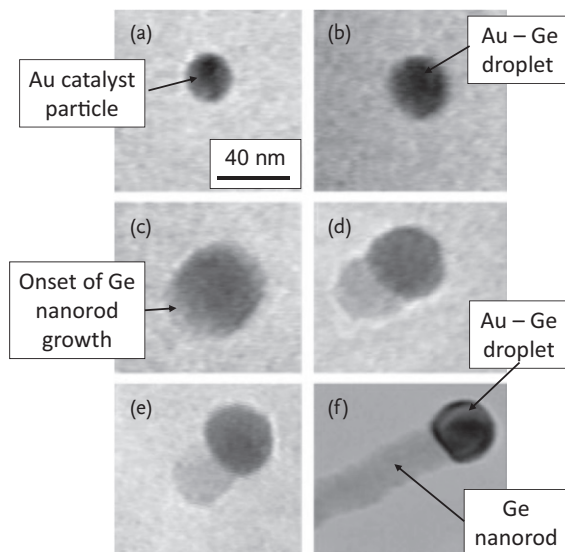
(a) Au catalyst particle

40 nm

(b) Au – Ge droplet

(c) Onset of Ge nanorod growth

(d)

Au – Ge droplet

(e)

(f)

Ge nanorod

Figure 5.33 Series of electron micrographs depicting the temporal development of a germanium nanorod [22]. (a) The process starts with a gold particle as catalyst. Precursor for germanium is the iodide, GeI_2. (b) The iodide decomposes at the surface of the gold particle, a gold–germanium alloy particle is formed. In the steps designated c–f, one realizes the growing germanium nanorod. In every micrograph, c–f one realizes the nanorod, which is capped by the catalyst particle. (Reproduced with permission by The American Chemical Society.)

one realizes the increase of the catalyst diameter, germanium, stemming from the dissociated iodide, dissolves in the gold particle. (As bulk material, the gold–germanium binary system has the eutectic temperature of 630 K.) After nucleation, the nanorod starts growing. One always sees the catalyst particle at the tip of the germanium nanorod.

Box 5.9   Synthesis of a ZnO Nanotube

As an example of a synthesis of a nanotube from a material not crystallizing in a layered structure, the synthesis of a ZnO nanotube is explained. The synthesis starts from an small zinc embryo. As zinc crystallizes highly unisotropic (hexagonal) the embryo is, because of the differences in surface energy, hexagonal in shape. This metallic zinc embryo is carefully oxidized at a temperature in the range between 700 and 800 K. At this temperature, the less stable lateral surfaces of the metallic prism start to oxidize. Therefore, the oxide grows in the direction perpendicular to the hexagonal base plane. Now, the interior size of the ZnO tube is equal to the outer dimension of the metallic embryo. The vapor pressure of the pure metal is significantly higher than that of the oxide; therefore, the material of the starting embryo is evaporated

and consumed by the growing nanotube. In a simplified way, this process is depicted in Figure 5.34.

Electron micrographs of such zinc oxide nanotubes are displayed in Figure 5.35. The two ZnO nanotubes have entirely different dimensions. The one displayed in Figure 5.35a [24], which is rather a micro- than a nanotube, has an edge length of more than 1 μm and a wall thickness of approximately 200 nm. Entirely different is the nanotube displayed in Figure 5.35b [25]. In that case, the edge length is ca. 200 nm, and the wall thickness less than 50 nm. Looking in detail at the micrograph in Figure 5.35b, it is most interesting to see that, possibly, this nanotube grew as a spiral.

Growing ZnO nanotube

Zn embryo

(a)   (b)   (c)
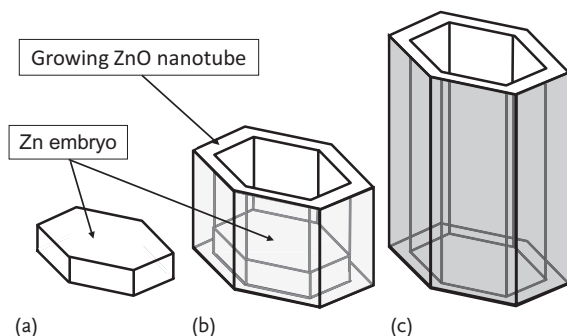
Figure 5.34 Growth of a ZnO nanotube from a metallic zinc particle having formed a shape with minimum surface energy. (According to Xing *et al.* [23]) (a) The tube is formed by the oxidation of the lateral surfaces of the zinc embryo. (b). As long as there is material supplied from the metallic embryo, the nanotube grows. The growth comes to an end when the zinc reservoir is depleted.
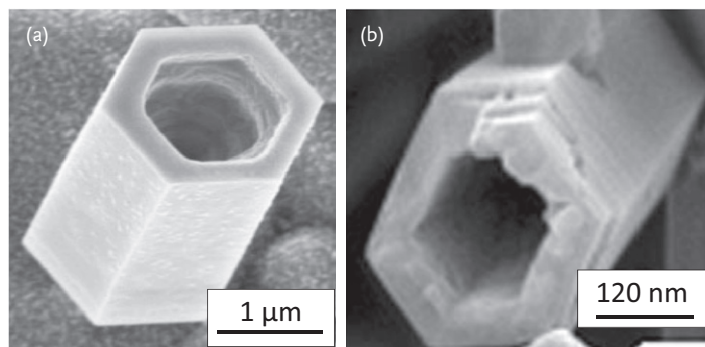

(a)   (b)

1 μm   120 nm

Figure 5.35 Hexagonal ZnO nanotubes grown from metallic zinc embryos. In case (a), the outer surface is very flat, whereas the inner surface is corrugated [24] (Reproduced with opermission by John Wiley & Sons.). In the case of the smaller zinc oxide nanotube, (b) it is interesting to see that the tube has grown, possibly, as a spiral [25]. (Reproduced with permission by Elsevier.)

References

1 Georgobiani, A.N., Gruzintsev, A.N., Kozlovskii, V.I., Makovei, Z.I., Red'kin, A.N., and Skasyrskii, Y.K. (2006) *Neorganicheskie Materialy*, **42**, 830–835.

2 Yun, Y.J., Park, G., Ah, C.S., Park, H.J., Yun, W.S., and Haa, D.H. (2005) *Appl. Phys. Lett.*, **87**, 233110–233113. Fig. 1a,b, Fig. 3b, Fig. 2e.

3 Du, J., Liu, Z., Wu, W., Li, Z., Han, B., and Huang, Y. (2005) *Mater. Res. Bull.*, **40**, 928–935.

4 Lee, Y., Kim, B., Yi, W., Takahara, A., and Sohn, D. (2006) *Bull. Kor. Chem. Soc.*, **27**, 1815.

5 Koenderink, G.H., Kluijtmans, S.G.J.M., and Philipse, A. (1999) *J. Colloid Interface Sci.*, **216**, 429–431.

6 Sazonova, V., Yaish, Y., Üstünel, H., Roundy, D., Arias, T.A., and McEuen, P.L. (2004) *Nature*, **431**, 284–287.

7 Jensen, K., Kim, K., and Zettl, A. (2008) *Nature Nanotechnol.*, **3**, 533–537.

8 Kroto, W., Heath, J.R., O'Brien, S.C., Curl, R.F., and Smalley, R.E. (1985) *Nature*, **318**, 162–163.

9 Banhardt, F., and Ajayan, P.M. (1996) *Nature*, **382**, 433–435.

10 Zhang, T., Simens, A., Minor, A., Liu, G. (2006) *Carbon Nanotube-Conductive Polymer Composite Electrode for Transparent Polymer Light Emitting Device Application*, PMSE.

11 Pang, H., Chen, T., Zhang, G., Zeng, B., Li, Z.-M. (2010) *Materials Letters* **64**, 2226–2229.

12 Geim, A.K., and MacDonald, A.H. (2007) *Phys. Today*, **60**, 35–41.

13 Choi, W., Lahiri, I., Seelaboyina, R., and Kang, Y. (2010) *Crit. Rev. Solid State Mater. Sci.*, **35**, 52–71.

14 Tenne, R., Margulis, L., Genut, M., and Hodes, G. (1992) *Nature*, **360**, 444–446.

15 Vollath, D., and Szabo, D.V. (1998) *Mater. Lett.*, **35**, 236–244.

16 Vollath, D., and Szabo, D.V. (2000) *Acta Mater.*, **48**, 953–967.

17 Rapoport, L., Fleischer, N., and Tenne, R. (2005) *J. Mater. Chem.*, **15**, 1782–1788.

18 Gilman, J.W., Jackson, C.L., Morgan, A.B., Harris, R., Jr., Manias, E., Giannelis, E.P., Wuthenow, M., Hilton, D., and Phillips, S.H. (2000) *Chem. Mater.*, **12**, 1866–1873. Figure 5.

19 Fu, X., and Qutubuddin, S. (2001) *Polymer*, **42**, 807–813.

20 Rybczynski, K.J., Huang, Z., Gregorczyk, K., Vidan, A., Kimball, B., Carlson, J., Benham, G., Wang, Y., Herczynski, A., and Ren, Z. (2007) *Adv. Mater.*, **19**, 421–426. Fig. 2.

21 Lin, M., Tan, J.P.Y., Boothroyd, C., Tok, E.S., and Foo, Y.-L. (2006) *Nano Lett.*, **6**, 3449–3452.

22 Wu, Y., and Yang, P. (2001) *J. Am. Chem. Soc.*, **123**, 3165–3166.

23 Xing, Y.J., Xi, Z.H., Zhang, X.D., Song, J.H., Wang, R.M., Xu, J., Xue, Z.Q., and Yu, D.P. (2004) *Solid State Commun.*, **129**, 671–67.

24 Gao, P.X., Lao, C.S., Ding, Y., and Wang, Z.L. (2006) *Adv. Funct. Mater.*, **16**, 53–62. Fig. 9a.

25 Liu, J., and Huang, X. (2006) *J. Solid State Chem.*, **179**, 843–848. Fig. 2c.

6
Nanofluids

6.1
Background

Nanofluids are stable suspensions of nanoparticles in a liquid, generally, water or oil. Suspensions are, in most cases unstable. The particles have the tendency to agglomerate and to sediment. This tendency is avoidable by adding colloid stabilizers (surfactant) to the liquid. There are many possibilities to stabilize a colloid. The most important are steric and electrostatic stabilization. Figure 6.1 displays these two possibilities in a simplified way.

In Figure 6.1a, steric stabilization is sketched. Simply stated, steric stabilization is obtained by adding long organic molecules perpendicular at the surface of the particles. Now, these molecules act as distance holders, they avoid direct contact in-between the particles and, therefore, agglomeration. In Figure 6.1a the distance-holder molecules are perpendicular to the surface. When they are not well ordered, one obtains a transition to the gel network stabilization. When the molecules carry electric dipole moments, they can form an electrostatic double layer. As the surfaces of the particles now carry electrostatic charges of equal sign, they repel each other. (It is important to mention that the net charge of each particle remains nil.) In both cases, the particles are kept at a certain distance, this thwarts the formation of *van der Waals* bond clusters. Therefore, the *Brownian* molecular movements of the particles, kept at a distance, prevents sedimentation of the particles.

As a general rule, one can say that a nanofluid contains up to 10 vol% particles and approximately the same amount of surfactants.

6.2
Nanofluids for Improved Heat Transfer

In general, the heat capacity of nanoparticles is larger than that of liquids; additionally, the same is valid for the thermal conductivity. Therefore, it seems straightforward to add nanoparticles to coolants to improve their performance. In fact, these expected phenomena were found. The remaining open questions are the compatibility of the particles in the fluids with the technical environment to be
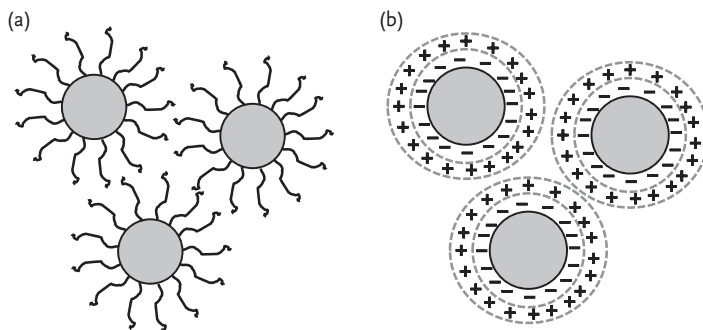
(a)

(b)

Figure 6.1 The two most important principles to stabilize a suspension. (a) Steric stabilization. In this case, long organic molecules are attached at the surface. These molecules act as distance holders. The second possibility, electrostatic stabilization (b) is also (in most cases) obtained by adding organic molecules, exhibiting an electrostatic dipole moment, at the surface. The molecules form a kind of electrostatic double layer. As the surface of the particles is now covered with electric charges of the same sign, the particles repel each other.
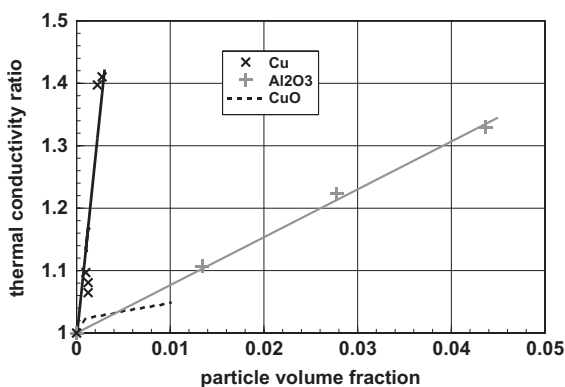
Figure 6.2 Influence of nanoparticle addition on the thermal conductivity of a nanofluid based on ethylene glycole and copper or alumina, respectively. The thermal conductivity ratio is defined as the thermal conductivity of the nanofluids over that of pure ethylene glycol. The experimental data for copper additions were taken from Keblinsky *et al.* [1], Eastman *et al.* [2], those for the alumina additions from Masuda *et al.* [3], and for CuO from Kwak and Kim [4].

cooled and the long-term stability. Figure 6.2 depicts experimental results obtained by Keblinski *et al.* [1] and Eastman *et al.* [2] for copper additions, Masuda *et al.* [3] for additions of alumina, and for CuO additions from Kwak and Kim [4]. It is well known that the thermal conductivity of copper is better than that of alumina or copper oxide, the tendency, visible in this figure is not surprising. However, even when the results of the different groups differ significantly, what is surprising, in fact, is the significant improvement of the thermal conductivity.
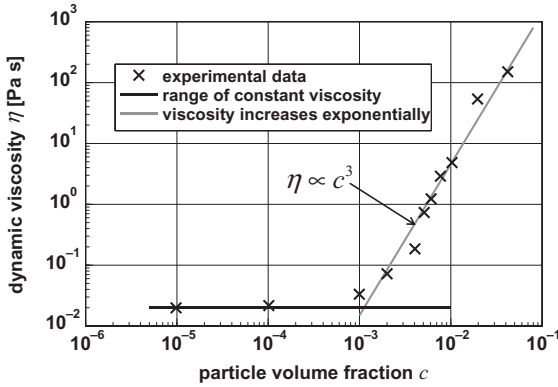
Figure 6.3 Dynamic viscosity of an ethylene glycol / CuO nanofluid as a function of the volume content of nanoparticles plotted in a double-logarithmic system [4]. Up to a particle volume fraction of 10^{-3}, the viscosity is not influenced by the additions of nanoparticles. At higher concentrations, the dynamic viscosity increases exponentially, to the power of three, $\eta \propto c^3$.

In view of the technical applications, besides heat capacity and thermal conductivity, the influence on the rheological properties is of essential importance. Figure 6.3 displays, as an example, the dynamic viscosity η of a nanofluid consisting of CuO nanoparticles in ethylene glycol as a function of the volume fraction c of nanoparticles [4]. These results are very important, as they show that, for particle concentrations higher than 10^{-3} (=0.1%), the dynamic viscosity increases exponentially with a power of three, $\eta \propto c^3$.

Summarizing the content of Figures 6.2 and 6.3 one realizes a very promising improvement of the coolant liquid, as the dramatic increase of the dynamic viscosity above a volume content of 10^{-3} is out of the range, where an interesting increase of the thermal conductivity is observed. These improved properties allow the design of smaller highly efficient cooling systems, which may be of great importance in microtechnology. Looking at applications in the automotive industry, the long-term stability has to be analyzed in great detail. Such long-term applications could be impeded by a tendency of sedimentation or thermophoresis.

6.3
Ferrofluids

6.3.1
Properties of Ferrofluids

Ferrofluids are a special type of nanofluids. As nanoparticles, superparamagnetic ceramic particles are applied. (For "superparamagnetism", please see Chapter 8.) The importance of ferrofluids is based on their broad range of applications in

engineering, medicine, and biotechnology. The stabilization of ferrofluids is thus more difficult as compared to the other nanofluids, as in-between the ferromagnetic particles, there is a dipole–dipole interaction, with the tendency to form lumps. Furthermore, besides segregation due to gravity and thermophoresis, one must take note of segregation of the particles in an external magnetic field. Magnetic unmixing is avoided by limiting the size of the magnetic particles; on the other hand, magnetic phenomena depend strongly on the particle size. Therefore, a compromise, optimal for the specific application, must be sought. Ferrofluids for technical applications contain between 3 and 8 vol% magnetic nanoparticles and usually more than 10 vol% surfactant. Depending on the application, water or oil are applied as carrier liquid.

In the absence of an external magnetic field, the magnetic moment of a ferrofluid is nil. In the presence of a magnetic field, the particles adjust within milliseconds in the direction of the magnetic field and after removing the external field, the orientation of the magnetic dipoles (the particles) randomize again. The dynamics of this process is known as *Brown*'s superparamagnetism. In a magnetic-field gradient, the whole fluid moves to the region of highest flux. This propensity is the basis of series of interesting phenomena connected to ferrofluids. In a famous book, *Rosenzweig* [5] gives a complete theory of ferrofluids and describes or predicts a series of phenomena carrying his name.

The most famous one of the *Rosenzweig* phenomena is depicted in Figure 6.6. It displays the surface of a ferrofluid in an inhomogeneous magnetic field. The unbiased thinker expects just a convex surface, showing a tendency of attracting the magnetic fluid by the magnetic field. However, things are more complicated, as this simple way of looking at the things did not consider the interaction between the inhomogeneous magnetic field, gravity, and surface energy. Because of this complicated interaction, one observes a spiked surface, where the spikes follow the direction of the gradient of the magnetic field. The forces acting at magnetic fluids are proportional to the gradient of the magnetic field (Figure 6.4).
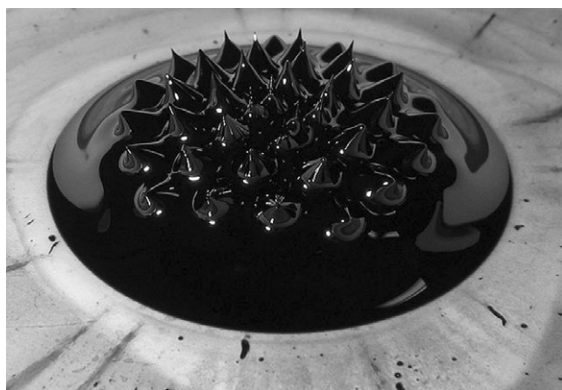

Figure 6.4 *Rosenzweig* phenomenon, interaction of a ferrofluid in an inhomogenous magnetic field with gravitation and surface energy [6].
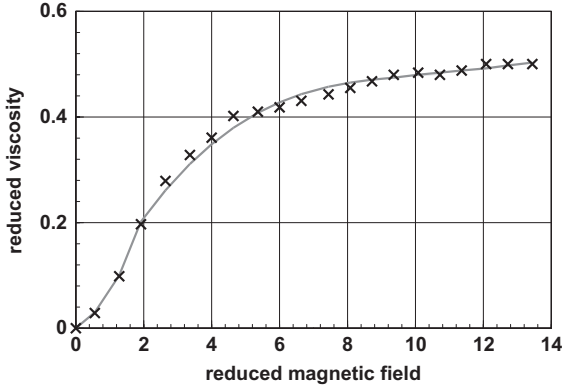
Figure 6.5 Viscosity of a ferrofluid consisting of kerosene as liquid and magnetite particles [7]. The reduced magnetic field is temperature compensated $H_{red} = \alpha \dfrac{H}{T}$, the reduced viscosity is defined as $\eta_{reduced} = \dfrac{\eta_H}{\eta_{H=\infty}}$ (For $H = 0$, $\eta_{H=0} = 0$), the viscosity at the magnetic field H, η_H divided by the asymptotic value of the viscosity at infinite magnetic field $\eta_{H=\infty}$.

Looking at technical applications of ferrofluids, one has to analyze the properties of these nanofluids. Most importantly, in this context, is the possibility to control the dynamic viscosity using an external magnetic field. Figure 6.5 displays the influence of an external magnetic field on the viscosity of a ferrofluid consisting of kerosene as liquid and magnetite, Fe_3O_4 particles. Assuming a log-normal distribution of the particle sizes, the mean particle sizes was around 13 nm.

To generalize the results, in Figure 6.5, the absolute values of the magnetic field H and the viscosity η were not plotted; instead, more generalized reduced values were plotted. In this case, the reduced viscosity is defined as $\eta_{reduced} = \dfrac{\eta_H}{\eta_{H=\infty}}$, the viscosity at the magnetic field H, η_H divided by the asymptotic value of the viscosity at infinite magnetic field $\eta_{H=\infty}$. (The values for η_H are defined in such a way that $\eta_{H=0} = 0$ is valid.) In the case of the magnetic field, one makes use of the temperature compensation, which is typical for superparamagnetic materials, as the quotient $\dfrac{H}{T}$ is temperature independent (see Chapter 8). In the abscissa of Figure 6.5, an additional constant factor $\alpha = \dfrac{m}{k}$ was applied, with m the magnetic moment of one particle and k the *Boltzmann* constant. With respect to the experimental conditions, which lead to the data shown in this figure, one may roughly estimate the magnetic field in *Tesla* by dividing the values given in the abscissa by 100. Analyzing Figure 6.5 in detail, one realizes that, especially in the range of relatively small magnetic fields, it is possible to influence the viscosity of a ferrofluid significantly. Looking at alternating magnetic fields, the situation is significantly more complex. At low frequencies, there is not too much difference as compared to a constant magnetic field, whereas at higher frequencies of the magnetic field, the contribution to the viscosity is negative.
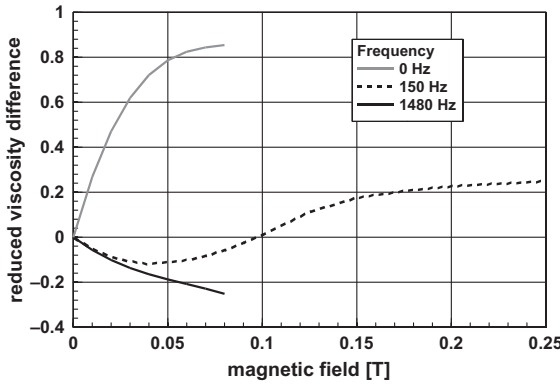

Box 6.1   Viscosity of a Ferrofluid in an Alternating Magnetic Field

Figure 6.6   Reduced viscosity difference $\Delta\eta_{\text{reduced}}$ of a ferrofluid, 20 vol% CoFe$_2$O$_4$ in water, as a function of the external field and the frequency of the magnetic field [8].

Intuitively, the viscosity of a ferrofluid should increase with increasing external magnetic field. However, with increasing frequency of the magnetic field, one finds a reduction of the viscosity. Experimental data describing this phenomenon are depicted in Figure 6.6.

Figure 6.6 displays the reduced viscosity difference of a ferrofluid consisting of 20 vol% CoFe$_2$O$_4$ particles with a medium size of 10 nm in water. The ordinate is defined as

$$\Delta\eta_{\text{reduced}} = \frac{\eta_{H,f} - \eta_{H=0,f=0}}{\eta_{H=0,f=0}}. \tag{6.1}$$

The quantity $\eta_{H,f}$ stands for the viscosity at the magnetic field H and the frequency f; $\eta_{H=0,f=0}$ for the viscosity ot the magnetic field $H = 0$ and the frequency $f = 0$. The cobalt ferrite used in these experiments has a relatively high energy of unisotropy; therefore, these particles did not show *Néel* superparamagnetism. The nanofluid shows only *Brown*ian superparamagnetism.

To understand this effect, one has to look at the individual particles: Applying an external magnetic field to a ferrofluid, the magnetic vector of each particle is turned into the direction of the field. It is obvious that as long as the particle can follow changes of the direction of the magnetic field, as there is no preference, to a first approximation, half of the particles turn clockwise and the other half counterclockwise. Hence, macroscopically, from the outside, there is no rotation observable. However, any local vortex results in the nonzero angular velocity of the particles. This leads to the decrease of the effective viscosity; a negative contribution to the viscosity. A detailed derivation of this quite complicated phenomenon is given by Shliomis and Morozov [9].

6.3.2
Applications of Ferrofluids

For applications, the possibility to adjust viscosity with an external magnetic field is most important. This property allows adjustment of shock absorbers of cars or of high-performance CD or DVD players within milliseconds to changing external conditions. In particular, for precision instrumentation, systems using ferrofluids may replace piezoelectric devices. Lastly, the application of ferrofluids allows controlling powers in the kilowatt range with a few *Watt*. Furthermore, ferrofluids are applied to transfer magnetic fields or to close magnetic circuits in a simple way without complicated shaped parts. A further broad range of technical applications is found in the visualization of magnetic structures, which are essential in quality control of magnetic devices and, most importantly, for searching small defects in cast parts and weldings. For these applications, quite often one applies external magnetic fields to enhance the contrast. In addition, the application of bifunctional magnetic particles, exhibiting luminescence besides ferromagnetism, is often of advantage. The last point in this listing are medical applications, for example, to increase the contrast in nuclear spin tomography by locally influencing the magnetic field.

The most famous application of ferrofluids in engineering are gas-tight fluid dynamic bearings. In this case, the oil receives additions of ferromagnetic particles, a ferrofluid is used. Now, the ferrofluid, whose viscosity is increased by a magnetic field, acts as lubricant and as sealant, too. To keep the oil in place, it is held by a system of permanent magnets. Figure 6.7 shows such a design.
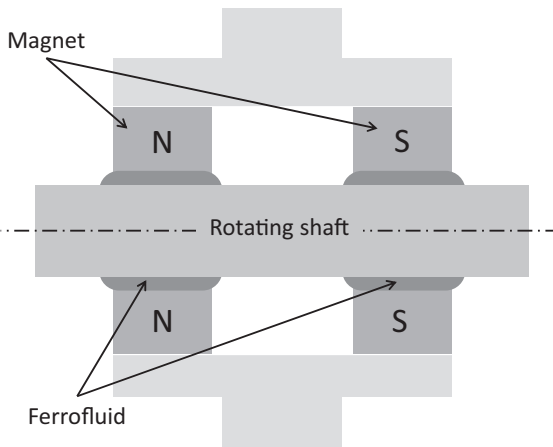
Figure 6.7 Design of a gas-tight hydrodynamic bearing using a ferrofluid as sealant and as lubricant. In special cases, such a design is more reliable compared to a standard design using elastic sealing rings. This application applies the increase of the viscosity of a ferrofluid in a magnetic field.
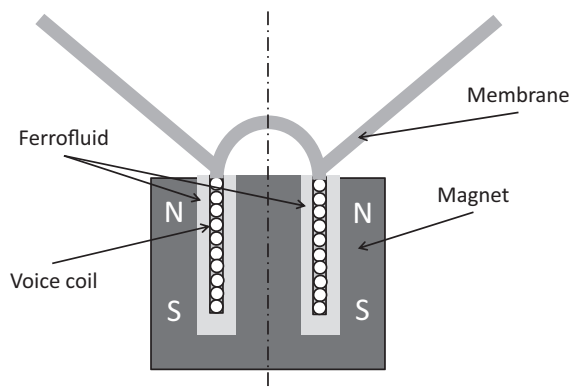
Figure 6.8 Design of a high-performance loudspeaker using a ferrofluid.

Commercially most successful is the application of ferrofluids in high-performance loudspeakers. Figure 6.8 displays the general principle of such a speaker. Looking at this application, there is a series of advantages: One of the most important parts of the loudspeaker is the magnetic system. The higher the magnetic field in the gap, where the voice coil is located, the more is it possible to reduce the electric current in this coil, and, therefore, the *Ohm*ic losses. Placing a ferrofluid in the gap instead of air increases the magnetic field around the coil. Furthermore, the ferrofluid has a significant better thermal conductivity as compared to air. This improves cooling of the coil, reduces the temperature and, therefore, *Ohm*ic losses. Not least, the liquid around the voice coil acts as a damping medium and reduces unwanted vibrations, it improves the klirr factor.

An application of increasing importance is the use of ferrofluids as a means to improve the contrast in nuclear magnetic resonance imaging (NMR) (often called nuclear magnetic resonance tomography) in medical diagnostics. In NMR, the spin resonance of protons (hydrogen nuclei) is determined. As this resonance frequency depends on the magnetic field, any local variation of the magnetic susceptibility leads to a variation in the resonance signal. Technically, an NMR system consists of a large coil, a source of an intense constant magnetic field, and a second system of coils superimposing a small high-frequency magnetic field. In the static magnetic field, the spins of the protons are either parallel or antiparallel to the field. The superimposed high-frequency magnetic field causes a flipping of the spins. The resonance frequency of this flipping process is the intended signal for imaging. This resonance frequency is proportional to the magnetic field, and, therefore, it follows local variations of the susceptibility. As the ferrofluid is injected into the blood of the patient, blood vessels will become visible. If the surface of the magnetic particles is covered with proteins or enzymes, which are characteristic for a specific organ or tumor, the particles are collected at these places. This greatly improves the contrast. Figure 6.9 displays a typical example.
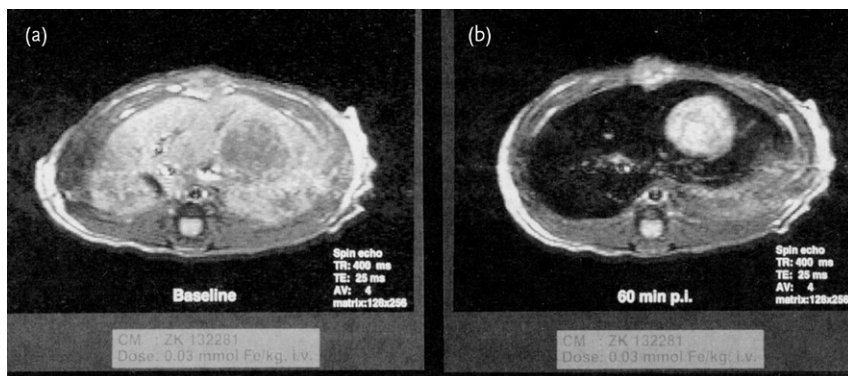
Figure 6.9 Comparison of two NMR tomographs of a tumor in a rat liver (Novikoff-Hepatoma) [10], without contrast enhancement (a) and showing the influence of γ-Fe_2O_3 nanoparticles on the contrast (b). On comparing these two figures, the contrast enhancement is striking.

References

1 Keblinski, P., Phillpot, S.R., Choi, S.U.S., and Eastman, J.A. (2002) *Int. J. Heat Mass Transfer*, **45**, 855–863.

2 Eastman, J.A., Choi, S.U.S., Li, S., Yu, W., and Thomson, L.J. (2001) *Appl. Phys. Lett.*, **78**, 718.

3 Masuda, H., Ebata, A., Teramae, K., and Hishinuma, N. (1993) *Netsu Bussei*, **4**, 227–233.

4 Kwak, K., and Kim, C. (2005) *Korea-Aust. Rheol. J.*, **17**, 35.

5 Rosenzweig, R.E. (1985) *Ferrohydrodynamics*, Cambridge University Press, Cambridge.

6 http://de.wikipedia.org/w/index.php?title=Datei:Ferrofluid_in_magnetic_field.jpg&filetimestamp=20060704102520. http://www.flickr.com/photos/jurvetson/136481113/. This image was originally posted to Flickr by jurvetson at http://www.flickr.com/photos/jurvetson/136481113/. It was reviewed on 9. December 2006 by the FlickreviewR robot and confirmed to be licensed under the terms of the cc-by-2.0.

7 Patel, R., Upadhyay, R.V., and Metha, R.V. (2003) *J. Colloid Interface Sci.*, **263**, 661.

8 Bacri, J.C., Perzynski, R., Shliomis, M.I., and Burde, G.I. (1995) *Phys. Rev. Lett.*, **75**, 2128–2132.

9 Shliomis, M.I., and Morozov, K.I. (1994) *Phys. Fluids*, **6**, 2855–2861.

10 Kresse, M., Pfefferer, D., and Lawaczeck, R. (1994) *Dtsch. Apoth. Ztg.*, **134**, 3079–3089.

7
Thermodynamics of Nanoparticles and Phase Transformations

7.1
Basic Considerations

The surface over volume ratio of nanoparticles is significantly larger as compared to that of macroscopic parts (see Chapter 3). As a surface is always connected to surface energy this large surface contributes significantly to the energy of a particle. Therefore, thermodynamic considerations must take note of this additional factor. Furthermore, one has to realize that nanoparticles are small; therefore, all quantities depending on the size have to be analyzed. Looking at heat capacity, one would not expect a significant influence. However, knowing that heat capacity is based on lattice vibrations, which depend on the atomistic nature of the particles, one realizes that the amount and the modes of possible lattice vibrations in a small particle are different as compared with a large particle. Similar considerations are valid when looking at polycrystalline bodies consisting of grains in the nanometer range. In this case, the volume fraction of grain-boundary material is significant. As grain boundaries are less ordered as compared to well-crystallized material, one has to expect a notable influence on the thermodynamic quantities.

7.2
Influence of the Particle Size on Thermodynamic Properties and Phase Transformations

The free enthalpy of one particle, *Gibbs* enthalpy g, is defined as

$$g = u - Ts + \gamma a. \tag{7.1a}$$

In Eq. (7.1) u is the enthalpy, T the temperature, s the entropy, γ the surface energy, and a the surface of one particle. If the equation is related to one mole, the quantities are written in capital letters, as

$$G = U - TS + \gamma A. \tag{7.1b}$$

The surface energy γ is independent of the quantity, however, there is a dependency on the particle size, which is often observed, but until now not really

quantified; therefore, in most cases, this quantity is assumed to be independent of the particle size. To a first rough approximation, the molar quantities U and S may also be assumed to be particle-size independent. This allows us to rewrite Eqs. (7.1a) and (7.1b) as functions of the particle diameter d, using $u = \dfrac{U}{N} = U\dfrac{\rho \pi d^3}{6M}$, $s = \dfrac{S}{N} = S\dfrac{\rho \pi d^3}{6M}$, $a = \dfrac{A}{N} = A\dfrac{\rho \pi d^3}{6M}$, and $a = \pi d^2$,

$$g = U\frac{\rho \pi d^3}{6M} - TS\frac{\rho \pi d^3}{6M} + \gamma d^2 \pi, \tag{7.2a}$$

$$G = U - TS + \gamma \frac{M}{\rho v} a = U - TS + \gamma \frac{M}{\rho} \frac{6}{d}. \tag{7.2b}$$

In these equations, N stands for the number of particles per mol, M for the molecular weight and ρ for the density of the material. For thermodynamic considerations, most important are the molar quantities as they are given in Eq. (7.2b). To analyze phase transformations; the surface energy of the different phases, for example, solid or liquid must be taken into account. The same is valid for the volume change connected to phase transformations. Looking at Eq. (7.2b), one realizes that the free enthalpy increases with decreasing particle diameter. As an example, Figure 7.1 displays the molar surface energy of solid and liquid gold in comparison to the molar enthalpy of melting.

Analyzing Figure 7.1, one realizes that the surface energy in the solid and liquid states are significantly larger than the enthalpy of melting; even the difference of the surface energies is, in the case of small particles in the same range of energy as the enthalpy of melting. Therefore, one may expect a significant influence of particle size, via the surface energy, on the melting behavior. This statement is valid not only for the melting process, but for any other phase transformation, too.
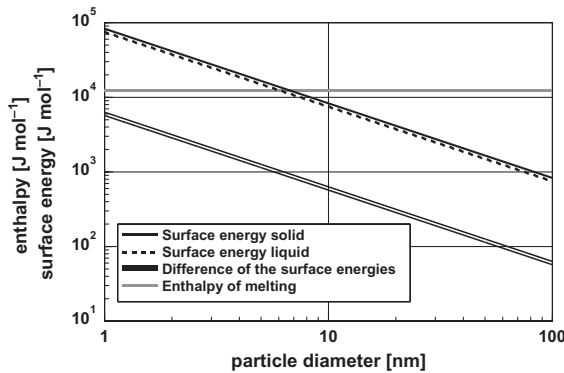
Figure 7.1 Surface energy of solid and liquid gold in comparison with the enthalpy of melting. One sees that the difference of the two surface energies is close to the enthalpy of melting. This graph was calculated assuming that the quantities U, S, and γ are independent of the particle size.
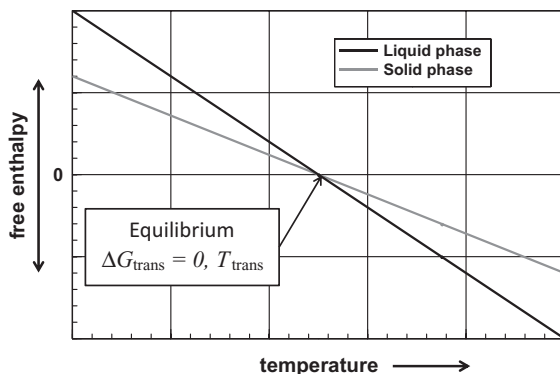
Figure 7.2 Free enthalpy in the case of a phase transformation, in this case melting or crystallization. At the equilibrium point, where both enthalpies are equal, the transformation temperature is called the "crossing temperature".

The question on the influence of the particle size on the melting temperature is quite old. The first answers, based on strict application of equilibrium thermodynamics, were given at the end of the nineteenth century. More generally, to calculate the influence of the particle size on phase transformations, one has to look at the equilibrium between the parent phase, called "*old*" and the other phase, called "*new*". At equilibrium, the relation

$$G_{old} = G_{new} \tag{7.3}$$

is valid. Figure 7.2 depicts this situation for the case of melting, respectively, crystallization as phase transformation. The temperature, where the free enthalpy of the parent phase (e.g., solid phase) G_{old} is in equilibrium with the new phase (in this example the liquid phase), G_{new} is often called the "crossing temperature". At this temperature, the difference of the free enthalpy ΔG_{trans} is nil.

Box 7.1 Entropy of the Different Phases

In Figure 7.2 one realizes that the entropy of the high-temperature phase (in this case the liquid phase) is higher than the one of the low temperature phase (solid phase). Higher entropy is – in statistical physics – related to higher symmetry. However, in this context, one must not use the term "symmetry" in the way it is used in crystallography or geometry. In this context, symmetry must be understood in a statistical sense. That means in a liquid and even more so in a gas, each point may act as center of symmetry that means for any symmetry operation a partner is possible. Important: It is possible but not necessarily present.

Assuming isothermal conditions, at the transformation temperature, T_{trans} this leads to

$$U_{\text{old}} - T_{\text{trans}}S_{\text{old}} + \gamma_{\text{old}}A_{\text{old}} = U_{\text{new}} - T_{\text{trans}}S_{\text{new}} + \gamma_{\text{new}}A_{\text{new}}.$$

Using the differences $\Delta U_{\text{trans}} = H_{\text{new}} - H_{\text{old}}$, and $\Delta S_{\text{trans}} = S_{\text{new}} - S_{\text{old}}$ Eq. (7.3) boils down to:

$$\Delta G_{\text{trans-nano}} = \Delta U_{\text{trans}} - T_{\text{trans}}\Delta S_{\text{trans}} + \gamma_{\text{new}}A_{\text{new}} - \gamma_{\text{old}}A_{\text{old}} = 0. \tag{7.4}$$

Following this equilibrium condition consequently and using Eq. (7.2b), one obtains the important relation

$$\Delta T_{\text{trans}} = T_{\text{trans-bulk}} - T_{\text{trans-nano}} = \alpha \frac{1}{d_{\text{new}}}. \tag{7.5}$$

In Eq. (7.5) $T_{\text{trans-bulk}}$ stands for the melting temperature of the bulk material and $T_{\text{trans-nano}}$ for that of small particles. This equation, called the *Thomson* equation (sometimes also called the *Gibbs–Thomson* equation) documents that the difference melting temperature of small particles and bulk material is inversely proportional to the particle size.

Box 7.2   Influence of the Particle Size on the Temperature of Phase Transformation

For reasons of clarity and comprehensibility, these considerations are made for spherical particles; furthermore, the influence of thermal expansion is neglected. These two simplifications do not influence the physical message; rather, the resulting dependencies are clearly visible. Castro *et al.* [1]. extended the approach to melting of nanoparticles considering thermal expansion and temperature-dependent surface energy.

The starting point is the equilibrium as defined in Eq. (7.4). There are three factors influencing phase transformation: The surface of the particles, the changes of surface energy and density as a consequence of phase transformation. For spherical particles, the surface per mol is given by $A = \dfrac{6M}{\rho d}$. From simple geometric considerations, one obtains for the diameter ratio of two particles with the same mass $\dfrac{d_{\text{new}}}{d_{\text{old}}} = \left(\dfrac{\rho_{\text{old}}}{\rho_{\text{new}}}\right)^{1/3}$. After inserting in Eq. (7.4) and using the relation $\Delta U_{\text{trans}} = T_{\text{trans}}S_{\text{trans}}$ one obtains

$$\Delta G_{\text{trans-nano}} = \Delta U_{\text{trans}} - T_{\text{trans}}\Delta S_{\text{trans}} + \gamma_{\text{new}} \frac{6M}{\rho_{\text{new}}d_{\text{new}}}$$

$$- \gamma_{\text{old}} \frac{6M}{\rho_{\text{new}}D_{\text{new}}} \left(\frac{\rho_{\text{new}}}{\rho_{\text{old}}}\right)^{2/3}. \tag{7.6}$$

At equilibrium temperature, $\Delta G_{\text{trans–nano}} = 0$. For the transformation temperature of nanoparticles, one obtains

$$T_{\text{trans}} = \frac{\Delta U_{\text{trans}}}{\Delta S_{\text{trans}}} + \frac{6M\gamma_{\text{new}}}{\rho_{\text{new}}d_{\text{new}}\Delta S_{\text{trans}}}\left[1 - \left(\frac{\gamma_{\text{old}}}{\gamma_{\text{new}}}\right)\left(\frac{\rho_{\text{new}}}{\rho_{\text{old}}}\right)^{2/3}\right]. \tag{7.7}$$

Using the abbreviation $T_{\text{bulk}} = \dfrac{\Delta U_{\text{trans}}}{\Delta S_{\text{trans}}}$ one obtains the important relation

$$\Delta T = T_{\text{trans}} - T_{\text{bulk}} = 6M\frac{T_{\text{bulk}}}{\Delta U_{\text{trans}}}\frac{\gamma_{\text{new}}}{\rho_{\text{new}}}\frac{1}{d_{\text{new}}}\left[1 - \left(\frac{\gamma_{\text{old}}}{\gamma_{\text{new}}}\right)\left(\frac{\rho_{\text{new}}}{\rho_{\text{old}}}\right)^{2/3}\right]$$

$$= \alpha\frac{1}{d_{\text{new}}}. \tag{7.8}$$

Equation (7.8) represents the inverse linear relationship between the reduction of the phase-transformation temperature and the particle size, in this equation, the term in the square brackets is most interesting, as this term rules the sign of the temperature difference.

$$\alpha = \left[1 - \left(\frac{\gamma_{\text{old}}}{\gamma_{\text{new}}}\right)\left(\frac{\rho_{\text{new}}}{\rho_{\text{old}}}\right)^{2/3}\right]. \tag{7.9}$$

Looking at the melting process (old = solid, new = liquid), α is always negative, as, $\left(\dfrac{\gamma_{\text{old}}}{\gamma_{\text{new}}}\right)\left(\dfrac{\rho_{\text{new}}}{\rho_{\text{old}}}\right)^{2/3} > 1$ is always valid, as $\left(\dfrac{\gamma_{\text{old}}}{\gamma_{\text{new}}}\right) > \left(\dfrac{\rho_{\text{new}}}{\rho_{\text{old}}}\right)^{2/3}$ is always observed.

Even exceptional cases, where the density increases during melting, for example, in the cases of bismuth and germanium, do not alter this rule. This may be seen in Table 7.1.

Table 7.1 Parameters of Eq. (7.9) for different elements.

	$\dfrac{\gamma_{\text{solid}}}{\gamma_{\text{liquid}}}$	$\left(\dfrac{\rho_{\text{liquid}}}{\rho_{\text{solid}}}\right)$	$\left(\dfrac{\rho_{\text{liquid}}}{\rho_{\text{solid}}}\right)^{2/3}$	$\dfrac{\gamma_{\text{solid}}}{\gamma_{\text{liquid}}}\left(\dfrac{\rho_{\text{liquid}}}{\rho_{\text{solid}}}\right)^{2/3}$
Copper	1.11	0.9	0.93	1.03
Silver	1.22	0.89	0.92	1.12
Gold	1.15	0.9	0.93	1.08
Germanium	1.35	1.05	1.03	1.39
Bismuth	1.32	1.16	1.1	1.45

The general law expressed by Eq. (7.5) is experimentally very well verified. Figure 7.3 displays the melting temperature of gold nanoparticles as a function of the inverse particle diameter. The experimental results of Castro *et al.* [1] show two separated ranges. The range indicated with Castro *et al.* I, which follows exactly the inverse linear relationship of Eq. (7.5) and a second range, which is nearly
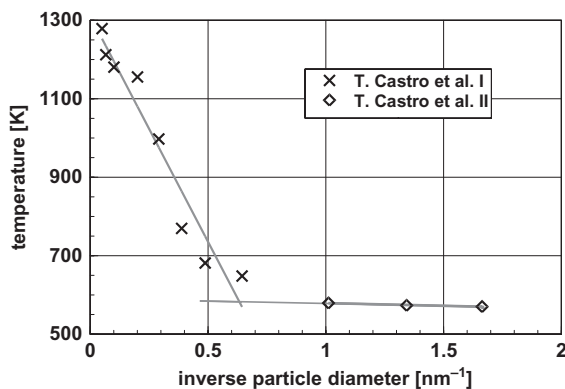
Figure 7.3 Melting temperature of gold nanoparticles plotted versus the inverse particle diameter from experimental results by Castro *et al*. [1]. It is important to realize that the linear relationship based on Eq. (7.5) breaks down at a particle size of ca. 1.6 nm (0.63 nm⁻¹).

particle-size independent (Castro *et al.* [1]) Extrapolating the latter values, one find a particle size around 1.6 nm (=0.63 nm⁻¹), where the inverse linear relation breaks down.

Such a break down of this simple relation is not only found at small particle sizes, but at larger ones, too. This is demonstrated using the example of lead, which is depicted in Figure 7.4. In this figure, the experimental data are plotted versus the particle diameter and, additionally, versus the inverse particle diameter. The latter plot is more interesting and gives additional information. One realizes a significant deviation from the inverse linear relationship in the case of particles larger than approximately 6.5 nm in diameter.

Calculations by Coombes [2] result in a surface layer of roughly 3 nm, where melting starts. Therefore, it is not surprising that the linear approximation fits up to an inverse particle diameter of approximately 0.145 nm⁻¹, corresponding to a particle diameter of roughly 6.5 nm. The core of the particles melts in a second step. In the case of smaller particles, this means that for particles with a radius smaller than this surface layer, the whole particle melts at once. This, and only this, range follows Eq. (7.5).

How to explain this behavior that does not follow elementary thermodynamic considerations? Based on theoretical considerations, using *Landau*'s parameter of ordering Chang and Johnson [3] showed that small nanoparticles do not have the same degree of ordering that is observed in bulk materials. *Landau*'s order para- mameter is defined in a way that, for a perfect crystal, it is one and for a liquid it is zero. Based on the results of Chang and Johnson [3] Figure 7.5a shows this parameter *M* for three particles of different size as a function of the radial position. Looking at the largest particle with a radius of 10 nm one sees perfect ordering in the center of the particle. The more it approaches the surface, the less ordering is observed. One sees a 3-nm layer with reduced ordering. This behavior is more

(a)

(b)
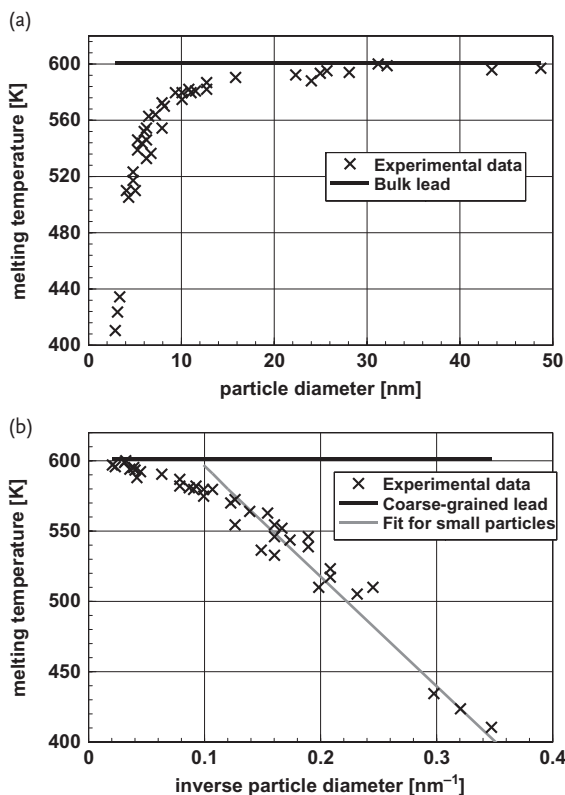
Figure 7.4 Melting of lead nanoparticles as a function of the particle diameter. The experimental data are according to Coombes [2]. (a) Experimental results of the melting point plotted versus particle diameter. (b) Experimental results as shown in Figure 7.4a, however, plotted versus the inverse particle diameter. It is important to realize the deviation of the inverse linear relationship at larger particle diameters (smaller inverse diameters). For small particle sizes, a linear fit is shown.

pronounced when the particle gets smaller. A particle with a radius of 5 nm shows a similar lack of ordering at the surface; however, in addition, one sees imperfect ordering in the center of the particle, too. This tendency is increased for a particle with a diameter of 4 nm. In this case, in the center, the order parameter is just a little more than 0.5; whereas this parameter is less than 0.25 at the surface. These calculations confirm the considerations and the experimental results of Coombes [2]. The relation of decreasing order with decreasing particle size and from the interior to the outside is even clearer in Figure 7.5b. In this figure the order parameter in the center and at the surface is plotted versus the particle size. Looking at the smallest particles, one has the impression that they are closer to a liquid than to a solid.

(a)

(b)
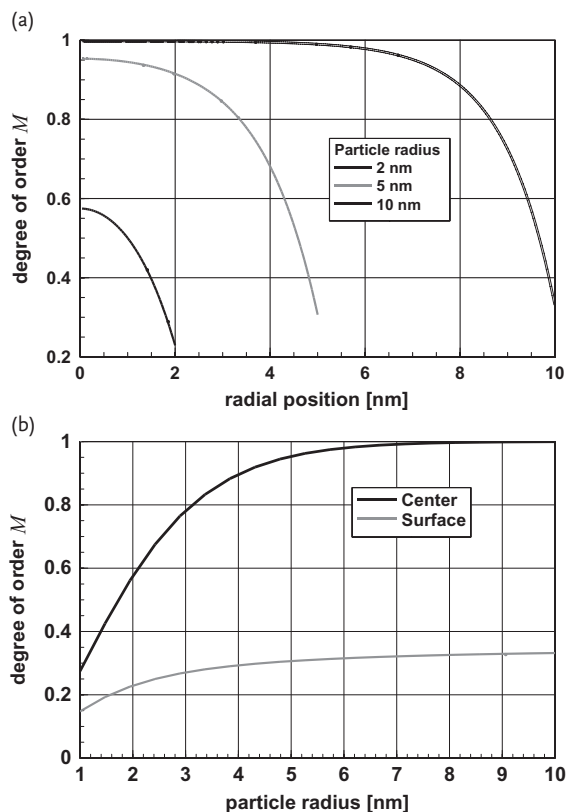
Figure 7.5 *Landau* order parameter *M* for nanoparticles of tin as a function of the radius and particle size [3]. This parameter is, as per the definition, one for perfect crystallized material and zero for a liquid. The degree of order decreases from the interior to the outside of the particles and with decreasing particle size (a). This steady decrease of order is also visible if one looks only at this parameter in the center and the surface (b) as a function of the particle radius.

Analyzing Figures 7.5 one realizes that materials, crystallizing well as bulk material, show, as nanoparticles, a reduced propensity to crystallize in a similarly perfect way. This phenomenon is observed, to some extent drastically, also with ceramic materials. As an example, maghemite, $\gamma\text{-Fe}_2\text{O}_3$, does not crystallize as particles smaller than approximately 3 nm. Such a limit also exists for alumina, Al_2O_3, where the crystallization limit is around 20 nm.

Not only the difference of the melting point, but also the total enthalpy of melting is inversely proportional to the particle size, as, in this case, one has to add to the enthalpy of melting caused by the change of entropy the difference of the surface energy in the solid and liquid state.

Box 7.3   Total Enthalpy of Melting of Nanoparticles

Defining the total energy of melting as the sum of the melting enthalpy and surface energy, the difference of the melting enthalpy of the bulk material and nanoparticles $\Delta U_{\text{trans-nano}}$ is based on Eq. (7.4), in a simplified way, given by:

$$\Delta U_{\text{trans-nano}} = \Delta U_{\text{trans}} + \gamma_{\text{new}} A_{\text{new}} - \gamma_{\text{old}} A_{\text{old}}$$

$$= \Delta U_{\text{trans}} - 6M \frac{\gamma_{\text{new}}}{\rho_{\text{new}}} \frac{1}{d_{\text{new}}} \left[1 - \left(\frac{\gamma_{\text{old}}}{\gamma_{\text{new}}} \right) \left(\frac{\rho_{\text{new}}}{\rho_{\text{old}}} \right)^{2/3} \right]. \tag{7.10}$$

This formula can be simplified as

$$\Delta U_{\text{trans-nano}} = \Delta U_{\text{trans}} - \kappa \frac{1}{d}, \tag{7.11}$$

showing the inverse proportionality of the enthalpy for transformation with particle size, where κ is a proportionality factor. This relationship is experimentally well proven.
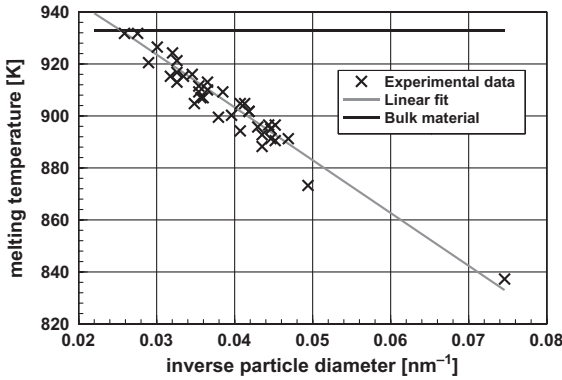
Figure 7.6 Melting temperature of nanoparticulate aluminum, produced by grinding, according to Eckert *et al.* [4]. Clearly, within the precision of the measurements, the melting temperature of these particles follows exactly the inverse proportionality of the melting temperature as a function of the particle diameter.

The inverse relationship of melting point and enthalpy of melting will be demonstrated, using aluminum as an example. Figure 7.6 shows the melting temperature of aluminum nanoparticles as a function of the particle size. To demonstrate the validity of *Thomson*'s equation again, the melting temperature is plotted versus the inverse particle diameter.

Analyzing Figure 7.6 in more detail, one realizes that the extrapolation of a linear fit of the melting temperatures of aluminum particles, produced by grinding, crosses at a particle size of ca. 45 nm the melting temperature of the bulk material.
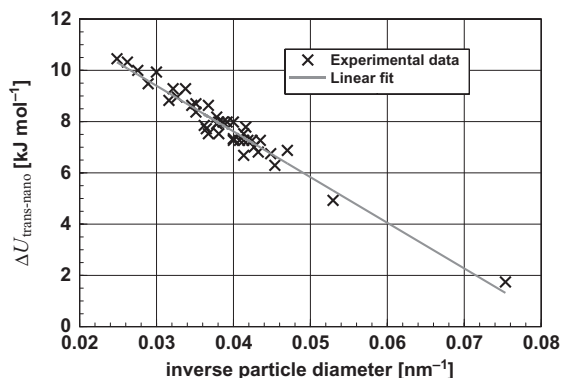
Figure 7.7 Enthalpy of melting of aluminum nanoparticles determined by calorimetric measurements [4]. These experimental data follow quite exactly the fit according to Eq. (7.11).

Eckert *et al.* [4] also made calorimetric measurements to determine the melting enthalpy of aluminum nanoparticles produced by grinding. These experimental results, together with a linear fit according to Eq. (7.11), are depicted in Figure 7.7. It is interesting to see that the experimental results are nearly perfect fitted with the inverse linear relation.

The fit for the experimentally determined values of the melting enthalpy depicted in Figure 7.7 may be extrapolated to large particles, i.e. bulk material. On doing this one finds a melting enthalpy for the bulk material of 14.7 kJ mol^{-1}. This value is significantly larger than the one listed for bulk material, which is given as 10.7 kJ mol^{-1}. This discrepancy may be explainable by storing of deformation energy in particles, as they were produced by grinding. This may, possibly, also explain the missing surface effect, as was demonstrated in the example of lead particles (See Figure 7.4.)

Equation (7.7) is very general in its validity, it may be applied to more fields of material science. A further problem, where extremely small particles, nanosized particles, play an essential role is nucleation. When the temperature of a melted material is reduced, crystallization starts. However, crystallization needs starting points, the nuclei. Replacing the surface energy in Eq. (7.7) by the interface energy solid–liquid, this equation describes the temperature of the formation of crystallization nuclei. Lastly, the *Thomson* equation describes in a simple way the necessity of supercooling of liquids for the formation of the first crystal nuclei (homogenous nucleation); the temperature of the melt has to be reduced to a level where the smallest nuclei are formed. Furthermore, the relationships as described above are valid for any phase transformation, for example, also for ceramic materials. As an example, the transformation monoclinic–tetragonal of zirconia, ZrO_2, as a function of particle size will be explained.

Bulk crystallized zirconia exists, depending on the temperature, in three different modifications. From room temperature, the monoclinic modification is stable up to 1450 K, followed by the tetragonal phase, which transforms around 2950 K into the cubic modification. With respect of technical applications, the tetragonal
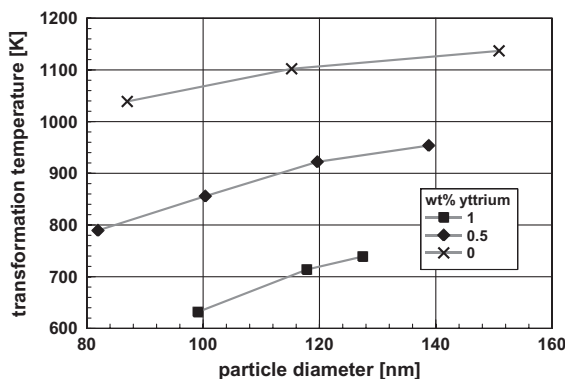
Figure 7.8 Temperature of the transformation monoclinic–tetragonal of zirconia as a function of grain size and yttria addition [6]. This figure makes it clear that a reduction of the grain size has a similar influence on the transformation temperature as yttria additions.
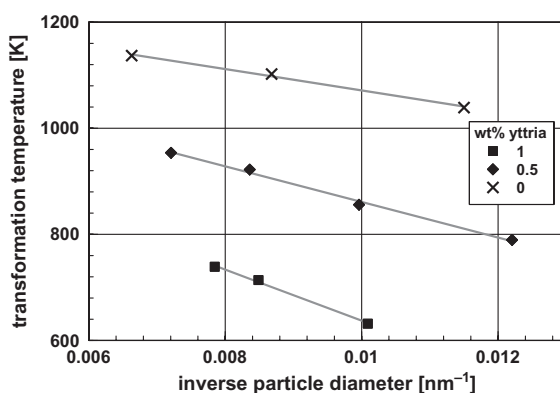

Figure 7.9 The monoclinic–tetragonal transformation of zirconia as a function of particle size and yttria content [6]. To demonstrate the validity of Eq. (7.7), as abscissa, the inverse diameter was selected.

phase is the most important one. This phase can be stabilized down to room temperature by adding a few weight percent yttria, Y_2O_3, or magnesia, MgO. Small grain sizes reduce the transformation temperature to the monoclinic phase. With this background, the behavior of nanocrystalline zirconia, with and without additions of yttria seems to be of special interest. Figure 7.8 displays the influence of small grain size and yttria addition on the temperature of the tetragonal–monoclinic transformation [6].

Even when the particle sizes were, in most cases, not smaller than 100 nm, a significant influence of the small grain size with respect to a reduction of the transformation temperature is readily visible. Certainly, one realizes, too, that the influence of a reduction of the grain size is, compared to the effect of yttria additions, minor. To check if such a solid-state transformation also follows *Thomson*'s equation Eq. (7.7) the experimental data are plotted versus the inverse particle size. This plot is given in Figure 7.9.

The graph in Figure 7.9 shows that, as theoretically expected, solid-state transformations also follow the simple considerations, which led to Eq. (7.7). However, this very general statement needs a caveat: The transformation tetragonal–monoclinic is, in the case of zirconia, a martensitic transformation, which means that the whole particle transforms within an extremely short time interval. The experimental proof would be significantly more difficult in the case of a diffusion-controlled transformation, which takes time.

7.3
Thermal Instabilities Connected to Phase Transformations

In the previous section, phase transformations of nanoparticles were treated in a particular way, as they would be, except for the surface energy, more or less identical to phase transformation in the world of macroscopic objects. The validity of this approach is, however, limited. It does not take note that nanosized objects are small. The thermal energy u of an object at a temperature T, independent of its size, is according to *Boltzmann*

$$u = kT. \tag{7.12}$$

The quantity k in Eq. (7.12) is the *Boltzmann* constant. (The denomination *Boltzmann* constant was introduced by *Max Plank*. Interestingly, *Ludwig Boltzmann* himself thought that it would be more or less impossible to determine the exact numerical value.) As the free enthalpy of phase transformation for one particle g is proportional to its mass, the energy needed, respectively, released at the phase transformation of one particle gets smaller when the mass of the particle is reduced. There it is possible that the thermal energy of a particle gets larger than the energy necessary for phase transformation. This leads to the limiting condition

$$\Delta g \leq kT, \tag{7.13}$$

where thermal instabilities are expected. Thermal instabilities lead to fluctuations, which are, in this context defined as: "*spontaneous transitions from an equilibrium phase to a nonequilibrium phase, followed by a back-transformation*" [5]. As the first question may be: Is this pure theory or is there experimental evidence supporting these considerations? Therefore, first some experimental findings, which are not explicable without the assumption of thermal fluctuations, are presented.

Iijima and Ichihashi [6] made a series of high-resolution electron micrographs of gold particles with 2 nm diameter. One of these series is presented in Figure 7.10.

The series of high-resolution electron micrographs presented in Figure 7.10 shows pictures of one individual particle, which were taken in time intervals of $\frac{1}{60}$ s at a temperature around 370 K. The short time that was available for one picture, explains the blurring by noise. (Normally, taking electron micrographs
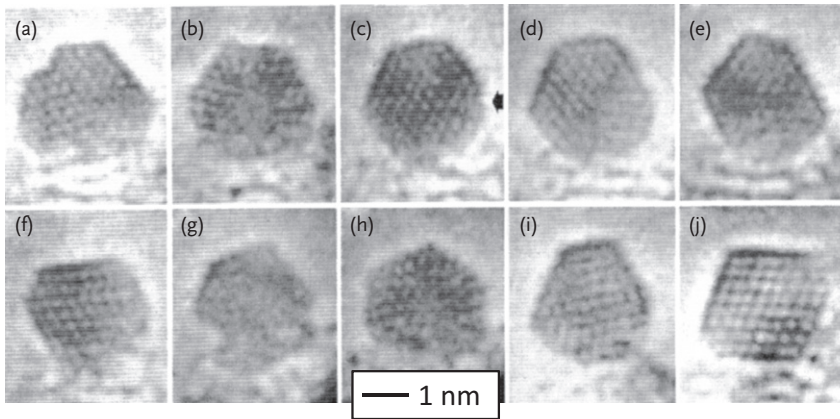
Figure 7.10 Time series of one gold particle taken at time intervals of $\frac{1}{60}$ seconds by Iijima and Ichihashi [6]. These micrographs, taken at a temperature around 370 K, show that the shape of this particle is not stable; it fluctuates spontaneously. The habit of this particle changes from single twins (a, d, and i) to multiply twinned icosahedral particles (b and h), and to cuboctahedral shapes (e, f, and i). The quality of these micrographs is certainly not "poor". The blurring by noise is caused by the short time interval between the micrographs. (Reproduction with permission by Sumio Iijima and the American Physical Society.)

with atomic resolution needs a minute or even more time for recording.) It is important to realize that the shape of the particle is different from picture to picture. It changes from single twins (a, d, and i) to multiply twinned icosahedral particles (b and h), and to cuboctahedral shapes (e, f, and i). The lattice fringes visible correspond to the (111) lattice plane; from this observation, one may realize that the particle did not rotate. The series of micrographs presented in Figure 7.10 suggests the assumption that the difference of energy in the different shapes is smaller than the thermal energy; the different shapes are energetically equivalent. The shape is no longer stable; it fluctuates.

Not only are the shapes unstable, the phases and the phase content are also unstable. Oshima and Takayanagi [7] observed that the phase might also be unstable. In electron micrographs of a liquid tin particle, they found crystallized ranges. A typical example is depicted in Figure 7.11. In this figure, a time series of electron micrographs of one particle is shown. The time difference between each one of the micrographs was again $\frac{1}{60}$ s. Within this particle with a diameter of ca. 6 nm, they found crystallized ranges of about 2 nm. However, these crystallized ranges appeared and disappeared. This phenomenon may be interpreted as the formation and redissolution of crystalline embryos or as a particle containing one embryo, which rotates in a way that the lattice fringes are visible or not. However, as it was possible to define clearly separated areas in the phase diagram where this phenomenon was observable, it is obvious that it has nothing to do with rotation of the embryo.
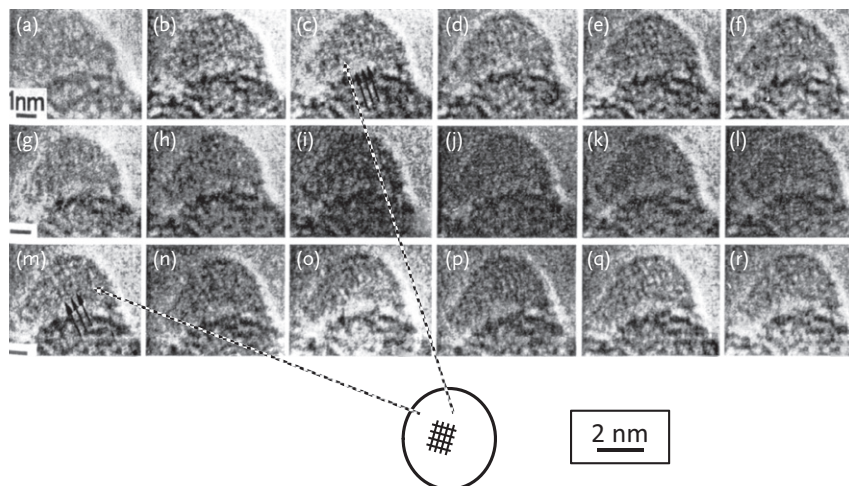
Figure 7.11 Time series of one liquid tin particle taken in time differences of $\frac{1}{60}$ s [7]. Within the particle, sometimes a tiny crystallized area of ca. 2 nm is visible. For two of these frames, an arrow indicates the position of these embryos. The authors denominate these particles as "pseudocrystalline". (Reproduced with permission by Springer.)

The authors give clearly separated ranges of temperature and particle size, where this phenomenon is observed. These ranges form a phase diagram, as is depicted in Figure 7.12.

The phase diagram depicted in Figure 7.12 shows a few essential features that are characteristic of small particles. Certainly, most important for the authors' viewpoint was the delimitation of the field, where the they found crystallized embryos within the melted droplets, the range was denominated "pseudocrystalline". Furthermore, they found a field where the crystallized particles steadily change their habit, called a "crystalline quasimelt". Lastly, this is the same phenomenon as earlier observed by Iijima and Ichihashi [6] (see Figure 7.10). Obviously, this is a very general phenomenon. It can be explained and calculated with good approximation by consequent application of classical thermodynamics, Ajayan and Marks [8]. These authors calculated the free enthalpy of gold particles as a function of particle size, shape, and temperature. Using gold as an example, these calculations led to the phase diagram that is depicted in Figure 7.13.

The phase diagram depicted in Figure 7.13 shows all the features expected for small particles in the vicinity of the melting temperature. Obviously, there is a field where the particles are liquid. After reducing the temperature or increasing the particle size, the next field is called the "quasimelt", where the crystallized particles perpetually change their habit, as may be seen in the series of electron micrographs in Figure 7.10. As the next step, one enters fields where specific shapes, such as decahedral or icosahedral, show maximal stability. However, there is also a range, where any habit is stable, denominated as "single crystal" in Figure
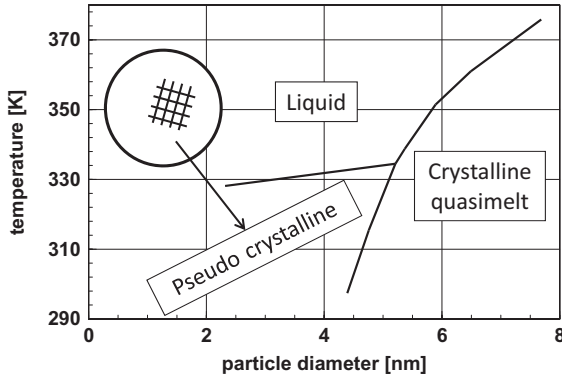
Figure 7.12 Phase diagram for tin particles as a function of the particle diameter according to Oshima and Takayanagi [7]. In this phase diagram, the different ranges are denominated. "Crystalline quasimelt" is the denomination for the range, where the habit of the solid particles is unstable. The field where the particles contain crystallized embryos within the melted droplets is denominated as "pseudo crystalline".
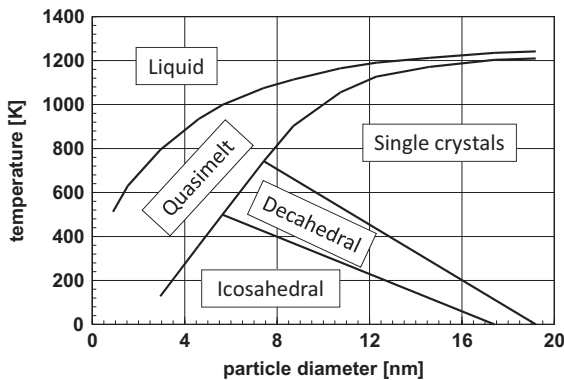
Figure 7.13 Phase diagram for gold nanoparticles calculated by Ajayan and Marks [8]. This diagram shows well-separated areas for the different phases. It is most important that there are ranges, where well-defined particle shapes are in equilibrium (decahedral or icosahedral), a range where any shape is possible (single crystal), the range quasimelt, where the particles perpetually change their habit, and certainly, the range where the particles are liquid.

7.13. Certainly, one must not forget that the calculations leading to Figure 7.13 are approximations, One realizes this looking at the limitation of the phase field "quasimelt", which approaches asymptotically, a behavior that is, as may be seen in Figure 7.12, not observed experimentally.

In Eq. 7.13, a condition for thermal instability of one particle is given. As in general, thermodynamic considerations must refer to one mol, this limiting condition expressed in mol is
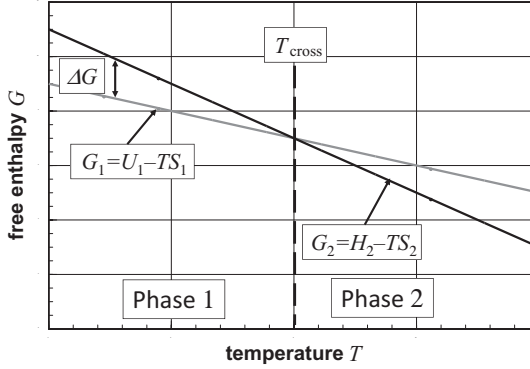
Figure 7.14 Free enthalpy of a phase transforming system in the vicinity of the transformation temperature. Additionally, the ranges where the phase 1 and phase 2 are stable, are indicated.
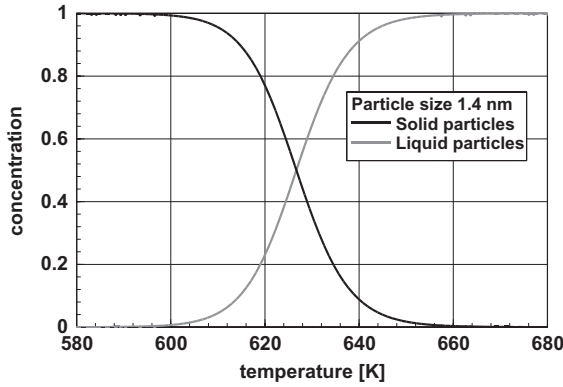
Figure 7.15 Concentration of 1.4-nm gold particles of an ensemble in the solid, respectively liquid, phase in an isothermal system. There is a broad range of temperature, where, to some extent, both phases coexist [5].

$$\Delta g = \frac{M}{N}\Delta G = \frac{M}{N}(G_1 - G_2) \le kT. \tag{7.14}$$

The quantity M stands for the molecular weight and n for the number of particles per mol. This relation is depicted in Figure 7.14. The temperature where $\Delta G = 0$ is valid is called the "crossing temperature". Looking at this figure one realizes that in the temperature range, where the difference of the free enthalpy is within the limits given by Eq. (7.14) phase transformation is possible. Certainly, the larger the distance to the crossing temperature, the smaller is the probability for transformation.

Figure 7.15 displays this fact, it shows the probability to find the particle transformed in the vicinity of the crossing temperature. At the crossing temperature,

the transformation temperature per se, the probability is 0.5, as the particle may be either in phase 1 or phase 2. Furthermore, an additional remark is necessary: Until now, the discussion was related to one particle. Do things change if there is instead of one particle an ensemble of many particles? Not at all! From statistical thermodynamics it is well known that the probability to find one particle in a certain phase or the concentration of particles belonging to an ensemble are equivalent (the ergodic theorem).

Box 7.4   Some Terms Used in Thermodynamics

In the following, a few often-used terms are explained in a simplified way:

Ensemble
An ensemble consists of many identical objects; generally, the number of these objects is known; however, this number may be infinite, too.

Isotherm
A process is isothermal if, for example, in the case of a phase transformation or whatever else happens, the temperature does not change. Lastly, one assumes that the process happens in a bath of infinite size and constant temperature.

Adiabatic
A process is adiabatic, if, for example, in the case of a phase transformation, there is no flow of energy; therefore, the temperature changes. This is the idea that there is an ideal thermal insulation around the objects (particles). Looking at adiabatic ensembles, for example, undergoing phase transformations, one has to distinguish two cases:

- *Local enclosure:* In this case each particle has an individual adiabatic enclosure [5].
- *Global enclosure:* The whole ensemble is in an adiabatic enclosure; therefore, heat exchange between the particles is possible [5].

Ergodic theorem
This is an important theorem in statistical physics, the "ergodic theorem", stemming from *Boltzmann* and *Gibbs*, saying, drastically simplified, that one may replace a time average by an ensemble average. This sounds complicated; however, it simplifies the considerations. Lastly, this theorem says that there is no difference in the result if one takes one particle and repeats an experiment say a thousand times or one takes a thousand particles, makes one experiment and measures the property of each one of these particles. Hence, one may interpret the experimental result either as the probability to find one particle in a certain phase or as concentration, which is the number fraction, of particles in this phase.
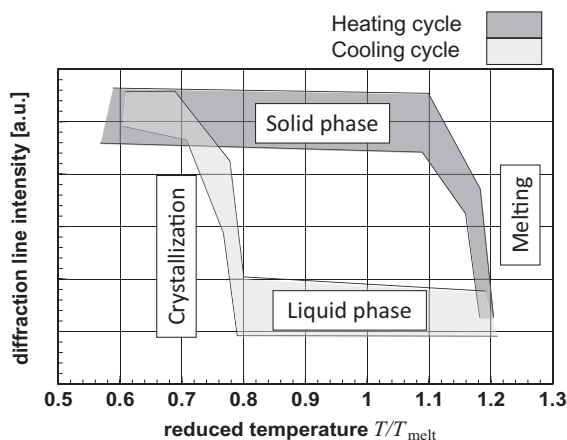
Figure 7.16 Melting and crystallization of germanium nanoparticles as function of the reduced temperature $\dfrac{T}{T_{melt}}$ related to the melting temperature of the bulk material. As the measurements show some scatter, the diffraction intensities, representing the concentration of the crystallized material are given as scattering bands and not as curves [9].

Assuming an ensemble of particles, Figure 7.15 shows that there is a temperature range, where the probability to find particles of both phases is not nil. This transition range widens with decreasing particle size; therefore, looking at bulk materials, this phenomenon is not observed, one finds a well-defined temperature of phase transition, for exmple, the melting point. This figure was calculated under the assumption of an isothermal system. Certainly, this is an idealization, which is not found in experimental reality, as least, because it takes time to transport heat to or from the particles to the surrounding bath of constant temperature. Therefore, one has to expect that all experiments are at least to some extent adiabatic. This has severe consequences. As an example, Figure 7.16 displays the concentration of the crystallized phase of germanium nanoparticles embedded in silica. The amount of crystallized material was determined by X-ray diffraction. Embedding the particles in a matrix has the advantage that any coagulation of the particles is thwarted.

From Figure 7.16 one learns that in the heating cycle the temperature of the phase transformation is higher as compared to the temperature in the cooling cycle. This is readily understood keeping in mind that for melting, additional energy must be transported to the transforming particles, vice versa; the same is valid in the cooling cycle, where heat has to be removed from the material. Theoretical analysis of adiabatic processes is challenging. A detailed analysis shows that one has to distinguish two different cases [5]:

- Each particle is in an adiabatic enclosure, the "*local case*". In this case, one assumes that each one of the particles has an ideal thermal insulation; there is no heat exchange between the particles.
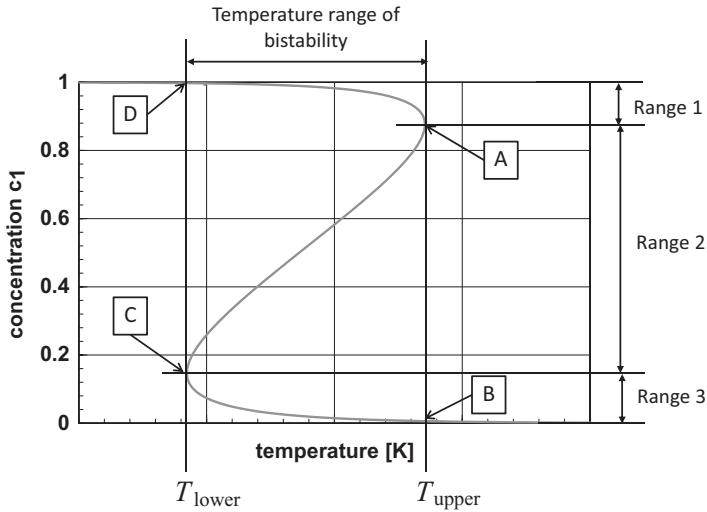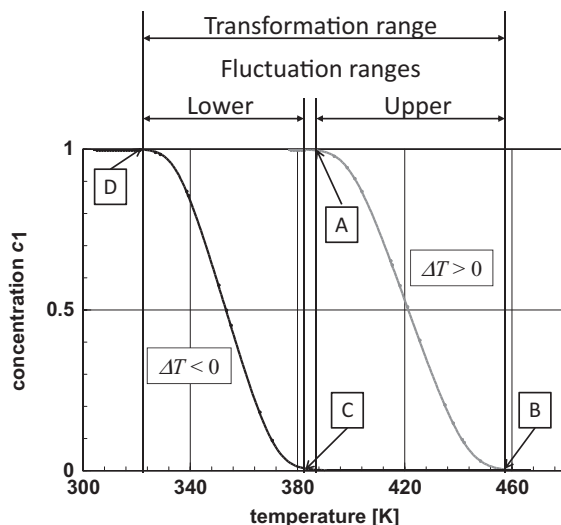
Figure 7.17 Course of the concentration of the low-temperature phase in the case of a "local enclosure" [5]. This behavior is called bistability. The ranges 1 and 3 are reached during the heating, respectively, cooling cycle. The range 2 is not accessible at all.

- The whole ensemble of the particles has a common thermal insulation against the surrounding world, "*global case*". Within the ensemble, the heat exchange between the particles is instantaneous.

Theoretically calculated graphs depicting the course of the concentration of the low-temperature phase as a function of the temperature (this is the average temperature of the ensemble, which could be measured experimentally) is shown in the following figures. Figure 7.17 displays the relations in the local case. In this graph, the course of the concentration of the low-temperature phase has the shape of a question mark. This means that there is a temperature range where for one temperature three different concentrations are possible. Experimentally, this is impossible. So, what will happen in the case of increasing temperature? When the temperature approaches the transformation temperature (as this is a random process, where the value nil is not existent, one can just give a temperature, where a measurable amount of material transforms), an onset of the transformation will be observed, until the point **A** is reached. As the temperature cannot go into reverse, the concentration jumps instantaneously from point A to point **B**. Now, the whole ensemble is transformed. Reducing the temperature, on the way back, in the vicinity of the transformation temperature, back-transformation starts until the point **C** is reached. Again, as the temperature cannot go into reverse, the concentration jumps to point **D**. Now, the back-transformation is completed.

In Figure 7.17, one realizes three concentration ranges: Range 1, which is accessed during a heating cycle, Range 3, accessible during the cooling cycle, and

Figure 7.18 Course of the concentration of the low-temperature phase in the case of "global enclosure" [5]. This behavior is called hysteresis. Fluctuation between the two phases are observed in-between the points **A** and **B**, in the case of heating, and the points **C** and **D** in the cooling cycle.

Range 2, which is not accessible at all. In the range in-between the vertical tangents, between the temperatures T_{lower} and T_{upper}, one finds different concentrations in the heating and cooling cycle. Such a behavior is called bistability. The behavior is entirely different in cases where the whole ensemble is adiabatically enclosed, the "global case". This is depicted in Figure 7.18. The behavior in the global case is thus different from the previous one, as one observes hysteresis and not bistability. Looking at a heating cycle, one observes in the vicinity of point **A** the onset of the transformation, which come to an end near the point **B**. In the cooling cycle, the transformation starts around point **C** and is more or less finished at point **D**. The cooling and the heating cycle show hysteresis. It is important to realize that there are separated temperature ranges for heating and cooling, the fluctuation ranges, where the main part if the transformation occurs.

In Figures 7.17 and 7.18 two "pure" cases of adiabatic behavior are demonstrated. In reality, these well-defined cases do not exist, experimentally, one will always find a mélange of isothermal and the different adiabatic systems. Comparing the figure, one may conclude that the experimental results depicted in Figure 7.16 stem from a predominantly adiabatic system, it comes close to the behavior in the local case. This is readily understood, as each one of the germanium particles is separately enclosed in a silica matrix.

7.4
Heat Capacity of Nanoparticles

The heat capacity C of a solid object is defined as the absorbed heat ΔE that is necessary to increase the temperature by ΔT.

$$C = \frac{\Delta E}{\Delta T}. \tag{7.15}$$

The numbers given in tables are either for 1 g (specific heat capacity) or 1 mol, (molar heat capacity). Analyzing the behavior of nanoparticles, often the heat capacity of one particle is taken as a reference. For gases, it is important to take care whether the heat capacity refers to constant pressure or constant volume; as, in case of solids, the thermal expansion are comparatively small, this difference is not significant.

The heat capacity of crystallized solids is well understood. It is the sum of the energy of lattice vibrations. As, in a crystallized solid, the atoms are in well-defined regular distances, only a limited number of vibrations, the phonons, is possible. Certainly, the longer the wavelength, the lower is the energy of the phonons, the more phonons are active, the higher is the heat capacity. Therefore, as nanoparticles are small, only a smaller number of phonons, as compared to bulk materials, is possible. Hence, one expects a reduced heat capacity. However, there is a second effect influencing the heat capacity: In a disordered system like a liquid, for the atoms there are more degrees of freedom to vibrate, as they are no longer fixed in a lattice. Therefore, one expects a higher heat capacity. The same, however, to a reduced extent is observed for amorphous material and, therefore, one may expect this for grain boundaries, too. As was shown in Chapter 3, in the case of small nanoparticles, a significant amount of the volume is on the grain boundaries, one has to expect a significant effect, superimposing or even exceeding the effect of smallness on the phonon-influenced part of the heat capacity.

Box 7.5   Heat Capacity of a Small Crystal

To elucidate the statement that the heat capacity caused by lattice vibrations of a small particle should be smaller than that of bulk material, the dependency of the possible number of phonons on the crystal size is estimated. To clarify the idea, a linear model of a crystal will be used, for further simplification, it is assumed that the ends of this crystal are fixed and the number of atoms is odd. Figure 7.19 displays this model crystal that consists of n atoms, each one at a distance of a, the lattice parameter. The size of this crystal l is given by $l = (n - 1)a$.

As stated in the boundary conditions, vibrations of such a chain have nodes at its ends. Furthermore, only those vibrations are possible that have nodes at
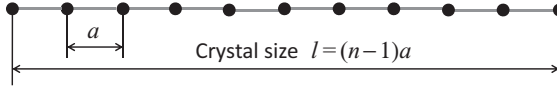
Figure 7.19 Linear crystal with the lattice constant *a*, consisting of *n* atoms as model for a nanoparticle to estimate heat capacity.

the position of a lattice point (atom); the vibrations are quantized. Therefore, only a limited number of vibrations is allowed. This is valid for transversal and longitudinal vibrations. Looking at the geometry of the system, it is obvious that the vibration with the longest wavelength is given by $\lambda_{max} = 2l = 2(n-1)a$ and the shortest possible wavelength is $\lambda_{min} = 2a$. The corresponding frequencies are: $\nu_{max} = \dfrac{c}{2a}$ and $\nu_{min} = \dfrac{c}{2(n-1)a}$. The quantity *c* is the speed of elastic waves in the material. Within a linear crystal with length *l*, vibrations with the following wavelength

$$\lambda = \frac{2(n-1)a}{1}, \frac{2(n-1)a}{2}, \frac{2(n-1)a}{3}, \dots \frac{2(n-1)a}{i}, \dots \frac{2(n-1)a}{(n-1)}, \quad (7.16a)$$

with the frequencies

$$\nu = \frac{c}{2(n-1)a}, \frac{2c}{2(n-1)a}, \frac{3c}{2(n-1)a}, \dots \frac{ic}{2(n-1)a}, \dots \frac{(n-1)c}{2(n-1)a} \quad (7.16b)$$

are possible. Having the frequencies, one can, using *Planck*'s formula for the energy *E* of a vibration $E = h\nu$, where *h* is *Planck*'s constant, calculate the thermal energy of a crystal, which is the sum of the energy of all vibrations

$$E = \sum_i n_i \nu_i h. \quad (7.17)$$

The numbers of vibrations n_i with the frequency ν_i, depending on the temperature, follows the *Bose–Einstein* statistics.

From the *Planck* relation it is obvious that the vibration with the lowest energy is the one with the longest wavelength. From Eq. (7.16) it is visible that the possible number of vibration modes, especially the number of modes with long wavelength, is reduced for small particles, it is obvious that the heat capacity based on lattice vibrations is also reduced.

Figure 7.20 displays the heat capacity of sintered nanocrystalline and bulk palladium. One sees that the values for the nanocrystalline material are significantly higher as compared to those of the bulk material. Obviously, the influence of the higher heat capacity of the grain boundaries overcompensates the reduction of the heat capacity caused by the reduction of vibration modes. In this context it is important to mention that nanocrystalline particles have an increased tendency to dissolve light elements, such as hydrogen. Because of their larger degrees of
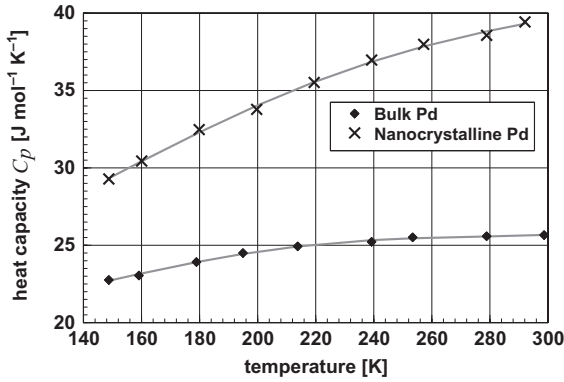
Figure 7.20 Comparison of the heat capacity of bulk and sintered nanocrystalline palladium [10]. It is important to realize that the heat capacity of the nanocrystalline material is larger as compared to the bulk material. In this graph, the heat capacity for constant pressure is plotted; however, for solids these values are practically identical with those for constant volume.
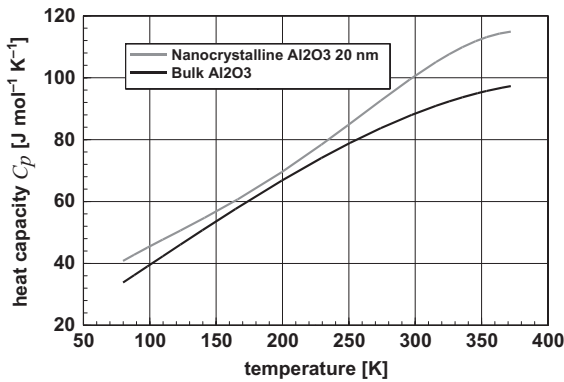
Figure 7.21 Heat capacity of bulk and sintered nanocrstalline alumina, Al_2O_3 with a grain size around 20 nm. In this example, comparable to the one depicted in Figure 7.20 for palladium, the heat capacity of the nanocrystalline material is higher than that of the bulk material [13].

freedom for vibration, these impurities contribute overproportional to the heat capacity. This was experimentally proven using the example of platinum [10].

The same arguments and phenomena as described for metals are valid for ceramic materials. As an example, Figure 7.21 displays the heat capacity for bulk and nanocrystalline alumina [11]. As the sintered nanocrystalline material had a grain size around 20 nm, it was, as the bulk material, in the hexagonal *a*-phase. The minor content of ca. 1% γ-phase in the nanocrystalline specimen is assumed to be negligible. The experimental results show increased heat capacity at low
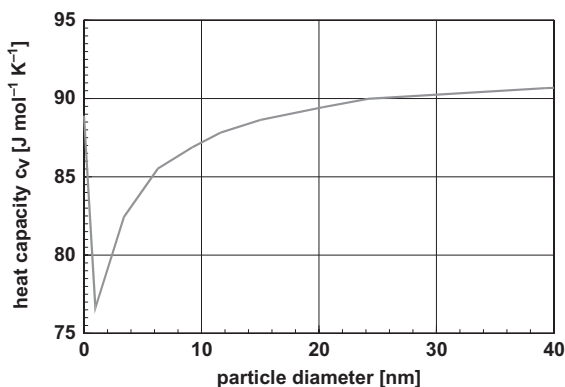
Figure 7.22 Calculated values for the heat capacity of indium oxide, In_2O_3 as function of the particle size [12]. As the reference temperature, a value of 298 K was selected. Please note the dramatic increase of the heat capacity at particle sizes below 1.2 nm.

temperatures and even more striking, at temperatures above 250 K, which is explained by increased freedom for vibration of the ions at the grain boundaries. This material had a reduced density of 89% (this density reduction is not due to porosity), which is explained by the reduced density of the material at grain boundaries.

Precise and very detailed theoretical calculations of heat capacity as a function of the particle size of indium oxide, In_2O_3 [12] led, as expected, to a decrease of heat capacity with decreasing particle size. Most importantly, however, is the deviation of this tendency at the smallest grain sizes. This increase at particle sizes below 1.5 nm is due to the fact that, at this particle size, the material consists of surface only. Surface is, as demonstrated for example, in Figures 7.4 and 7.5, highly disordered; and disordered material has, because of the increased number of possible vibration modes, higher heat capacity (Figure 7.22).

References

1 Castro, T., Reifenberger, R., Choi, E., and Andres, R.P. (1990) *Phys. Rev.*, **42**, 8548–8556.

2 Coombes, C.J. (1972) *J. Phys. F*, **2**, 441–448.

3 Chang, J., and Johnson, E. (2005) *Philos. Mag.*, **85**, 3617–3627.

4 Eckert, J., Holzer, J.C., Ahn, C.C., Fu, Z., and Johnson, W.L. (1993) *Nanostruct. Mater.*, **2**, 407–413.

5 Vollath, D., and Fischer, F.D. (2011) *Prog. Mater. Sci.*, **56**, 1030–1076.

6 Iijima, S., and Ichihashi, T. (1986) *Phys. Rev. Lett.*, **56**, 616–619, figure 1.

7 Oshima, Y., and Takayanagi, K. (1993) *Z. Phys. D*, **27**, 287–294.

8 Ajayan, P.M., and Marks, L.D. (1988) *Phys. Rev. Lett.*, **60**, 585–587.

9 Xu, Q., Sharp, D., Yuan, C.W., Yi, D.O., Liao, C.Y., Glaeser, A.M., Minor, A.M.,

Beeman, J.W., Ridgway, M.C., Kluth, P., Ager, J.W., III, Chrzan, D.C., and Haller, E.E. (2006) *Phys. Rev. Lett.*, **97**, 155701–1–4.

10 Rupp, J., and Birringer, R. (1987) *Phys. Rev.*, **36**, 7888–7890.

11 Wang, L., Tan, Z., Meng, S., Liang, D., and Li, G. (2001) *J. Nanopart. Res.*, **3**, 483–487.

12 Malinovskaya, T.D., and Sachkov, V.I. (2003) *Russ. Phys. J.*, **46**, 1280–1282.

8
Magnetic Nanomaterials, Superparamagnetism

8.1
Magnetic Materials

On putting any material into a magnetic field, one observes two, more or less distinct, reactions: the material is pulled into the magnetic field – paramagnetic behavior – or it is repelled from the magnetic field – diamagnetic behavior. Both reactions are connected to the electronic structure of the atoms, molecules, or solids. Any material is diamagnetic; however, in many cases, this diamagnetism is superimposed by paramagnetism, which is stronger; therefore, these materials belong to the group of the paramagnetic materials.

Diamagnetism is caused by the movement of the electrons around the atomic nucleus. According to *Faraday*'s law of magnetism (more specifically known as *Lenz*'s rule) the magnetic field caused by the circular motion of the electrons is oriented opposite to the external field. The electrons move not only around the nucleus, they also rotate around their axis. This spin of the electrons also causes a magnetic moment. In cases, where the electrons are paired, the spins are directed opposite. Therefore, in an atom with an even number of electrons, the magnetic moments of the spins compensate each other; these atoms are diamagnetic. All the other atoms are paramagnetic. The same rules are valid in the case of compounds. For the further discussion in connection to nanoparticles and nanomaterials, only paramagnetic materials in their different varieties are of importance.

Figure 8.1 displays the situation for a crystallized solid without an external magnetic field. This figure shows the cases where the orientation of the elementary dipoles are disordered, paramagnetism, and the one, with ordered magnetic dipoles, ferromagnetism. In ferromagnetic materials, the dipoles interact; a process leading to a long-range ordering, lining up the dipoles parallel, or in the case of antiferromagnetic materials, antiparallel. A ferromagnetic body, as depicted in Figure 8.1b, also shows in the absence of an external magnetic field a magnetic dipole moment. In the case of paramagnetic materials, an external magnetic field results in a partial ordering of the elementary dipoles, which, in detail, depends on the temperature and the strength of the external magnetic field. The scatter of the dipole orientation is due to the distribution of thermal energy among the individual atoms.

(a)   (b)
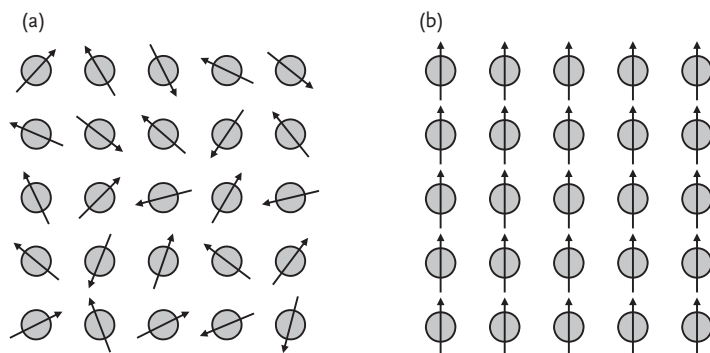
Figure 8.1 Distribution of the orientation of the elementary magnetic dipoles in a paramagnetic (a) and a ferromagnetic (b) material.

(a)   (b)
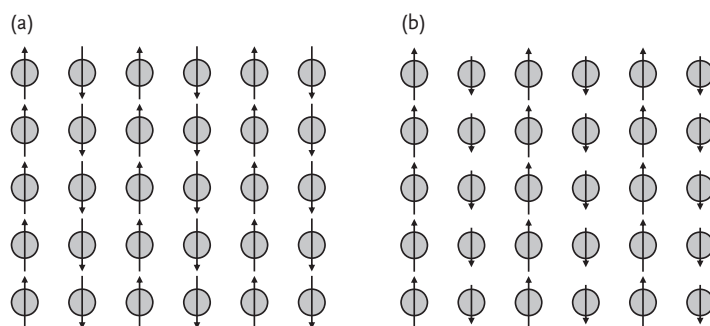
Figure 8.2 Antiferromagnetic crystals show antiparallel ordering of the elementary dipoles (a), which are arranged in two different sublattices. As the elementary dipoles compensate each other, such an object has no resulting magnetic moment. This is different for ferrimagnets (b), where the compensation of the spins is not complete; therefore, these materials have a resulting magnetic moment.

As mentioned above, magnetic ordering leads to parallel or antiparallel ordering of the elementary dipoles. Antiparallel ordering is observed in metals, for example, chromium and manganese, and many oxides. The overall magnetic moment of an antiferromagnetic material is nil (Figure 8.2a). In the case of many iron oxides and iron-based oxides one finds a special variety of antiferromagnetism, ferrimagnetism. In a ferrimagnetic material, the strength of the opposed dipole moments are not equal, there remains a residual magnetic moment. This situation is depicted in Figure 8.2b.

In view of nanoparticles, antiferromagnetic materials, especially the ferromagnetic variety, are of special importance. In antiferromagnetic compounds like MnO, FeO, α-Fe_2O_3, etc. an equal number of spins with antiparallel orientation is arranged in two different sublattices (Figure 8.2a). The magnetic moment of these

two sublattices cancels out. This is different in the case of ferrimagnetic compounds, where the magnetic moment of these two sublattices is different.

All ferrimagnetic oxides contain iron. They consist either of iron ions with different valency or besides the iron ions a second metal oxide. Typical examples are $Fe_3O_4 = Fe^{2+}O \cdot Fe_2^{3+}O_3$ for an iron compound or $MgFe_2O_4 = MgO \cdot Fe_2O_3$ as ternary iron compound. A special case in this context is maghemite, γ-Fe_2O_3. This compound is ferrimagnetic, because the second sublattice is partly occupied by vacancies. Therefore, the exact formula would be $(Fe_8^{3+}O_{12}) \cdot (Fe_{40/3}^{3+}\square_{8/3}O_{20})$, where $\square$ stands for vacancies replacing the second type of ions.

The temperature range where ferromagnetism and ferrimagnetism exist is limited. The temperature where ferromagnetic or ferromagnetic materials transform into paramagnetic material is called the *Curie* temperature. In the case of antiferromagnetic materials this temperature is the *Néel* temperature. Above these critical temperatures, the thermal energy destroys the magnetic coupling of the spins.

Looking at a ferromagnetic (which stands here and also later for ferrimagnetic) single crystal, for energetic reasons, one observes a subdivision into magnetic domains of different magnetic orientation. Depending on the material, the size of the domains is in the range of a few hundred nanometers up to a tenth of a millimeter. In-between the magnetic domains, one finds a quasicontinuous transition between the two orientation. The transition range, called a *Bloch* wall, usually has a thickness of a hundred or more atoms. This situation, where a *Bloch* wall connects two magnetic domains with opposite direction of magnetization is depicted in Figure 8.3. Besides this 180° *Bloch* wall, as depicted in Figure 8.3, 90° walls are also possible. (To simplify the figure, in the graph the *Bloch* wall consists of only three lattice planes, which is far from reality.)

Putting a ferromagnetic material into an external magnetic field, one measures the magnetization curve. An example of such a magnetization curve, labeled with
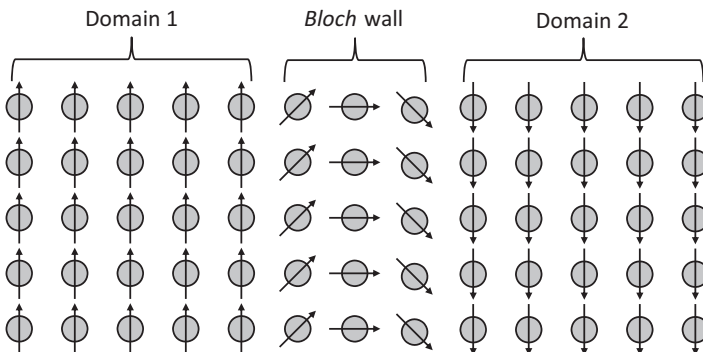
Figure 8.3 Two magnetic domains of a ferromagnet connected with a *Bloch* wall. The orientation difference of the domains is 180°. In this simplified illustration, the *Bloch* wall consists of three lattice planes.
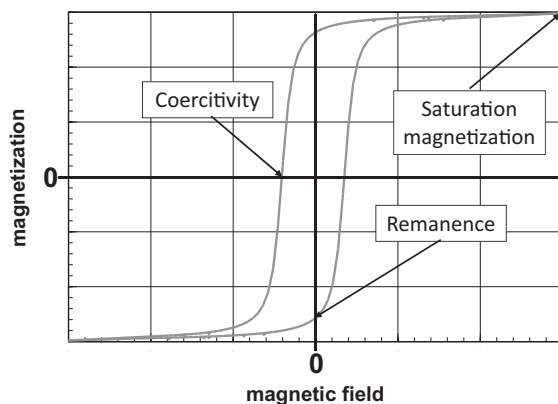
Figure 8.4 Magnetization curve of a polycrystalline ferromagnetic material. At high fields, the magnetization reaches "saturation magnetization". After reducing the field, a "remanence" remains. To set the magnetization of the specimen to zero, an opposite field, the "coercivity" is necessary.

the most important terms is depicted in Figure 8.4. This is the magnetization curve of a polycrystalline material or of an ensemble of many monocrystalline particles, as one obtains the same magnetization curve in the case of an ensemble of particles consisting of only one domain.

The characteristic parameters indicated in Figure 8.4 are: "saturation magnetization", the magnetization that is measured at high fields, the "remanence", the magnetization that remains after removing the external field, and the "coercivity", the field that is necessary to remove the magnetization of the specimen completely. The tendency of the specimen to remember the magnetic history is called the "hysteresis". The product coercivity times remanence is called "energy product", an important attribute to describe permanent (=hard) magnets.

On putting a polycrystalline specimen, where each grain consists of several domains separated by *Bloch* walls, into a magnetic field, the domains will be oriented into the direction of the magnetic field. This happens by movement of *Bloch* walls; the existence of *Bloch* walls makes it easier for the domains to change the direction of magnetization. On the other hand, assuming a specimen consisting of only one magnetic domain and, therefore, without *Bloch* walls. Following the preceding explanations, it is obvious that it is difficult to change the direction of magnetization of this particle. Consequently, this leads to a hypothetical magnetization curve as depicted in Figure 8.5.

The magnetization curve shown in Figure 8.5 is typical for a spatially fixed particle that consists of only one magnetic domain and, therefore, no *Bloch* walls. To change the direction of magnetization it is necessary to increase the external field up to a level where the magnetization of the whole particle is changed in one step. This magnetic characteristic is the intended one for particles applied in magnetic data storage. Based on the preceding considerations it is obvious that grain size has
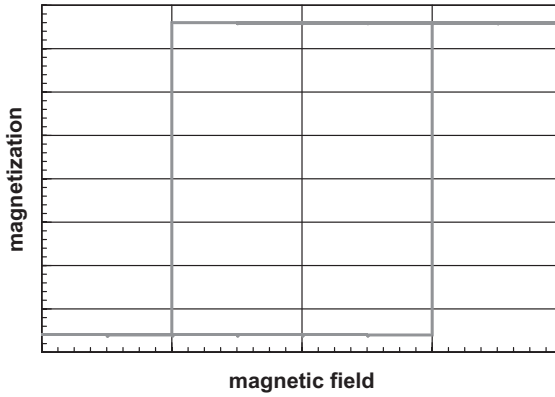
Figure 8.5 Hypothetical magnetization curve of a single one-domain particle. The magnetization remains constant until the external magnetic field is able to change the direction of the magnetization without a *Bloch* wall.
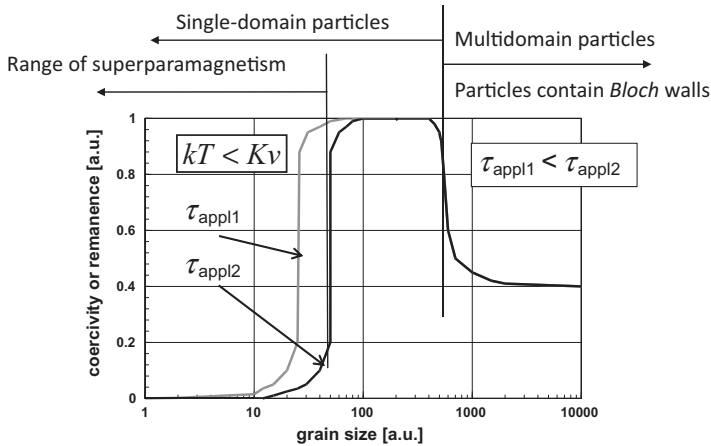
Figure 8.6 Dependency of the coercivity or remanence of the grain size. One realizes two important ranges: Multi- and single-domain particles; the latter may be subdived into a range with high coercivity and one with zero coercivity.

only a minor influence on the magnetization curve, as long as the grains are large enough to contain a few magnetic domains and *Bloch* walls. Therefore, one does not expect any dependency on the grain size. On the other hand, changing the direction of magnetization of one domain particles (see Figure 8.5) is, because of the missing *Bloch* walls, difficult. These considerations are correct. They lead, in connection with experimental results, to the diagram depicted in Figure 8.6. In this graph, coercivity or remanence are plotted versus particle size.

Analyzing Figure 8.6 in detail, one realizes different ranges of particle sizes. As explained above, as long as the particles are large enough to contain a few magnetic

domains, coercivity or remanence are independent of the particle size, as changing the direction of magnetization is eased by the movement of *Bloch* walls. Things are different once the particles do not contain *Bloch* walls. In this case, remanence and coercivity increase drastically. This is the range where magnetization curves look like the one in Figure 8.5. This is the range of magnetic properties, which are sought for magnetic data storage. Further reduction of the grain size leads to an unexpected sudden reduction of the coercivity to zero. This phenomenon is thus very special, as the particle size of this decrease depends on the time constant of determination. The property observed in the range where coercivity and remanence are nil is called superparamegnetism.

8.2
Fundamentals of Superparamagnetism

Superparamagnetism is a phenomenon based on thermal instability. Assuming a spherical magnetic particle, fixed against rotation, situated in an external magnetic field, allows superparamagnetism to be described. Furthermore, it is assumed that the magnetic axis of this particle is exactly in the direction of the external field. If the direction of the magnetic field is changed, the direction of the magnetization of the specimen will also change. However, one has to overcome the energy of magnetic anisotropy. In the case of superparamagnetism, thermal energy helps to change the direction of the magnetization. The energy of anisotropy is given by Kv, where the quantity K stands for the constant of magnetic anisotropy and v for the volume of the particle. This energy must be seen in relation to the thermal energy kT, where k stands for the *Boltzmann* constant and T for the temperature. If the condition

$$kT \geq Kv \tag{8.1}$$

is fulfilled, the thermal energy is larger than the energy of magnetic anisotropy. In this case, the direction of magnetization fluctuates thermally. This has the important consequence that the magnetization of the specimen may follow any change of an external magnetic field without needing extra energy. The direction of the magnetization may be changed without any losses! Certainly, superparamagnetism is possible only when the volume of the particles is very small. Superparamagnetism is found only in connection to very small particles, nanoparticles, generally, with sizes below 10 nm. From Eq. (8.1) one may derive for the temperatures where superparamagnetism occurs

$$T \geq \frac{Kv}{k}. \tag{8.2a}$$

The lowest temperature, where superparamagnetism is observed, the "blocking temperature" T_B is given by

$$T_B = \frac{Kv}{k}. \tag{8.2b}$$

The term "superparamagnetism" stems from the physical behavior of an ensemble of such particles in a magnetic field. As for paramagnetic materials superparamagnetic materials follow *Langevin*' formula for magnetization:

$$M = nm\left[\coth\left(\frac{mH}{kT}\right) - \frac{kT}{mH}\right] = nmL\left(\frac{mH}{kT}\right).$$

(8.3a)

In this equation, m stands for the magnetic moment of one particle, which is, to a first approximation, proportional to the volume of the particle, n the number of particles, and H the applied magnetic field. For paramagnetic materials, the magnetic moment of one atom or molecule is very small, in most cases it is just one *Bohr* magneton, μ_B. The abbreviation $L\left(\frac{mH}{kT}\right)$ is called the *Langevin* function. In the case of superparamagnetic materials, the magnetic moment of one particle is in the range of a few hundred, may be up to thousands of *Bohr* magnetons. The product nm stands for the saturation magnetization. Analyzing Eq. (8.3a) in detail, one realizes that is it possible to define a temperature compensated field $H^* = \frac{H}{T}$ (the term $\frac{m}{k}\frac{H}{T}$ is often called the "reduced field".). Using this temperature-compensated field, Eq. (8.3a) becomes

$$M = nm\left[\coth\left(\frac{m}{k}H^*\right) - \frac{k}{m}\frac{1}{H^*}\right].$$

(8.3b)

As a consequence of Eq. (8.3b), one can check the magnetization curve for superparamagnetism by plotting the data obtained at different temperatures versus H^*.

Box 8.1   Néel and Brownian Superparamagnetism

Both phenomena follow the *Langevin* formula, Eq. (8.3) and the magnetization curve does not show any hysteresis, even when they are in their physical background, entirely different. The *Brown*ian superparamagnetism is observed in the case of free magnetic particles suspended in a liquid. Immersed in a liquid, the particles are able to follow any change of direction of an external magnetic field by rotation. The relaxation time, τ_B, the time needed by the particle to follow a change in the direction of the magnetic field, is given by [1]

$$\tau_B = \frac{3v\eta}{kT}.$$

(8.4)

The quantity η stands for the viscosity of the liquid and v for the volume of the particle. The *Brown*ian superparamagnetism is often called extrinsic in contrast to *Néel*'s intrinsic superparamagnetism. In the *Néel* case, a spatially fixed particle is assumed. Therefore, if the external magnetic field changes its direction,

the direction of the magnetization of the particle has to be changed. The *Néel* relaxation time, τ_N is calculated using [1, 2]

$$\tau_N = \tau_0 \exp\left(\frac{Kv}{kT}\right). \tag{8.5}$$

The constant τ_0 is in the range between 10^{-13} and 10^{-9} s. For 10-nm particles, the *Brown*ian relaxation time is in the microseconds region; whereas, in *Néel*'s case, the relaxation time is one nanosecond or shorter. For magnetic particle with sizes around 1 μm, suspended in a liquid, the *Brown*ian relaxation times may be up to one second. At this particle size, *Néel*'s superparamagnetism is impossible.

Based on these considerations, in analogy to Figure 8.1a, one can draw a picture of a superparamagnetic ensemble, as is depicted in Figure 8.7a. To exhibit superparamagnetism, there is one additional prerequisite: The particle must not be connected by dipole–dipole interactions, because interacting particles behave like a large particle and superparamagnetism is no longer observable. However, there is one very special kind of interaction: In a superparamagnetic ensemble, the magnetic orientation of the particles is random. Provided the particles are equal in size, there is the possibility of self-organization and forming an ordered system of particles connected by dipole–dipole interactions. This is depicted in Figure 8.7b. This very special state was discovered by Morup [3], it is called superferromagnetism, as it shows all the characteristics of a ferromagnetic body, except for the fact that the magnetic elements are particles and not atoms.

(a)

(b)
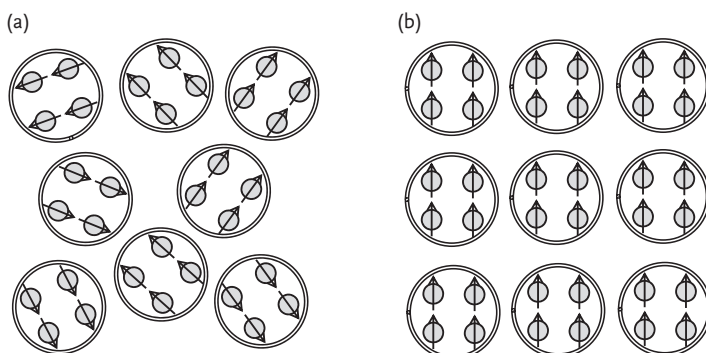
Figure 8.7 Model of superparamagnetic materials. In a superparamagnetic material, the individual magnetic particles are not interacting and their directions of magnetization are distributed randomly (a).

Morup and Christiansen [3] found that the particles may form a magnetically and geometrically ordered structure, called superferromagnetism.

Box 8.2 Constants of Magnetic Anisotropy

Magnetic anisotropy or, in this context more precise magnetocrystalline anisotropy, is an intrinsic property of any crystalline magnetic material, independent of particle size. It depends on the crystalline structure of the material and introduces a preferential direction of magnetization, the so-called "easy direction". This is the direction of spontaneous magnetization, provided the specimen is spherical. Additionally, there is a magnetically hard direction; to keep the vector of magnetization in this direction, additional energy is necessary.

In cubic materials, for any arbitrary direction, the energy of anisotropy can be calculated using three materials constants K_0, K_1, and K_2. The energy of anisotropy is calculated for any direction with the angle α_1 to the [100], α_2 to the [010], and α_3 to the [001] axis, by:

$$K = K_0 + K_1\left(\cos^2\alpha_1\cos^2\alpha_2 + \cos^2\alpha_2\cos^2\alpha_3 + \cos^2\alpha_1\cos^2\alpha_3\right)$$
$$+ K_2\cos^2\alpha_1\cos^2\alpha_2\cos^2\alpha_3. \tag{8.6}$$

K_1 is known for many magnetic substances; K_2 is known only for very few, K_0 is unknown for most materials. Table 8.1 gives values of K_1 for a few ferrites.

The constant of magnetic anisotropy K_1 may be positive or negative. The sign of K_1 determines the crystallographic orientation of the easy and hard direction of magnetization.

To present a demonstrative graph Figure 8.8 is restricted to a magnetization vector in the (100) plane of a cubic system. Therefore, the relations $a_3 = 90° \Rightarrow \cos^2 a_3 = 0$, and $a_2 = 90 - a_1 \Rightarrow \cos a_2 = \sin a_1$ are valid. This simplifies Eq. (8.4) to the relation

$$K = K_0 + K_1\left(\cos^2\alpha_1\sin^2\alpha_1\right), \tag{8.7}$$

which is valid for the energy of anisotropy in the (001) plane.

Table 8.1 Constants K_1 of magnetic anisotropy.

Ferrite	Constant of anisotropy [J m^{-3}]
Fe_3O_4	-11×10^3
$MnFe_2O_4$	-2.8×10^3
$CoFe_2O_4$	90×10^3
$NiFe_2O_4$	-6.2×10^3
$MgFe_2O_4$	-2.5×10^3

Figure 8.8 Dependency of the magnetic anisotropy constant on the direction in the (100) plane in a polar coordinate system. The calculations were performed for negative and positive values of K_1.
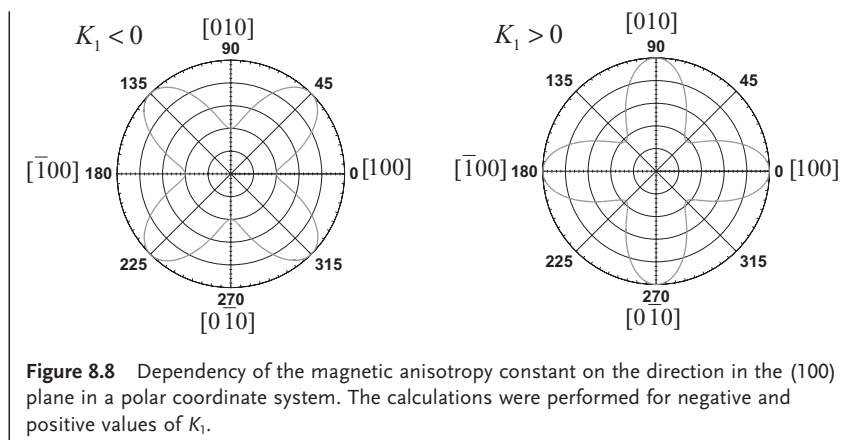
Figure 8.8 makes visible that for $K_1 < 0$ the easy direction is the direction of the edge of the cube, $\langle 100 \rangle$, whereas in the case of $K_1 > 0$ the easy direction is the direction of the diagonal, $\langle 100 \rangle$. It is obvious that changing the sign of K_1, rotates the easy and hard direction by $45°$. In hexagonal crystals, usually, the soft directions are in the hexagonal basal plane, whereas the magnetically hard direction is perpendicular to the basal plane.

To clarify the process of fluctuation of the direction of magnetization, Figure 8.9 depicts the energy of anisotropy for a cubic crystal for $K_1 > 0$ in *Cartesian* coordinates.
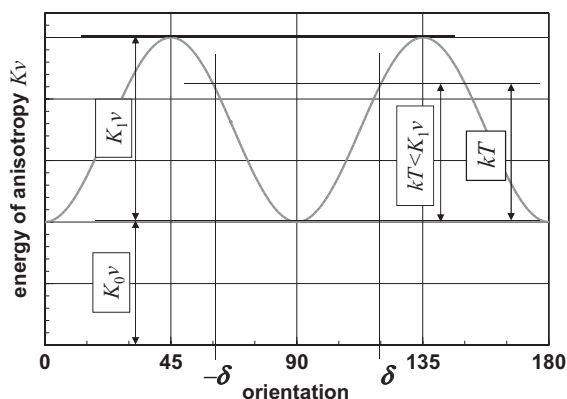
Figure 8.9 Energy of magnetic anisotropy as a function of the orientation in a *Cartesian* system of coordinates. Additionally, the different contributions to the energy of magnetic anisotropy and the thermal energy are indicated. At any temperature, the direction of magnetization fluctuates between the directions $-\delta$ and $+\delta$. When the temperature is high enough, and fulfills the condition $kT \geq K_1 v$, the magnetization can jump to the next stable directions at $0°$ and $180°$.
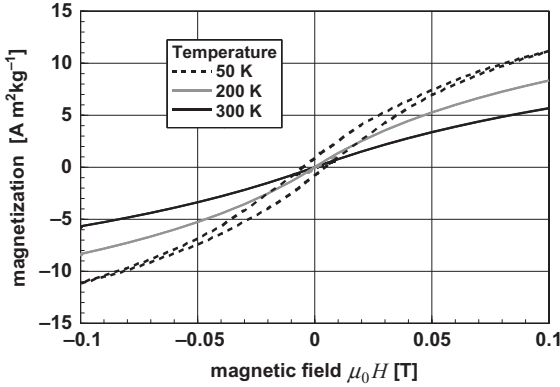
Figure 8.10 Magnetization curves of a superparamagnetic nanocomposite consisting of polymer-coated γ-Fe_2O_3 particles. At temperatures of 300 and 200 K there is no hysteresis visible; the material is superparamagnetic. At 50 K the magnetization curve clearly shows hysteresis, the temperature is below the blocking temperature; therefore, the material is no longer superparamagnetic.

Besides the two contributions to the energy of magnetic anisotropy, $K_0\nu$ and $K_1\nu$, the thermal energy kT is indicated. Without an external magnetic field, the direction of lowest energy for the magnetization is at 90°. At zero *Kelvin*, it will be found in this position. At any higher temperature, the direction will fluctuate between the angles $-\delta$ and $+\delta$. When the thermal energy kT exceeds $K_1\nu$ the vector of the magnetization is able to overcome the hard direction at 45° or 135° and jump into the next stable position at 0° or 180°. Now, the particle is superparamagnetic.

Superparamagnetism has severe influences on the magnetization curve. As the direction of the magnetization fluctuates thermally between the different magnetic orientations, there is no energy necessary to change the direction of the magnetization. The magnetization curve does not show any hysteresis. This behavior is shown in Figure 8.10. This figure displays the magnetization curves for a nanocomposite consisting of maghemite, γ-Fe_2O_3 particles coated with a polymer. This coating is necessary to keep the particles at a distance; otherwise, there would be a dipole–dipole coupling, which destroys superparamagnetism. In this graph, there are results obtained at three different temperatures, 50, 200, and 300 K. At 50 K the magnetization shows distinct hysteresis; at this temperature superparamagnetism is not observed. This is different at the two higher temperatures, where hysteresis is not observed.

Figure 8.10 shows, in addition to the possible observation of superparamagnetism one additional feature: The saturation magnetization gets smaller with increasing temperature. Analyzing the *Langevin* function, valid for superparamagnetic materials, given in Eq. (8.3a) one obtains as the limit for high temperatures (now neglecting the fact that ferromagnetism has a maximal temperature, the *Curie*-temperature)
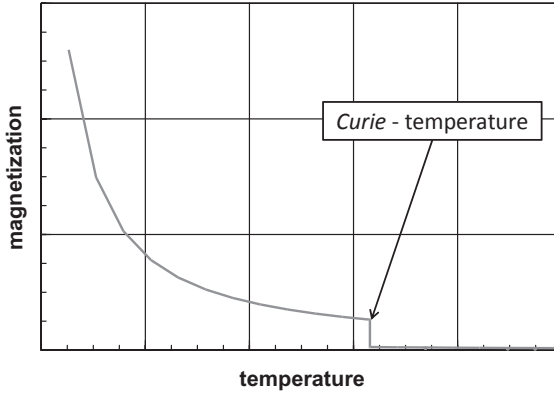
Figure 8.11 Dependency of the magnetization of a superparamagnetic ensemble as a function of the temperature. The magnetization decreases with increasing temperature continuously up to the *Curie* temperature, where the magnetization drops to the paramagnetic value.

$$M|_{T\to\infty} = \lim_{T\to\infty}\left[nmL\left(\frac{mH}{kT}\right)\right] = 0. \tag{8.8}$$

Figure 8.11 displays the temperature dependency of the magnetization of the temperature. One sees the steady decrease of the magnetization until the *Curie* temperature is reached. At this critical temperature the ferromagnetic coupling of the spins breaks up thermally, the material is just paramagnetic with its low value of magnetization.

The experimental result confirms this boundary value as correct. Diminishing small hysteresis is a necessary but not a sufficient prerequisite for superparamagnetism. A better indicator is a plot using the temperature-compensated field, which led to Eq. (8.3b). Such a graph is plotted in Figure 8.12.

In Figure 8.12, the experimental data measured at 200 and 300 K are on one curve. This indicates that the specimen was superparamagnetic in the temperature range of the experiment. However, the validity of this statement has to be restricted thus as it is valid only for the time constant of the measurements (for this type of measurement ca. 100 s) or longer times. Under these restrictions, one may say that, for this specimen, the blocking temperature is below 200 K.

Comparing the saturation magnetization in the range between 5 and 10 Am^2 kg^{-1} with values known from bulk material of γ-Fe$_2$O$_3$, lying around 75 Am^2 kg^{-1}, one wonders about these small values. This phenomenon is observed regularly. As an example, Figure 8.13 displays the saturation magnetization of manganese ferrite, MnFe$_2$O$_4$ nanoparticles as a function of the specific surface [4]. (For the specific surface, please see Chapter 12.) Certainly, it is difficult to understand why the magnetization in reduced with increasing surface of the material. However, the important point is: the specific surface is indirectly proportional to the particle
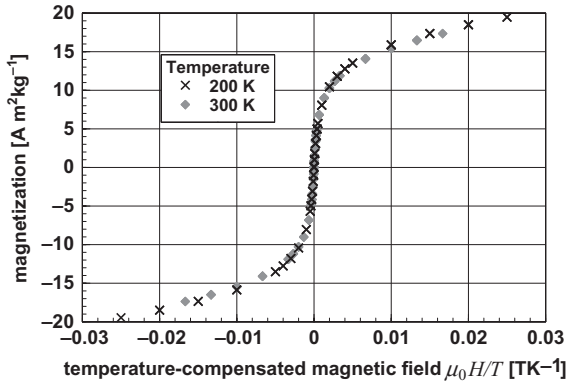
Figure 8.12 Magnetization curves of polymer-coated γ-Fe$_2$O$_3$ particles as depicted in Figure 8.10. However, in this graph the plots are versus the temperature-compensated magnetic field $H^* = \dfrac{H}{T}$. The experimental points obtained at the temperatures of 200 and 300 K fall, within the accuracy of the experiment, together. This is a clear indicator that the specimen was superparamagnetic with respect to the time constant of the measurements. Accepting the restriction with respect to the time constant, this is a very sensitive proof for superparamagnetism.
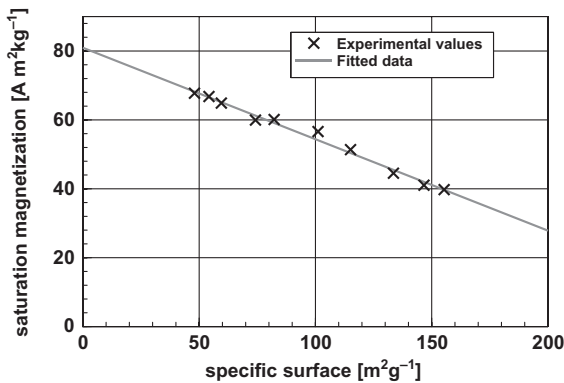
Figure 8.13 Saturation magnetization of manganese ferrite, MnFe$_2$O$_4$ nanoparticles as a function of the specific surface area of the specimen. One observes a linear decrease with increasing specific surface of the particles [4]. The range of ca. 50 to 150 m^2 g^{-1} is equivalent to a range of mean particle diameters from 7 to 25 nm.

diameter. Hence, one may conclude: the saturation magnetization gets smaller with decreasing particle size.

In Chapter 7, Figure 7.5, it was shown that the degree of order at the surface is significantly reduced as compared to the interior of a particle or even to an ideal crystal. As the type of ferromagnetism discussed in this chapter depends on a perfectly ordered crystal, it can be easily understood that the ranges of a particle

that are close to the surface, exhibit reduced saturation magnetization. In fact, this reduced order is observed experimentally and theoretically well understood. Simply stated, the spins at the surface of a magnetic nanoparticle are ordered not as perfect as in the interior [5]. This phenomenon is called spin canting. The surface/volume ratio of nanoparticles is a few orders of magnitude larger as compared to conventional materials; hence, the contribution of spin canting at the surface to the magnetization is of increasing importance with decreasing particle size. Therefore, one has to expect a significant reduction of the saturation magnetization with decreasing particle size.

As the reduction of the saturation magnetization of nanoparticles is a surface phenomenon, it is possible to approximate it by a two-zone model: an interior perfectly ordered ferromagnetic crystal and a nonmagnetic surface layer. Assuming magnetic nanoparticles with a diameter d and a nonmagnetic surface layer with the thickness δ, a ferromagnetic core with a diameter $(d - \delta)$ remains [6]. This allows a reduced saturation magnetization to be approximated

$$M_{\text{nanoparticle}} = \frac{(d - 2\delta)^3}{d^3} M_{\text{macroscopic}}.$$ (8.9)

The quantity $M_{\text{nanoparticle}}$ is the saturation magnetization of the specimen consisting of nanoparticles with the diameter d and $M_{\text{nanoparticle}}$ the saturation magnetization of perfect macroscopic particles. Figure 8.14 displays the dependency of the saturation magnetization as a function of the particle size according to Han *et al.* [7]. together with a fit based on Eq. (8.9).

Fitting the experimental data depicted in Figure 8.14 using Eq. (8.9) led for the thickness of the "nonmagnetic" surface layer to a value of 0.8 nm for γ-Fe$_2$O$_3$ and 1 nm for CoFe$_2$O$_4$. Performing the same fitting procedure for the data depicted in Figure 8.13 leads to a thickness of 0.7 nm for the surface layer. Taking all the uncertainties connected to experimental data, especially with respect to particle
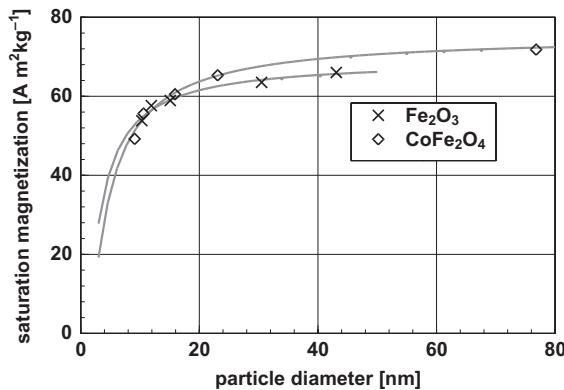
Figure 8.14 Saturation magnetization of γ-Fe$_2$O$_3$ and CoFe$_2$O$_4$ plotted versus particle diameter. The fitted curve was calculated using Eq. (8.9). The experimental data were taken from Han *et al.* [7].

sizes, into account, one may say that the thickness of the nonmagnetic surface layer is in the range of a little less than 1 nm. It is interesting to realize that the thickness of this surface layer is exactly one lattice constant. Looking at larger particles, say 100 nm, the influence of this thin surface layer is no longer measurable.

With respect to applications, the existence of this surface layer has severe consequences: for example, assuming a size of the magnetic particles of 5 nm, the 1-nm surface layer takes 80% of the particle volume, with the consequence that the saturation magnetization is reduced to 20% of the bulk value. This reduces the use of magnetic nanoparticles in applications demanding high magnetization.

Antiferromagnetism is possible because of a two antiparallel oriented, mutually compensating magnetic sublattices. For complete compensation of the magnetic moments of the two sublattices, perfect ordering is necessary. How do antiferromagnetic nanoparticles behave? Also in this case, one expects reduced order in the regions near to the surface. Reduced perfection of the magnetic sublattices means, for antiferromagnetic particles, incomplete compensation of the antiparallel spins. Therefore, a residual magnetic moment is anticipated. In fact, the experiments deliver exactly this result. Figure 8.15 shows magnetization of nanoparticulate chromia, Cr_2O_3 [8], an antiferromagnetic oxide, determined in the temperature range from 10 to 300 K.

The magnetization curves depicted in Figure 8.15 are thus interesting as they show in the temperature range between 40 and 300 K no hysteresis; at 10 K, minor hysteresis is visible, Furthermore, even up to a field of one *Tesla*, there is no indication of saturation. No hysteresis means that the direction of magnetization can be changed even less at very low temperatures. This is an advantage compared to ferromagnetic materials, as all of them exhibit significant hysteresis at low
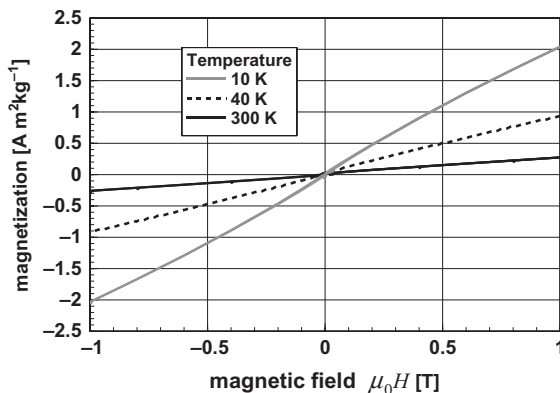
Figure 8.15 Magnetization curves of antiferromagnetic chromia, Cr_2O_3 at 10, 40, and 300 K. The measured magnetic moment is primarily due to incompletely compensated spins in the surface layer. Even at a temperature of 40 K this material does not exhibit hysteresis [8].

temperatures. Other antiferromagnetic compounds that are possibly of interest in this context are FeO and MnO.

8.3
Susceptibility of Superparamagnetic Materials

The susceptibility χ of a magnetic material is defined as $\chi = \left.\dfrac{\partial M}{\partial H}\right|_{H=0}$, the change of the magnetization with the external magnetic field. Generally, the susceptibility is given at low fields, in the vicinity of $H = 0$. Therefore, the magnetization, given by the *Langevin* formula, Eq. (8.3a), is developed in a *Taylor* series around $H = 0$, where the first element is used

$$M|_{H \to 0} = nm\left[\coth\left(\frac{mH}{kT}\right) - \frac{kT}{mH}\right]_{H \to 0} \approx nm\left[\frac{kT}{mH} + \frac{mH}{3kT} - \frac{kT}{mH}\right] = \frac{nm^2 H}{3kT}.$$

(8.10)

This leads for the susceptibility to

$$\chi = \left.\frac{\partial M}{\partial H}\right|_{H \to 0} = \frac{nm^2}{3kT} \propto \frac{nv^2}{kT} = \frac{vV_{\text{specimen}}}{kT}.$$

(8.11)

Equation (8.11) used the proportionality between the magnetization and the volume of a particle (more exactly stated: the magnetically active volume). At constant volume of the specimen $V_{\text{specimen}} = nv$, the susceptibility is larger if the volume of the specimen is larger. Lastly, this says: if one wants to obtain material with high susceptibility, one has to look for the largest possible particles.

There is a second property that must be taken into account; this is the relaxation time, which determines the maximal frequency for application. As shown in Eq. (8.5) the relaxation time τ_N for Néel superparamanetism, τ_0 is set constant [1], an assumption simplifying the considerations and not impairing the general tendency. To obtain more precise quantitative results, the refined theory of Aharoni [2] should be applied.

$$\tau_N = \tau_0 \exp\left(\frac{K_1 v}{kT}\right).$$

(8.12)

From Eq. (8.12), one learns that the relaxation time increases exponentially with increasing particle volume, which means with increasing particle size. In view of the technical applications, selecting an appropriate particle size, one has to make a compromise between high susceptibility, demanding large particles, and short relaxation time, which is necessary for high-frequency applications, demanding small particles. Certainly, with respect to the relaxation time, the magnetic anisotropy constant of the selected material is a further degree of freedom in design.

Typical values for the susceptibility as function of frequency. of different nanoparticulate ferrites are, in comparison with data for conventional ferrites, depicted in Figure 8.16.
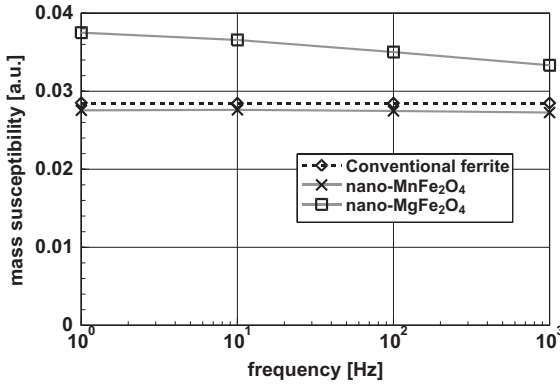
Figure 8.16 Magnetic susceptibility of two polymer-coated nanoparticulate ferrites compared with one conventional commercial ferrite. For the nanoscaled material, the weight of the necessary coating is included in the mass evaluation. In contrast to the behavior of the conventional ferrite, the susceptibility of the nanoscaled ferrites decreases slightly with increasing frequency.

In Figure 8.16, one sees that the susceptibility for both types of ferrites is of the same order of magnitude; however, one peculiarity is immediately visible: Whereas, in the observed frequency range, the susceptibility is constant for conventional ferrites, it decreases for the nanoferrites with increasing frequency. The reason for this reduced susceptibility is quite complex, there are a few phenomena acting in this direction. To reduce dipole–dipole interactions of the nanoparticles, coating is necessary. However, this is a reduction of the interaction and not an elimination, as this would need too thick a coating, which impairs the volume filling with ferrite nanoparticles. The influence of this interaction increases with increasing frequency. Furthermore, the particles, necessarily, have an energy distribution. Those particles on the low-energy side of the *Boltzmann* distribution (which is equivalent to a lower temperature) have, according to Eq. (8.12) a longer relaxation time; therefore, they are unable to follow the change in the direction of the external field.

8.4
Superparamagnetic Particles in the *Mößbauer* Spectrum

In case of *Néel* superparamagnetism, the dependency of the relaxation time of superpamagnetic particles on particle size and temperature was discussed in the previous sections. For processes with a time constant larger than the relaxation time, the particles are superparamagnetic, for faster processes, the particles are ferromagnetic. To some extent, this situation is unsatisfying, as it gives no clear-cut definition. Therefore, one has to search for the fastest method to decide
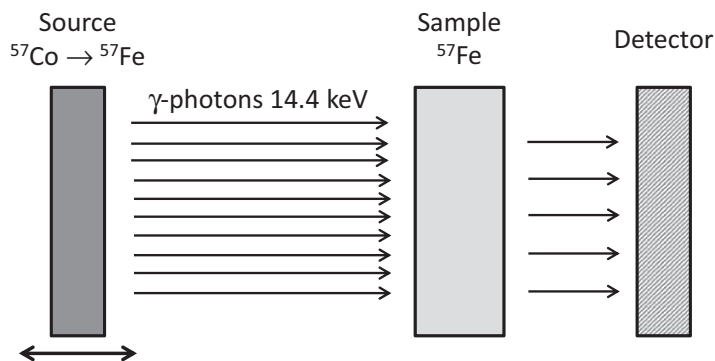
Figure 8.17 Basic design of a *Mößbauer* experiment to determine the absorption spectrum of an iron-containing specimen. The source is vibrating with different velocities. It emits γ-photons with an energy of 14.4 keV. The sample and detector are fixed.

if a material is superparamagnetic. This method was found to be the *Mößbauer* effect of ^{57}Fe.

The *Mößbauer* effect applies the resonant absorption of γ-quanta in the iron nucleus. Using this effect, one measures the influence of the chemical bonding and external magnetic fields on the energy levels of a nucleus. In its elementary form a *Mößbauer* experiment uses the decay of ^{57}Co that leads to ^{57}Fe in an exited state, which emits, besides others, a γ-photon with energy of 14.4 keV. The natural line width of this emission is 10^{-8} eV. The emitter and the absorber are fixed in a solid; therefore, the photons do not lose energy by recoil phenomena, as would be observed, for example, in a gas. (In a gas, the energy of the emitted quanta would be altered by ca. 10^{-3} eV.) Figure 8.17 displays the basic principle of such an experimental device to measure the *Mößbauer* effect in absorption.

In its basic design, an experimental *Mößbauer* device consists of an emitter vibrating with different velocities. The emitter is moved with a speed of a few millimeters per second. By moving the emitter, the energy of the emitted photons is altered (*Doppler* effect), so resonance absorption of the specimen will be possible. This experimental procedure allows extremely small differences of energy to be measured.

Box 8.3   Background of Mößbauer Spectrometry

To understand the results of *Mößbauer* experiments, it is necessary to analyze the energy levels of an excited ^{57}Fe nucleus. They are shown in Figure 8.18.

The excited ^{57}Fe shows quadrupole splitting caused by the electrical quadrupole field of the nucleus. The energy splitting of the level is proportional to the product of the gradient of the electrical field *V* and the electrical charge of the nucleus *Q*. This leads in the excited state to two energy levels. In an external
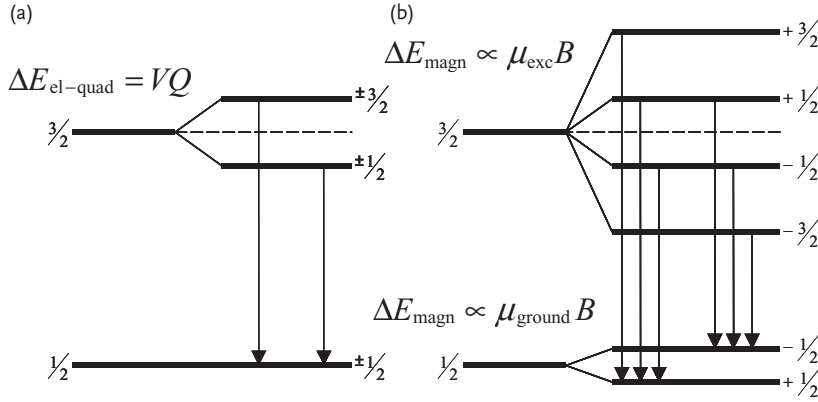
Figure 8.18 Energy levels in a ^{57}Fe nucleus with and without a magnetic field. In the excited state, the energy levels without an external magnetic field show electric quadrupole splitting. (a) According to the selection rules for radiative transitions, two emission lines are possible. In an external magnetic field, the quadrupole levels are split additionally (spin-up and spin-down). In this configuration, six transitions are allowed. (b).

magnetic field, these levels are split additionally, because of the two possible orientations of the spin (spin-up and spin-down). The energy splitting of these levels is proportional to the product of the magnetic moment of the nucleus in the excited, μ_{exc} respectively, ground state, μ_{ground} and the magnetic field B, in the case of crystalline materials, this is the magnetic crystal field Therefore, one observes in the ground state two and in the excited state four energy levels. In Figure 8.18, at the right side of each energy level, the magnetic quantum number M (careful—in this case, as is common in the literature, M is **not** the magnetic moment but the magnetic quantum number!) is indicated. The quantum-mechanical selection rules for radiative transitions allows transitions with a difference ΔM of the quantum numbers

$$\Delta M \in \{-1, 0, 1\}. \tag{8.13}$$

Equation (8.13) allows two transitions without a magnetic field and six transitions in the presence of an external magnetic field. The allowed transitions are indicated in Figure 8.18. (For example: The quantum number in the excited state $+\frac{3}{2}$ has an allowed transition to the ground state $+\frac{1}{2}$, the transition to $-\frac{1}{2}$ is forbidden.) This selection rule allows two lines, a doublet, for nonmagnetic specimens and six lines, a sextet, for magnetic materials. The width of the splitting of the absorption lines allows the surrounding magnetic field, which is, in the case of magnetic materials, the magnetic crystal field to be calculated.
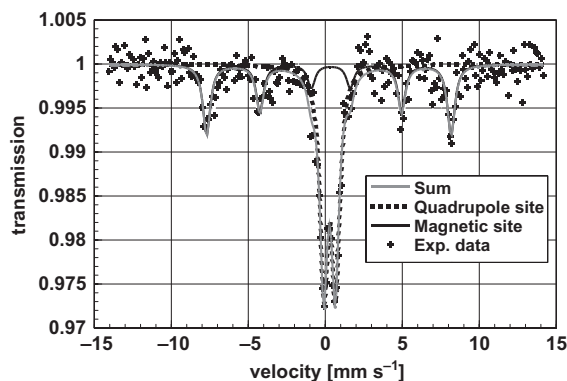
Figure 8.19 *Mößbauer* spectrum measured at 300 K on a specimen consisting of ferrimagnetic and superparamagnetic particles of γ-Fe$_2$O$_3$. One sees the doublet stemming from the quadrupole splitting and a sextet stemming from the magnetic splitting. Additionally, the experimental points, indicating some scatter, are plotted.

A *Mößbauer* spectrum shows either a doublet or a sextet of emission lines. (The following explanation is a narrative image of a quite elaborate quantum-mechanical theory; even when it is, in the sense of quantum mechanics incorrect, it gives some insights to the processes.) The doublet is observed where there is no external magnetic field acting on the iron nucleus. The doublet structure is caused by the splitting of the energy levels into two levels in the gradient of the electrical field (a quadrupole field) of the nucleus. An external magnetic field leads to a further splitting of the energy levels of the ground and the excited state. In the case of an additional external magnetic field, a sextet of emission lines is observed. The number of emission lines is limited by the selection rules of quantum mechanics. This explanation makes it clear that a magnetic material should be characterized by a sextet in the *Mößbauer* spectrum.

Figure 8.19 displays a *Mößbauer* spectrum determined at 300 K on a specimen, which contained a mixture of ferromagnetic and superparamagnetic particles. The spectrum shows a doublet and a sextet of absorption lines. How to explain the doublet, which is characteristic of an absent magnetic field, in other words, for nonmagnetic materials?

To understand the appearance of the quadrupole doublet in Figure 8.19, one has to look a little deeper into the atoms. The nucleus of an atom is rotating; in an external magnetic field it does an additional precession movement – the *Larmor* precession, the number of these revolutions per second is called *Larmor* frequency. The *Larmor* frequency is in the range of 10^9 Hz. Now, one has two independent movements different from each other: Thermal fluctuations of the direction of the magnetization of the particle and the rotation of the nucleus. For the formation of the *Mößbauer* spectrum it is important to know that the magnetic field that leads to the magnetic splitting of the energy levels is the mean value, which is seen by the nucleus during one revolution. Now, one can distinguish two extreme cases:
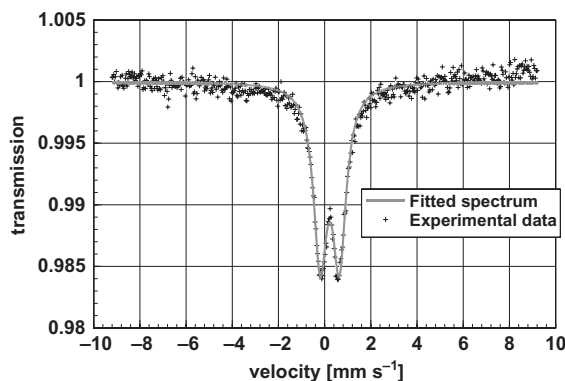
Figure 8.20 *Mößbauer* spectrum of $MnFe_2O_4$ using a polymer as distance holder determined at 300 K. This spectrum shows the doublet stemming from the electric quadrupole splitting. The specimen was perfectly superparamagnetic.

The fluctuation frequency of the magnetization is lower than the *Larmor* frequency. This is the standard case, the average magnetic field at the nucleus is equal to the external field, as a consequence a sextet is observed. The other extreme case is found in the situation where the frequency of the thermal fluctuation is higher than the *Larmor* frequency. In this case, the average magnetic field, felt by the nucleus during one revolution, is nil. Therefore, one observes the doublet stemming from quadrupole splitting. In Figure 8.20 the *Mößbauer* spectrum of a nearly ideal superparamagnetic ferrite, in this case $MnFe_2O_4$ measured at 300 K, is presented.

Figure 8.20 does not show any sign of the sextet. This allows the conclusion to be drawn that this material is superparamagnetic with relaxation time of the thermal fluctuations of the magnetization of less than 10^{-9} s. Lastly, the examples given in Figures 8.19 and 8.20 show that a *Mößbauer* experiment is the ultimate proof for *Néel* superparamagnetis. (The *Brown*ian superparamagnetism does not influence the *Mößbauer* spectrum, as its relaxation time is by far too long.) From Figure 8.19, where the doublet and the sextet occur, one can conclude that, in this example, the specimen had a relatively broad particle-size distribution; so some of the particles were superparamagnetic and others not. Nowadays, a material is called superparamagnetic if there is only the doublet visible in the *Mößbauer* spectrum.

From the viewpoint of solid-state physics, analyzing a *Mößbauer* spectrum may give a lot of information. From the splitting of the energy levels, which is proportional to the magnetic field, one can calculate the magnetic crystal field and connected to this, an exact value of the blocking temperature. Figure 8.21 displays such an example. This figure displays the magnetic crystal field of ferrite, γ-Fe_2O_3 particles as a function of the temperature. At low temperature, in this case 4 K, a magnetic field of 50 T was calculated. With increasing temperature, a decrease of this field was calculated. At a temperature of 80 K a value of 0 T was found.
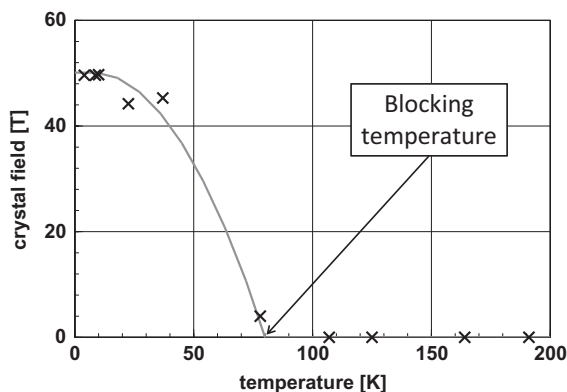
Figure 8.21 Magnetic crystal field of a γ-Fe$_2$O$_3$ specimen. The particles were coated with zirconia, ZrO$_2$, as a distance holder. The magnetic crystal field was calculated from the splitting of the energy levels represented by the sextet in the *Mößbauer* spectrum A crystal field zero characterizes superparamagnetic material.

However, these values must be interpreted with extreme care. Yes, the value at the lowest temperature is correct; this is the magnetic crystal field. At higher temperatures, due to the thermal fluctuations of the magnetization vector, the average value of the magnetic field that the nucleus "feels" during one revolution gets smaller. At the blocking temperature, this average field is nil; therefore, above 80 K, this material is superparamagnetic. Now, the *Mößbauer* spectrum shows only the doublet.

The definition of the blocking temperature given above is applicable for specimens with narrow particle-size distributions. In all other cases, one defines the temperature, where half of the material is superparamagnetic as blocking temperature.

On putting a superparamagnetic specimen into an external magnetic field, a certain part of the magnetic moments of the particles becomes aligned in the direction of the field. Increasing the external field up to a value where saturation is observed, the *Mößbauer* spectrum no longer shows the doublet but the sextet, as thermal fluctuations are thwarted.

8.5
Applications of Superparamagnetic Materials

The best chances for economically successful applications are found in the utilization of particulate composites and ferrofluids. The properties making the application of superparamagnetic nanocomposites attractive are the avoidance of the formation of magnetic clusters, the relatively high magnetic moment per particle (as compared to a paramagnetic molecule), and the possibility to manipulate these particles with an external magnetic field.

Applications in medicine and biotechnology are, from the standpoint of economy, the most successful ones. As already mentioned in Chapter 6 on nanofluids, the application as a means to improve the contrast in magnetic resonance tomography (MRT) (also called nuclear magnetic resonance imaging, NMR or MRI) [9] is very successful; suspensions of superparamagnetic particles replace, to some extent, gadolinium salts, which are now in use. The application of particles has an additional advantage, as it allows functionalization of the surface with proteins or enzymes, which are characteristic of a specific organ or tumor. The contrast improvement by superparamagnetic nanoparticles is based on the local change of the magnetic susceptibility caused by local differences of the concentration of these particles, which, locally, changes the magnetic field. This changes the nuclear spin resonance frequency, which is used as a signal for imaging. In particular, magnetic particles functionalized to attach locally, promise many advantages. For application, the superparamagnetic particles are suspended in a suitable, water-based liquid. The patient gets this suspension injected with a syringe. Figure 8.22 shows a comparison between an MRT image taken without contrast enhancement and one taken with a superparamagnetic fluid for contrast enhancement.

A further example is directed to biotechnology. Often, there is the necessity to separate cells from other objects in a suspension. This is a very time-consuming and expensive task as, conventionally; it is done by hand under observation in a microscope. The idea is to use magnetic particles, which are functionalized to attach exactly on the type of cells in question. To do this, a suspension of these functionalized superparamagnetic particles is added to the suspension containing the cells. It is intended that the cells with the attached magnetic particles
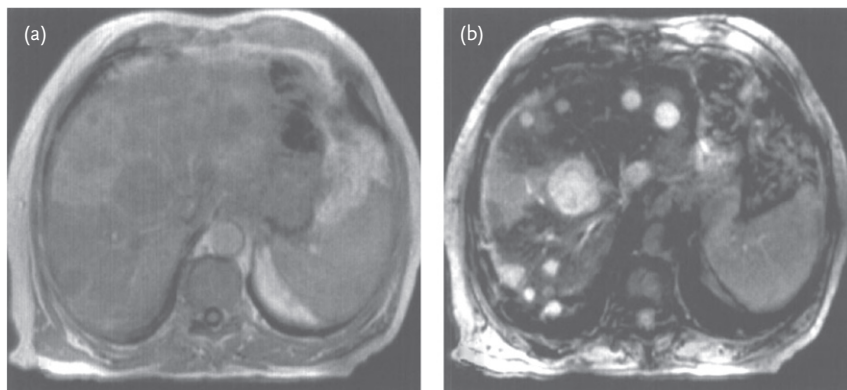
Figure 8.22 Contrast enhancement in NMR imaging of a metastases of a gall bladder carcinoma using superparamagnetic γ-Fe$_2$O$_3$ particles [10]. (a) Image recorded shortly after the application. (b) Image contrast improved by injecting water-suspended superparamagnetic γ-Fe$_2$O$_3$ particles into the patient's blood. The bright spots represent the metastasis of the tumor. (Courtesy of Tombach, B. Department of Radiology, University Hospital Muenster, Germany, private communication).
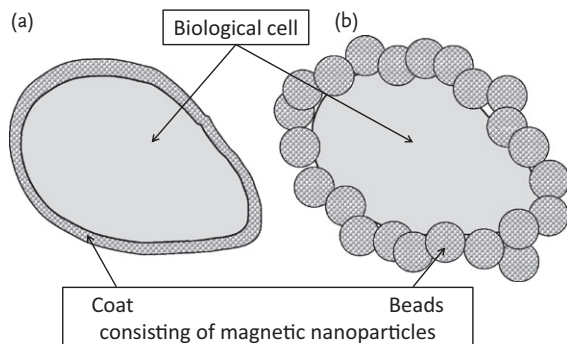
Figure 8.23 A biological cell with attached superparamagnetic nanoparticles for magnetic cell separation. The functionalized particles are either directly attached like a coat at the surface of the cells (a) or they are grouped in beads, which are attached (b).

be separated using an external magnetic field. For this application, two different approaches, as depicted in Figure 8.23, are possible.

Both designs, as shown in Figure 8.23, are applicable; however, it seems that the possibility as depicted in Figure 8.23b is the more successful one. In this context it is necessary to mention that it is quite a difficult task to produce the beads consisting of superparamagnetic particles in a narrow size distribution without losing superparamagnetism.

An application that may become important in the coming years is the superparamagnetic refrigerator. This home appliance will be important for two reasons: (i) Magnetic refrigeration avoids the application of ozone-depleting chemicals and (ii) the electrical efficiency is better as compared to the conventional units. Magnetic refrigeration uses the magnetocaloric effect. This effect describes the phenomenon that leads, under adiabatic conditions, to an increase of the temperature of paramagnetic materials, if it is brought into a magnetic field. This process is reversible, when the material is removed from the magnetic field.

Box 8.4 Magnetocaloric Effect

Assume a paramagnetic material has outside of a magnetic field, $H = 0$ the temperature T. At these conditions, the spins are not ordered. The material has the entropy $S_{H=0}$. Bringing this material into a magnetic field leads to an ordering of the spins, the entropy, $S_{H>0}$ decreases.

$$S_{H=0} > S_{H>0}. \tag{8.14}$$

(In this context, it is important to note that the entropy of a disordered state is always higher than the entropy of an ordered state. This means, for example, the entropy of a gas is higher than that of a liquid, which is higher than the

entropy of a crystal, being the state with the highest degree of order.) As in these considerations, only the differences of the thermodynamic quantities caused by the magnetic field are under consideration, one may set $S_{H=0} = 0$ and consequently $S_{H>0} < 0$. The change of enthalpy U_{magn} due to an external magnetic field H, is $U_{magn} = TS_{H>0}$. The magnetic energy of a specimen with the susceptibility x is given by

$$U_{magn} = \frac{1}{2}\chi H^2. \tag{8.15}$$

Assuming an adiabatic process, one has the thermodynamic equilibrium

$$C_v T + U_0 = C_v(T + \Delta T) + U_0 - U_{magn}$$
$$0 = C_v \Delta T - \frac{1}{2}\chi H^2. \tag{8.16}$$

Inserting the value for x given in Eq. (8.11) and the proportionality between the magnetization and the number of unpaired spins $N \propto nm$, one obtains

$$\Delta T = \frac{1}{2}\chi \frac{H^2}{C_v} = \frac{1}{2}\frac{nm^2}{3kT}\frac{H^2}{C_v} \propto Nm\frac{H^2}{T}. \tag{8.17}$$

This result proposes to use particles with large magnetic moment to maximize the magnetocaloric effect. Additionally, one sees that this effect works best at low temperatures.

It is possible to maximize the magnetocaloric effect by using a material with a large number of unpaired spins per particle or molecule. Additionally, as this effect is indirectly proportional to the temperature, it works best at low temperatures. These are the reasons why this phenomenon was applied until now at temperatures close to zero *Kelvin* using rare-earth salts as paramagnetic materials. The situation has changed since the superparamagnetic particles have been available, as instead of a few unpaired spins per molecule, now a few thousand unpaired spins per particle are available. This allows application at room temperature in refrigerators. As the lowest temperature in such household appliances is rarely below 250 K the low-temperature limit, restricted by the blocking temperature, is not essential.

Looking at the technical realization, one has to realize that the possible temperature difference is proportional to the magnetic field squared; therefore, the application of high-performance permanent magnets is necessary and expensive. One could improve the cooling effect by selecting a material where the *Curie* temperature is in the temperature window passed during the cooling cycle; in this case, the enthalpy of phase change is added to the change of the magnetic energy.

In technical realization (Figure 8.24), magnetocaloric cooling is applied in a circular process in four steps:
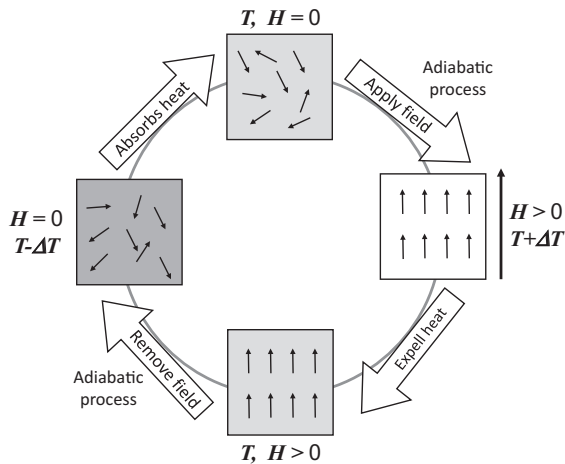
Figure 8.24 Schema of the four step circular process applied in a magnetocaloric cooling device.

- The superparamagnetic material, which is at a temperature T is brought adiabatically into a magnetic field H. Therefore, the temperature increases to the level $T + \Delta T$.

- In the next step, the material is moved, still in the magnetic field, into a heat exchanger. Here, the temperature is reduced to T again.

- After the heat exchanger, the material leaves the magnetic field in an adiabatic environment. Therefore, the temperature is reduced to $T - \Delta T$.

- The next station is a second heat exchanger, where the temperature increases to T again.

For technical realization, the magnetocaloric material may be fixed on a rotating disk, which moves between two heat exchangers. One of the heat exchangers is incorporated into the magnetic field. A further possibility is to replace the rotating disk with a ferrofluid, which is pumped in-between the heat exchangers. The basic principles of a design using a rotating disk is depicted in Figure 8.25.

The technical realization of magnetocaloric refrigerators is close to market maturity, as nowadays it is possible to reach magnetic fields up to one *Tesla* and even more with permanent magnets. Such devices reach a cooling power up to 100 W and a temperature difference up to 25 K. The power consumption of the most recent design is about 60% of that for a conventional refrigerator. A great review on magnetocaloric cooling systems was published by Gschneider and Pecharsky [11].

Some further applications of superaramagnetic fluids are described in Chapter 6.
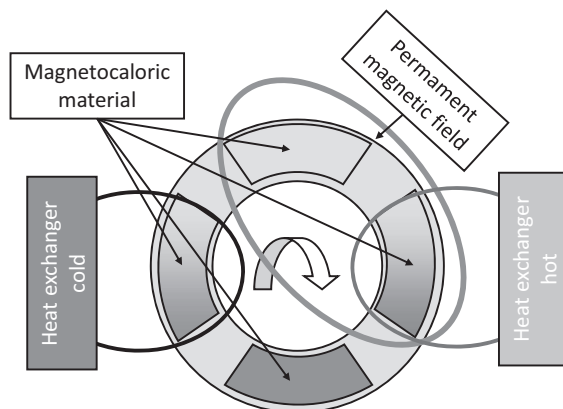
Figure 8.25 Basic principle of a technical design for a refrigerator applying the magnetocaloric effect. The rotating disk covered with the superparamagnetic material conveys the material between two heat exchangers; one of these heat exchangers is in a magnetic field.

8.6
Exchange-Coupled Magnetic Nanoparticles

Caused by the dipole moment of magnetic particles, they interact. In view of superpramagnetism, this phenomenon is adverse. On the other hand, why not use this interaction to create new materials. This is exactly what *Kneller* and Hawig [12] did; by wise combination of different nanoscaled magnetic materials they developed new materials. The basic idea may be summarized as follows: Magnetically hard particles will keep their direction of magnetization also when other magnetic particles come close. Magnetically soft particles tend to rotate the direction of magnetization into the direction of an external field, certainly, also into the direction of a field created by an other particle. Therefore, *Kneller* and Hawig combined magnetically soft with magnetically hard particles. In other words: The soft magnetic particles, in most cases superparamagnetic particles, directly adjacent to a hard magnetic particle are forced by the hard magnetic particles in their direction. As a result, the whole composite is magnetically oriented into the same direction. This has the following advantages:

- The magnetically soft particles have higher magnetization as compared to magnetically hard materials. In combination, one expects better magnetic properties with higher magnetization.

- Magnetically hard materials are significantly more expensive than magnetically soft materials; therefore, one expects a cheaper composite material.

The forced orientation of the soft magnetic particles in the magnetic field of the magnetically hard particles is depicted in Figure 8.26. The magnetically soft and hard particles are exchange-coupled. *Kneller* and Hawig [12] estimated that a
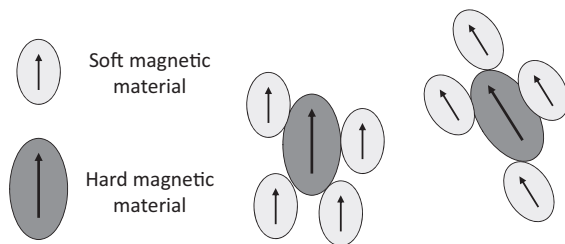
Figure 8.26 Combining magnetically hard and soft particles leads to an orientation of the magnetization of the magnetically soft particles into the direction of the magnetically hard particles. Now, the cluster of these two different types of particles acts like one large magnetically hard particle.

volume fraction of magnetically hard particles in the range of 10 vol% is sufficient to obtain a superior magnetically composite.

Figure 8.26 shows an essential feature of exchange-coupled particles: The magnetic moments of the exchange-coupled particles are parallel oriented. This is an important difference from dipole–dipole coupled particles, because in this case the particles are antiparallel oriented. This is explained simplest using electrically charged particles, where always positive and negative charged ends are mutually attracted. In the case of magnetic particles, these are the north and the south pole attracting each other. Magnetic exchange coupling leads to a parallel orientation of the magnetic moments of the particles surrounding a magnetically hard particle. In special cases, the volume where the particles are exchange-coupled may include the whole specimen. In this connection, the question on the possible size of the volume, where the particles are parallel oriented, the "correlation volume" [13], arises. *Herzer* gives for the size of the correlation volume V_{corr}

$$V_{corr} = \left(\frac{A}{K}\right)^6 \frac{1}{v^3}. \tag{8.18}$$

In Eq. (8.18) the quantity A stands for the exchange constant for nanoparticles being the range of $10^{-12}\,J\,m^{-1}$, K is the constant of magnetic anisotropy, and v the volume of one particle, assuming that all particles have the same volume. This equation shows that magnetic exchange coupling is a phenomenon related to small particles, nanoparticles, as the exchange volume increases with decreasing particle size. Furthermore, this phenomenon must be exiting for soft magnetic materials, too, as the correlation volume increase dramatically (power of six!) with decreasing constant of magnetic anisotropy. Looking at hard magnetic materials and assuming a particle size of 5 nm, one calculates a diameter of the correlation volume in the range of 100 nm.

The effect of combining two different types of magnetic materials is sketched in Figure 8.27. In this figure, two features are essential: The magnetically hard particles show a broad hysteresis; however, relatively low magnetization. The magnetically soft particles are superparamagnetic, they show no hysteresis, but a
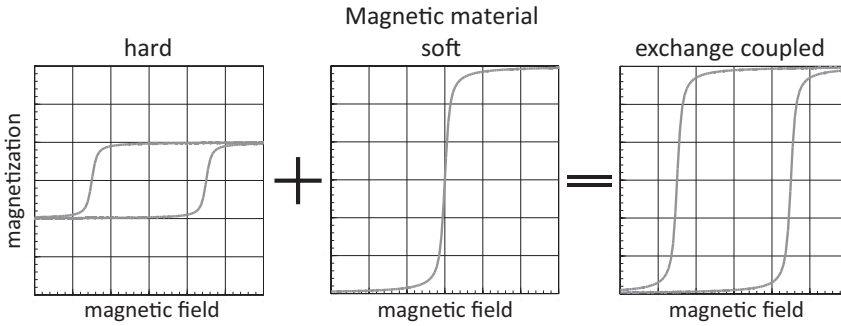
Figure 8.27 The background of the idea of combining magnetically hard materials (high coercivity) with magnetically soft materials (high saturation magnetization) to obtain a new magnetic composite with superior performance exhibiting high saturation magnetization and high coercivity.
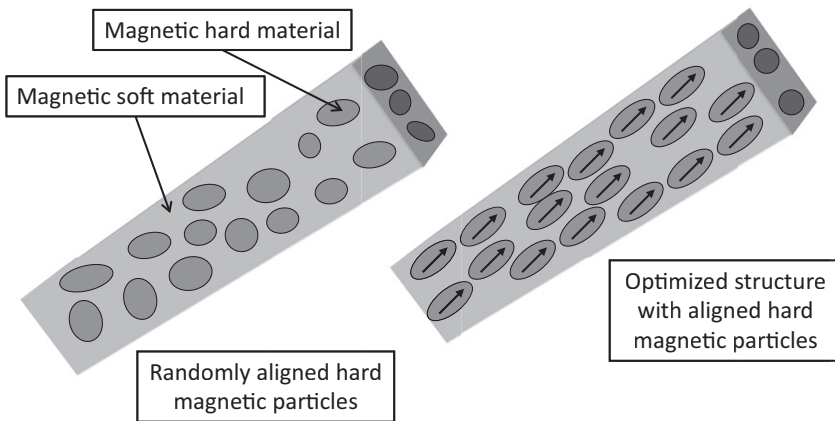
Figure 8.28 Two bars of exchange-coupled magnetically hard materials. The two parts differ in the arrangement of the magnetically hard particles: They are either oriented randomly or aligned in one direction.

high saturation magnetization. Combining these two different materials should result in a new material with high saturation magnetization and high coercivity; in particular the energy product (the product remanence times coercivity) increases significantly. This is plotted in a symbolic manner in Figure 8.27.

In the actual technical realization such a new, exchange couples hard magnetic composite has a structure, which is depicted in an idealized way in Figure 8.28. In this figure, there are two types of this material, one with randomly aligned vectors of magnetization and a second one where the vectors of magnetization

were preoriented during the fabrication process. Generally, magnetic composites of this type are produced by means of powder metallurgical methods.

There are two different types of exchange-coupled hard magnetic materials. In both cases, the magnetic hard phase is embedded in a soft magnetic matrix. The varieties differ in the arrangement of the hard magnetic phase. On the left-hand side, the particles with broad size distribution are oriented randomly, whereas, on the right-hand side, the material exhibits an optimized structure, where the hard magnetic particles with uniform particle size are oriented parallel close to the axis of the work piece. It is important to mention that in exchange-coupled magnetically hard materials the amount of the expensive hard component is small, in many cases, a volume fraction of 10 vol% is sufficient; it is rarely more than 50 vol%. Provided the particles are sufficiently small, the effective constant of anisotropy of such a system is close to that of the hard magnetic phase even for equal volume fractions of both magnetic phases.

There is a lot of scientific research going on in the area of exchange-coupled magnetic materials, as these are the best magnetically hard materials that are known currently. Figure 8.29 displays an electron micrograph of such an experimentally realized material, realized by Zeng *et al.* [14]. This material consists of magnetically hard particles with the composition $Fe_{58}Pt_{42}$. As soft phase, these particles were coated with Fe_3O_4. In this realization, the magnetically hard particles had a diameter of 4 nm and the magnetically soft material was applied as a coating with different thicknesses, in the range between 0.5 and 2 nm.

In Figure 8.29, the darker regions are the 4-nm $Fe_{58}Pt_{42}$ particles, which are coated with 0.5-nm Fe_3O_4. The magnetization curve of such a product; however,
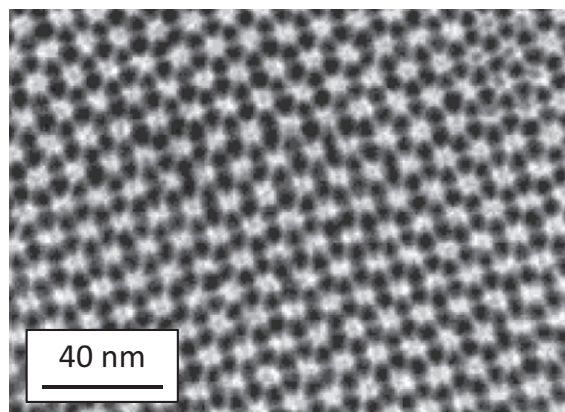
Figure 8.29 Electron micrograph of a hard magnetic composite consisting of $Fe_{58}Pt_{42}$ particles with a diameter of 4 nm as the hard magnetic phase and a Fe_3O_4 coating with a thickness of 0.5 nm as soft magnetic phase. In this micrograph, the darker region represents the $Fe_{58}Pt_{42}$ particles, the lighter ring the Fe_3O_4 coating [14]. From the geometry, one can estimate that just half of the volume was filled with the expensive platinum alloy. (Reproduction with permission by the American Chemical Society.)
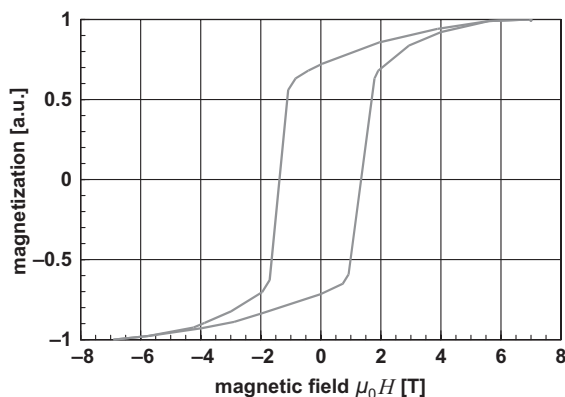
Figure 8.30 Magnetization curve of an exchange-coupled composite. The magnetically hard phase consists of $Fe_{58}Pt_{42}$ particles with a diameter of 4 nm; the magnetically hard phase was introduced as a 1-nm Fe_3O_4 coating [14]. The energy product of this composite is approximately 38% higher than the highest value, theoretically possible for FePt bulk material. In this case, the fraction of the platinum-containing phase was 30 vol%.

with a coating thickness of 1 nm is displayed in Figure 8.30. In this case, the volume fraction of the expensive platinum-containing phase was 30%. The energy product, the quantity to evaluate the quality of magnetic materials was 38% higher as compared to the significantly more expensive bulk FePt.

Local hyperthermia is an important means in treatment of cancer. To do this, magnetic nanoparticles are either directly injected into the tumor or their surface is functionalized with molecules that attach directly at the tumor. In both cases, the particles are heated using an external high-frequency magnetic field. Heat production has two sources: Losses caused by the change of the direction of the magnetization and *Ohmic* losses caused by the electrical conductivity of the particles (eddy-current losses). Figure 8.31 displays the losses of pure and coated ferrite particles. Even when an interpretation of the data is, due to different particle sizes, difficult, the results suggest that the coated particles, where core and coating are exchange-coupled, exhibit higher losses as compared to uncoated particles. Conventional medication for hyperthermia has losses in the range the uncoated particles.

Equation (8.18) shows that the correlation volume of exchange-coupled particles increases with decreasing magnetic anisotropy constant with the power of six. This means, for example, using a ferrite that has an anisotropy constant that is one tenth of that of a magnetically hard material, the correlation volume increases by a factor of 10^6, implying that the diameter of an equivalent sphere has a hundred-fold diameter. This suggests the design of special magnetically soft materials. In fact, these materials, called "superferrite" or "ultrasoft materials", were successfully developed. Successful realizations apply metallic particles. To
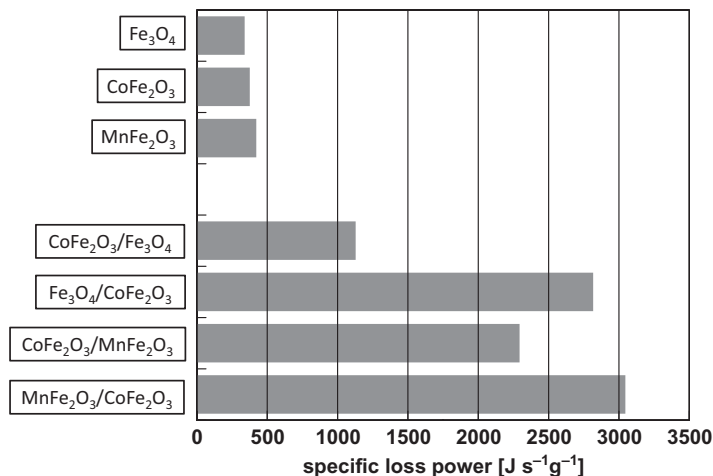
Figure 8.31 Specific loss power of ferrite nanoparticles. These are uncoated and ferrite-coated particles. Due to different particle sizes, an exact interpretation of the results is difficult; however, one can conclude that the coated, exchange-coupled particles show higher losses [9]. (At the coated particles, the first mentioned compound is the core, the second one the coating.)

reduce eddy-current losses, often the particles are coated with an insulating layer. In most cases, however, these materials are produced by annealing of metallic glassy ribbons. In this context alloys with compositions based on FeSiBNbCu or FeZrB are under discussion. As the constant of magnetic anisotropy of these materials is well below $10^3\,$J m^{-3}, the correlation volume is of macroscopic size. These materials have been commercialized for many years, the same is valid, for example, for composites consisting of metallic particles coated with silica.

References

1 Néel, L. (1949) *C. R. Acad. Sci. Paris*, **228**, 664–666.

2 Aharoni, A. (1964) *Phys. Rev. A*, **132**, 447–440.

3 Morup, S., and Christiansen, G. (1993) *J. Appl. Phys.*, **73**, 6955–6957.

4 Tang, Z.X., Sorensen, C.M., Klabunde, K.J., and Hadjipanayis, G.C. (1991) *Phys. Rev. Lett.*, **67**, 3602–3605.

5 Kodama, R.H., Berkowitz, A.E., McNiff, E.J., and Foner, S. (1997) *J. Appl. Phys.*, **81**, 5552–5557.

6 Vollath, D., and Szabó, D.V. (2002) *Innovative Processing of Films and Nanocrystalline Powders* (ed. K.-L. Choy), Imperial College Press, London, pp. 219–251.

7 Han, D.H., Wang, J.P., and Luo, H.L. (1994) *J. Magn. Magn. Mater.*, **136**, 176–182.

8 Vollath, D., Szabó, D.V., and Willis, J.O. (1996) *Mater. Lett.*, **29**, 271–279.

9 Lee, J.-H., Jang, J.-T., Choi, J.-S., Moon, S.-H., Noh, S., Kim, J., Kim,

J.-G., Kim, I.-S., Park, K.I., and
Cheon, J. (2011) *Nature Nanotechnol.*,
6, 418–422.

10 Lawaczeck, R., Menzel, M., and Pietsch,
H. (2004) *Appl. Organomet. Chem.*, **18**,
506–513.

11 Gschneidner, K.A., Jr., and Pecharsky,
V.K. (2000) *Annu. Rev. Mater. Sci.*, **30**,
387–429.

12 Kneller, E.F., and Hawig, R. (1991) *IEEE
Trans. Magn.*, **27**, 3588–3560.

13 Herzer, G. (1997) *Handbook of Magnetic
Materials*, vol. 10 (ed. K.H.J. Buschow),
Elsevier Science, Amsterdam, p. 415.
Chap.3.

14 Zeng, H., Jing, L., Wang, Z.L., Liu, J.P.,
and Shouheng, S. (2004) *Nano Lett.*, **4**,
187–190.

9
Optical Properties

9.1
General Remarks

There are many applications of nanoparticles and nanocomposites exploiting the special size-dependent optical properties. These applications have great importance in science and the economy. The most important groups of applications are:

- adjusting the index of refraction of a polymer;
- visually transparent UV-absorber;
- pigments;
- luminescent particles, primarily for applications in displays, medicine, and biotechnology;
- photo- and electroluminescence;
- combined optical and magnetic applications.

The relative importance of these, characterized by revenues, is changing with time, depending on the economic maturity of the different developments.

9.2
Adjustment of the Index of Refraction and Visually Transparent UV Absorbers

There are many applications of polymers where the index of refraction and the optical dispersion of polymers must be adjusted precisely. This may be needed for new optical systems or just for a glue connecting optical fibers for data transmission. Assuming a small concentration of particles with an index of refraction $n_{particle}$ in a polymer matrix with an index of refraction n_{matrix}, such a composite, with small concentration c of particles, has a resulting index of refraction

$$n_{composite} = (1-c)\,n_{matrix} + c\,n_{particle} = n_{matrix} + c\left(n_{particle} - n_{matrix}\right). \tag{9.1}$$

This linear relationship of the index of refraction is experimentally very well verified. As an example, Figure 9.1 displays the index of refraction of the composite titania, TiO_2–polyvinyl alcohol, PVA as a function of the particle concentration [1].
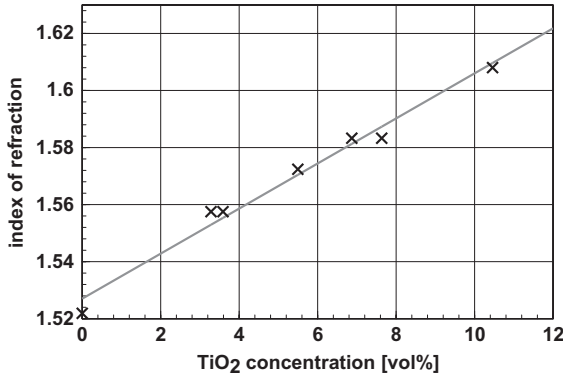
Figure 9.1 Index of refraction of a composite consisting of polyvinyl alcohol, PVA as matrix and titania, TiO$_2$, nanoparticles to adjust the index of refraction as function of the particle concentration [1]. The linear relation, given in Eq. (9.1) is, within the accuracy of the measurements, perfectly fulfilled.

Analyzing Figure 9.1, one sees that the linear relationship indicated from Eq. (9.1) is perfectly justified by experimental results. This is thus remarkable, as a concentration of 10 vol% is no longer "small".

In these cases, the particles introduced into the polymer must be sufficiently small to avoid scattering. The amount of light, the power $P_{scatter}$, scattered in a composite material consisting of a matrix with the index of refraction n_{matrix} filled with spherical particles having the index of refraction $n_{particle}$ is given the *Rayleigh* formula

$$P_{scatter} \propto P_0 c \frac{n_{particle} - n_{matrix}}{n_{matrix}^2} \frac{d^6}{\lambda^4}. \tag{9.2}$$

In Eq. (9.2), P_0 stands for the power of the incident light, d for the diameter of the particles and λ for the wavelength of the light in the matrix, which is given by $\lambda = \dfrac{\lambda_{vacuum}}{n_{matrix}}$; the quantity c again stands for the volume fraction of the particles in the composite. Analyzing Eq. (9.2), one sees an extreme influence of the particle size. This influence enforces the application of particles with very narrow size distribution. This importance may be demonstrated in a simple example: Assuming a size distribution where only 10% (in particle numbers) of the particles is double in diameter, this small amount stands for nearly 200% of the scattered light, as compared to particles with only one size. To obtain optically transparent composites, the particle sizes have to be selected carefully. As a certain distribution of particle sizes is unavoidable, the mean particle size must be selected in such a way that the contribution of the largest particles is negligible. As a rule of thumb, one can say: To obtain perfect optical transparent composites, the largest particles

should be smaller than one tenth of the shortest wavelength under consideration. For a transparent composite in the visual range, which is for human beings the range from 400 to 800 nm, the maximum particle size in such a composite must be less than 40 nm.

Furthermore, as the next step, one has to look at the production process of such a composite. Assuming the particles of equal size and individualized are put into the precursor of the polymer. After the process of blending, there is a concentration c of particles in the mixture. Even when the concentration of particles is small, there is a probability of forming clusters. The probability c_i that there is a cluster of i particles is estimated by

$$c_i = c^i. \tag{9.3}$$

This equation proposes to keep the concentration of particles in the composite as low as possible to avoid the formation of clusters. Low concentration of particles results in the use of particles with high index of refraction, as there are for example, ZrO_2 and TiO_2. On the other hand, these oxides, like all oxides from transition metals, are photocatalysts. When, besides visible or infrared, IR, light, there is also ultraviolet, UV, present, composites containing these oxides have a propensity to self-destruction. In such cases, the application of silica, SiO_2, or alumina, Al_2O_3, is recommended. The other possibility is to coat the highly UV-absorbing oxides with alumina or silica.

Looking at Eqs. (9.1) and (9.2), both are linear in concentration and the difference in the indices of refraction, it makes no difference for the power of the scattered light, if the modification of the index of refraction is obtained by high concentration and a small difference of the indices of refraction or vice versa. Therefore, particle size and clustering are the criteria for decisions. When one applies particles coated with the matrix polymer, the risk of particle clustering is avoided. Lastly, if possible, one should seek this choice (see Chapters 2 and 4).

Additions of ceramic nanoparticles to a polymer not only alters the index of refraction. By proper selection of particle composition and size, one can produce composites that are transparent in the wavelength range of the visible light but nontransparent for UV in the wavelength range below 400 nm. When designing such composites, it is necessary to select the particle size in a way to obtain optimal absorption in the intended range of wavelength. Figure 9.2 displays the wavelength-dependent absorption of titania with different particle sizes. This figure demonstrates two important phenomena: It is very well visible, that with decreasing particle size, the maximum of the absorption is found at shorter wavelength; one observes a blueshift with decreasing wavelength. Furthermore, it is important to realize that the particle-diameter distributions with mean values of 45 and 145 nm were very broad, whereas that for particles with 4.5 nm diameter was narrow. A broad size distribution results in a broad absorption maximum, and vice versa. For 145-nm particles, this is an intended effect, as this is a white pigment. Therefore, any preferred wavelength in the absorption spectrum is detrimental. Other oxides used for UV absorption, which are, as small particles, colorless to
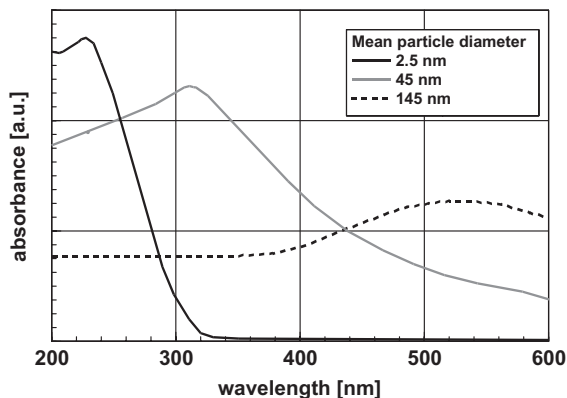
Figure 9.2 Absorption spectra of titania particles with different particle sizes. The particles with mean particle diameters of 45 and 145 nm are industrially produced materials (pigments) [2], whereas the product with 2.5 nm mean particle diameter was an experimental product [1]. The blueshift of the absorption maximum with decreasing particle size is evident. A flat onset of the absorption indicates a very broad particle-size distribution, which is intended for white pigments.

the human eye, are ZnO and ZrO_2. However, as these oxides are photocatalysts, one has to be very careful when using them as UV absorber, as this may lead to self-destructing systems. A possibility to eliminate this problem is coating the absorber particles with silica or alumina, as these oxides are not active as catalysts. Furthermore, the particle size has to be carefully related to the onset wavelength of absorption.

9.3
Size-Dependent Optical Properties – Quantum Confinement

As was already shown in Figure 9.2 with respect to optical absorption, many essential optical properties of particles depend on their size. To start analysis of these phenomena, first, the influence of the particle size on the electronic structure of a solid will be discussed.

Looking at the energy levels of one single atom, one sees discrete energy levels, each one, according to *Pauli*'s principle, occupied by one electron. However, one has to take into account that each of these electrons is connected to a spin. There are two possibilities: spin-up and spin-down. As a consequence, one may find two electrons with different spins at one level. Adding a second atom leads to a splitting of the energy levels. Adding further atoms leads to further splitting of the energy levels, the number of splittings is exactly equal to the number of atoms in the system. Lastly, in a bulk solid, there are so many sublevels at one energy level
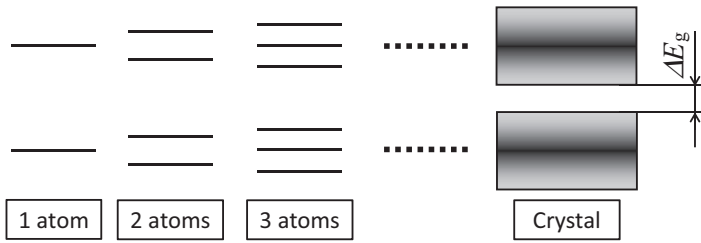
Figure 9.3 Energy levels of a system consisting of one, two, or more atoms, up to a bulk crystalline solid. According to *Pauli*'s principle, the energy levels are split for each added atom, the number of splittings is equal to the number of atoms. In the case of a bulk solid, each energy level is subdivided in many sublevels, one has a quasicontinuous "energy band". Consequently, the energy of the gap ΔE_g in-between two levels decreases with increasing number of atoms in the system.

that one observes a quasicontinuous system of "energy bands". This is depicted in Figure 9.3.

The energy of the gap between two levels decreases with increasing number of atoms in the system. Alternatively, looking at solid particles, the energy of the gap ΔE_g decreases with increasing particle size. There is a theoretically and experimentally well-established relation for this energy difference for nanoparticles as

$$\Delta E_{g-nanoparticle} = \Delta E_{g-bulk} + \frac{\alpha}{d^2}. \tag{9.4}$$

In this equation, $\Delta E_{g-nanoparticle}$ and ΔE_{g-bulk} are energy differences of the gap in nanoparticles with the diameter d and the bulk material, respectively. The quantity α is a proportionality factor.

In the subsequent discussion, one has to distinguish between metals, which are electrical conductors, semiconductors, showing electrical conductivity under special conditions, and insulators, without any electrical conductivity. The energy bands of these three types of materials are depicted in Figure 9.4.

In a metal, the last energy band is not filled completely; therefore, there are empty energy levels for electrons to move under the influence of an external field. In an insulator, the last band is filled completely with electrons; therefore, electrical conductivity is impossible. Electrons in an incompletely filled conduction band of a metal are called "free electrons". In a semiconductor, the situation is thus different from an insulator, as the energy gap in-between the last filled band and the first empty band is so narrow that some of the electrons are able to jump, thermally activated, into the empty band. Therefore, electrical conductivity is possible. In technical reality, there are many more variants of conductors and semiconductors possible. Most important are semiconductors, which obtain their electrical conductivity by doping with different elements. Doping creates isolated energy levels, located in the bandgap. These energy levels are so narrow to the filled bands that electrons are able to jump to these levels by thermal activation.
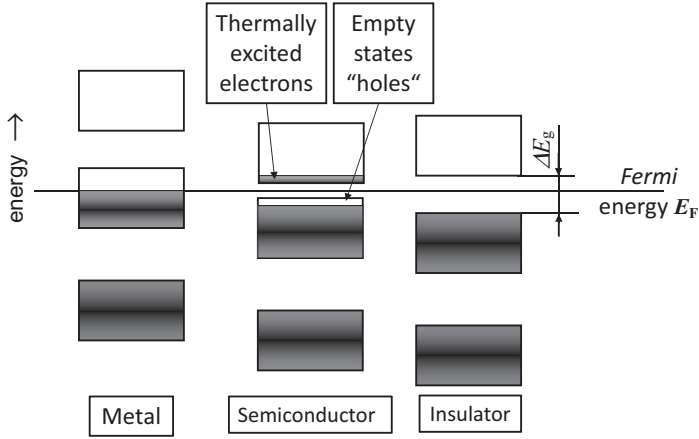
Figure 9.4 Energy bands in metals, semiconductors, and insulators. Metals are electrical conductors, because the last energy band is not completely filled with electrons. In semiconductors, the energy gap is so narrow that the electrons are able to jump, thermally activated, into the next empty band; therefore, there are empty energy levels usable for electric conductivity. In insulators, the last energy band is full, additionally, the energy gap is so wide that the electrons are unable to jump, thermally activated, into the empty band. Additionally, the level of the *Fermi* energy E_F, the energy level of the least tightly bond electron within a solid is indicated.

Additionally, in Figure 9.4, the level of the *Fermi* energy is indicated. At absolute zero temperature, the *Fermi* energy E_F is the energy level of the least tightly bond electron within a solid. In the case of insulators and semiconductors, this level is close to the middle of the energy gap.

The description given above is a very crude summary of results obtained by solutions of the *Schrödinger* equation, the fundamental equation describing quantum phenomena. On calculating the energy levels in a particle using the *Schrödinger* equation, one obtains the probability distribution of finding electrons in different energy levels. Summarizing these results, one can say that the energy difference between two adjacent energy levels ΔE_g is

$$\Delta E_g \propto \frac{1}{d^2}, \tag{9.5}$$

where d is the particle diameter. This important relation is experimentally very well verified. It says that the energy difference of the gap increases quadratically with the inverse particle diameter. As a practical consequence, one can say: It is possible to design optical properties of particles by varying the diameter, as an increase of ΔE_g with decreasing particle size leads necessarily to a blueshift of the absorption or emission of photons. As mentioned above, it is possible to calculate the electron density (probability to find an electron) as a function of the energy
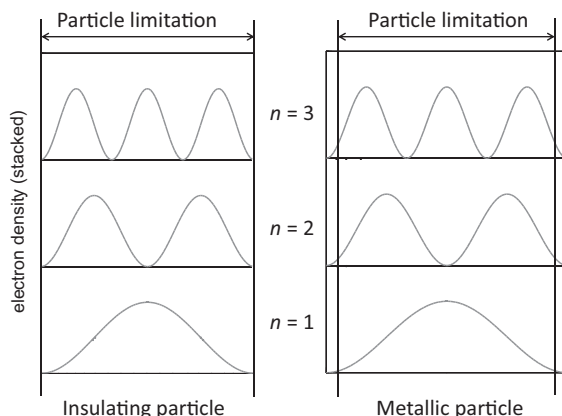
Figure 9.5 Electron density distribution (probability to find an electron) as function of the energy, radius, and the type (insulating or metallic) of the particle. It is important to realize that, in the case of metallic particles, the electron density outside of the particle is not nil. A metallic particle is surrounded by a cloud of electrons. The vibrations of this electron cloud, which are quantized, are called "plasmons".

level for small particles. Figure 9.5 displays such results for insulating and metallic particles.

The solutions of the *Schrödinger* equation for insulating and metallic particles depicted in Figure 9.5 show one important difference: In the case of an insulator, the electron density at the surface is nil, in the case of metallic particles, the electron density at the surface is larger than zero, one finds electrons outside of the particles. This electron cloud oscillates. These oscillations are quantized, the different modes are are called "*plasmons*".

As a consequence of the absorption of a photon in a nonmetallic particle, an electron is pushed off from its place into the empty conduction band. At the original position of this electron, there is now a positively charged "hole", h^+. The electron, which is now free, circles around this hole. The negatively charged electron and the positively charged hole form a "pseudohydrogen". This electron–hole combination is called an "*exciton*". The radius of the circling electron around the hole is called the *Bohr* radius. Comparing the *Bohr* radius with the radius of the particle, one has to distinguish two different cases: (i) The *Bohr* radius is smaller than the particle radius, in this case, there is, if any, only a minor dependency of the optical properties related to absorption and emission on the particle size. (ii) The *Bohr* radius is larger than the radius of the particle. This case is called "quantum confinement". Now the absorption and emission properties depend quadratically on the particle diameter. In this range, Eq. (9.5) is valid. Figure 9.6 depicts these relationships in a simplified way graphically.

$$d > 2r_{\text{exciton}}$$

$$d < 2r_{\text{exciton}}$$

$d \ldots$ particle diameter
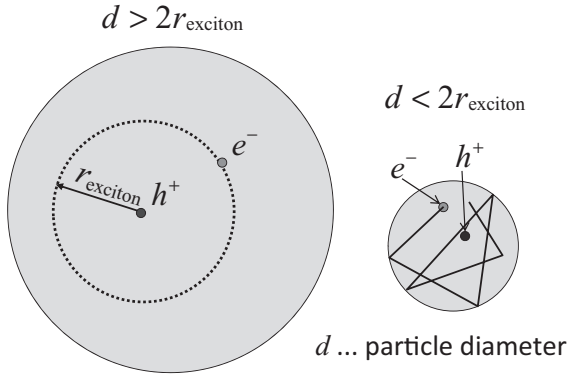
Figure 9.6 Comparison of the radius of a particle with the radius of an exciton. When the exciton radius is smaller than that of the particle, there is only a minor dependency of the optical absorption and emission on the particle size. In the other case, called "quantum confinement", exciton formation is not possible. Now an inverse quadratic dependency of the wavelength of the emitted lines is observed.

Box 9.1   Energy of an Electron in a Small Particle – Quantum Confinement

Mathematically, it is possible to solve the *Schrödinger* equation for an electron in a spherical particle. However, the gain of such a complex procedure is smaller than the benefit in clarity. Therefore, one uses the model of an electron in a one dimensional box to describe the solution of this problem. Using this approach, this problem can be simplified even more, as follows:

The "particle in a box" problem can be described with an approach using the basic laws of quantum mechanics. In a one-dimensional system, the condition for a standing wave consisting of n half-waves of the wavelength λ_n in a box with the size l is:

$$\frac{n\lambda_n}{2} = l. \tag{9.6}$$

Substituted into the *DeBroglie* relationship this leads to:

$$p = mv = \frac{h}{\lambda_n} = \frac{nh}{2l}. \tag{9.7}$$

In Eq. (9.7), p is the momentum, m the mass and v the velocity of the electron, h is *Planck*'s constant. The energy E_n and one obtains

$$E_n = \frac{mv^2}{2} = \frac{p^2}{2m} = \frac{n^2h^2}{8mL^2} \propto \frac{n^2}{L^2}. \tag{9.8}$$

Equation (9.8) gives the main characteristic of quantum-confinement systems: The energy of the electron is inversely quadratically proportional to the particle

size. This results in a blueshift of the absorption and emission spectrum with decreasing particle size. The energy difference ΔE between two quantum levels n and $n + 1$ describes the energy of an emitted photon.

$$\Delta E = \frac{h^2}{8ml^2}\left[(n+1)^2 - n^2\right] = \frac{(2n+1)h^2}{8ml^2} \quad \text{leading to} \quad \lambda = \frac{8mcl^2}{(2n+1)h}. \quad (9.9)$$

Equation (9.9) clearly shows the blueshift with decreasing size l of the box, which is equivalent to the particle diameter d, or, the wavelength of the emitted photon increases quadratically with the particle diameter d. One has to bear in mind that blueshift is not only observed in the quantum-confinement case (see also Eq. (9.5)).

9.4
Semiconducting Particles in the Quantum-Confinement Range

Sufficiently small semiconducting nanoparticles show the properties of quantum-confinement systems. The width of the energy gap and, therefore, the wavelength of the emitted photons depends on the particle size. This allows particle size to be used as a design element for absorbers and emitters of light. This has an important advantage: Varying particle size of a nanoparticle allows optical properties to be varied without changing the chemistry of the surface. This possibility is of special importance for functionalizing the particles for applications, for example, in the fields of biochemistry or medicine. Figure 9.7 displays the absorption of light as a function of the wavelength for CdTe nanoparticles in silica or suspended in a liquid and particle diameter [3]. Analyzing this figure one sees that, as expected,
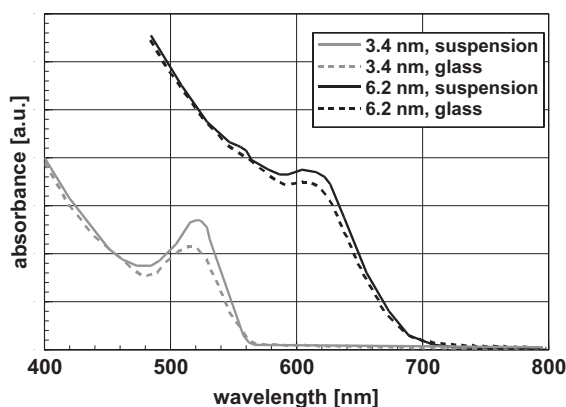
Figure 9.7 Absorption spectrum of CdTe nanoparticles in glass and suspended in a liquid according to Li and Murase [3] as a function of the wavelength and the particle diameter. It is essential to realize the minor influence of the matrix surrounding the particles; whereas, the influence of the particle diameter is as expected.
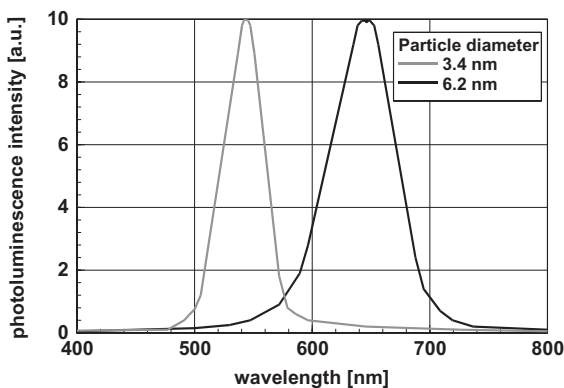
Figure 9.8 Emission spectra of CdTe according to Li and Murase [3]. This figure visualizes the strong influence of the particle diameter on the emission spectrum. The blueshift, predicted by theory, is perfectly verified. The line width of the emitted lines is relatively small; this indicates a narrow particle-size distribution.

the wavelength of the maximum of absorption gets, according to Eqs. (9.5) and (9.9), shorter if the particles are smaller. The second observation: there is only a minor influence of the surrounding medium on the spectrum of the absorption, especially on the position of the maximum.

In the emission spectrum one expects, according to the rules for particles showing quantum confinement, a shorter wavelength of the emitted light for the smaller particles, and, as may be expected from Figure 9.7 no influence of the surrounding matrix. Exactly these expectations are verified for CdTe. Figure 9.8 displays the emission spectra of the same specimen, from which the absorption spectra depicted in Figure 9.8 stem.

As a second example, lead sulfide, PbS is discussed. The bandgap of lead sulfide increases from 0.41 eV in bulk crystals up to a few electron volts in nanoparticles. This is visible in the optical appearance. Bulk lead sulfide absorbs throughout the visible; hence, it appears black. With decreasing crystal size, the color changes to dark brown. Suspensions of lead sulfide nanoparticles are clear and reddish.

Reisfeld [4] synthesized nanoparticulate lead sulfide particles and determined their optical properties. Figure 9.9 displays the absorbance as function of wavelength and particle diameter in the visible range between 400 and 800 nm. One sees a blueshift of the absorption with decreasing particle size. The blueshift of the absorbance found with decreasing particle size is correlated to a widening of the bandgap. The insert in Figure 9.9 shows the width of the energy gap as a function of the squared inverse particle size. As, in this plot, the experimental data lie quite perfectly on a straight line, one can conclude that relationships that lead to Eqs. (9.5) and (9.9) are perfectly fulfilled.

The considerations leading to Eq. (9.9), which are perfectly verified in the example of lead sulfide, are not always valid. In general, they are valid for one
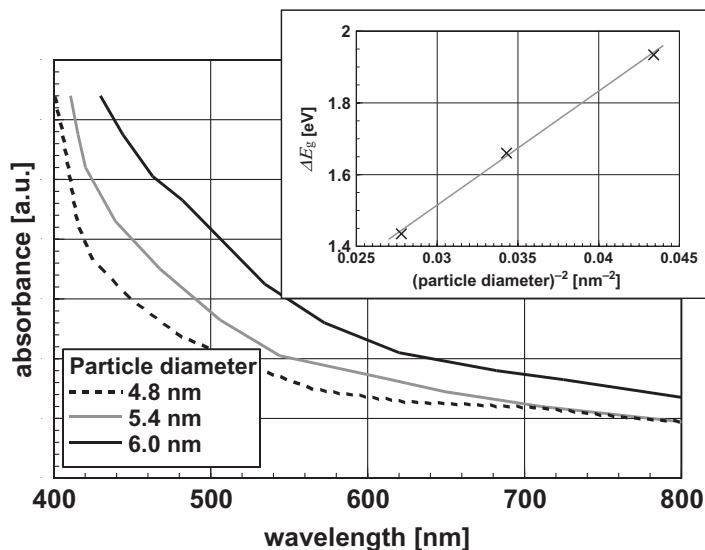
Figure 9.9 Absorbance of lead sulfide in the visible range as a function of the wavelength and particle size according to Reisfeld [4]. One sees the blueshift with decreasing particle size. The insert gives the width of the energy gap plotted versus the inverse squared wavelength, confirming the relationship given in Eq. (9.5).

isolated particle, which means in reality, for systems with extremely low concentrations. In many cases, there are a few more phenomena influencing the systems of quantum confinement stemming, for example, from the interaction of the particles. Often, excited particles form dipoles. Such dipoles have a maximum distance of interaction in the range between 10 and 15 nm. Within this distance, dipolar particles interact; they form an *excimer*, a process influencing the optical properties significantly. (*Excimer* formation is often observed in the case of organic lumophores.) An example for the dipole–dipole interaction of excited nanoparticles is zinc oxide, ZnO [5]. This influences the emission wavelength of the composites significantly. In a system with high concentration, where dipole–dipole interaction occurs, the energy of the emitted photons is not proportional to $\frac{1}{d^2}$ (d ... particle diameter), rather a dependency like $\frac{1}{d^3}$ is theoretically predicted and experimentally observed [5, 6]. Figure 9.10 displays the emission wavelength of ZnO coated with poly methyl methacrylate (PMMA) as a function of the particle size [6]. The insert displays the proportionality of the photon energy (inversely proportional to the wavelength) with the particle diameter. The rectification was obtained by plotting against $\frac{1}{d^3}$. This fulfills exactly the theoretical considerations of Monticone *et al.* [5] for particles showing dipole–dipole interactions. The minor deviations of the experimental data from the fitted line are due to experimental uncertainties, in special related to the determination of the particle size.
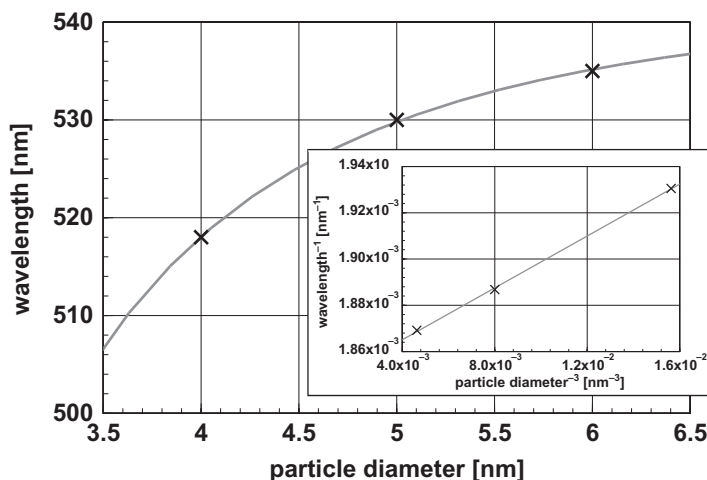
Figure 9.10 Particle-size dependency of the emission wavelength of zinc oxide, ZnO in the visible range [6]. The insert displays the rectification of the experimental data from according to Monticone *et al.* [5], using the proportionality $\frac{1}{\lambda} \propto \frac{1}{d^3}$. The experimental data follow perfectly this relation; this indicates dipole–dipole interaction between the excited particles.

Box 9.2   Excimer Formation

Excited particles or organic molecules often form a dipole. Such dipoles interact, within a maximal distance of 10 to 15 nm. In cases where the excited particles or molecules form dipoles and these objects are close enough excimers are formed. Hence, an excimer is a dimer, formed by dipole–dipole interactions, when such an excited molecule or particle comes in close contact to a second one of the same type. Therefore, one has to distinguish between the spectra of the molecule or isolated particle and that of the excimer. This process is shown in Figure 9.11 in a drastically simplified manner.

Excimer formation leads to changes in the energy levels. Antiparallel coupling reduces, and parallel coupling of the dipoles increases, the energy of the energy levels. Parallel arrangement or arrangement in chains of the molecules or particles are extreme possibilities of dimer formation. However, most probable are oblique arrangements, where, by the quantum selection rules, many different angles are allowed. This broad range of possibilities leads to broad, unstructured spectra. In general, dipolar arrangements reducing the energy of the system are the most probable ones.

As mentioned above, at low concentrations of particles or molecules, for example, suspended in a liquid, one finds the spectrum of the monomer, which means of a single isolated particle or molecule. At high concentrations, where the interaction probability of the objects is high, the dimer spectrum is observed. At medium concentrations, the two types of spectra are found in different intensity ratios. This is depicted in Figure 9.12.
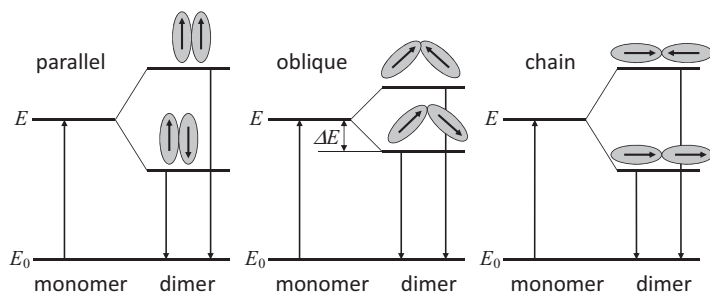
Figure 9.11 Different types of dipole–dipole coupling to form an excimer. It is obvious that the coupling of parallel oriented particles or molecules needs more energy as compared to the antiparallel orientation. Besides the extreme cases of forming parallel or chains of dimers, many other oblique arrangements are possible. However, by quantum selection rules, not all possible combinations are allowed. In the oblique case, many different angles are allowed; therefore, in general, the dimer spectrum is quite broad and not structured.
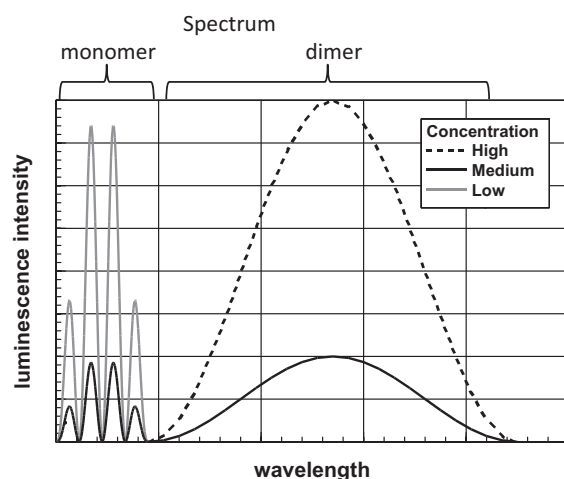
Figure 9.12 Spectra of molecules or particles, which form excitons, as a function of the concentration. At low concentration the spectrum of the monomer, at high concentrations that of the dimer is observed. At medium concentrations, different ratios of these two spectra are found.

Some systems of particles (this is also known for molecules) showing luminescence show a further interesting property: The spectra of absorption and emission are overlapping. This leads to the surprising fact that the emission of one particle can excite a further particle of the same kind. This phenomenon can be exploited to transport information from one particle to the next. Figure 9.13 shows this, using the example of zinc selenide, ZnSe, particles embedded in silica, SiO_2.
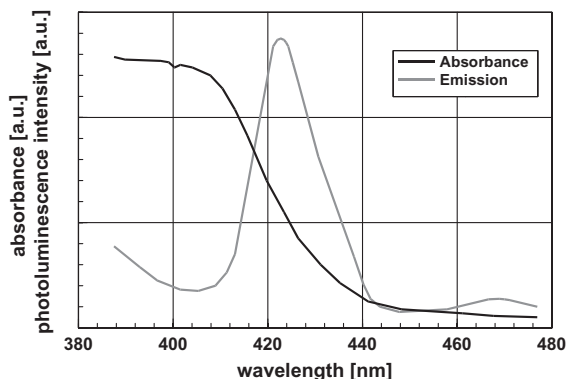
Figure 9.13 Absorption and emission spectra of zinc selenide, ZnSe, particles embedded in silica, SiO$_2$ [7]. In this example, absorption and luminescence spectra are overlapping. Therefore, the emission of one particle can excite a further particle of the same kind.
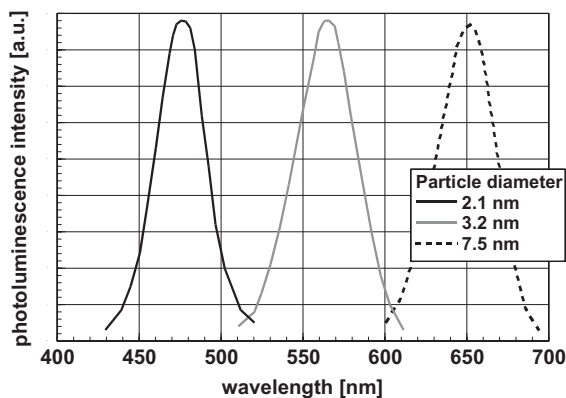
Figure 9.14 Emission spectra of cadmium selenide, CdSe nanoparticles of different size [8]. This example shows perfectly the blueshift with decreasing particle size.

The most important semiconducting compounds used for luminescent systems are the sulfides, selenides, and tellurides of zinc and cadmium; this huge group of compounds, which show at least some mutual solubility, also zinc oxide is an important often used material. In the following example, the properties and applications of cadmium selenide, CdSe, are explained. Figure 9.14 displays the emission spectra of this compound for three different particle sizes. The particles used for the measurements of the emission spectra had a very narrow size distribution; therefore, the emission spectra of the different sizes are well separated.

Figure 9.14 demonstrates the blueshift of the emission spectrum with decreasing particle size clearly. Furthermore, this figure demonstrates the necessity of a particle-size distribution that is as narrow as possible. Otherwise, a discrimination of objects characterized by particles with different functionalization, would
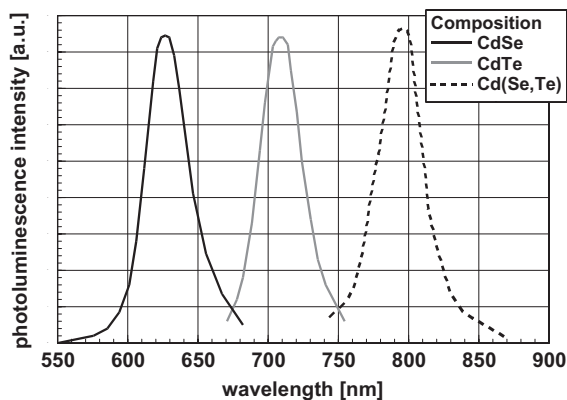
Figure 9.15 Emission spectra of cadmium selenide, cadmium telluride, and solid solution of both compounds [8]. In all three examples, the particle diameter was approximately 5.5 nm. The exchange of selenium by tellurium leads to an additional redshift of the emission beyond that of pure CdTe.

be impossible. The color of the emitted light can be influenced, as depicted, by the particle size and additionally by the composition of the particles. This is demonstrated in Figure 9.15, where the emission spectra of cadmium selenide, cadmium telluride, and a solid solution of both compounds Cd(Se,Te) are presented. Even when the variation of the composition is an elegant means to influence the emission spectrum, there are inherent disadvantages connected to this approach. The most important problem connected to this approach is the fact that the surface chemistry is altered, which means that for functionalization the chemical processes must be adapted.

Analyzing the spectra given in Figure 9.15, one sees that the emission wavelength of the telluride is significantly longer than that of the selenide. It is to some extent surprising that additions of tellurium to the selenide in solid solution leads to an extra redshift, beyond that observed with the pure telluride.

The preceding discussion made clear that the emitted wavelength decreases with decreasing particle size. There was no discussion about size limits. Now one may ask, what happens when the particles get so small that they start fluctuating between phases. Experiments have revealed that Eq. (9.9), which is perfectly validated in many examples, for example, with Figure 9.14 is is no longer valid when the structure of the particle is no longer stable and starts fluctuating (see Chapter 7), the emission spectra are no longer clearly defined. Figure 9.16 shows the emission spectrum of CdSe particles with sizes around 2 nm. This spectrum has no longer any similarity with the ones depicted in Figure 9.14. Electron microscopy and molecular dynamic calculations revealed that the structure of the particles was no longer stable. It fluctuated between different configurations of the atoms [9]. The broad emission spectrum of these small, fluctuating particles comes into the direction of white light.
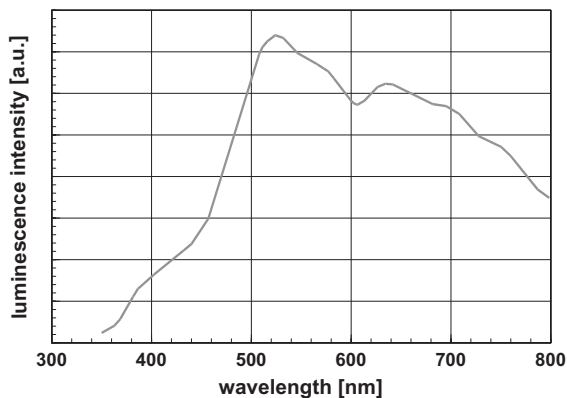
Figure 9.16 Emission spectrum of CdSe with particle sizes around 2 nm. As the structure of these small particles is no longer stable, they fluctuate. Therefore, the emission spectrum is very broad [9].
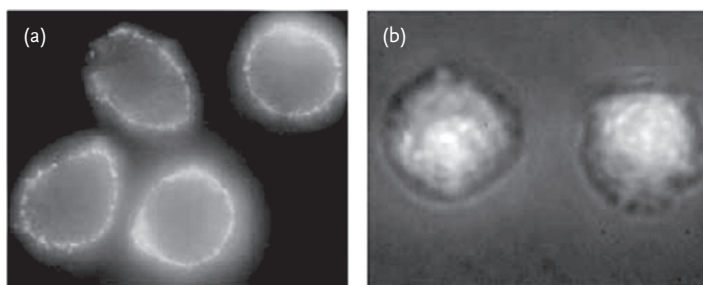
Figure 9.17 Cadmium selenide, CdSe particles coated with zinc sulfide, ZnS functionalized to stain different parts of living cancer cells according to Smith *et al*. [8]. For such an application, the surface is functionalized with antibodies, peptides or proteins to attach exactly at the intended cell receptor. (a) The nanoparticles are functionalized to attach at the cell surface. (b) Due to different functionalization, the quantum dots are localized in the cell nucleus. (Reproduced with permission of John Wiley & Sons.)

Applications that are most interesting from scientific and economic viewpoints are found in biotechnology and medical diagnostics. To attach the particles exactly at the targets, it is necessary to attach antibodies, peptides or proteins at the surface of the particles. These compounds are selected to attach exactly at the intended receptor. A typical example is displayed in Figure 9.17 [8]. In this figure zinc-sulfide-coated cadmium selenide particles, (CdSe)(ZnS) were functionalized for two different targets, one to attach at the surface (Figure 9.17a) and the other one localizes in the cell nucleus. (Figure 9.17b).

9.5
Metallic Nanoparticles – Plasmon Resonance

Metallic nanoparticles are surrounded by a cloud of free electrons stemming from the incompletely filled conduction band. This electron cloud moves in quantized discrete waves around the particle. The quantized oscillations of the electron cloud, relative to the lattice of the positively charged atomic cores of the metal, are called "*plasmons*". The plasmons control the optical appearance of the metals. As most of the metals have plasmon frequencies in the ultraviolet, they have a "*metallic luster*" in the visible range. A few metals, like copper and gold and a few alloys, have plasmon frequencies in the visible range. This is the reason for their typical color. Highly doped semiconductors show plasmon frequencies in the infrared; therefore, they often appear black.

Figure 9.18 depicts, as a model, the lattice of the atomic cores and the oscillating electron cloud.

One distinguishes surface plasmons, as depicted in Figure 9.19 and plasmons in the interior of the particles. As the penetration depth of surface plasmons is approximately 50 nm, only surface plasmons are discussed with respect to spherical nanoparticles. Furthermore, under these conditions, the plasmon resonance frequencies are, to a first approximation, independent of the particle size. This is different looking at for example, prolate ellipsoids, where one has to distinguish between transversal and longitudinal plasmon waves. Surface plasmons interact with the electromagnetic waves of the light. This leads to plasmon resonances in the absorption spectra. In the case of nonspherical particles, one may observe different resonances for the transversal and the longitudinal waves, the latter are found at longer wavelengths.

Describing the optical behavior of metals by interaction with plasmons is not only a "comfortable" image of the theoreticians. In fact, it is possible to perform experiments, to visualize plasmons. Figure 9.19 displays a gold nanorod surrounded by the electron cloud of a longitudinal plasmon. This picture was taken
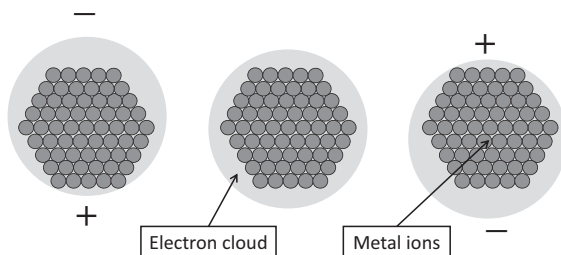
Figure 9.18 Metallic nanoparticle. The figure displays the lattice of the positively charged atomic core surrounded by an oscillating electron cloud. These quantized oscillations are called plasmons.
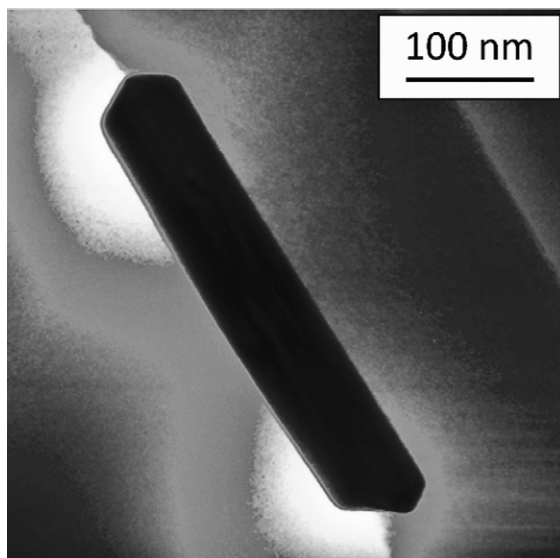
Figure 9.19 Electron micrograph of a gold nanorod taken in the EELS mode (see Chapter 12). For this electron micrograph only those electrons contribute that lost 1 eV by passing the electron cloud of the transversal plasmon (Schaffer, B. (2012). University of Technology Graz, Austria, private communication.)[10]. The picture shows the maximum of the amplitude of the plasmon vibration. The brightness represents the number of electrons in the area.

in an electron microscope in the EELS mode (see Chapter 12). The brightness visible in this micrograph is a measure for the number of electron that lost 1 eV by collision with an electron in the electron cloud surrounding the nanorod.

By solving the *Schrödinger* equation, it is possible to calculate the plasmon frequencies. An example for prolate gold spheroids (a spheroid is an ellipsoid with two equal axis) of different axis ratio and different diameter of the circular cross section is given in Figure 9.20 [11].

The results displayed in Figure 9.20 are typical for surface plasmons. The frequencies of the transversal modes are, in-between the 10 and 40 nm diameter of the cross section nearly equal, and there is also no influence of the axis ratio. Looking at the spheroid diameter of 90 nm, one sees a slight shift to longer wavelength. The relations are entirely different for the longitudinal modes: In this case, the influence of the spheroid diameter and, particularly visible for the longitudinal modes, is significant. These theoretical results can be understood simply by remembering the penetration depth of surface plasmons. The experimental verification of the relationships displayed in Figure 9.20 is nearly perfect. As an example, Figure 9.21 displays the absorption spectra of spherical nanoparticles and nanorods.
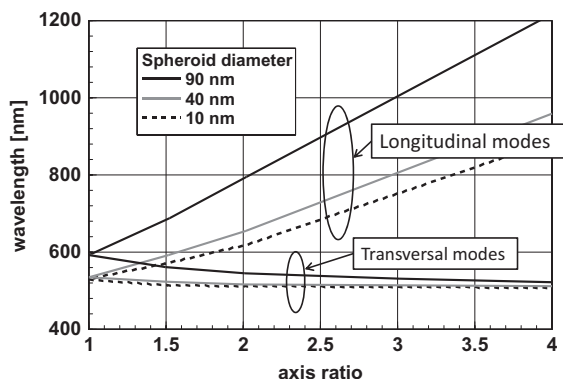
Figure 9.20 Plasmon resonance frequencies for prolate gold spheroids. It can be seen clearly that the transversal modes are nearly independent of the particle diameter and the axis ratio, as may be expected for surface plasmons, whereas the longitudinal modes depend strongly on the axis ratio [11].
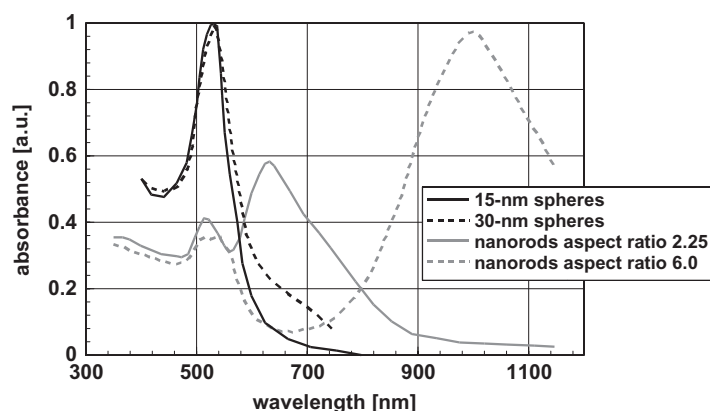
Figure 9.21 Absorption spectra of spherical particles and gold nanorods. One sees the absorption maximum of the transversal modes around 520 nm, which is nearly independent of particle size for spherical particles and for nanorods. The maxima for the longitudinal modes strongly depend on the aspect ratio [12].

The experimental results depicted in Figure 9.21 reflect exactly the outcome of the theoretical studies that led to Figure 9.20. Plasmon resonances of spherical particles with a diameter of 15 and 30 nm are identical; they are at the same frequency as the transversal resonances of the nanorods, independent of their aspect ratio. Furthermore, with increasing aspect ratio, which means with increasing length of the nanorods, as a shift of the longitudinal resonances towards longer wavelength is observed. It is significant that the peaks of the transversal modes are quite narrow; this indicated that, as shown in Figure 9.20, these resonances
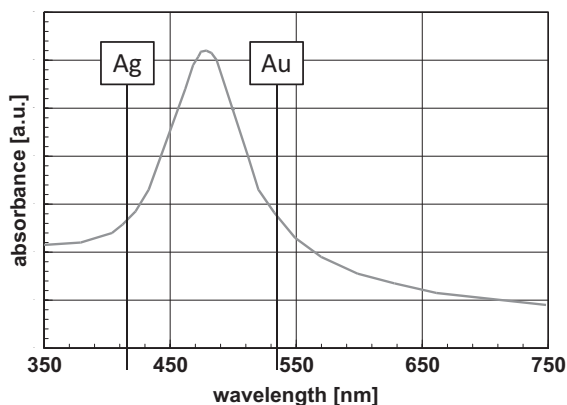
Figure 9.22 Absorption spectrum of a gold–silver alloy with a Au/Ag ratio of 1/2 [13]. For better orientation, the position of the absorption maxima of pure silver and gold nanoparticles with equivalent size are indicated. This figure demonstrates the possibility of alloying to adjust absorption spectra according to the requirements.

are to a certain degree independent of the particle or rod diameter; this not an indicator of a narrow distribution of the diameters of these objects. This is different for the peak of the longitudinal resonances. They are very broad; as these resonances are strongly dependent of the aspect ratio (see Figure 9.20), this indicates a broad distribution of the length of the nanorods.

Gold nanoparticles were the first man-made nanoparticles. The Sumerians, more than 2500 years ago, used inclusions of gold nanoparticles to obtain red coloration. This material, called "gold ruby glass" is still produced (see also Chapter 2). High-quality gold ruby glasses excel in a red color with a slight blue hue obtained by nearly ideally spherical particles. In glasses, the particle size of the gold nanoparticles is stabilized by adding tin dioxide into the glass matrix. Besides gold, nanoparticles of silver, copper, and platinum, or alloys of these metals are often used as colorants for glasses. As an example of an alloy, the absorption spectrum of a gold–silver alloy with Au/Ag ratio of 1/2 is displayed in Figure 9.22 [13]. In Figure 9.22, the position of the absorption maxima of pure silver and gold nanoparticles with equivalent sizes are indicated. A complete theoretical description of the color of metallic nanoparticles in glass is given by Quinten [14].

9.6
Luminescent Nanocomposites

Even when there is a large variety of semiconducting compounds for application as luminescent nanoparticles, this number is by far surpassed by the number of luminescent organic compounds. Therefore, it seems natural to apply some of

these compounds for luminescent composites. All the more so, as many of the elements for the semiconducting compounds, cadmium, selenium, tellurium, etc. are toxic or carginogenic. Furthermore, most of the luminescent compound used for quantum dots lack stability against oxidation and hydrolysis. Under certain circumstances, these problems make handling and, therefore, application of these materials difficult. Furthermore, especially applications in biotechnology and medical diagnostics have a need for bifunctional particles combining luminescence and ferromagnetism. This demand cannot be satisfied with any of the semiconducting compounds. This necessity was the starting point for the development of new types of luminescent particles. One direction to overcome these problems was based on semiconducting particles based on rare-earth-doped insulating oxides. However, these materials do not exhibit ferromagnetism.

A completely new approach [6, 15, 16] to overcome the problems described above, uses insulating oxide nanoparticles coated with a layer of an organic lumophore, and a polymer coating at the outside. Figure 9.23 displays the design of these new composites. In this design, the oxide core is selected according to the demanded properties, for example, one may select a magnetic material. The polymer at the surface has to provide contact to the surrounding medium, for example, it may be hydrophilic or hydrophobic, or may carry any other functionalization. For the organic lumophore, there are, except for the problems connected to synthesis, no limitations.

The design depicted in Figure 9.23 has one more essential advantage as compared to quantum dot particles: The emission color of quantum dots is determined by the particle size. If one needs two or more different colors in one application, one has to synthesize for each one of these colors particles of a well-defined size in a narrow size distribution. This is a very difficult task. In contrast, the emission
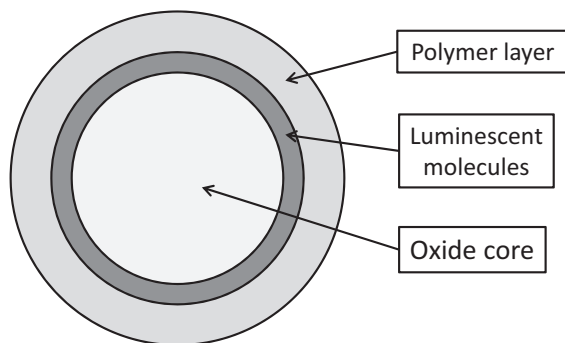
Figure 9.23 Luminescent composite according to Vollath [6, 15, 16] consisting of an oxide core, a luminescent layer and an external polymer layer. The ceramic core is selected according to the demanded properties, whereas the polymer coating has to mediate to contact to the surrounding medium.

(a)

(b)
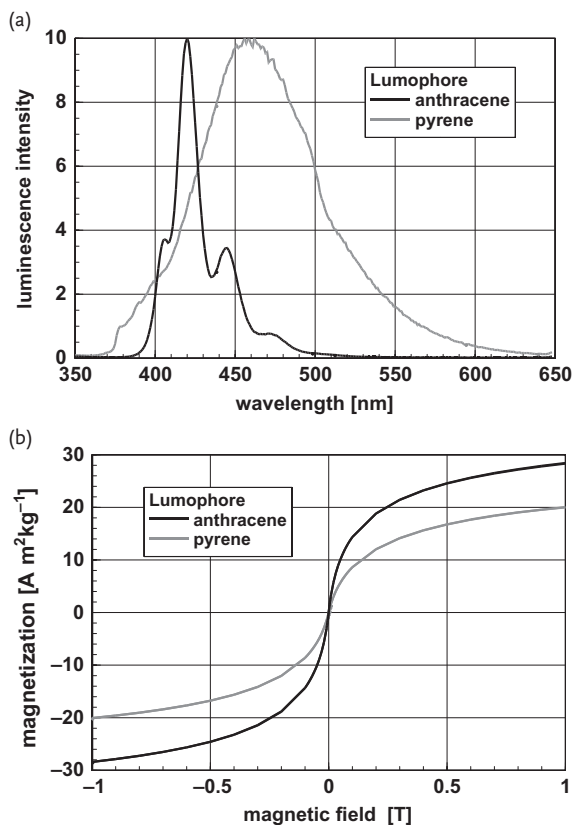
Figure 9.24 Two examples of composite magnetic nanoparticles with additional luminescence properties. Anthracene and pyrene were selected as lumophores. The figure displays the luminescence spectra (a) and the magnetization curves (b). The difference in saturation magnetization is caused by different particle sizes and not by the lumophore [16].

color of the design according to Figure 9.23 is size independent. It depends only on the selected lumophore.

As an example, the design of luminescent magnetic particles is explained. This example is thus very special, as magnetism and luminescence are never found together in nature. As mentioned above, this combination of properties, combined with special functionalization, is needed in applications connected to biotechnology and medical diagnosis, such as magnetic cell separation, identification, and quantification. Figures 9.24a, b display luminescence spectra and magnetization curves of Fe_2O_3/anthracene/PMMA and Fe_2O_3/pyrene/PMMA nanocomposites. The difference in the saturation magnetization, visible in Figure 9.24b is caused by different particle sizes and not by the lumophore.

Box 9.3   Structure of the Molecules Pyrene and Anthracene

Pyrene and anthracene are polycyclic aromatic molecules. They are widely used as lumophores and educt for further organic synthesis. As each carbon atom has only three neighbors, there is always one of the neighbors with a double bond. However, these electrons are, similar as in graphene, not localized (Figure 9.25).
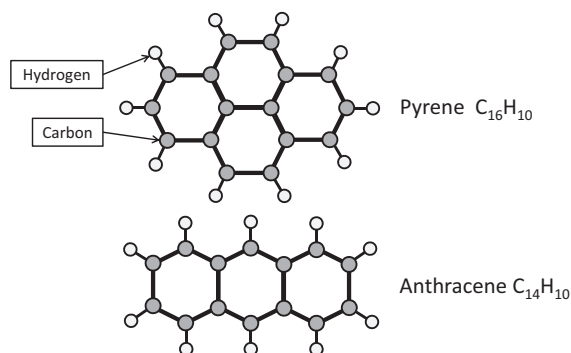
Figure 9.25   Molecular structure of pyrene and anthracene.

At the surface of a nanoparticle, the lumophore molecules are extremely tight side to side. Now one may ask if there is an interaction between the molecules, sitting at the surface, to form an excimer. This interesting question was analyzed using pyrene-covered alumina nanoparticles. Figure 9.26 presents the results. This figure compares the spectra obtained from these particles as powder and suspended in a liquid. One sees the excimer spectrum in case of the powder, which is not surprising, as the particles are close together. More surprising is the spectrum of the particles suspended in a liquid in extremely low concentration. In this case, the molecule spectrum appears. Obviously, the excimer formation is only from particle to particle and not from molecule to molecule sitting on the same particle.

The next open question is of a possible interaction between the oxide core and the organic lumophore at the surface. The background to this question is twofold: Where are the UV photons absorbed and what is the oxide core's influence on the emission spectrum? The reason for the first question is obvious. One can think that the large amount of material in the particle core acts as a parasitic absorber reducing the efficiency of the nanocomposite. An answer to this question is obtained by analyzing a series of composites consisting of different oxide cores, the same lumophore, in this case pyrene, and a PMMA layer at the outside. The results of these experiments are summarized in Figure 9.27. For these experiments, the series of oxides from silica, SiO_2, with the lowest molecular weight,
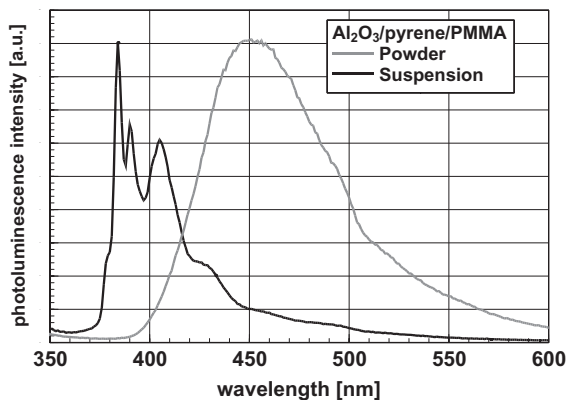
Figure 9.26 Emission spectrum of composites consisting of an alumina core coated with pyrene as lumophore and an outside layer of PMMA. The spectrum of the powder is the excimer spectrum, whereas in a liquid suspension with low concentration, the molecule spectrum appears, obviously, the molecules sitting on the particle are not interacting. In contrast to the powder, in a diluted suspension, the molecule spectrum is emitted [6].
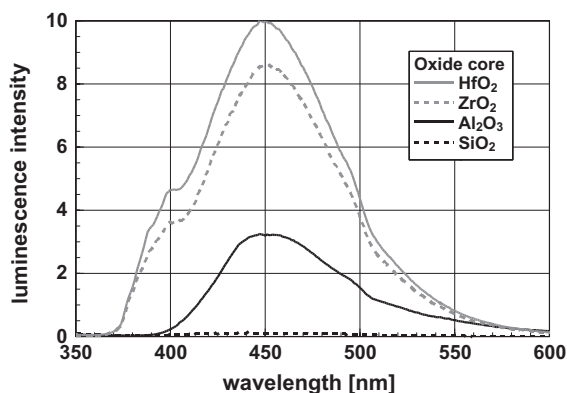
Figure 9.27 Luminescence intensity of nanocomposite particles with different oxides as core, pyrene as lumophore, and an outside layer of PMMA. It is readily visible that the luminescence intensity increases from silica over alumina and zirconia to hafnia. For excitation, a wavelength of 325 nm was chosen. The influence of the ceramic core on the luminescence intensity is readily visible [6].

over alumina, Al_2O_3, and zirconia, ZrO_2, to hafnia, HfO_2, with the highest molecular weight. For excitation, UV photons with a wavelength of 325 nm were applied.

Analyzing Figure 9.27, one sees a strong dependency of the intensity of the emitted light on the oxide core. It seems to be obvious that the intensity increases with increasing atomic number of the metal ion in the oxide. This relationship suggests a correlation with the UV absorption in the oxide core. Therefore, the
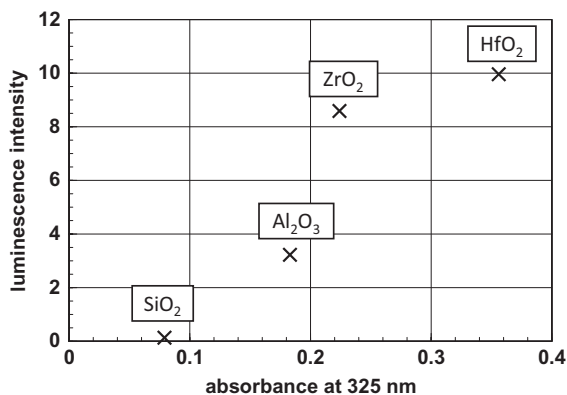
Figure 9.28 Luminescence intensity of nanocomposite particles with different oxide cores and pyrene as lumophore at the surface as a function of the absorbance at the excitation wavelength. One sees a direct relationship between the UV absorption in the oxide core and the luminescence intensity [6].

absorption at the excitation wavelength of 325 nm in a suspension of these particles was measured. The results are depicted in Figure 9.28. In this graph, the intensity of the emission maximum is plotted versus the absorbance at 325 nm. The result of these measurements is unequivocal. With increasing absorption, an increasing luminescence intensity is observed. These results propose a two-step mechanism: the photons are absorbed in the oxide core and the excitation is transferred to the pyrene at the surface. Lastly, the oxide core acts as an amplifier for the luminescence in the system. The oxide cores used for display of the results in Figures 9.27 and 9.28 are insulators. In the case of a semiconducting oxide core, say, for example, zinc oxide, luminescence of the coating is not observed, as the core itself has the possibility to emit light; therefore, there remains no excitation to be transferred to the pyrene at the surface.

As mentioned above, one has to ask if there is an influence of the oxide ceramic core on the emission spectrum of the composite. This question will be answered using nanocomposite particles with maghemite, γ-Fe_2O_3 as core and different lumophores. (The results for other oxide core particles are more or less identical.) Figure 9.29a displays the emission spectrum of such a composite with pyrene as lumophore. For comparison, the excimer emission spectrum of pure solid pyrene is also plotted. One sees that the spectrum of the nanocomposite is quite similar to that of the pure lumophore. One sees a slight blueshift of ca. 15 nm and, more prominently, the spectrum of the composite has lost the fine structure, characteristic of pyrene. In the case of anthracene at the surface of oxide nanoparticles, the observations are different. Figure 9.29b displays the spectra of pure anthracene and that of the nanocomposite particle. The spectrum of anthracene is more structured as compared to the pyrene excimer spectrum. Each maximum of the pure material, enumerated from one to six in Figure 9.29b and additionally, the

(a)

(b)
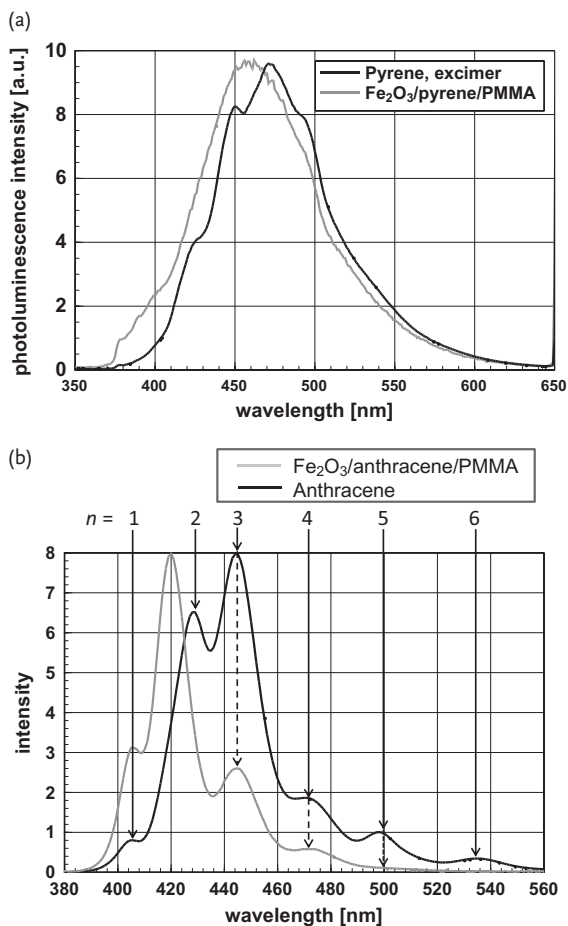
Figure 9.29 Influence of the oxide core on the luminescence spectrum of the lumophore applied as coating. (a) Photoluminescence spectra of a nanocomposites powder consisting of maghemite as core, pyrene as lumophore, and PMMA as outer layer in comparison to the excimer spectrum of pure pyrene [6, 15]. (b) Luminescence spectra of pure anthracene and the composite γ-Fe_2O_3/anthracene/PMMA. Each of the maxima in the spectrum can be associated with a vibration mode. The main difference between these two spectra is the strongest line of the composite, positioned between the modes 5 and 6, that do not appear in pure anthracene [6, 15].

spectrum of the composite particle is shown in this figure. However, there is one exception: The mode $n = 2$ is, in case of the composite particle either shifted to shorter wavelength, or the composite particle shows this extra line. This, until now unexplained phenomenon, is important with respect to technical applications: Using this type of composite materials, for example, as a security marker, one has a unique feature, which cannot be faked easily. This phenomenon is not restricted

to iron oxide as the core; it is rather found with any other insulating oxide as the core.

In the previous section, the case of increasing the luminescence efficiency by the application of an insulating particle as a photon absorber and transfer of this excitation to an organic lumophor at the surface was discussed. Now, a different type of increase in the luminescence efficiency will be discussed. Assume a semiconducting nanoparticle as the core and again an organic lumophor as embedding matrix. The particle and lumophore are selected in such a way that the emission of the core excites the coating. Liu *et al.* [17] developed on the combination of CdSe(ZnS) nanoparticles as the core with an organic lumophore, a triplet iridium(III) complex (Bis(4-trifluoro-methyl)-2-phenyl-benzothiazolatoacetylacetonate-iridium(III)). Furthermore, this specific combination was selected because the emission of the organic lumophore comes close to white light. In this study, the CdSe(ZnS) particles with sizes around 1 nm, covered gold nanoparticles with 5 nm diameter. The proximity of the CdSe/ZnS clusters to the gold nanoparticles leads to a slight blueshift as compared to pure CdSe(ZnS) nanoparticles. Interestingly, the photoluminescence intensity of the gold-containing agglomerates exceeds that of isolated CdSe(ZnS) nanoparticles.

Figure 9.30 displays the emission spectrum of the CdSe(ZnS) nanoparticles together with the absorption spectrum of the organic iridium(III) complex. One sees that the emission of the core has the ability to excite the organic coating, as the emission line is just in the center of the absorption range.

The advantage of this nanocomposite is visible in Figure 9.31. In this figure, besides the spectrum of the composite with a ratio of 1 : 3 of the Ir complex to the CdSe(ZnS) nanoparticles, the spectrum of the pure organic lumophore is shown.
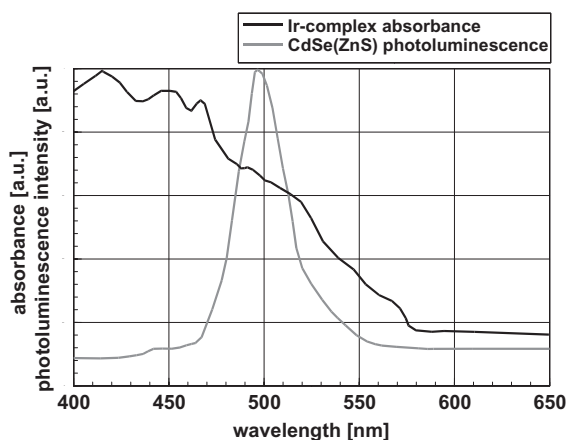
Figure 9.30 Spectral absorbance of the Ir(III)-complex, as described in the text and the emission spectrum of CdSe(ZnS). One sees that the emission of the semiconducting particle is exciting the organic lumophore [17].
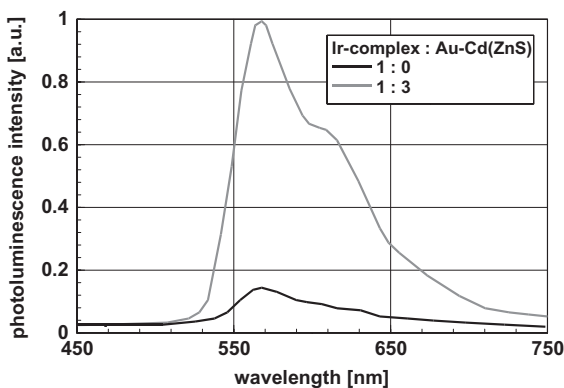
Figure 9.31 Photoluminescence spectra of the pure Ir-complex and a nanocomposite with a ratio of 1 : 3 of the Ir-Complex to the CdSe(ZnS) nanoparticles [17]. The significant increase of the photoluminescence intensity by energy transfer from the nanoparticles to the organic lumophore is clearly visible.

Analyzing Figure 9.31, one sees an improvement with respect to the luminescence intensity of a factor of nearly seven. Furthermore, as the emission maximum of the particles at ca 500 nm is not visible at all, the spectrum suggests that the intensity of the primary radiation of the CdSe(ZnS) particles was absorbed completely in the organic matrix. Lastly, this is a similar excitation transfer that leads to higher intensity, as discussed in the previous example, where insulating oxide particles were applied as the absorber. Additionally, the authors show that the described composite may also be used for electroluminescence devices.

In the previous sections, phenomena were discussed that were altered by the particle size or the combination with nanoparticles. Now an optical luminescence phenomenon will be discussed, which is not known, may be impossible, with bulk materials. It was found that insulating oxide nanoparticles, coated with PMMA show luminescence. In Figure 9.32, besides the broad luminescence peak, one sees the marker of the exciting laser radiation at 325 nm. This figure displays experimental results obtained with hafnia, HfO_2, zirconia, ZrO_2, alumina, Al_2O_3, and tin oxide, SnO, as the core. One sees that the insulating particle show a broad luminescence, but, the semiconductor tin oxide shows no luminescence at all. It is striking that the composite with hafnia as the kernel has the highest and that with the silica kernel the lowest luminescence intensity. Therefore, as in the case of lumophore-coated particles (see Figure 9.27), one can plot the luminescence intensity versus the absorbance at the excitation wavelength of 325 nm. Suspending these nanocomposite particles in a liquid in high or at low concentration leads to identical spectra.

In Figure 9.32, one sees that the luminescence intensity of the PMMA-coated composite particles increases from alumina through zirconia to hafnia. These three oxides are wide-gap insulators. The composite with tin oxide as the core does not show any luminescence. Plotting the luminescence intensity versus the
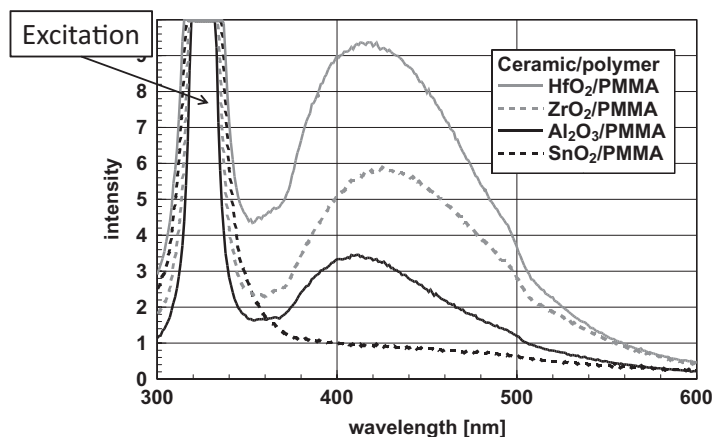
Figure 9.32 Luminescence of oxide nanoparticles coated with PMMA. It is remarkable that luminescence is observed only with insulating oxide cores. The semiconducting core tin oxide does not show this phenomenon [16].
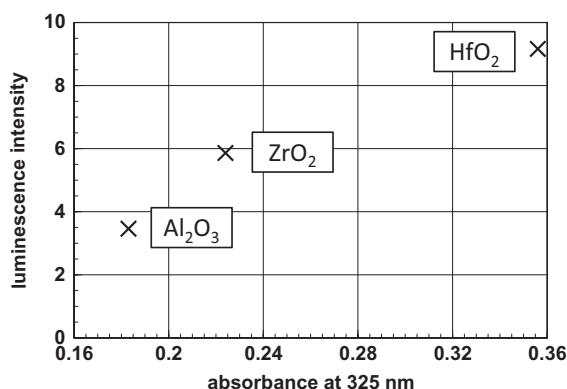
Figure 9.33 Luminescence intensity of three different composite particles with PMMA coating as a function of the absorbance. One sees that an increasing absorbance of the excitation wavelength of 325 nm leads to increased luminescence intensity [16].

absorbance at the excitation wavelength, one obtains a graph, Figure 9.33, which is nearly identical to Figure 9.27. Obviously, in both cases, the same mechanisms are active. This means that the exciting photons are absorbed in the oxide and as a second step; the excitation is transferred to the coating where the luminescence occurs.

To analyze the mechanism leading to luminescence of these oxide / PMMA nanoparticles, one has to look at the interface of an oxide with PMMA. In the literature, it is shown that PMMA directly touching the oxide surface is bound with an ester-like linkage [18, 19] to the surface (Figure 9.34). This means that the
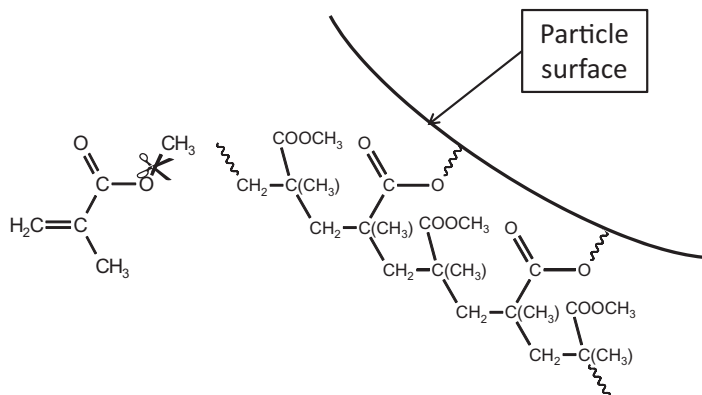
Figure 9.34 Model of the MMA molecule and its polymerisate at the surface of an oxide according to Meyer *et al.* [19] and Weng *et al.* [18] To bind these molecules at the surface, the (CH₃) group is cut off. Now, the carbonyl group (C=O) directly touches the surface. The remaining oxygen is now part of the oxide particle.

CH$_3$ group adjacent to an oxygen ion is cut off (see insert in Figure 9.34). Therefore, the polymer at the surface is a modified PMMA (m-PMMA). Based on these results, nanocomposite particles consisting of an oxide core bonded to a modified PMMA may be described as one huge molecule, R-(C=O) – O-(oxide particle). The structure formula of MMA and a model of the connection of the polymer to the particle are given in Figure 9.34, additionally; the bonding where the (CH$_3$) group is cut off is indicated in the insert. The oxygen atom adjacent to the carbonyl group is now part of the oxide. The most important is the carbonyl group directly at the surface of the nanoparticle, as this group is responsible for the luminescence. This is similar to, for example, in biacetyl, CH$_3$–(C=O)–(C=O)–CH$_3$, where the two carbonyl group are responsible for luminescence [20]. Therefore, one may assume to a first approximation that in the m-PMMA / oxide system, where a carbonyl group is close to the ceramic surface, the same mechanism acts.

Box 9.4   How to Prove the Luminescence Oxide PMMA Mechanism?

It sounds odd, but there are oxide particles that do not show luminescence, coated with a polymer, not showing fluorescence, that together as a nanocomposite, show luminescence. The questions arise: Why is luminescence observed at all? Why do we know that it is exactly the carbonyl group adjacent to the oxygen atom that is responsible for the luminescence phenomenon? Obviously, it is the combination, the nanocomposite, that provokes this effect.

This was proven using the smallest molecule having a carboxylate group binding similarly to the ceramic surface. Formic acid methylester (FAME), H–(C=O)–O–CH$_3$, was selected to coat the particles instead of MMA. These

molecules bind, similarly as m-PMMA, to the surface forming H–(C=O)–O– (oxide particle).

Figure 9.35 displays the luminescence spectrum of these particles with a zirconia core. This spectrum is nearly identical to that found with m-PMMA-coated materials, as is shown in Figure 9.32. This is thus remarkable as aqueous solutions of formic acid methylester show luminescence with a few isolated lines. These findings indicate that the carbonyl group of these compound, bonded to the particle surface, is responsible for the emission spectrum.

This experiment proves unequivocally that the luminescence of oxide/PMMA nanocomposites is a surface-related phenomenon, stemming from the carbonyl group directly adjacent to the surface.
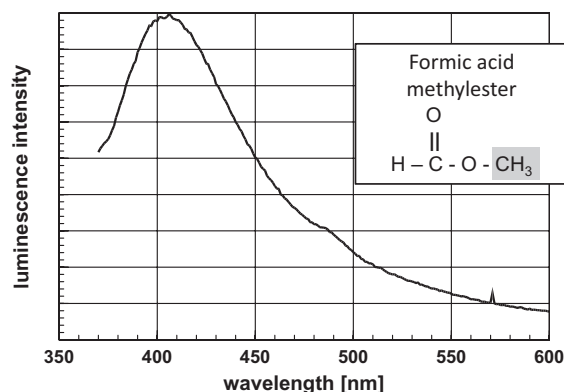
Figure 9.35 Luminescence spectrum of formic acid methyl ester as coating at the surface of zirconia. During binding this molecule at the particle surface, the gray shaded methyl group was removed and the remaining oxygen atom became part of the particle [6]. The carbonyl group, the only residue of the original molecule is responsible for the luminescence.

Now, one asks if there is any particle-size dependency of the luminescence of the oxide / PMMA nanocomposite particles. Experiments in this direction resulted in Figure 9.36. In this figure, the luminescence intensity of ZrO_2/PMMA nanocomposites particles is plotted as a function of the inverse particle size. For this figure, the intensity maximum in the spectrum was taken as the intensity. To improve visibility of the relevant laws, this and the next graph are modified.

The linear relation between luminescence intensity and inverse particle size, visible in Figure 9.36 may be described by the equation

$$I = I_0 + \frac{b}{d}. \tag{9.10}$$

The quantity I stands for the luminescence intensity, I_0 and b are fitting parameters, and d is the particle diameter.
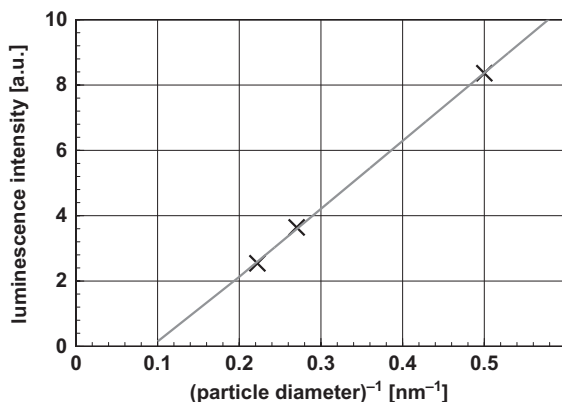
Figure 9.36 Luminescence intensity of ZrO$_2$/PMMA nanocomposites as a function of the inverse particle size following Eq. (9.10). The proportionality with $\dfrac{1}{d}$ indicates a proportionality of the intensity to the surface of the particles [6].

For a given quantity of material, the number of particles is proportional to d^{-3}, the surface of one particle is proportional to d^2; therefore, at the surface this quantity of particulate matter is proportional d^{-1}. Therefore, Eq. (9.10) says that the luminescence intensity is directly proportional to the surface area of the particles. This direct proportionality between luminescence intensity and the particle surface is an additional proof of the idea that the ceramic/polymer interface is the source of the luminescence. Figure 9.36 shows diminishing small luminescence intensities for particle sizes larger than ca. 10 nm. Certainly, this is why this phenomenon was discovered with nanocomposites and not earlier.

The next question relates to the particle-size dependency of the emitted wavelength λ at the maximum. The experimental results are depicted in Figure 9.37. Mathematical fitting leads to the relation

$$\frac{1}{\lambda} = \frac{1}{\lambda_0} + bd^3. \tag{9.11}$$

This relation allows rectification on the coordinate system with the $\left(\dfrac{1}{\lambda}\right)$ as abscissa and d^3 as ordinate. The quantities λ_0 and b are fitting parameters; d is the diameter of the ceramic core of the nanocomposite.

Analyzing the dependencies depicted in Figure 9.37 and based on Eq. (9.11), one sees that the wavelength of the emitted light increases with increasing particle diameter. The sign of the exponent of particle diameter is different from that of any other described mechanisms. This means that there is a blueshift with increasing particle diameter.

Similarly to the blueshift with decreasing particle size, a reduction of the line width at half-maximum intensity with decreasing particle size was observed [6, 15].
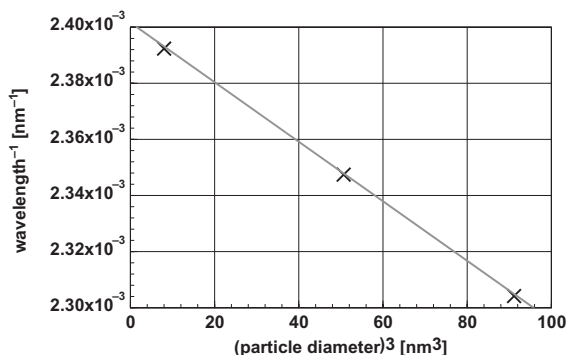
Figure 9.37 Dependency of the wavelength of the maximum of the emitted light of a ZrO$_2$/PMMA nanocomposites as a function of the particle diameter [7]. The mathematical description underlying this graph

$$\frac{1}{\lambda} = \frac{1}{\lambda_0} + bd^3$$ (Eq. (9.11)) is fundamentally different from that for quantum confinement, as the exponent of the particle diameter has a different sign. In contrast to all other mechanisms, an increasing particle size leads to longer wavelength.)

9.7
Selection of a Lumophore or Absorber

In the previous sections, a series of different nanoparticles and nanocomposites with special optical properties with respect to absorption and emission were discussed. Now the question arises which one of these possibilities is best for a specific application. A first clue for an answer may be found in Figure 9.38. In this figure, the emission spectra of three different types of emitters are presented. Obviously, generally, one has to distinguish between particles emitting in a broad band and particles emitting a relatively sharp line. In the class of the broadband emitter, one finds organic / inorganic nanocomposites, whereas, only quantum dots emit in a narrow spectrum. The latter statement is true only in cases where the particle-size distribution is narrow. On the other hand, quantum dots stemming from a production that delivers a broad particle-size distribution, may also be useful as broadband emitter. Besides the emission spectra, other criteria are necessary for selection. Such criteria are stability against UV-radiation and, not least, stability against oxidation and hydrolysis. In particular, many types of quantum dots are sensitive to chemical degradation. The narrow-band emitters, such as the quantum dots, have their main application in medicine and biology, where it is often necessary to provide particles, emitting in different colors; however, with the same surface chemistry. This makes multiplexed detection of different biological targets possible. The tunability of the emitted wavelength, of quantum dots, gives the possibility to adjust the emission in the near-IR, allowing fluorescence imaging in living organisms. It is well known that many of the semiconducting compounds that may be used for quantum dots are sensitive to
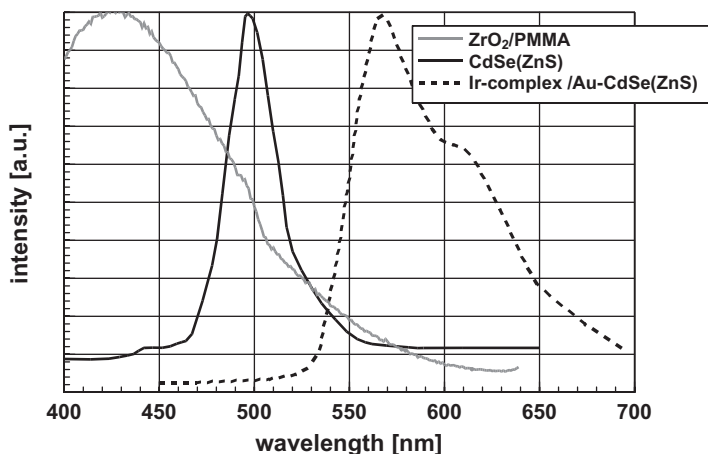
Figure 9.38 Comparison of the spectral properties of different luminescent systems. It is remarkable that the composite systems ZrO₂/PMMA [6] and CdSe(ZnS) embedded in an Ir-complex [17] excel in broad emission lines, whereas the CdSe(ZnS) [17] quantum dot is characterized by a narrow emission line.

oxidation and hydrolysis. For protection, coating with a polymer is advised. This leads to the necessity of nanocomposites. Looking at the special type of nanocomposites with a ceramic core and an organic lumophore, one has the huge advantage of a nearly infinite number of compounds with different properties. Furthermore, these composites are the only chance to combine optical and magnetic properties in one particle.

The considerations are different, looking the optical absorbance. Knowledge of the absorbance is necessary to find an optimal wavelength for excitation and, most importantly, in the case of application as a pigment. In particular, for the application as a pigment, detailed considerations with respect to long-term stability are necessary. Sometimes, this point makes the application of some particles difficult, or, the final product must be protected against too much light, oxidation, and hydrolysis. A comparison of three different types of optical absorbers is given in Figure 9.39. It compares the behavior of an organic compound (FTIC, fluorescein isothiocyanate) with a metal, Au, and a semiconductor, ZnSe. The semiconductor excels in a clear expressed absorption edge. With respect to pigments, this gives by far the best colors. The metallic absorber is characterized by the plasmon resonance peak and on the short-wavelength side of this peak a minimum of the absorbance. This minimum is the reason for a slight discoloration. In the case of gold particles, a red pigment, this gives rise to a slight blue hue, which is typical of the so-called gold ruby glass. Looking at the organic absorber, one sees similar problems as described in the case of gold; however, it is much more pronounced.
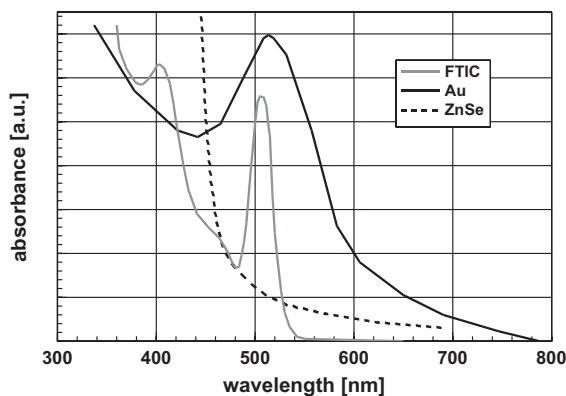
Figure 9.39 Comparison of the absorbance of different types of optical absorbers. The organic compound, FTIC (fluorescein isothiocyanate) [17] shows a sharp absorption maximum in the visible range and increased absorbance in the blue and UV. The plasmon resonance absorption of gold is similar; however, the minimum of the absorbance in the blue is not significant. The absorbance of the semiconducting particles of ZnSe, which exhibit a clear-cut absorption edge, is very different. This type of pigments gives the clearest colors [7].

9.8
Electroluminescence

In electroluminescent devices, light emission is stimulated by electric fields instead of energy-rich photons. Therefore, light emission can be controlled easily by means of electronic devices. The electrical stimulation may be provided by the electric field in a field-effect-like structure or by injection of charge carriers. Presently, the latter process is the one with significantly better chances for broad industrial application.

With respect to economical applications, electroluminescence has an extremely high potential. Primarily, in consumer products, such as TV sets, cell phones, or monitors, there is the potential to replace the back-lit systems working with liquid crystals devices (LCD). Looking at these applications, systems working with special organic particles (OLED) are the most progressed. Figure 9.40 displays the basic setup of an electroluminescence device. Such a device is based on a glass substrate, which is coated with ITO (indium tin oxide), an optically transparent electrical conductor. The next layer contains the luminescent particles. This layer is covered with a counterelectrode, in most cases made of aluminum. In-between the electrodes there is the electrical field, which stimulates light emission. Even when the stimulation of light emission by injection of charge carriers is a direct current, DC, phenomenon, in many cases the application of alternating current, AC, is of advantage.
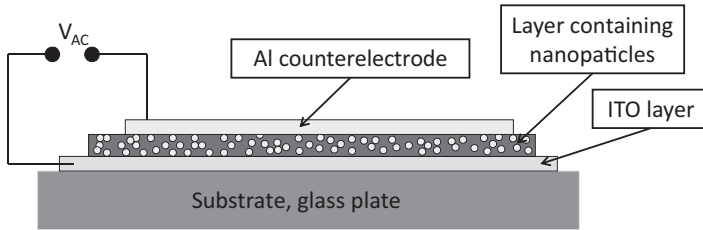
Figure 9.40 Electroluminescent device. Usually, it consists of a glass substrate coated with an optically transparent electric conductor (ITO). The next layer contains the electroluminescent particles, which is coated with the aluminum counterelectrode.

Box 9.5   Physical Background of an Electroluminescence Device with Charge-Carrier Injection

Figure 9.41 displays the general design of an electroluminescence device together with the energy levels of the materials in use. The glass substrate is coated with ITO (indium-tin-oxide), a material with a high work function (= the energy necessary to emit electrons, to a good approximation, about a half of the ionization energy of an isolated atom of the metal; equal to the *Fermi* energy), has besides its transparency and electrical conductivity the additional advantage of injecting positively charged holes into the layer of nanoparticles.

The next layer carries the nanoparticles. As counterelectrode, a sputtered aluminum layer, with a very low work function for electrons to inject electrons into the system, is applied.
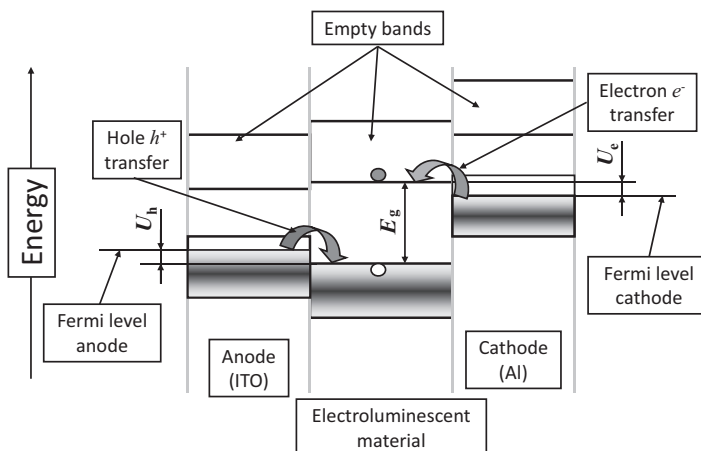
Figure 9.41 Electroluminescence system based on charge transfer. The anode emits holes and the cathode electrons into the bands of the luminescent material. Light is emitted as result of the electron–hole recombination.

When this device, depicted in Figure 9.41, is connected to a direct electric current source, the cathode, aluminum, emits electrons e^-, jumping from the conduction band of the metal into the lowest unoccupied band of the luminescence material. The anode, ITO, releases holes h^+ into the luminescent material. In reality, an electron jumps from the highest occupied band of the luminescence material into the conduction band of the anode, releasing a positively charged hole, in the luminescence layer. The energy necessary for this process is U_e at the side of the cathode and U_h at the anode's side. The anode material must be selected in such a way that the energy to emit electrons, the work function, is significantly larger than that of the cathode material. Radiative recombination of the hole in the highest occupied band of the electroluminescent material and the electron in the conduction band leads to the emission of light. In the simplest case, the wavelength of the emitted light λ can be calculated using the energy of the bandgap E_g: $\lambda = \dfrac{ch}{E_g}$ (c is the velocity of light, h is the *Planck* constant) To emit light, one of the electrodes must be made of transparent or translucent material, usually ITO. Doping of the luminescence material may modify the process without changing the basic principles. From this idea, the device shown in Figure 9.41 is a direct current system; however, experimental experience shows that the application of an alternating current source increases the efficiency of the system.

A summary of the electric properties of electroluminescence cells was given by Nelson and Fothergill [21].

The concept to apply quantum dots as emitters in electroluminescence devices has a series of advantages. The main advantage may be found in the fact that the emission wavelength can be adjusted by the particle size. This allows the design of multicolor screens using only one type of particle. Therefore, the chemistry of the system is independent of the color. Furthermore, using appropriate intermediate layers it is possible to design systems with a multitude of layers to improve the efficiency of the system. These additional organic layers, charge-carrier emitter layers, are placed between the different layers of nanoparticles. This provision is necessary to repeat the active layer system a few times to increase the efficiency of the system.

The light emitter in electroluminescence devices based on charge transfer may be set up with with particles and with nanorods. There are indications that the application of nanorods may increase the efficiency. This phenomenon is displayed in Figure 9.42. Furthermore, this figure contains a juxtaposition of experimental spectra obtained by photo- and electroluminescence.

Figure 9.42 displays the spectral intensity distribution of ZnS nanorods with a length of 400 nm and a diameter of roughly 35 nm in comparison to ZnS nanoparticles with a mean diameter of 4 nm synthesized by an equivalent process. To obtain a broad emission band, the particles and the rods were doped with 0.13%
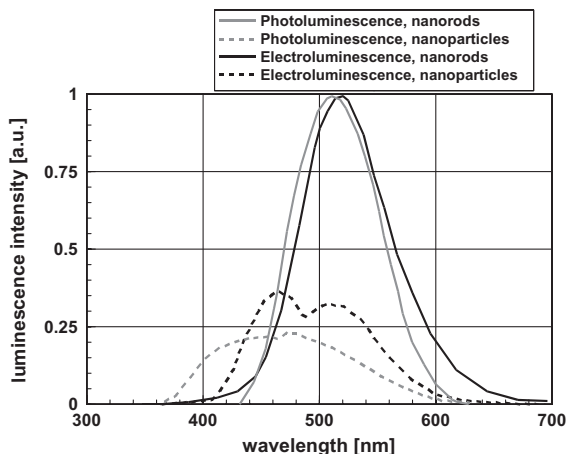
Figure 9.42 Electroluminescence and photoluminescence spectra of doped ZnS nanoparticles ans nanorods. It is important to realize that the electroluminescence spectrum shows a slight shift to longer wavelenth. In this example, nanorods exhibit higher intensities as compared to the particles. The wavelength shift of the maxima of particles and rods is caused by the different size of particles and rods [22].

Cu^+ and 0.1% Al^{3+}. As zinc is present as Zn^{2+} in the lattice, this doping creates positively charged holes and additional electrons in the energy bands. In this example, the significantly larger nanorods exhibit higher luminescence intensities as compared to the particles.

Comparing the photo- and electroluminescence spectra, an interesting, often observed, redshift in the case of electroluminescence is visible. A lot of work was done in the direction of multilayer systems to increase the luminescence yield. A typical example of a multiplayer system using CdSe nanoparticles and a PPV (poly(*p*-phenylene vinylene) layer as charge-carrier emitter was published by Gao *et al.* [23]. Figure 9.43 displays the electroluminescence spectra of a CdSe / PPV multilayer system, consisting of 20 double layers, for different voltages. The emission spectrum is very broad; it starts at 500 nm and reaches beyond 800 nm into the near-infrared region. As expected, the emitted intensity increases with increasing voltage applied to the system.

The finding depicted in Figure 9.43 becomes systematic in Figure 9.44. In this figure a plot of the dependency of the emitted intensity at the emission maximum at 657 nm versus the applied voltage is depicted. Most striking is the existence of a threshold voltage close to 3.5 V to obtain the first emission.

The dependency of the emitted light of the voltage allows analog control of the brightness. However, as the intensity of the emission increases more than proportional to the applied voltage, a brightness control by digital voltage pulses may promise better efficiency. In contrast to the multilayer technology, which is most appropriate for rigid substrates, the monolayer technology is better for printable applications, allowing the design of flexible display screens.
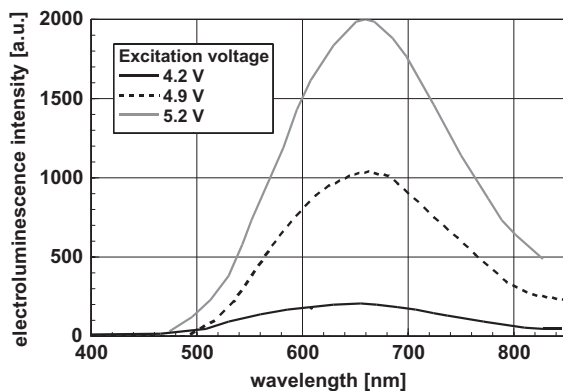
Figure 9.43 Electroluminescence spectra of a CdSe / PPV multilayer system, consisting of 20 double layers, for different voltages. The emitted intensity increases with increasing voltage, the spectral distribution remains unchanged [23].
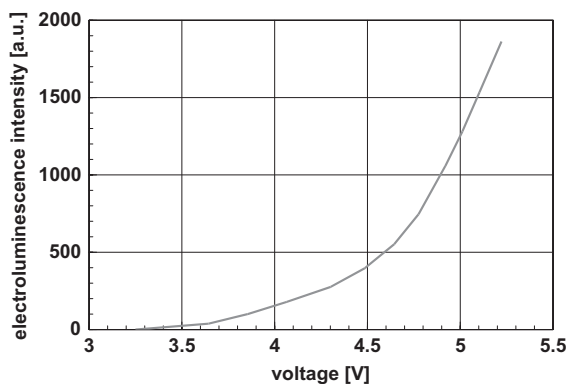
Figure 9.44 Electroluminescence intensity of a ZnS/PPV multilayer system with twenty double layers as a function of the applied voltage. The intensity at the emission maximum (657 nm, see Figure 9.42) was taken. At a voltage of ca. 3.5 V a threshold is clearly visible [23].

9.9
Photochromic and Electrochromic Materials

9.9.1
General Considerations

Photochromic materials change their color under the influence of light, electrochromic materials do so under the influence of an electrical field. The changes in color are reversible. Generally, photochromic materials are white or colorless in the dark; and in sunlight or ultraviolet radiation they change color. The intensity of coloration is a function of light intensity. After removing the light source, the

material loses coloration. Electrochromic material changes color when connected to a source of electricity. When not connected to an electrical field, their color is white. To change color, in most cases only small electric charges are necessary. Both photochromic and electrochromic materials have a huge economic potential for applications. Most important applications are found, for example, in windows, which are either self-darkening by light or that are controlled during darkening with an electronic control system.

However, in technical applications, both types of materials suffer a few crucial problems: They change color, which means they get a new distinct color, in most cases blue or green. However, most of the customers in large-volume technical applications prefer the change from white, respectively, colorless to gray or even black. The second problem is the time constant of the color change. Generally, the consumer wants an immediate reaction to a change of external conditions. This may be the change in sunshine intensity in the case of photochromic windows or just the necessity of changing the illumination level in rooms by the use of electrochromic materials. In view of environmental protection, both types of materials have a high potential to save energy as they can regulate illumination levels, as well as glare, heat gain or loss. Buildings supplied with these windows use less energy for air conditioning, save money and reduce air pollution associated with energy production. Further applications include large-scale electrochromic display panels, front and rear windows, and mirrors for cars and trucks. In particular, the latter applications need fast response of the material to changing conditions, which is, until now, not available. For broader applications in electronic display systems, materials or a combination of materials leading to red and yellow colors are missing. However, besides all these problems, windows based on the photochromic and especially electrochromic effect are already commercially available.

Photochromic and electrochromic materials apply the fact that in a few oxides, such as WO_3 or MoO_3, the metal ion changes easily its valency. As long as these oxides consist of ions with the valency 4^+ and 6^+ only, they are white, respectively, colorless; In the case of the appearance of 5^+ ions, these oxides are colored. (Strictly speaking: Photochromic and electrochromic devices use these oxides always in the hypostoichiometic state, therefore, the exact formula is MeO_{3-x}. As the deviation from ideal stoichiometry is small, for reasons of brevity, in the following text, generally the shorter version MeO_3 is used.) The photochromic or electrochromic properties of these oxides are related to electron–hole pairs directly connected to deviations from the perfect stoichiometry. Both types of materials differ only in the way how the change in stoichiometry is provoked.

9.9.2
Photochromic Materials

The best-known photochromic materials are WO_3, MoO_3 and Nb_2O_5. Whereas WO_3 and Nb_2O_5 change from white to blue, MoO_3 changes from white to green. The presence of water in the atmosphere around the photochromic device or at the surface is a necessary prerequisite for the change of color. When photochromic

oxides are excited by energy-rich photons, positively charged holes and free electrons are formed. The holes react with adsorbed water and produce protons:

$$H_2O + 2h^+ \Rightarrow 2H^+ + O. \tag{9.12a}$$

The protons react with the oxide, which changes the stoichiometry

$$MeO_3 + xH^+ + xe^- \Rightarrow H_xMe_{1-x}^{6+}Me_x^{5+}O_3. \tag{9.12b}$$
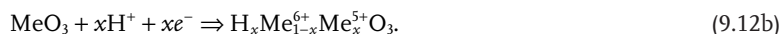
The material formed according to Eq. (9.12b) changes color to blue or green. The oxygen radicals either occupy vacancy sites inside the material or escape from the particle. The possible immediate recombination of the charge carriers, $h^+ + e^- \Rightarrow$ heat, reduces the performance of the material. As the reaction according to Eq. (9.12a) needs exchange with the surrounding atmosphere, controlling the performance is difficult. The reaction according to Eq. (9.12a) is rate controlling occurring at the surface, the step according to Eq. (9.12b) is diffusion controlled. However, even when the diffusion of protons is relatively fast, lastly, this is the rate-controlling step.

The phenomena provoked by protons may be obtained with alkaline-metal doping, too. For alkaline-metal-doped materials, Eq. (9.12b) writes:

$$MeO_3 + xA^+ + xe^- \Rightarrow A_xMe_{1-x}^{6+}Me_x^{5+}O_3. \tag{9.13}$$
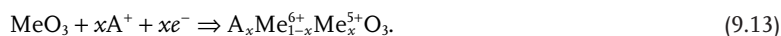
A^+ is a monovalent ion, generally an alkaline ion. However, also in doped materials, the efficiency of the system depends on the number of free electrons that can react with the metal Me.

A typical example of the absorption spectra of MoO_3 nanoparticles indicating photochromic behavior is shown in Figure 9.45 [24]. This graph displays the absorption of MoO_3 in the bleached state (0 s illumination time) and after two different times, 360 and 2160 s, of irradiation with a pulsed laser emitting 72 mW/pulse at 308 nm.
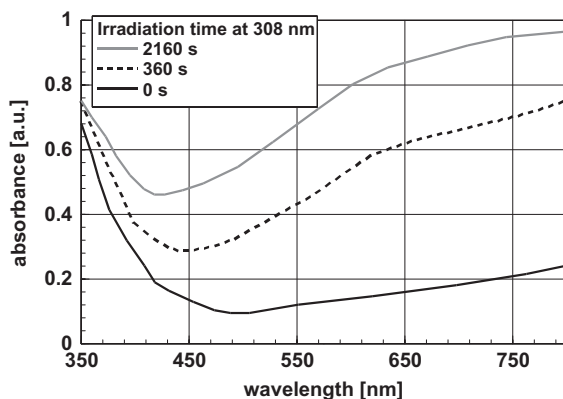
Figure 9.45 Absorption spectra of photochromic MoO_3, the parameter is the irradiation time with a 308-nm pulsed laser. At 0 s, the material is in the bleached state, at 2160 s the coloration has reached the saturation level [24].
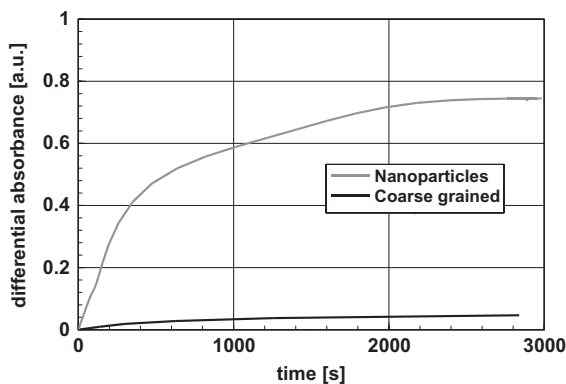
Figure 9.46 Differential absorption during illumination with a 308-nm pulsed laser at a wavelength of 750 nm as a function of the illumination time for nanoparticulate and coarse-grained MoO_3. (The differential absorbance is the difference of the absorbance between the bleached and the colored state.) The significantly faster reaction of the nanoparticles as compared to conventional coarse-grained material proves that the photochromic reaction is at least partly controlled by a diffusion process [24].

From Figure 9.45 it is obvious that the intensity of coloration increases with time. However, the time needed for saturation is very long; a photochromic change of the color up to the saturation level is a very slow process. A clear indication that the proton diffusion within the particles is rate controlling and, therefore, responsible for the long time, is given in Figure 9.46. In this figure, the time evolution of the color change is plotted for two different grain sizes, nanoparticles and coarse-grained MoO_3 at a wavelength of 750 nm. This graph indicates clearly the advantage of applying nanoparticles instead of coarse-grained material. As the diffusion time is indirectly proportional to the particle size squared this result clearly proves that a diffusion process is, at least to a certain extent, rate controlling. Trying to come to a numerical relation encounters some difficulties. Assuming a relation of the particle size one to ten, one has to expect a time relation of one to one hundred. The experiment, however, delivers a relation of one to thirteen. Lastly, this says that there are other processes controlling the reaction rate. This may be the reaction according to Eq. (9.12a) or just, as in the case of sensors, the gas diffusion in-between the particles.

9.9.3
Electrochromic Materials

The most important electrochromic materials are MoO_3, WO_3, V_2O_5, and Nb_2O_5. The electrochromic effect can be improved by doping with small ions like Li^+, H^+ or P^{5+}. These ions are dissolved in the host material. The electrochromic effect is based on the reaction

$$MeO_3 + xA^+ + xe^- \Leftarrow \text{electrical current} \Rightarrow A_xMe^{6+}_{1-x}Me^{5+}_xO_3. \tag{9.14}$$
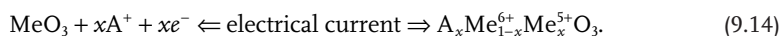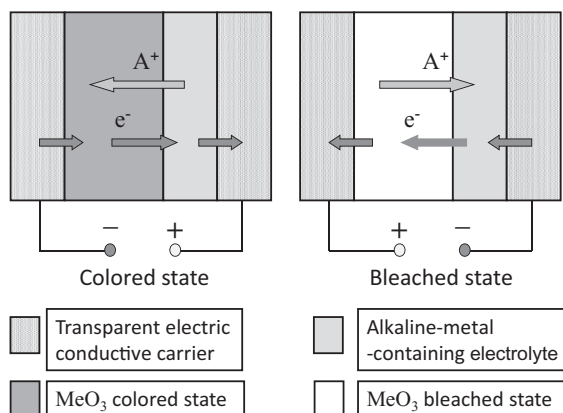
Figure 9.47 Setup of an electrochromic cell. Due to the transport of alkaline ions into or out of the electrochromic layer, the cell is colored or bleached. A^+ is, in most cases, an alkaline ion; also systems working with protons are possible. MeO_3 stands for WO_3 or MoO_3; however, the same mechanism is valid for all other electrochromic oxides based on a metal that can change valency.

Again, A^+ stands for an alkaline ion. To enable Eq. (9.14), an electrochromic cell must provide a reservoir of alkaline ions. In the case of oxides with layered structures, such as MoO_3, WO_3, etc. these ions are intercalated in-between the layers. This leads to the highest possible mobility of these charge carriers. The necessity of a reservoir for alkaline ions and transparent electrical electrodes leads to a design as depicted in Figure 9.47. This system consists of two transparent carrier plates each with one conductive surface. In-between these two plates, there is a layer of the electrochromic material and an additional electrolyte layer containing the alkaline ions. The electrolyte layer may, for example, consist of propylene carbonate containing a few tenths of a mol% of $LiClO_4$ as electrolyte. To switch the system between the bleached and the colored state, a voltage is applied across the system to move the monovalent ions into the photochromic layer or out of this layer by changing the polarity of the cell. Looking at the reaction in Eq. (9.14), by changing the polarity of the cell, the equilibrium state is either on the left-hand side (bleached) or on the right-hand side (colored). The voltage necessary to switch the cell is less than one volt, independent of the polarity.

The transmission of such an electrochromic cell is shown in Figure 9.48. This figure displays the absorbance of WO_3 in the bleached and the colored state. Furthermore, this figure compares the doped and undoped material.

The transmission spectra depicted in Figure 9.48 show some specific features: The electrochromic effect is most distinctive at long wavelengths, at wavelengths below 400 nm, the effect is not that important. This structure of the transmission spectrum in the colored state, high transmission in the blue and reduced transmis-
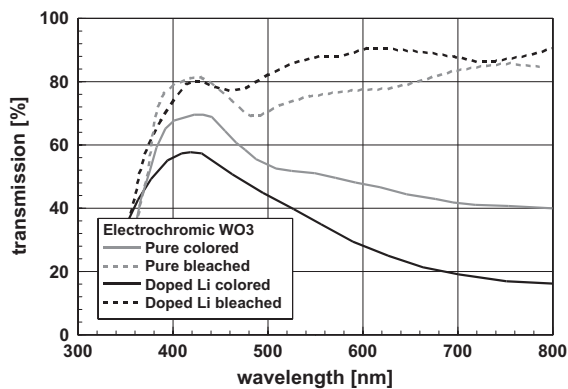
Figure 9.48 Transmission of an electrochromic cell in the bleached and colored state based on WO$_3$. Furthermore, this graph shows the significant advantage of doping with lithium. In the colored state, the transmission is reduced in the yellow and red range; therefore, in the colored state, the cell allows transmission of blue light [25].

sion in the yellow and red, leads to a blue appearance of the transmitted light in the colored state. Furthermore, it is interesting to see that the lithium-doped material has improved properties in the whole wavelength range; however, doping does not change the color impression.

The last important open question is related to the time response, because the time response of these cells is decisive for the commercial success. A typical example for the time response, comparing pure and phosphorous, P^{5+}-doped WO$_3$ is shown in Figure 9.49.

As already mentioned, the response time is of extreme importance. Figure 9.50 displays the temporal response measured at a wavelength of 633 nm with voltages alternating between −0.8 V in the colored state and +0.8 V in the bleached state; each applied for 15 s. In both cases, the bleaching process for both doped and undoped WO$_3$ films was completed, however, bleaching and coloration of the doped film is significantly faster than the undoped one. In the case of the doped material, five seconds are sufficient. Furthermore, it is important to realize that the transmission in the colored state is significantly smaller for the doped material as compared to the undoped one.

9.10
Magneto-Optic Applications

One of the most important magneto-optical materials are magnetic composites exhibiting as additional property luminescence. This combination of properties, which is never found in nature, is already discussed in Section 9.6 in Figures 9.24a,b.
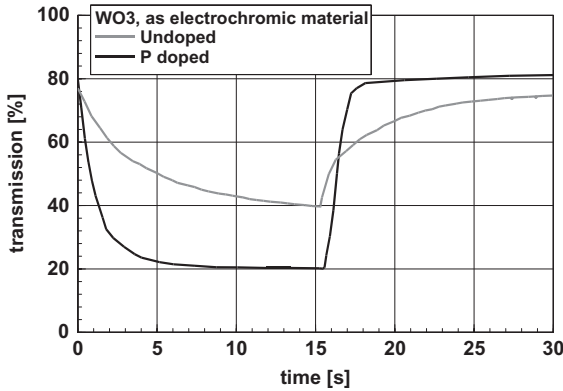
Figure 9.49 Temporal response of the transmission of an electrochromic cell based on WO₃. One sees that doping the tungsten oxide with phosphorous, P^{5+}, reduces the time to change the color or to bleach significantly. In both cases, the transmittance was measured at a wavelength of 633 nm: The voltage was −0.8 V to obtain the colored and +0.8 V to obtain the bleached state [26].
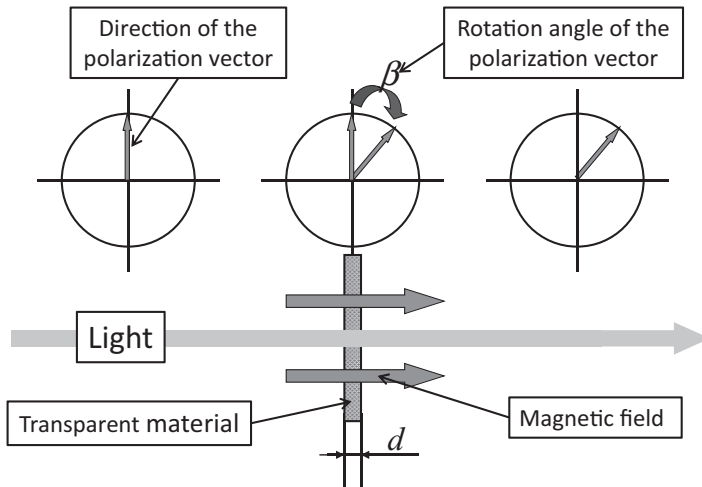
Figure 9.50 Arrangement to measure or exploit the *Faraday* effect. When the light passes a magnetic material placed in a magnetic field, the polarization vector (direction) is rotated. This rotation is controlled by the strength of the magnetic field and the *Verdet* constant of the material (see Eq. (9.15)).

Composites, consisting of ferromagnetic particle in a polymer matrix are very interesting materials with respect to the *Faraday* effect, describing the rotation of the plane of polarization of light in transmission during passing a magnetic material in an magnetic field. (An analog, the *Kerr* effect describes the rotation of the polarization plane after reflection at the surface of magnetic materials.)
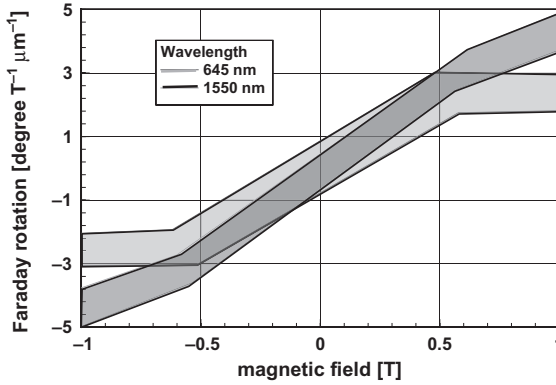
Figure 9.51 *Faraday* rotation of γ-Fe₂O₃ at wavelength of 645 and 1550 nm as function of the magnetic field [28].

Usually, for optomagnetic devices, thin films of ferromagnetic materials are used. There are attempts in the direction of using nanoparticulate ferrites in a polymer matrix [27].

Figure 9.50 displays the general outline of an arrangement using the *Faraday* effect. The rotation angle β of the polarization plane of the outgoing against the incoming light in a transparent medium exhibiting *Faraday* rotation is given by

$$\beta = vd|B|, \tag{9.15}$$

where v is the *Verdet* constant, d the thickness of the active medium, and $|B|$ the strength of the magnetic field.

Figure 9.50 shows the polarization plane of the incoming light, which is, during the passage through the material with the thickness d in the magnetic field, rotated by the angle β after passing the layer. Figure 9.51 displays experimentally determined values for the *Faraday* rotation of γ-Fe₂O₃ nanoparticles [28]. These data are given within a relative broad scattering band, as the absorption in the magneto-optic active layer of γ-Fe₂O₃ nanoparticles is quite high, and, therefore, the experimental results contain uncertainties.

The data given in Figure 9.51 may be used to calculate the *Verdet* constant for γ-Fe₂O₃.These calculations yielded in values in the range of between 2×10^6 and 4×10^6 degree $T^{-1} m^{-1}$. These values of the *Faraday* rotation are significantly larger as compared to those of garnets with the compositions $Tb_3Ga_5O_{12}$ or $(Tb_x, Y_{1-x})_3Fe_5O_1$, the best magneto-optic active materials, with *Verdet* constants in the range of a few degrees per Tesla and meter. In contrast to the highly transparent garnets, ferrites can be used only as thin films in the range of a few micrometers, only, or equivalently diluted suspensions stabilized by surfactants. On the other hand, ferrites, especially maghemite are significantly cheaper than the above-mentioned garnets. Therefore, this material has a great potential for applications. These statements, related to the absorption, are correct in the visible range only.
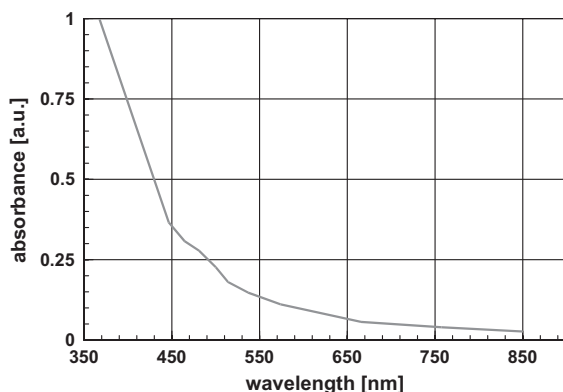
Figure 9.52 Absorbance of 12-nm γ-Fe$_2$O$_3$, maghemite, particles as a function of the wavelength [29]. This graph shows that in the wavelength range above ca. 700 nm, the absorbance is so small that technical application is not excluded.

As may be seen in Figure 9.52, things are different on the red or infrared side of the spectrum. In this range of the spectrum, the absorbance is so small that technical applications, exploiting the relatively low price, are not excluded.

References

1 Nussbaumer, R.J., Caseri, W.R., Smith, P., and Tervoort, T. (2003) *Macromol. Mater. Eng.*, **288**, 44–49.

2 Wu, M.K. (1995) Nanostructured Materials and Coatings, Gorham/Intertech Consulting, KEMIRA Pigments Inc.

3 Li, C., and Murase, N. (2004) *Langmuir*, **20**, 1–4. Published on Web 12/06/2003 LA035546O.

4 Reisfeld, R. (2002) *J. Alloys Compd.*, **341**, 56–61.

5 Monticone, S., Tufeu, R., and Kanaev, A.V. (1998) *J. Phys. Chem.*, **102**, 2854–2862.

6 Vollath, D., and Szabo, D.V. (2004) *Adv. Eng. Mater.*, **6**, 117–127.

7 Wanga, Y., Yaoa, X., Wanga, M., Konga, F., and Heb, J. (2004) *J. Cryst. Growth*, **268**, 580–584.

8 Smith, A.M., Gao, X., and Nie, S. (2004) *Photochem. Photobiol.*, **80**, 377–385.

9 Pennycook, F.T.J., McBride, J.R., Rosenthal, S.J., Pennycook, S.J., and Pantelides, S.T. (2012) *Nano Lett.*, **12**, 3038–3042.

10 Schaffer B., Hohenester U., Trügler A., and Hofer F. (2009) *Phys. Rev. B*, **79**, 041401-1-041401-4.

11 Abdolvand, A. (2006) Modification of optical and structural properties of glass containing silver nanoparticles via dc electric field and moderately elevated temperatures.. Dissertation. Martin-Luther-Universität Halle-Wittenberg.

12 Eustis, S., and El-Sayed, M. (2005) *J. Phys. Chem.*, **109**, 16350–16356.

13 Cattaruzzaa, E., Battaglina, G., Calvellia, P., Gonellaa, F., Matteib, G., Mauriziob, C., Mazzoldib, P., Padovanib, S., Pollonia, R., Sadab, C., Scremina, B.F., and D'Acapitoc, F. (2003) *Compos. Sci. Technol.*, **63**, 1203–1208.

14 Quinten, M. (2001) *Appl. Phys.*, **73**, 317–326.

15 Vollath, D., and Szabo, D.V. (2004) *J. Nanopart. Res.*, **6**, 181–191.

16 Vollath, D. (2010) *Adv. Mater.*, **22**, 4410–4415.

17 Liu, H.-W., Laskar, I.R., Huang, Ch.-P., Cheng, J.A., Cheng, S.-S., Luo, L.-Y., Wang, H.-R., and Chen, T.-M. (2005) *Thin Solid Films*, **489**, 296–302.

18 Weng, Y.X., Li, L., Liu, Y., Wang, L., and Yang, G.Z. (2003) *J. Phys. Chem.*, **107**, 4356–4363.

19 Meyer, T.J., Meyer, G.J., Pfennig, B.W., Schoonover, J.R., and Timpson, C. J., Wall, J. F., Kobusch, C., Chen, X. H., Peek, B. M., Wall, C. G., Ou, W., Erickson, B. W., and Bignozzi, C. A. (1994) *Inorg. Chem.*, **33**, 3952–3964.

20 Parker, C.A. (1968) *Photoluminescence of Solutions*, Elsevier, Amsterdam, p. 21.

21 Nelson, J.K., and Fothergill, J.C. (2004) *Nanotechnology*, **15**, 586–595.

22 Manzoor, K., Aditya, V., Vadera, S.R., Kumar, N., and Kutty, T.R.N. (2005) *Solid State Commun.*, **135**, 16–20.

23 Gao, M., Richter, B., Kirstein, S., and Möhwald, H. (1998) *J. Phys. Chem.*, **102**, 4096–4103.

24 Li, S., and El-Shall, M.S. (1999) *NanoStruct. Mater.*, **12**, 215–219.

25 Bueno, P.R., Faria, R.C., Avellaneda, C.O., Leite, E.R., and Bulhoes, L.O.S. (2003) *Solid State Ion.*, **158**, 415–426.

26 Avellaneda, C.O., and Bulhoes, L.O.S. (2003) *J. Solid State Electrochem.*, **7**, 183–186.

27 Ziolo, R.F., Giannelis, E.P., Weinstein, B.A., and O'Horo, M.P. (1992) *Science*, **257**, 219–223.

28 Moreno, E., Zayat, M., Morales, M., Serna, C., Roig, A., and Levy, D. (2002) *Langmuir*, **18**, 4972–4948.

29 Gallet, S., Verbiest, T., and Persoons, A. (2003) *Chem. Phys. Lett.* **378**, 101–104.

10
Electrical Properties

10.1
Fundamentals of Electric Conductivity; Diffusive versus Ballistic Conductivity

In a conventional metallic conductor, there is a huge number of electrons; after connecting a voltage, they move slowly from one to the other end of the wire. This is rather a drift than a directed movement. The electrons moving under the influence of an electrical field experience scattering processes leading to a change in momentum by interactions with electrons, phonons, impurities, or other imperfections of the lattice. These processes are responsible for the electric losses. Figure 10.1 displays these phenomena in a simplified way, where an *Ohm*ic conductor, for example, a metallic wire, is connected to an electric circuit, electrons are moving driven by the applied electric field.

The conventional process of electric conductivity called "diffusive conductance" is ruled by *Ohm*'s law

$$V = IR = \frac{I}{G} \quad \text{or} \quad G = \frac{I}{V}. \tag{10.1}$$

In Eq. (10.1), the quantity V is the applied voltage, I the electrical current, R the resistance, and G the electrical conductance. The validity of *Ohm*'s law implies that the electrical resistance depends only on the geometry and material of the conductor. The conductance $G = \frac{1}{R}$ of a wire depends on the geometrical parameters l, the length, and a, the cross section: $G = \sigma \frac{l}{a}$. The electric conductivity σ is a material parameter. For metallic conductors the conductivity is independent of the applied voltage and the electric current, for semiconductors or insulators, the electric conductivity usually increases with increasing applied voltage. Wires with dimensions in the nanometer range or molecular dimensions do not follow *Ohm*'s law in any case. In particular, the strictly linear relation between current and voltage is replaced by a nonlinear, non-*Ohmic* characteristic.

In metallic wires, electric conductivity is characterized by the mean free path of the electrons, which is, in most well-crystallized metals, in the range of 50 nm. When the geometric dimensions are in the range of or smaller than the mean free

Diffusive conductance
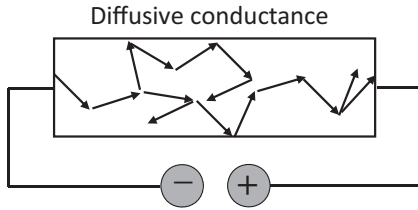
Figure 10.1 Electrical conduction mechanism in conventional metallic conductors. Diffusive conductance, active in this case, is characterized by scattering of free electrons in the conductor. Electric current is transported by free electrons performing a drift movement.

Ballistic conductance
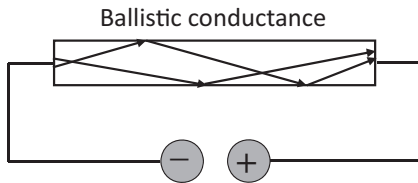
Figure 10.2 Ballistic conductivity of electrical current in a small electric conductor. As the geometric dimensions of the conductor are smaller than the mean free path length of the electrons, this conductivity mechanism is not characterized by scattering of the free electrons in the lattice.

path length of the electrons, the mechanism of conduction changes from a "diffusive" one to a "ballistic" one. The principle of ballistic conductivity is displayed in Figure 10.2.

As electron-scattering phenomena do not occur, classically, one expects zero resistivity and no losses. This is not observed because ballistic conductivity is ruled by, quantum-mechanical phenomena.

Box 10.1   Ballistic Electrical Conductivity

For a mathematical description of the ballistic electrical conductivity, Eq. (10.1) is rewritten in a way taking the transport by electrons into account. The current I transports within a time interval Δt the electrical charge $Q = I\Delta t$. As one electron carries the charge e, the charge Q is transported by $N = \dfrac{Q}{e} = \dfrac{I\Delta t}{e}$ electrons. The time interval Δt is estimated from the length l of the wire and the velocity of the electrons v_{e}. This allows rewriting Eq. (10.1)

$$G = \frac{I}{V} = \frac{Q}{\Delta t V} = \frac{Nev_{\mathrm{e}}}{Vl}. \tag{10.2}$$

Under the influence of the voltage V the electrons are accelerated, they obtain the energy $E = eV$. Applying *Planck*'s equation $E = \dfrac{h v_e}{\lambda}$ to express the energy of the electrons and inserting into Eq. (10.2), one finally obtains

$$G = \frac{N e v_e}{V l} = \frac{N e^2 v_e}{E l} = \frac{N e^2}{h} \frac{\lambda}{l} = \frac{N e^2}{h} \frac{1}{n}. \tag{10.3}$$

The term $n = \dfrac{l}{\lambda}$ stands for the electron wave mode number. Each electron wave mode may have two modes (spin up and spin down) leading to $N = 2n$, therefore, one finally obtains for the conductance of a short thin wire with one mode:

$$G = \frac{2 e^2}{h}. \tag{10.4a}$$

Assuming m active modes in a wire, the conductance is

$$G = m \frac{2 e^2}{h} = m G_0. \tag{10.4b}$$

Equation (10.4b) is fundamental; it says that the electric conductivity of a small thin wire increases stepwise with the increment $G_0 = \dfrac{2 e^2}{h} = 7.72 \times 10^{-5}$ S, the "*conductivity quantum*". In Eq. (19.4b), the length and the cross section of the wire no longer appear; therefore, in the ballistic case, the electric conductance is independent of material and geometry. The inverse value $R_0 = \dfrac{1}{G_0} = 26$ kΩ is called the "*resistance quantum*", also known as *von Klitzing* constant.

Analyzing Eq. (10.2), one learns that the conductance decreases with increasing voltage; however, because of the existence of the resistance quantum, this happens in steps. Except for graphene, the quantized phenomena described above are observed at low temperatures, only. Otherwise, thermal energy is larger than or in the range of the energy difference between two neighboring electron wave modes; hence the steps are smeared out, as the different modes may be activated thermally and not by the electric field. In such a case, the I–V diagram looks like one following *Ohm*'s law. A rigorous treatment of quantized electric conductance is given in a review paper of Datta [1].

Ballistic conductivity is independent of the material and the geometry of the wire. (This statement has to be taken cum grano salis (with a pinch of salt), as the free path length of the electrons depends on the material.) However, ballistic conductivity depends on the applied voltage, as the number of modes excited by the electrical field depends on the applied voltage. Each one of the excited modes contributes to the electrical conductivity in an equal step, the conductivity quantum. At low temperatures, the electrical conductivity increases in steps with the applied voltage. This is depicted in Figure 10.3.
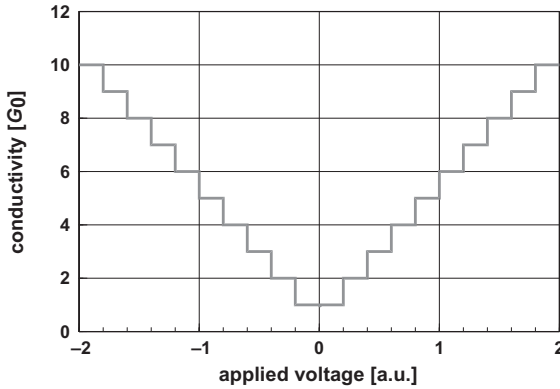
Figure 10.3 Dependency of the electrical conductivity on the applied voltage at low temperatures, close to zero *Kelvin*. One sees that the conductivity increases in steps of G_0.
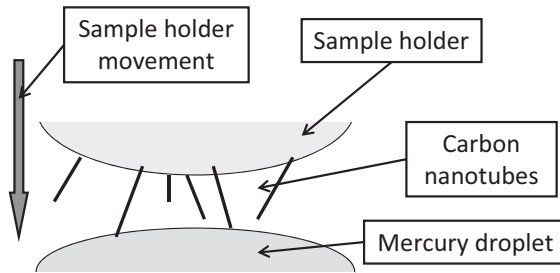
Figure 10.4 Experimental arrangement to measure electric conductivity of carbon nanotubes [2]. It is based on a bundle of carbon nanotubes of different length and orientation, which are fixed on a sample holder. The sampleholder is moved towards a mercury droplet. As length and orientation of the carbon nanotubes are different, they touch at different times the surface of the mercury. This gives information on the influence of the length of the carbon nanotubes on the resistance and the resistance of different nanotubes.

An interesting experimental device designed to demonstrate the basic properties of ballistic conduction is depicted in Figure 10.4. In this device, a few carbon nanotubes are fixed on a specimen holder. They are fixed in different orientations and length. Opposite the specimen holder is a drop of mercury. An electric circuit is connected to the sample holder and the mercury droplet. During the experiment, the specimen holder is moved slowly in the direction of the mercury drop. When the first carbon nanotube touches the mercury, an electric current will flow. Now the resistance is measured. During further movement of the specimen holder, the resistance is measured continuously. This experiment provides results on the resistance of different carbon nanotubes with different lengths.

The results of the measurements using the equipment shown in Figure 10.4, expressed as electric conductance, are shown in Figure 10.5.
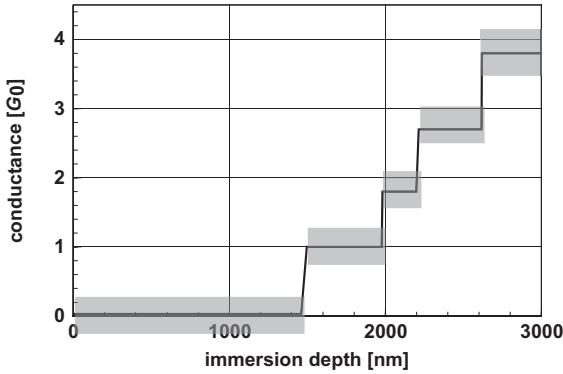
Figure 10.5 Experimentally measured electric conductivity of carbon nanotubes, determined in a device according to Figure 10.4 measured at a voltage of 0.1 V [2]. The conductance is given in multiples of G_0. One must be aware that the electrical currents in such a system are extremely small; therefore, the scattering ranges of the results are also indicated.

The experimental results obtained in a device according to Figure 10.4 are very instructive. Up to a movement of 1400 nm, there was no electrical contact. Then, the conductivity leapt to a value close to $1\,G_0$. After a few more hundred nanometers movement, the second nanotube touches the surface of the mercury and the electrical conductivity leapt upwards again. In spite of the scattering ranges because of the extremely small electrical currents in system, these experimental results show that the electrical conductivity of each of the carbon nanotubes is equal and independent of the immersion depth, which means independent of the length. Furthermore, the deviations of exact integer multiples of G_0 may be explained by contact resistance in the system. These are exactly the results that were expected from the laws of ballistic conductivity.

The possibility to measure electrical conductivity on small objects is surprising, if we extrapolated from the macroscopic experience to objects in the nanometer range. Considering that a conventional copper wire will explode if the electrical current density exceeds $200\,A\,mm^{-2}$ ($=2 \times 10^8\,A\,m^{-2}$) one assumes that, for example, the maximal current to be used in a wire with a diameter of 10 nm is at maximum $1.6 \times 10^{-8}\,A$. This current is so small that reliable measurements are nearly impossible. In reality, small wires and nanotubes are able to carry significantly higher current densities. The experimental results depicted in Figure 10.5 were obtained at 0.1 V; therefore, each one of the carbon nanotubes carried a current of $3.6 \times 10^{-6}\,A$. This current density is more than a hundred-fold larger than that leading to the explosion of a bulk copper wire. The ability to carry such huge current densities is not restricted to carbon nanotubes; it is a generally observed phenomenon. As an example, the capability of gold nanowires to carry electric currents was analyzed by Aherne *et al.* [3] as function of the diameter in a range from 65 to nearly 120 nm at room temperature. The results are depicted in Figure 10.6.
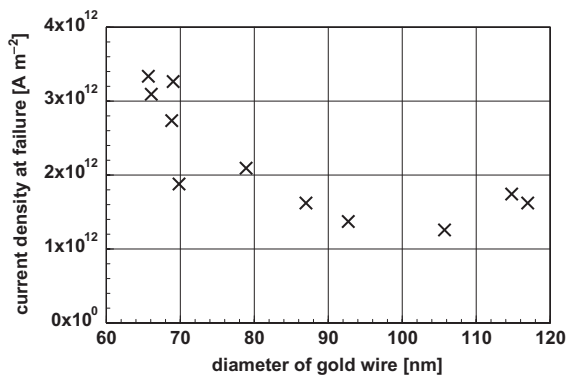
Figure 10.6 Current density to failure for gold nanowires of different diameter determined at room temperature. It is important to realize the increasing maximum current density with decreasing wire diameter [3].
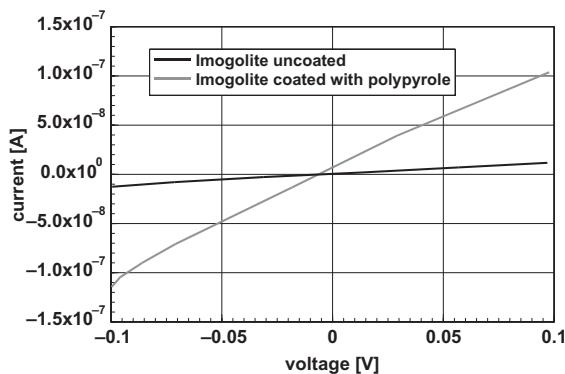
Figure 10.7 Effect of polypyrole coating of imogolite on the electrical conductivity. The figure depicts a plot of electrical current versus applied voltage for the pure and the coated imogolite fibers [4].

Not only metallic nanowires and carbon nanotubes are able to carry extremely high densities of electrical currents. Similar phenomena are found with polypyrole (an electrically conductive organic compound) coated imogolite (see Chapter 5), a silicate crystallizing in one dimension, only [4]. The effect of imogolite surface functionalization with polypyrole on the electric conductivity is given in Figure 10.7.

Figure 10.7 gives a current of 10^{-7} A at a voltage of 0.1 V. Even when the current is only in the range of 10^{-7} A, the current density, however, is, because of the small diameter of these fibers, huge, it is in the range of a few 10^{10} A m^{-2}. Again, this is by far more than it could be transported through a macroscopic copper wire. Even when the resistance of such wires is relatively high, the increase of the electrical conductivity of an order of magnitude promises many interesting technical appli-

cations. In particular, as it is possible to produce quite long imogolite fibers with diameters that are adjustable in a wide range, such products may have a great future in technological applications.

10.2
Carbon Nanotubes

As already explained in Chapter 5, depending on their chirality, some types of carbon nanotubes show metallic electric conductivity. As long as the length is limited, this is ballistic conductivity, as was demonstrated experimentally and depicted in Figure 10.5. Interestingly, multiwalled carbon nanotubes [2] and single layers of graphene [5] show a similar voltage dependency of the electric conductivity. In both cases, it was found experimentally that, above 100 mV, the conductivity increases with increasing voltage. For voltages below ca. 100 mV, the conductance is G_0.

$$
\begin{aligned}
G &= G_0 & |V| \le 0.1\,\text{V} \\
G &= G_0(\alpha + \beta|V|) & |V| > 0.1\,\text{V}
\end{aligned}.
$$

(10.5)

The quantities α and β are specimen-dependent factors ranging from 0.25 up to maximal 1.0. According to Eq. (10.5), a graph of the conductance is symmetric against $V = 0\,\text{V}$. Such a graph for multiwalled carbon nanotubes is depicted in Figure 10.8. Because of unavoidable contact resistance, the constant contribution to conductance is smaller than G_0. Furthermore, because of the thermal excitation observed at temperatures significantly above 0 K, the theoretically expected steps of the electrical conductivity (see Figure 10.3) are not observed.
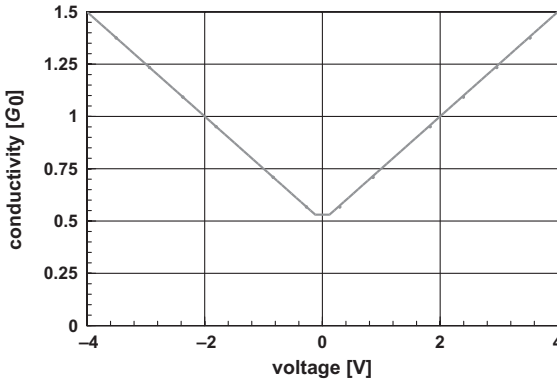
Figure 10.8 Electric conductivity of multiwall nanotubes [2]. For voltages above ca. 100 mV, the electric conductivity follows Eq. (10.5). Below that limit, the conductivity is constant. Single graphene layers show a similar behavior [5]. Because of unavoidable contact resistance, the minimum value of the conductivity is less than $1\,G_0$.
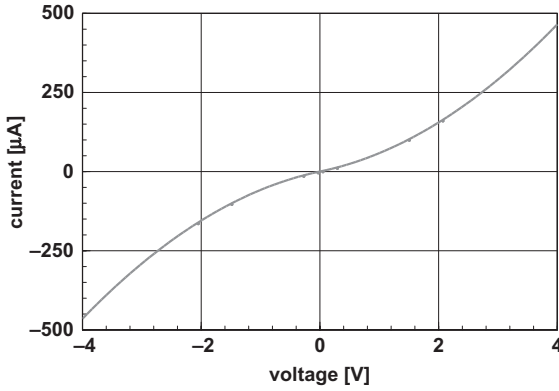
Figure 10.9 Current–voltage characteristics of a multiwalled carbon nanotube [2]. The graph, was calculated using Eq. (10.6) setting $\alpha = 0.5$ and $\beta = 0.25\,\mathrm{V}^{-1}$. The characteristic is similar to that observed for graphene and gold nanowires.

Equation (10.5) for the electrical conductivity leads to a voltage–current characteristic like:

$$I = VG_0(\alpha + \beta|V|). \tag{10.6}$$

This relationship is experimentally verified. Such experimental data, determined in multiwalled carbon nanotubes are depicted in Figure 10.9. For this graph, the values $\alpha = 0.5$ and $\beta = 0.25\,\mathrm{V}^{-1}$ were extracted from the experimental data. It is interesting to see that the current–voltage relation as described by Eq. (10.6) is similar to that observed for gold nanowires.

The relationship between electrical conductivity and voltage, as expressed in Eq. (10.5) is valid for multiwalled carbon nanotubes and graphene sheets only. In the case of long single-wall carbon nanotubes (ca. 1 µm) the experimental data are different. For single-walled carbon nanotubes, too, the electrical conductivity is constant up to a voltage of 0.1 V. However, in contrast to the multiwall carbon nanotubes, the current–voltage plot shows saturation at higher voltages. This behavior is depicted in Figure 10.10 [6].

The experimental results depicted in Figure 10.10 led to a saturation value of the electrical current of $I_0 = 25\,\mu\mathrm{A}$. This value was independent of the individual nanotube experimentally found and expected from theory. Most importantly, this value is independent of the length of the nanotube. Considering this saturation current and the dimensions, a single-walled nanotube can carry a current density in the range of $10^{13}\,\mathrm{A\,m^{-2}}$, which is equivalent to $10^9\,\mathrm{A\,cm^{-2}}$.

The course of the resistance that led to the current–voltage characteristics as depicted in Figure 10.12 is described by the equations

$$
\begin{aligned}
R &= R_0 & |V| &\leq 0.1\,\mathrm{V} \\
R &= R_0 + \frac{|V|}{I_0} & |V| &> 0.1\,\mathrm{V}
\end{aligned}
\tag{10.7}
$$
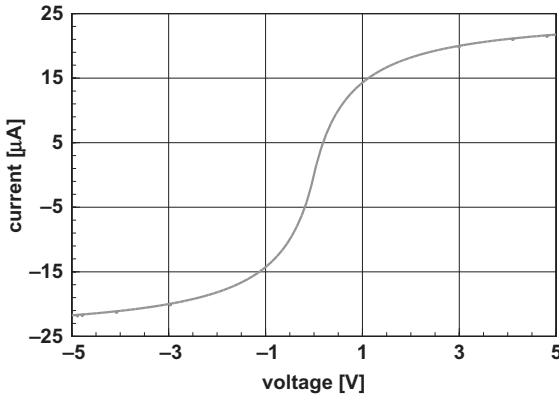
Figure 10.10 Experimental results obtained on a single-wall carbon nanotube [6]. The electrical current is plotted against the applied voltage. One sees that the electrical current approaches a saturation value.
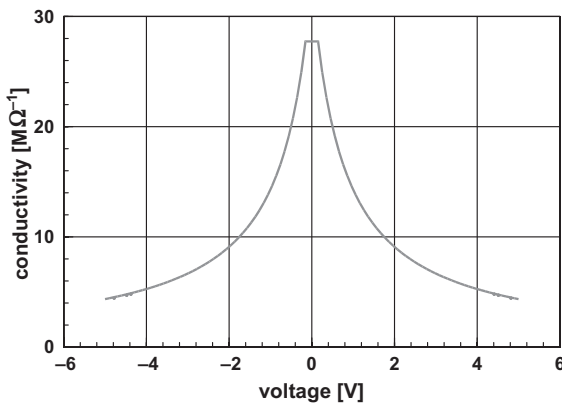
Figure 10.11 Dependency of the electric conductivity of a single-walled carbon nanotube as a function of the applied electric voltage [6]. In contrast to multiwalled nanotubes, the conductivity decreases with increasing applied voltage. With increasing voltage, the conductivity approaches a saturation value.

The quantities R_0 and I_0 are fitting parameters. In an ideal case without contact resistance, R_0 should be equivalent to the resistance quantum. Equation (10.7) has an interesting consequence: For large values of the voltage, the resistance will get very large; the electrical conductivity approaches zero. The course of the electrical resistance, as displayed in Figure 10.10, is described by a voltage-dependent resistance of the single-wall carbon nanotube. The electrical conductance, the inverse value of the resistance, calculated from the data according to Eq. (10.7) is depicted in Figure 10.11. This figure makes it clear that a saturation value of the electrical
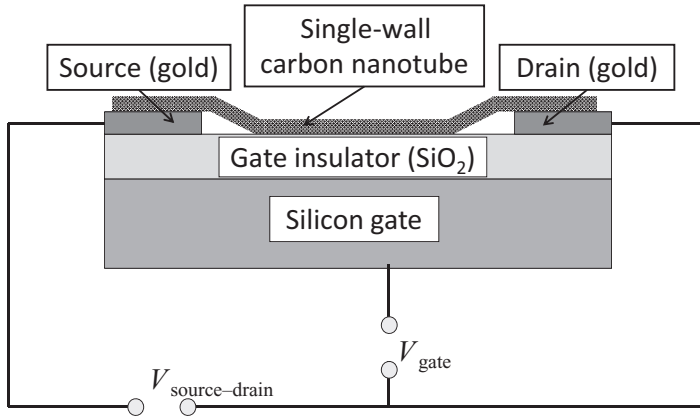
Figure 10.12 Field effect transistor based on one carbon nanotube [7]. The carbon nanotube, which connects source and drain electrode lies, separated by a silica insulation layer, on a silicon substrate used as gate electrode. In succession of this development, other authors have setup a complete logic circuit with one carbon nanotube.

current leads to a saturation value of the conductivity, which approaches zero for large values of the voltage.

$$G = \frac{I}{V} = \frac{1}{R_0 + |V|/I_0} \Rightarrow \lim_{V \to \infty} G = 0. \tag{10.8}$$

However, one must clarify one point: One must not take the mathematical description from Eq. (10.8) as unlimited physical reality. This equation says lastly that the number of modes available for transport of electrons (see Box 10.1) is limited.

The range of potential applications of carbon nanotubes is large. Most interesting is the fact that just using one carbon nanotube, one can produce a field effect transistor (FET). Figure 10.12 displays such a setup. It shows a silicon substrate acting as a gate. This substrate is covered with a silica layer as insulator, which carries gold electrodes as source and gate electrodes. A single-wall carbon nanotube lies on top of the silica insulator and connects the two electrodes [7]. The device displayed in Figure 10.12 was the first of its kind; the value of this development cannot be overestimated, even when later, exploiting this knowledge and experience, other authors made a whole logic circuit with one carbon nanotube.

Now the question arises if such simple equipment as depicted in Figure 10.12 is able to work with electrical currents large enough for useful handling. This condition was fulfilled with the experimental device. The characteristics of a field effect transistor based on a carbon nanotube are depicted in Figure 10.13.

The characteristic of the first field effect transistor based on one single carbon nanotube is thus remarkable as already in this design the electrical currents con-
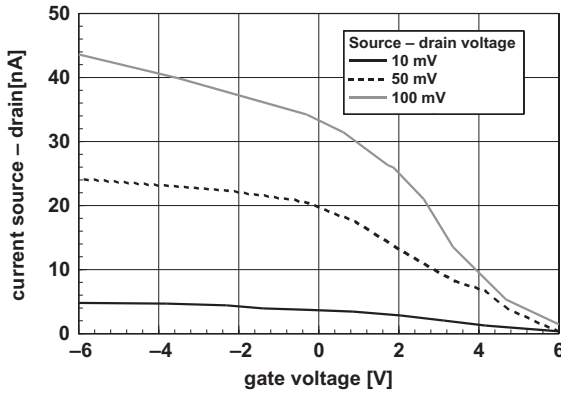
Figure 10.13 Characteristic of a field effect transistor made of one single-wall carbon nanotube according to Figure 10.12 [7]. A current in the range of a few tens of nanoamperes can be handled technically without too much problem. In the meantime, designs were published allowing higher current; however, this is the characteristic of the ground-breaking first design.

trolled by the gate voltage were in the range of a few tens of nanoamperes, a range that can be handled technically without severe problems. Certainly, this first design is not an endpoint. From Figure 10.10 it is clear that one single-wall carbon nanotube can carry electrical currents up to a few tens of microamperes without destroying it. This leaves a lot of space for future developments. Certainly, a crude and relatively large device as depicted in Figure 10.12 is not competitive with the latest developments of silicon technology; however, it reveals a series of unsuspected new technical possibilities.

10.3
Other One-Dimensional Electrical Conductors

As explained in Chapter 5, boron nitride is isostructural with graphite. Therefore, in the same way as isolated graphite layers, graphene, boron nitride forms nanotubes and fullerenes. However, there is one important difference: Whereas the carbon-based objects are electrical conductors, bulk boron nitride is a perfect insulator and the boron-nitride-based nano-objects are wide-gap semiconductors. A typical current–voltage diagram, measured at room temperature, of one double-layer boron nitride nanotube is depicted in Figure 10.14 [8]. The important feature of this plot is the fact that there is no conductivity in an interval of ±21 V and at higher voltages, there is, after a sudden jump, the expected increase of the current with voltage. The threshold, where electrical conductivity starts depends on the individual nanotube; it ranges from ca. 15 to 23 V. In general, the current–voltage
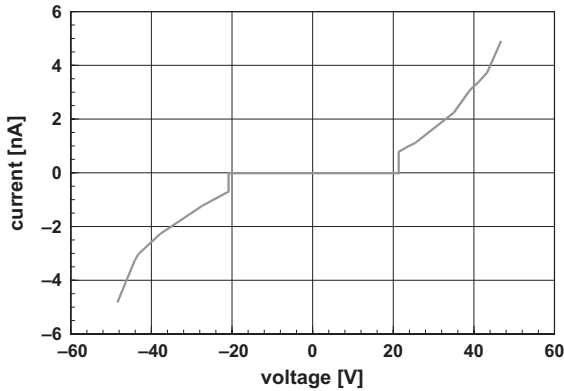
Figure 10.14 Current–voltage characteristic of double-wall boron nitride nanotubes determined at room temperature [8]. Except for the threshold voltage of 21 V, this characteristic is similar to that depicted in Figure 10.5 for multiwall carbon nanotubes.
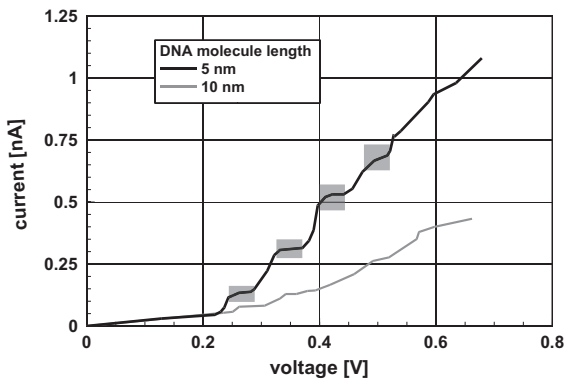
Figure 10.15 Current–voltage characteristic of two DNA molecules with different lengths [9]. These data were measured at room temperature. Obviously, at room temperature, the specimen length, where ballistic conductivity is observed, is very limited. For better visibility, the estimated scattering ranges of the steps are shaded.

characteristic of the double-walled boron nitride nanotubes is similar to that of multiwall carbon nanotubes (except for the broad voltage range without conductivity), which is depicted in Figure 10.5.

Ballistic electric conductivity is a size-dependent property independent of the kind of materials, which means this mechanism is not restricted to metallic or semiconducting materials. As typical example of a very different conductor, Figure 10.15 displays the current–voltage characteristic of two DNA molecules with different length. These experimental data were obtained at room temperature [9].

The current–voltage plot displayed in Figure 10.15 shows for the DNA molecule with a length of 5 nm distinct steps. Certainly, these steps are, due to noise, blurred. Therefore, for better visibility, the possible scattering ranges of the data are marked by shaded areas. It is obvious that the 10-nm DNA molecules no longer exhibit these characteristic steps, at least as distinct as for the shorter one.

10.4
Electrical Conductivity of Nanocomposites

Besides potential use as new electronic elements, the most important application of one- and two-dimensional electric conductors are as fillers in polymers to produce electrically conductive nanocomposites. The great specialty of these nanocomposites is their optical transparency. In other words: these nanocomposites have the potential to replace ITO (indium-tin-oxide) coatings, which are nowadays the means to obtain transparent electrical conductive coating applied in screens for TV sets, computer displays, etc. Potentially, these nanocomposites have the advantage of being elastic bendable and printable, even on soft screens. In contrast, ITO layers are produced by sputtering processes, a quite expensive production route, and are brittle. Therefore, ITO layers are restricted to stiff substrates only. A comparison of the spectral optical transmission of nanotube–polymer composites or graphene with ITO is given in Chapter 5.

To obtain an electrically conductive composite, the particles, mediating the transport of the electrical current must form a closed path, a percolating system. Such a system is depicted in Figure 10.16. In this figure, nanocomposites filled with one-dimensional electrically conducting particles are sketched. On the
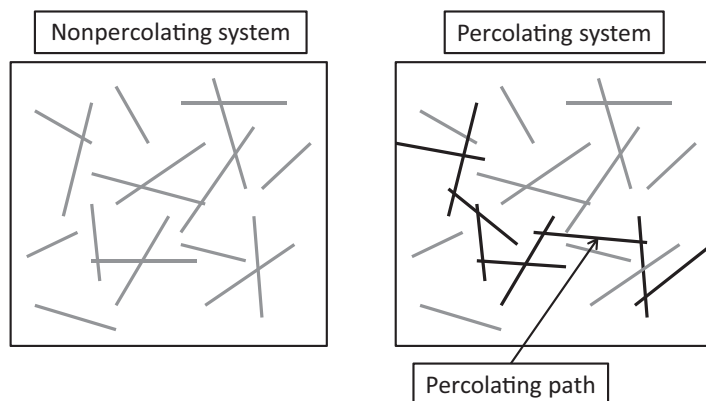
Figure 10.16 Schematic drawings of nanocomposites filled with one-dimensional particles. The two figures show a composite without (left-hand side) and with (right-hand side) percolation. Along the percolation path (black colored in the drawing), transport of electrical current is possible.
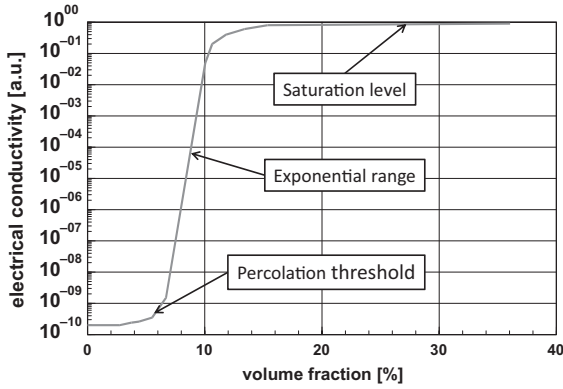
Figure 10.17 Dependency of the electrical conductivity of a composite with conductive filler as a function of the volume content of the filler. Characteristic ranges in this graph are: The percolation threshold, which is the concentration where the first electrical conductivity is observed. After that a range where the conductivity increases exponentially with the amount of filler and finally the range where saturation of the electrical conductivity is observed.

left-hand side, a nonpercolating system, that means a system without a closed path for electrical conductivity and on the right-hand side, a percolating composite, showing electrical conductivity, are plotted.

It can be understood easily that to obtain percolation by forming a percolation path, a minimum amount of filler is necessary. The general dependency of the electrical conductivity of the amount of filler is depicted in Figure 10.17.

The graph depicted in Figure 10.17 displays all the characteristic features of a nanocomposite filled electrically conductive particles. Assuming the matrix polymer has poor electrical conductivity, one finds at low concentrations of the filler only a minor, nearly negligible increase of the conductance with increasing filler content. When the filler concentration reaches a level where electrical conductivity is first observed, the percolation threshold is reached. Having passed this threshold, the electrical conductivity increases exponentially with the volume fraction of the filler until the saturation level is reached. A further increase of the electrical conductivity is impossible. Comparing the threshold concentrations of spherical particles and nanotubes or plates, it is easily understood; the percolation threshold is highest in the case of spherical particles. In fact, the threshold concentration p_c is proportional to the ratio of the average particle diameter d_m over its mean length l_m.

$$p_c \propto \frac{d_m}{l_m}. \tag{10.9}$$

As a consequence of Eq. (10.9), in general, spherical particles are not applied as filler to produce nanocomposites with good electrical conductivity.

Box 10.2 Percolating Systems

The theory of percolation is applied quite universally. In the case of nanocomposites it describes the trend of the electrical conductivity as a function of the filler shape and content, in the case of porous materials the same theory describes the permeability for gases as a function of the porosity, and there are many more applications.

In the theory of percolation, the crucial question is the estimation of the percolation threshold. Considering a composite consisting of prolate (a prolate body is an ellipsoid where one axis is longer than the diameter) particles (as a model, for example, for nanotubes) the diameter d and the length l of the particles rule the position of the percolation threshold. Following the theory of Balberg [10], the percolation threshold p_c, the concentration, where the first electrical conductivity is observed, is given by

$$p_c = 0.7 \frac{\langle l \rangle^3}{\langle l^3 \rangle} \frac{\langle d \rangle}{\langle l \rangle}. \tag{10.10}$$

The $\langle \rangle$ brackets stand for mean values of an ensemble. In any possible length distribution, $\frac{\langle l \rangle^3}{\langle l^3 \rangle} \leq 1$ is valid. To simplify the considerations, fibers of equal length l and equal diameter d are assumed; then Eq. (10.10) is simplified to:

$$p_c = 0.7 \frac{d}{l} \propto \frac{1}{a}. \tag{10.11}$$

It is an important characteristic of percolation that the percolation threshold increases with the mean aspect ratio $a = \dfrac{\langle l \rangle}{\langle d \rangle}$. As a consequence, one sees that the concentration of particles necessary for the onset of percolation is, for fibers, up to a few orders of magnitude less compared to spherical particles. Therefore, to obtain optically transparent electric conductive composites one has to apply extremely thin long fibers, usually realized with nanotubes or nanowires.

According to the considerations of Stauffer and Aharoni [11], above the percolation threshold p_c, the electrical conductivity σ is described by an exponential law:

$$\sigma = \sigma_0 (p - p_c)^t. \tag{10.12}$$

In Eq. (10.12) σ_0 is the conductivity of the conducting phase and p the volume fraction of the conducting phase. The exponent t reflects the dimensionality of the network; usually, it is found to be not an integer number; ranging between 1.3 and 3. This exponent is determined by plotting the experimental conductivity values linearized in a double-logarithmic graph, $\log(\sigma)$ versus $\log(p - p_c)$.
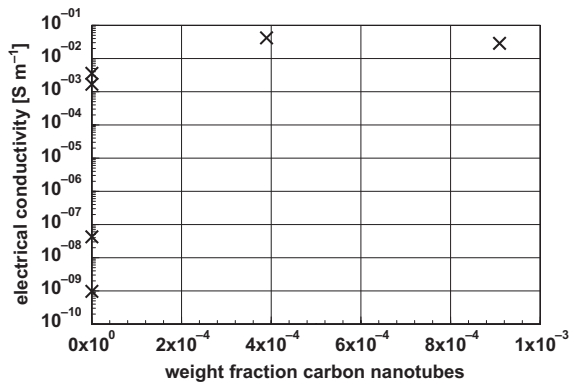
Figure 10.18 Electrical conductivity of a carbon nanotube–epoxy composite [12]. The percolation threshold of these well-distributed carbon nanotubes is at a weight fraction around 2.3×10^{-5}, which is equivalent to a volume fraction in the range of 10^{-5}. The transition to the saturation level is at a weight fraction of less than 4×10^{-4}.

In the following, two examples, confirming the general behavior, as displayed in Figure 10.17 and described by the Eqs. (10.11) and (10.12), are presented. Figure 10.18 presents the electric conductance of a nanocomposite with epoxy as matrix material and carbon nanotubes as conducting filler. Figure 10.18 shows that the percolation threshold is at such a low fiber content that it is not visible in this figure; the transition to the saturation value is at a weight fraction of less than 4×10^{-4}.

The double-logarithmic plot of the transition range between the percolation threshold and the saturation range, to prove the exponential increase of the electric conductivity, is presented in Figure 10.19.

This figure proves that the relationship according to Eq. (10.12) is, in this example, valid in a range of a reduced concentration $p - p_c$ over nearly four orders of magnitude in the range of reduced weight fractions from ca. 10^{-5} up to 10^{-1}. The exponent describing the dimensionality of this composite is 1.2. The percolation threshold of this material is at a weight fraction of less than 4×10^{-4}. One must be aware of the fact that the percolation threshold and the saturation value of the electrical conductivity depend strongly on the manufacturing process. One must not be surprised to find literature data describing a percolation threshold in the range of a few weight percent of carbon nanotubes. Certainly, looking at applications where maximal transparency and electrical conductivity are sought, only products exhibiting the lowest possible mass fraction at the percolation threshold are promising candidates. Significant differences in the percolation threshold are, in general, explained by more or less adequate processes for singularization of the carbon nanotubes and blending into the polymer matrix.

The second example uses $Mo_6S_{4.5}J_{4.5}$ fibers dispersed in PMMA as matrix material [13]. This compound crystallizes linearly in fibers with a diameter of ca. 1 nm, however, these fibers come in bundles, held together by *van der Waals* forces. As
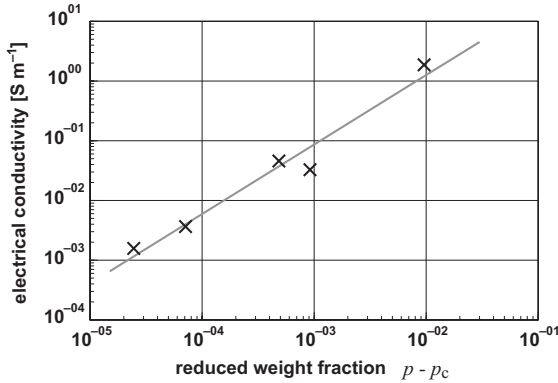
Figure 10.19 Carbon nanotube–epoxy nanocomposite. Replot of the experimental data displayed in Figure 10.18. This double-logarithmic plot of the electric conductivity versus the reduced weight fraction $p - p_c$ proves the validity of Eq. (10.12) for this example. It is obvious that the experimental data follow, up to a volume content of nearly 0.1 above the percolation threshold, this law exactly. The exponent describing the dimensionality of this composite is 1.2 [12].
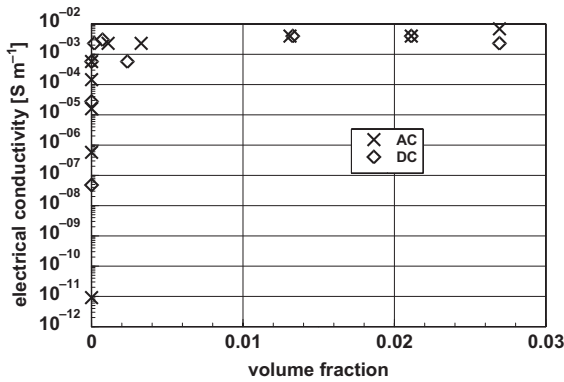
Figure 10.20 Plot of the electric conductivity, measured with alternating, AC and direct current, DC methods, of a nanocomposite consisting of $Mo_6S_{4.5}I_{4.5}$ fibers dispersed in PMMA [13]. The percolation threshold is found around a volume fraction of $p_c = 1.3 \times 10^{-5}$ and the transition to the saturation level at 10^{-3}. These are at such low volume fractions that they are not visible in this plot.

these are weak binding forces, it is possible to singularize these fibers by sonification. However, during this process, the length of the fibers is reduced to values around 1000 nm, resulting in an aspect ration of ca. 1000. Figure 10.20 displays the electric conductivity, determined by alternating, AC, and direct current, DC, methods, of these nanocomposites as a function of the fiber content.

Again, as in Figure 10.18, the values of the percolation threshold and the transition to the saturation value of the electrical conductivity are not recognizable, as
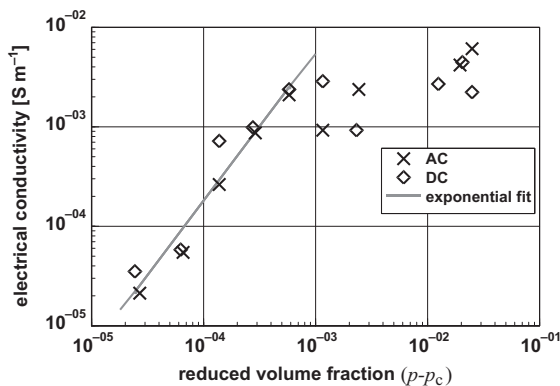
Figure 10.21 Electrical conductivity of a nanocomposite consisting of $Mo_6S_{4.5}I_{4.5}$ fibers dispersed in PMMA [13]. To show the true relationships this plot is double logarithmic. It reveales a percolation threshold at a volume fraction of 1.3×10^{-5} and a transition to the saturation value at a volume fraction around 10^{-3}. It is important to realize that there is no difference between the results obtained with AC or DC. The solid line represents the fit using the exponential function according to Eq. (10.12).

the values are very close to nil. Therefore, again, as in the previous example, the double-logarithmic plot according to Eq. (10.12) is presented.

Also, Figure 10.21 shows that the description of the transition range of the electrical conductivity by an exponential function is appropriate. A detailed analysis revealed a percolation threshold at a volume fraction of 1.3×10^{-5} and a transition to the saturation value at a volume fraction around 10^{-3}. This example proves the general validity of Eq. (10.12) for composite systems with fibers, too.

Comparing the characteristic data of the two examples of electrically conducting nanocomposites reveals that in well-prepared composites the amount of fibers necessary to obtain the electrical conducticity at all and the saturation value in particular, is not high. Therefore, one has a good chance to produce optically transparent composites that exhibit electrical conductivity. The filler material to be selected depends on the needs of the supporting electronic system.

Even when the theory of percolation, outlined in this section, was developed in view of zero- or one-dimensional fillers, cum grano salis, it may be applied for two-dimensional fillers, such as graphene, too. This is thus of special interest, as graphene exhibits good electrical conductivity and, in these layers, nearly perfect spectral optical transparency. Figure 10.22 displays the course of the electrical conductivity of a nanocomposite consisting of a variable amount of graphene as electrical conductor and polyethylene as matrix.

A detailed analysis of Figure 10.22 revealed a percolation threshold of 0.07 vol% and a dimensionality of 1.26. A double-logarithmic plot of the experimental data according to Eq. (10.12) results in a nearly perfect linearized region. This is depicted in Figure 10.23.
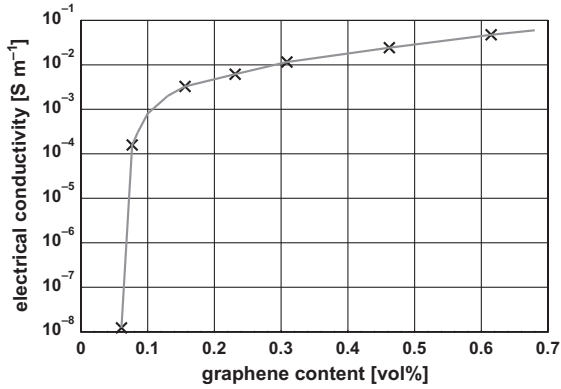
Figure 10.22 Electrical conductivity of a graphene–polyethylene nanocomposite [14]. Similar to the case of a one-dimensional filler, there is a sudden increase of the electrical conductivity at filler concentrations above a certain threshold.
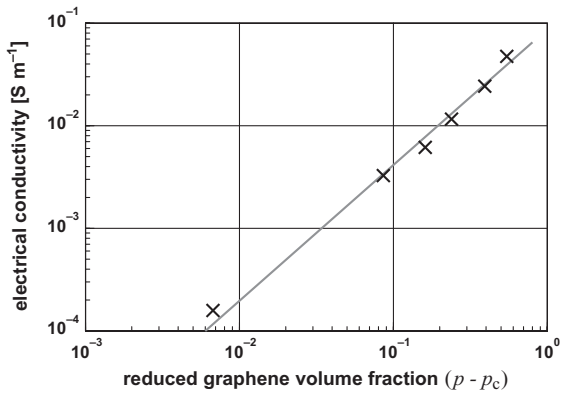
Figure 10.23 Double-logarithmic plot of the experimental data depicted in Figure 10.22 [14]. This plot reveals that the percolation theory, originally developed for one-dimensional fillers, may be applied in good approximation also for two-dimensional fillers.

The percolation threshold is, in the case of carbon nanotube composites, in the range of 10^{-8}, whereas this threshold was found in the described example to be in the range of 10^{-1}%. Looking at the saturation value of the electrical conductivity, a comparison of Figures 10.19 and 10.23 one sees that the electrical conductivity of the filled carbon nanotube is somewhat higher. At least in the data published until now, the amount of graphene to obtain comparable electrical conductivity is higher than that carbon nanotubes.

References

1 Datta, S. (2004) *Nanotechnology*, **15**, 433–451.

2 Poncharal, P., Frank, S., Wang, Z.L., and de Heer, W.A. (1999) *Eur. Phys. J.*, **9**, 77–79.

3 Aherne, D., Satti, A., and Fitzmaurice, D. (2007) *Nanotechnology*, **18**, 125205.

4 Lee, Y., Kim, B., Yi, W., Takhora, A., and Sohn, D. (2006) *Bull. Kor. Chem. Soc.*, **27**, 1815–1824.

5 Shklyarevskii, O.I., Speller, S., and van Kempen, H. (2005) *Appl. Phys. A*, **81**, 1533–1538.

6 Yao, Z., Kane, C.L., and Dekker, C. (2000) *Phys. Rev. Lett.*, **84**, 2941–2944.

7 Martel, R., Schmidt, T., Shea, H.R., Hertel, T., and Avouris, P. (1998) *Appl. Phys. Lett.*, **73**, 2447–2449 www. research.ibm.com/nanoscience/fet.html

8 Cumings, J., and Zettl, A. (2004) *Solid State Comm.*, **129**, 661–664.

9 Watanabe, H., Shimotani, K., Shigematu, T., and Manabe, C. (2003) *Thin Solid Films*, **438–439**, 462–466.

10 Balberg, I. (1985) *Phys. Rev. B*, **31**, 4053–4055.

11 Stauffer, D., and Aharoni, A. (1994) *Introduction to Percolation Theory*, 2nd edn, Taylor and Francis, London.

12 Sandler, J.K.W., Kirk, J.E., Kinloch, I.A., Shaffer, M.S.P., and Windle, A.H. (2003) *Polymer*, **44**, 5893–5899.

13 Murphy, R., Nicolosi, V., Hernandez, Y., McCarthy, D., Rickard, D., Vrbanic, D., Mrzel, A., Mihailovics, D., Blau, W.J., and Coleman, J. (2006) *Scr. Mater.*, **54**, 417–420.

14 Pang, H., Chen, T., Zhang, G., Zeng, B., and Li, Z.-M. (2010) *Mater. Lett.*, **64**, 2226–2229.

11
Mechanical Properties

11.1
General Considerations

In 1987 Gleiter and coworkers [1] published a paper on plastic deformation of CaF_2 at room temperature. This paper was the starting point for the huge scientific interest on nanomaterials. In the meantime, bulk nanomaterials and their mechanical properties are no longer at the center of the scientific interest as the thermodynamic stability of these materials is quite limited. However, the mechanical properties of nanocomposites filled with one- or two-dimensional nanoparticles are getting increasingly important, from both the scientific and commercial aspects. Additionally, a new type of material with extremely small grain size, materials produced by severe plastic deformation moved in the center of interest [2]. However, because of their relatively large grain size, in general, more than 100 nm, these materials, with excellent new properties, will not be discussed within this book.

The mechanical properties of bulk materials, independent of their grain size, are characterized by the stress–strain diagram. Such a stress–strain diagram, which is typical, for example, for metals is depicted in Figure 11.1.

The stress–strain diagram depicted in Figure 11.1 is typical for tension experiments with metallic specimen. The graph is characterized by the regions where the specimen is deformed elastically or plastically, separated by the yield stress. Further parameters characterizing the specimen are the ultimate strength and the rupture strain. The strain ε, as used in Figure 11.1 is defined as

$$\varepsilon = \frac{\Delta l}{l}, \tag{11.1}$$

where l is the length of the specimen and Δl the elongation of the specimen during the experiment. The stress σ is defined as

$$\sigma = \frac{P}{A}. \tag{11.2}$$

The quantity P stands for the force and A for the cross-sectional area of the specimen. Generally, it is difficult to determine the yield stress exactly; therefore, the
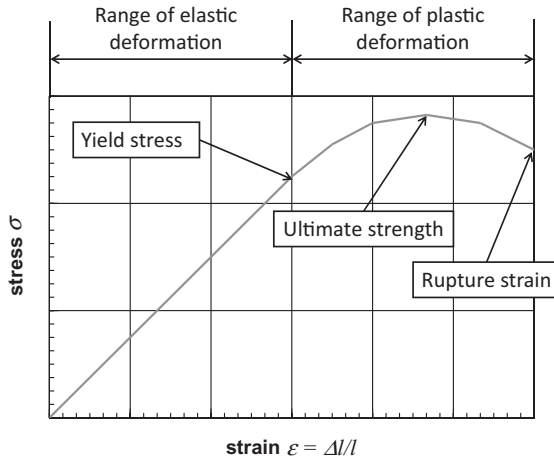
Figure 11.1 A stress–strain diagram, as obtained typically in a tension test of a metal. Such a stress–strain diagram is characterized by a range with elastic deformation followed by one with plastic deformation. These two ranges are separated by the yield stress. The experiment ends with the rupture of the specimen.

yield stress is often defined as the stress where the specimen was plastically deformed by 0.1%. This definition is possible, because in contrast to elastic deformation, plastic deformation is not reversible. In many cases, rupture occurs at the ultimate strength. From the deformation in the elastic region, the modulus of elasticity, also called *Young*'s modulus, is determined. It is defined as

$$E = \frac{\sigma}{\varepsilon}. \tag{11.3}$$

Equation (11.3) is also called *Hooke*'s law. However, it must be noted that there are many materials that lack this linear elastic range; often there is an overlapping of the elastic and plastic deformation. Furthermore, it must be mentioned that there are two types of stress–strain diagrams: The "engineering stress–strain diagram", where the original cross-sectional area of the specimen is used to determine the stress for every value of applied force, and the "true stress–strain diagram", where the applied force is divided by the actual value of the cross-sectional area of the specimen. Even when this difference is very important for engineering, for the basic explanation used in this book, it is not differentiated.

A stress–strain diagram as depicted in Figure 11.1 is the most common one. One finds it in the case of metals, ceramics (in compression), and pure and reinforced polymers. However, there are many other types of stress–strain diagrams known. The most important types are depicted in Figure 11.2.

The different stress–strain diagrams for metals, rubber, and collagen, as depicted in Figure 11.2, are, in reality, at significantly different stresses and strains, just to demonstrate their different course, they are plotted in comparable size in one
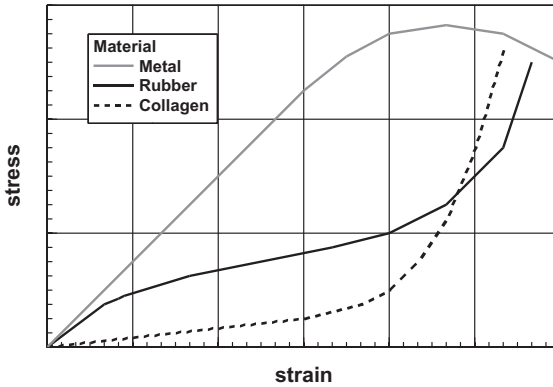
Figure 11.2 Most important types of stress–strain diagrams: the most common one is the one for metals, furthermore, diagrams found with rubber and collagen are depicted. It is important to note that the absolute values of stresses and strains are entirely different for these three materials; just for demonstration of the types, they were plotted in comparable ranges of stresses and strains.

diagram. The type, labeled as rubber, is typical of highly elastic materials, where *Hooke*'s law is not applicable. Also for the type labeled collagen, *Hooke*'s law is not valid. This material shows a behavior that is typical of biological materials. Certainly, in experimental reality, one observes stress–strain diagrams that could be described as a superposition of these three basic types.

11.2
Mechanical Properties of Bulk Nanocrystalline Materials

It is well-known that hardness and yield stress increase with decreasing grain size. The *Hall–Petch* relation describes this experimental correlation between yield stress σ_y; and grain size d mathematically

$$\sigma_y = \sigma_0 + \kappa d^{-0.5}. \tag{11.4}$$

In Eq. (11.4) σ_0 and κ are constant parameters, which are specific for the materials. The grain size d is related to the smallest units, which may be limited by small-angle grain boundaries and not necessarily defined by wide-angle grain boundaries. The exponent −0.5 is experimentally and theoretically well established; however, experiments sometimes lead to exponents in the range from −0.3 to −0.7.

   Experiments with nanomaterials sometimes lead to results deviating significantly from the *Hall–Petch* relation. Figure 11.3 displays a comparison of a stress–strain diagram of palladium with different grain sizes.

   The comparison depicted in Figure 11.3 contains a lot of information. One sees the higher yield stress of 259 MPa for the nanocrystalline material with a grain size of 14 nm, and a significantly lower value of 52 MPa for the coarse-grained
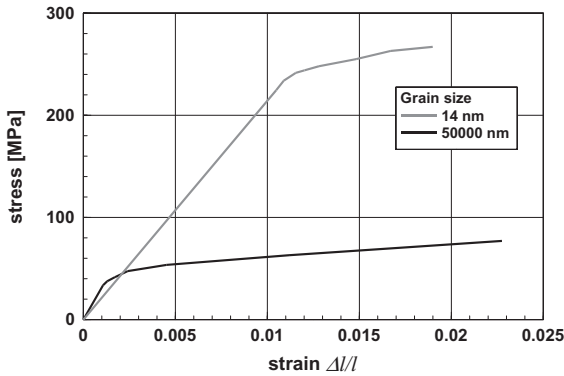
Figure 11.3 Stress–strain diagram of palladium with different grain sizes. The significant increase of the yield stress and a reduction of the *Young*'s modulus for the nanocrystalline material in comparison with the coarse-grained one are readily visible [3].
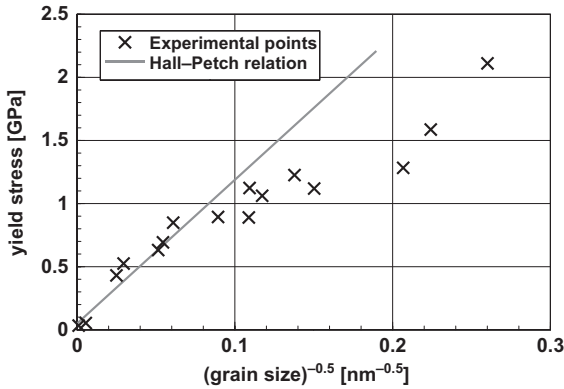
Figure 11.4 *Hall–Petch* plot of the yield stress of nanocrystalline nickel [4]. The experimental values deviate from the straight line represented by Eq. (11.4) for grains below 200 nm ($d^{-0.5} = 0.07\,nm^{-0.5}$). For smaller grains, the deformation mechanism that is the basis for the *Hall–Petch* relation is no longer acting.

material with 50 μm grain size. The ratio of the yield stresses is 4.89 and not, as expected from the *Hall–Petch* relation 60. This severe difference must be analyzed. Furthermore, the elastic modulus, *Young*'s modulus, of the nanocrystalline specimen is smaller than that of the coarse-grained material, a fact that is difficult to understand. As a further example, Figure 11.4 displays the yield stress of nickel [4] as a function of the grain size. To check the applicability of the *Hall–Petch* relation, in this plot, the yield stress is plotted versus the square root of the inverse grain size. In such a graph, the *Hall–Petch* plot, Eq. (11.4) is linearized.

Figure 11.4 shows two important facts: With respect to grain sizes, the validity of the *Hall–Petch* relation is limited. In the example of nickel, it may be applied

down to grain sizes of ca. 200 nm. For smaller grain sizes the experimentally observed yield stresses are lower than predicted by Eq. (11.4); therefore, additional or other deformation mechanisms must be assumed. The smallest grain sizes used in the experiments were 15 nm. It is striking that the smaller the grain sizes the larger was the scattering of the experimental data. This point needs additional discussion.

Bulk nanostructured parts are made by means of powder metallurgical methods. This means that the preparation starts with compression of the starting powder, followed by a sintering process at elevated temperature. This route of manufacturing leads, unavoidably, to materials with residual porosity. As nanocrystalline materials are, because of their high surface energy, far from thermodynamic equilibrium; any sintering process leads to grain growth. This means that preparation of specimens with different grain sizes is an extremely difficult task. One has to find a balance between grain growth to obtain the intended grain size and densification to reduce residual porosity. Lastly, this manufacturing problem leads to specimens that may have different porosities. Different porosity means different yield stress and deviating *Young*'s modulus (see Figure 11.3). This interdependency will be explained using the example of palladium, where the influence of grain size and porosity on yield stress and *Young*'s modulus were studied. Figure 11.5 displays the interdependency between grain size and porosity. One sees, as expected, an increasing grain size with decreasing porosity. This is readily understood, because to reduce porosity, longer sintering times are necessary, and a longer sintering time necessarily leads to larger grain size.

In this context, the porosity p is defined as

$$p = 1 - \frac{\rho_{\text{specimen}}}{\rho_{\text{theor}}}.$$ (11.5)
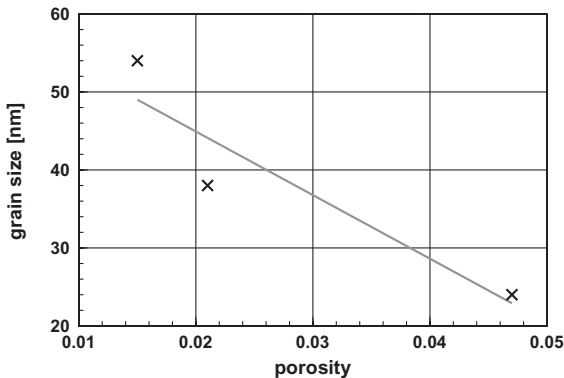
Figure 11.5 Example of the interdependency between porosity and grain size, determined on a palladium specimen [5]. It is important to realize the general fact of an increasing grain size with decreasing porosity. This is due to the necessary extended sintering time to reduce the porosity.

In Eq. (11.5) the quantity ρ_{specimen} stands for the actual, experimentally determined density of the specimen and ρ_{theor} is the theoretical density of the fully dense material.

Figure 11.5 makes it clear that on analyzing the mechanical properties of nanocrystalline materials the influence of porosity and grain size have to be taken into account. This means that whenever one analyzes, for example, the *Young*'s modulus as a function of the grain size, one must be aware that these measurements were obtained on specimens with different porosities and vice versa. The influence of the porosity on *Young*'s modulus has often been analyzed. An empirical approach to describe the influence of the porosity p, using a *Taylor* series development for the *Young*'s modulus E was made by MacKenzie [6].

$$E = E_0\left(1 + \alpha_1 p + \alpha_2 p^2 + \ldots\ldots\right). \tag{11.6}$$

In Eq. (11.6), E_0 is the *Young*'s modulus of the full dense material at $p = 0$ and α_1, α_2, etc. are fitting parameters. For small values of the porosity, the linear term is sufficient. For higher porosities, an increasing number of series elements are necessary. However, in the case of nanomaterials, because of the large scattering of the results caused by problems with the grain size, a first-order approximation is always sufficient.

Figure 11.6 depicts *Young*'s modulus for nanocrystalline palladium as a function of the porosity [7]. This example demonstrates the unavoidable scattering of the experimental values, due to different grain sizes for the specimen with different porosity. Looking at the heavily scattering experimental data, it is obvious that fitting with more than the linear element is not justified. However, besides this scattering data, the linear fit according to Eq. (11.6)

$$E_{\text{Pd}} = 132\left(1 - 2.5p\right)\left[\text{GPa}\right] \tag{11.7}$$

delivers for E_0 a value that is close to the bulk values found in coarse-grained materials. The reduction of the *Young*'s modulus with porosity, which is always
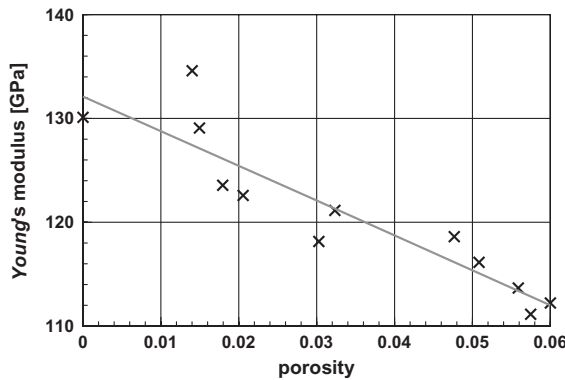
Figure 11.6 *Young*'s modulus of nanocrystalline palladium as a function of the porosity [7]. The wide scatter of the experimental values is, because of the unavoidable grain growth, inherent to experiments with nanocrystalline materials.
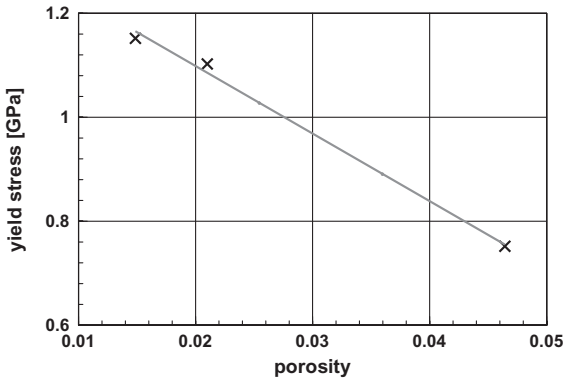
Figure 11.7 Yield stress of nanocrystalline palladium as a function of the porosity [5]. As is simply imaginable, the yield stress gets smaller with increasing porosity.

connected to sintered nanomaterials explains the reduced *Young*'s modulus of the nanocrystalline specimen in comparison to the coarse-grained one in Figure 11.3.

The yield stress is influenced by the porosity in a similar way. In this context, one can simply think of a reduction of the load-bearing cross section. Figure 11.7 displays the yield stress of nanocrystalline palladium again as a function of porosity [5].

In Figure 11.4, the experimental data for small particles deviate significantly from the values expected from the *Hall–Petch* relation. This deviation gets more prominent when the particles get smaller, and for the smallest particles, the trend in the *Hall–Petch* plot changes direction. This is shown in Figure 11.8, depicting the *Vickers* hardness of palladium as a function of the grain size. In this figure, blurred by severe scattering of the experimental data, it is clear that in comparison to Figure 11.4, the direction of the fitting straight line has changed its direction. (As was mentioned in connection with Eq. (11.4), for the hardness, the same functional relation is valid, as it is valid for the yield stress.) This experimental finding is called "inverse *Hall–Petch*" behavior.

11.3
Deformation Mechanisms of Nanocrystalline Materials

The *Hall–Petch* relation for the hardness and the yield stress is based on a deformation mechanism based on a dislocation mechanism. The experimental results, as depicted in Figure 11.4 and more prominently in Figure 11.8 suggests an additional or even entirely different mechanism acting at very small grain sizes. Experimental results obtained with a large range of grain sizes and different temperatures make it clear that there is a different mechanism acting. Having experimental data ranging from conventional grain sizes to extremely small ones, demonstrates these two mechanism for deformation are applicable. A typical example is shown in Figure 1.9. In this figure, the hardness of TiAl, an
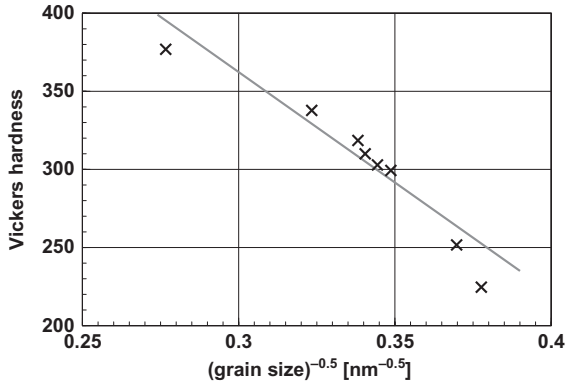
Figure 11.8 *Vickers* hardness of palladium as function of the grain size [8]. This *Hall–Petch* plot shows the existence of the inverse *Hall–Petch* relation, which is regularly found at small particle sizes.
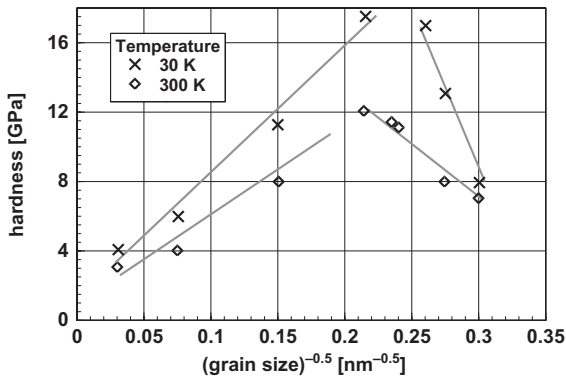
Figure 11.9 Hardness *Hall–Petch* plot of the intermetallic compound TiAl, at 30 and 300 K [9] At both temperatures, two ranges are visible. One shows an increase of hardness with decreasing grain size, as expected according to the *Hall–Petch* relation and a second one below approximately 20 nm, where the hardness decreases with decreasing grain size. At small grain sizes, one observes the "inverse *Hall–Petch*" behavior.

intermetallic compound, is plotted as a *Hall–Petch* plot, this means against the inverse square root of the grain size. The experimental data were measured at 30 and 300 K.

The course of the hardness depicted in Figure 11.9 shows, independent of the temperature, two different regions indicating two different mechanisms acting during deformation. At larger particle sizes, one finds the conventional *Hall–Petch* relation, which means an increasing hardness with decreasing particle size. At smaller particle sizes, perhaps below 20 nm, the trend is the reverse. In this
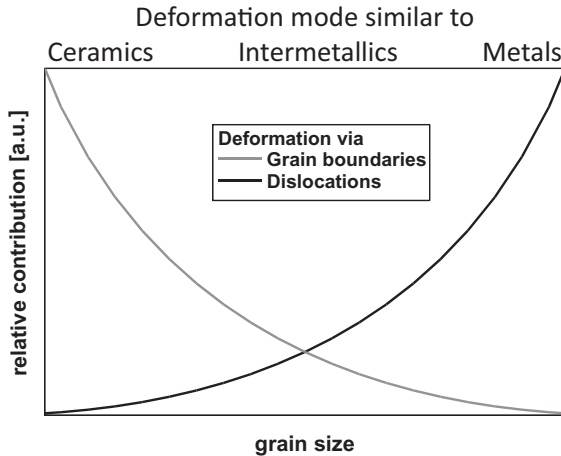
Figure 11.10 Comparison of the deformation modi of metals, intermetallic compounds, and ceramics with the mechanical behavior of metals with decreasing grain size [10]. This graph clearly indicates the decreasing importance of dislocation processes for plastic deformation with decreasing grain size; instead, the importance of grain-boundary processes increases.

range, the hardness reduces with decreasing particle size. This range is called the "inverse *Hall–Petch*" range. This behavior is very general, it is observed in pure metals, too. In this range of particle sizes, the deformation takes place via grain-boundary processes. This change in the deformation mechanism inspired Siegel and Fougere [10] to the graph shown in Figure 11.10. This graph is based on the fact that, at least at conventional grain sizes, metals are deformed via dislocation processes, whereas the deformation of ceramic materials occurs primarily via grain-boundary processes. As shown above, nanocrystalline metals are deformed primarily via grain-boundary processes; therefore, these materials behave like ceramic ones.

The graph of Siegel and Fougere [10] was ideally justified by model calculations related to the deformation modes acting in copper as a function of the grain size [11]. These results are depicted in Figure 11.11, where, at a strain rate of $10^{-5}\,s^{-1}$, the contribution of the dislocations and grain boundaries to the total strain rate as a function of the grain size are plotted. In this example, at a grain size of 35 nm, the relative contribution of dislocations and grain boundaries are equal. At smaller grain sizes, primarily grain-boundary processes are responsible for the plastic deformation. This is the range of the inverse *Hall–Petch* behavior.

Obviously, at small grain sizes the deformation mechanism is changing. To understand these changes, one has to analyze the deformation mechanisms. In conventional materials, plastic deformation is related to generation and movement of dislocations, which are one-dimensional lattice defects. Within a grain, there may be immobile and mobile dislocations. For plastic deformation, only the
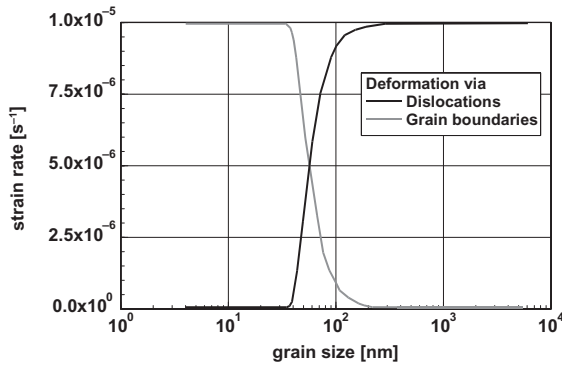
Figure 11.11 Contributions of the deformation modi via dislocation and grain-boundary processes for copper as a function of grain size and deformation rate. In this example, at a deformation rate of $10^{-5}\,s^{-1}$ at grain sizes below approximately 35 nm only grain-boundary processes contribute to deformation [11].
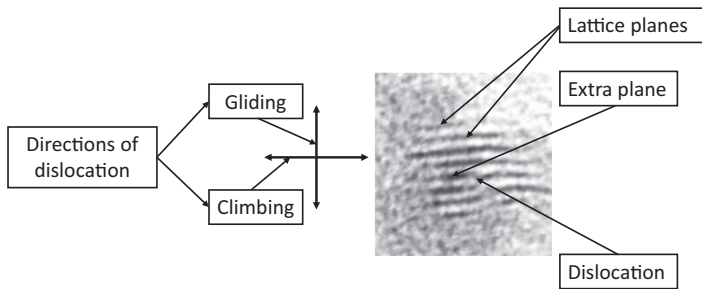
Figure 11.12 Electron micrograph of an edge dislocation in a crystal lattice. The possible directions of the different modi of movement are indicated. Movement of dislocations is possible only for mobile dislocations.

latter are of importance. Simply speaking, dislocations are caused by additional partial lattice planes in an otherwise perfect crystal. (More precisely, one has to distinguish between edge and screw dislocations; however, this is a topic for a specialized book.) During plastic deformation, dislocations may either glide or climb dislocation gliding always occurs after an increase of the stress beyond the yield stress, whereas dislocation climbing observed during creep deformation, is controlled by diffusion. Figure 11.12 displays this situation for an edge dislocation characterized by an extra lattice plane. Furthermore, the direction of movement during glide and climb processes are indicated in this figure.

The mode of dislocation movement, gliding or climbing, influences the shape of a specimen after deformation. This is, in a simplified manner for a single crystal depicted in Figure 11.13, where in the case of gliding the existence of only one gliding plane was assumed.
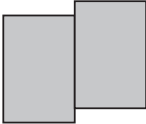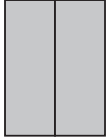
	Deformation by dislocation	
	Gliding	Climbing
Before deformation		
After deformation		

Figure 11.13 Influence of the deformation mode, dislocation gliding or climbing, on the shape of a single-crystal specimen after deformation.

Box 11.1   The *Frank–Reed* Mechanism as the Origin of Dislocations

The most important source of dislocations is the *Frank–Reed* source. To operate such a *Frank–Reed* source within a slip plane of one grain, one needs a dislocation, anchored at two fixed nodes. These nodes may be positioned within one grain, or at the grain boundary. Because of their high elastic energy, dislocations are connected to a line tension. Therefore, any dislocation has the tendency to shorten. An applied external stress bows the dislocation out. This leads to a change of its radius of curvature until the line tension is in equilibrium with the applied stress. Further increasing the line stress beyond a point where the dislocation is semicircular, creates a situation where the dislocation no longer has an equilibrium position. Therefore, the dislocation expands rapidly and rotates around the nodes until the loops meet each other forming a complete dislocation loop and a new line source between the nodes. Now this process may start again. This generation and movement of dislocations is connected to plastic deformation. This temporal sequence of the dislocation loop of a *Frank–Reed* source is, in three different time steps, depicted in Figure 11.14.

The stress necessary to activate a *Frank–Reed* source is given by

$$\tau = \frac{Gb}{l}. \tag{11.8}$$

In Eq. (11.8), τ stands for the shear stress in the plane of the dislocation, G the shear modulus and l the distance between the two nodes. The *Burgers* vector b, is characteristic of the type of dislocation and the crystal lattice; numerically, it is in the range of a few tenths of a nanometer. The shear stress necessary to activate a *Frank–Reed* source is, according to Eq. (11.8) indirectly proportional to the distance between the pinning points (nodes). The maximum possible distance between the pinning points is the grain size. Rewriting Eq.

t_1 t_2 t_3

$t_1 < t_2 < t_3$
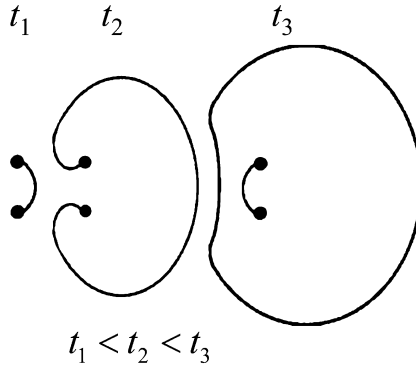
Figure 11.14 *Frank–Reed* source of dislocations in its temporal sequence. One sees the extension of a dislocation fixed at two pinning points under the influence of a stress and finally, the separation from the pinning points, leading to the formation of the next dislocation. Then, the cycle starts again.

(11.8) gives important information on the possibility of activating a *Frank–Reed* source

$$l_{min} = \frac{Gb}{\tau_{max}}.$$ (11.9)

The quantity l_{min} stands for the smallest distance of the pinning points, and τ_{max} for the maximal possible shear stress, which is, for metals, in the range between $10^{-3} \times G$ and $10^{-2} \times G$. The *Burgers* vector is in the range of 10^{-10} m; therefore, the minimal size l_{min} of a grain with an active *Frank–Reed* source may be estimated to be in the range between 10^{-8} m and 10^{-7} m. This says that the size limit of a particle that be deformed by dislocations created via a *Frank–Reed* source is in the range of 100 nm. Therefore, in most nanocrystalline materials, *Frank–Reed* sources for dislocation generation are impossible. Next, one may ask for dislocations already existing in nanocrystalline materials and their influence on plastic deformation. Around the edge of the extra plane of a dislocation, there is a stress field. Close to the surface, the dislocations produces a stress in the surface plane pulling them towards the surface. Provided the dislocation is mobile, it moves to the surface, where this dislocation will be annihilated. As in nanomaterials, with sufficiently small grain size, any point is close to a surface, mobile dislocations are impossible, and as *Frank–Reed* sources are, in most cases, impossible, too, deformation of these materials via dislocations is not possible.

The inverse *Hall–Petch* mechanism of deformation demands other deformation mechanisms as discussed above. In conventional materials, at high temperatures, especially for ceramics, plastic deformation via grain-boundary processes is possible. During deformation via grain-boundary processes, the number of grains remains constant, the shape of the grains, however, will be altered. This is sche-
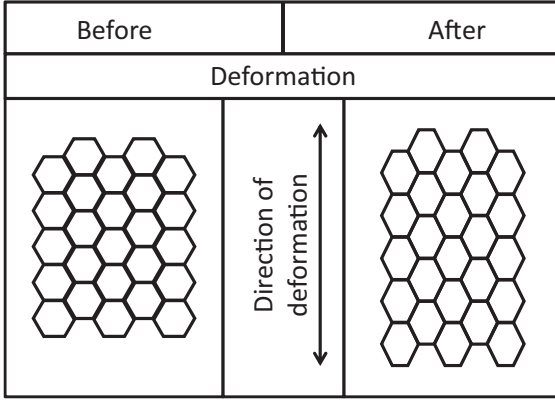
Figure 11.15 Modification of a specimen after deformation via grain-boundary processes. In an idealized manner, the grains are depicted as hexagons of equal size. It is important to note, and depicted in this figure, that numbers and arrangement of the grains remain unchanged.

matically depicted in Figure 11.15, where the grains are depicted as hexagons of equal size. This is extremely idealized; however, this configuration is best accessible for the theoretical considerations.

For technical materials, most important are the grain-boundary deformation processes described by *Nabarro–Herring* or *Coble*. Both of these processes are diffusion controlled. In general, they are described by the deformation rate $\dot{\varepsilon}$.

The *Nabarro–Herring* mechanism, acting via volume diffusion is described by,

$$\dot{\varepsilon} \propto \frac{D_{vol}\sigma}{d^2}, \tag{11.10}$$

whereas the *Coble* mechanism, controlled by grain-boundary diffusion follows

$$\dot{\varepsilon} \propto \frac{D_{GB}\sigma}{d^3}. \tag{11.11}$$

In Eqs. (11.10) and (11.11) σ stands for the acting stress and d for the grain size; D_{vol} for the volume diffusion coefficient and D_{GB} for the grain-boundary diffusion coefficient. Generally, one can say, the *Nabarro–Herring* mechanism acts at higher temperatures, close to the melting point and the *Coble* mechanism is active at lower temperatures.

As the *Nabarro–Herring* mechanism operates in a temperature range where nanocrystalline materials are, because of extensive grain growth, no longer stable, this mechanism can be excluded. Decisions about the *Coble* mechanism are a priori not possible; experimental results are necessary.

A further grain-boundary mechanism for plastic deformation, especially for nanocrystalline materials was proposed by Ashby and Verall [12]. This mechanism is called the "grain-switching" mechanism. The sketch in Figure 11.16 makes clear what was meant by this name. Even when the functional relations between
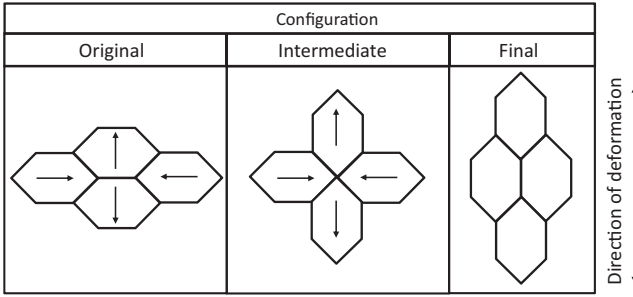
Figure 11.16 Deformation of a specimen by the *Ashby–Verall* "grain-switching" mechanism. The figure displays the original, an intermediary, and the final state. The grain-size dependency of this mechanism is d^{-3}.
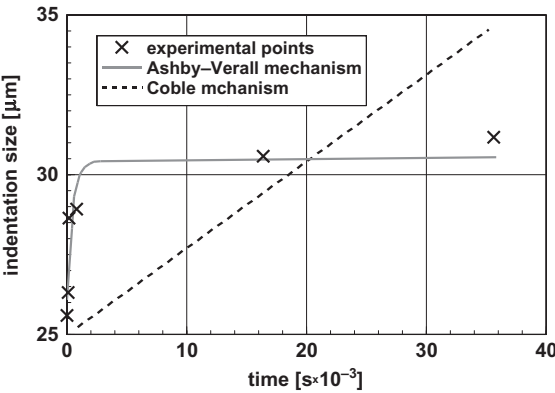
Figure 11.17 Size of the *Vickers* hardness indentation as a function of the indentation time. This graph compares model calculations based on the mechanisms of *Ashby–Verall* and *Coble*. In this example, TiAl deformation follows the *Ashby–Verall* mechanism [9].

deformation rate, stress, and grain size are more complex compared to the other deformation mechanisms, it must be noted that the deformation rate is proportional to d^{-3}.

As the mechanisms of *Coble* and *Ashby–Verall* show the same grain-size dependency, it is quite difficult to decide which one of these mechanisms is acting. By comparison of *Vickers* hardness measurements on TiAl specimens with model calculations, Chang *et al*. [9]. proved the validity of the *Ashby–Verall* process for the deformation process of nanocrystalline intermetallcs experimentally. Figure 11.17 displays the results of this study. In this graph, the size of the *Vickers* hardness indentation is plotted as a function of the time. For modeling, the mechanisms of *Coble* and *Ashby–Verall* were applied. Figure 11.17 shows that the experimental data are described quite well by the *Ashby–Verall* mechanism, whereas the assumption of the *Coble* process leads to a time dependency far from experimental reality.

11.4
Superplasticity

Superplasticity is a very special property allowing large plastic deformation. Generally, plastic deformations of significantly more than 100%, may be up to 1000%, are possible. In contrast to standard materials, which allow large plastic deformation, superplastic deformation has a unique feature: During plastic deformation, conventional materials show, for example, in a tension test a local narrowing before rupturing, superplastic materials becomes uniformly thinner. Superplasticity is restricted to very narrow ranges of small grain sizes and a quite narrow temperature window. For conventional materials, the temperature range, where superplasticity is found is around 0.5 T_m (T_m is the melting temperature in *Kelvin*). Furthermore, superplasticity is restricted to a quite narrow range of deformation rates. This phenomenon is observed in pure metals, alloys and ceramic materials, certainly, as ceramic bodies cannot be produced without any flaws (e.g., pores) one never reaches such huge strains as in metals. The deformation rate $\dot{\varepsilon}$ of a superplastic specimen is described by:

$$\dot{\varepsilon} \propto \frac{\sigma^n}{d^2}. \tag{11.12}$$

The stress exponent n in Eq. (11.12) is 1 for diffusion or grain-boundary processes and 2 for dislocation processes.

Two typical examples of superplastic materials will be used for demonstration. The examples are in both cases metallic. Figure 11.18 displays the stress–strain diagrams of Ni_3Al, an ordered intermetallic compound [13] with a grain size in the range between 80 and 100 nm, and the alloy Ti6Al4V [14], with a grain size between 30 and 50 nm. The deformation rate during the experiments displayed in Figure 11.18 was $10^{-3}\,s^{-1}$.
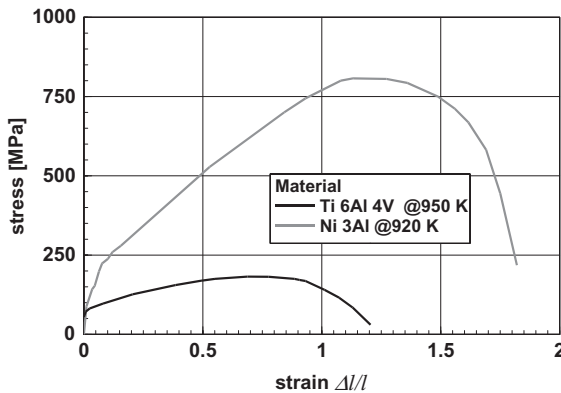
Figure 11.18 Stress–strain diagram for superplastic Ni_3Al with a grain size of 80 nm [13] and Ti6Al4V with a grain size in the range from 30–50 nm [14]. The large strain, exceeding 1 (>100%) is remarkable.

The stress–strain diagrams plotted in Figure 11.18 show strains far beyond 100%. These nanocrystalline specimen were produced by severe plastic deformation of conventional materials. Specimens produced by powder metallurgy will hardly reach such strains, as it is nearly impossible to obtain flawless parts by these processes. Analyzing the properties of these two specimens, it is remarkable that they show superplasticity at temperatures lower than observed in specimens with larger grains. For these two specimens, the temperature was low enough to inhibit grain growth. One may take as a rule that in nanocrystalline materials, superplasticity is observed in a particle size–temperature–stress regime, where the transition from dislocation to grain-boundary processes takes place.

Superplasticity is found in ceramic materials, especially in oxides, too. Certainly, as the ductility of ceramic materials is significantly lower than the ductility of metals, one may not expect huge plastic deformations, as are found in metals. Furthermore, ceramic parts are produced from powders by a sequence of pressing and sintering; therefore, as mentioned above, fully densified bodies are not possible. In particular, as the poor pressing behavior of nanoparticulate powders is not compensated by the excellent sintering properties, therefore, the specimens contain pores, which reduce the strength of a material by the reduction of the bearing cross-section. Perhaps more important in reducing strength and plasticity is the reduction of the maximal strength σ_{flaw} of a specimen caused by flaws of the size c, which is described by the proportionality

$$\sigma_{\text{flaw}} \propto \frac{1}{c^{0.5}}. \tag{11.13}$$

The existence of pores or other flaws leads to premature cracking, with the consequences of reduced strain and strength. Successful production of ceramic specimen exhibiting superplasticity is a reference for excellent abilities in ceramic technologies.

In spite of all these problems, it is possible to produce superplastic ceramic parts. As typical example for superplastic ceramics, Figure 11.19 displays a stress–strain diagram, taken in a tension test (the tension test must be noted, as in general, ceramic materials are tested in compression), of zirconia doped with 5 wt% yttria to stabilize the tetragonal phase [15] (see also Chapter 7). The density of the material was in the range from 84 to 94% of the theoretical density. The grain size was in the range from 45 to 75 nm. This material was sintered at 1420 K.

Figure 11.19 shows the elongation of the specimen of 37 and 52%, values, which are, for a ceramic material, extremely large deformations. The testing temperature was not significantly lower than the sintering temperature, therefore, substantial grain growth was observed during deformation. It could be that the superposition of plastic deformation with grain growth has a distinctive influence on this result. Grain-boundary sliding was identified as the deformation mechanism. Furthermore, these experiments showed that the deformation was directly connected to grain growth and a reduction in density.
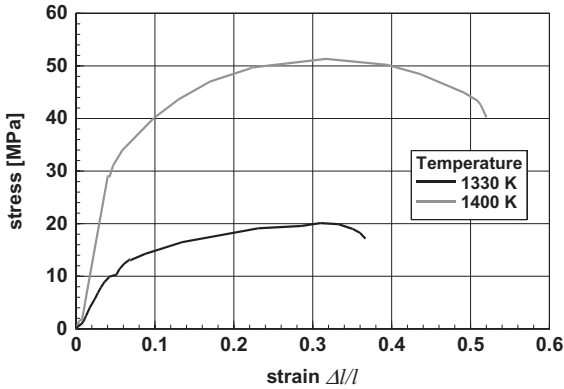
Figure 11.19 Superplastic deformation of ZrO$_2$ (5 wt% Y$_2$O$_3$) with grain size in the range from 45 to 75 nm and densities around 90% TD. The tests were performed under tension. As these tests were performed at elevated temperature, unavoidably, grain growth was observed during the experiments [15].

11.5
Filled Polymer Composites

11.5.1
General Considerations

Filled polymers have tremendous economic importance; this is because of their outstanding new or improved properties. The improvement may be in the field of strength, temperature resistance, or inflammability. The improved property depends strongly on the type of filler and the way of filling. The latter point is of special importance, as one may easily lose the specific advantages of nanoparticulate filler when the filler forms aggregates, mimicking large particles. It is easily understandable that one has to differentiate between more or less spherical particles as fillers, fibers, or platelets. Figure 11.20 displays stress–strain diagrams of pure and differently filled polymers. The lowest strength is found for the unfilled polymers, however, at least in the idealized case, the strain at rupture is largest.

Depending on the shape of the filler, particles, platelets, and on the degree of agglomeration the strength of such filled polymers is found in a broad range; however, in general, these are at higher values as compared to unfilled polymer. As a rule, one may say that the improvement of the properties becomes less pronounced if the particles get larger or agglomerated. Most interesting in this class of composites are ones filled with silicate platelets. Because of the significantly reduced inflammability, these materials have, at the moment, the highest economic importance. The highest strength combined with a reasonable ductility is obtained by filling the polymer with fibers, especially carbon nanotubes.
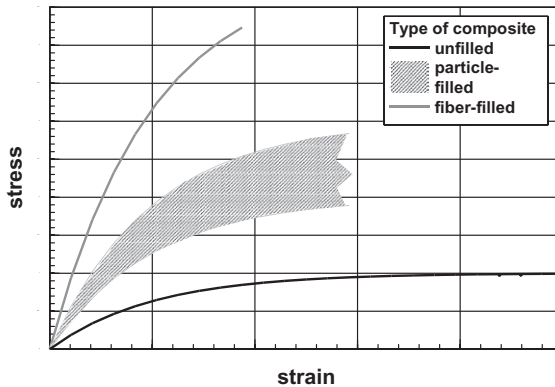
Figure 11.20 Stress–strain diagram of pure and filled polymers. In general, one obtains the best ductility with unfilled material. Adding particles lead to an increase of the strength combined with a reduction of the strain at rupture. Depending on the size, shape, and degree of agglomeration, the properties of these composites are found in a wide range. The highest strength is obtained by filling with fibers.

The properties of particle-filled polymers heavily depend on the production process. In the simplest way, powder and polymer are kneaded together. This process leads to the formation of clusters of particles that are, depending on the kneading time, more or less well distributed. Further, more advanced processes start with a suspension of the nanoparticulate powder in a liquid. This liquid is either a solvent for the polymer or a liquid precursor compound, like a monomer. The powders are brought into this liquid and equally distributed, perhaps by sonification. As last step, the liquid phase is either evaporated or polymerized. Processes starting with liquid suspensions lead to products of the highest quality. Applying a constant amount of second phase leads, as was proven experimentally, to an increase of strength if the particle size decreases. Also, clusters of small particles seem to have advantages over larger particles. This relation is sketched in Figure 11.21, which is an extension of a graph, drafted by Jordan *et al.* [16].

The ultimate strength of composites as depicted in Figures 11.21a–c may be understood readily after applying Eq. (11.13). The failures introduced by stresses into the specimen are larger in the case of larger particles (compare panels a and b); therefore the strength is reduced. In the case of clusters of small particles, generally, the crack goes through the cluster, hence, the crack is larger than in case of singularized particles but smaller than in the case of a single particle having the same size as the cluster. The considerations above assume perfect bonding between the particle and the polymer. When this binding is insufficient, the filler particles act as flaws and not as a strengthening element.

Most interesting are composites where the second phase consists of platelets. This design is often found in nature, in materials of biological origin, where high-strength nanocomposites, consisting of a mineral phase bond together by proteins, exist. Most important examples are bones and nacre (mother-of-pearl), where well-
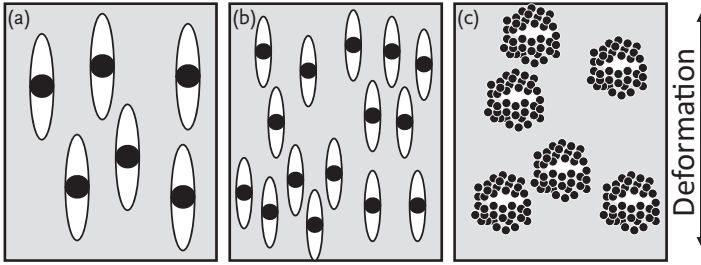
Figure 11.21 Influence of the size of the second-phase particles in ceramic–polymer nanocomposites on the behavior of the composite under tension. Larger particles lead to larger failures under load (compare panels a and b) reducing the maximum stress before cracking (as expected from Eq. (11.13)). Under load, agglomerates of small particles may also lead to large failures and, therefore, early cracking.
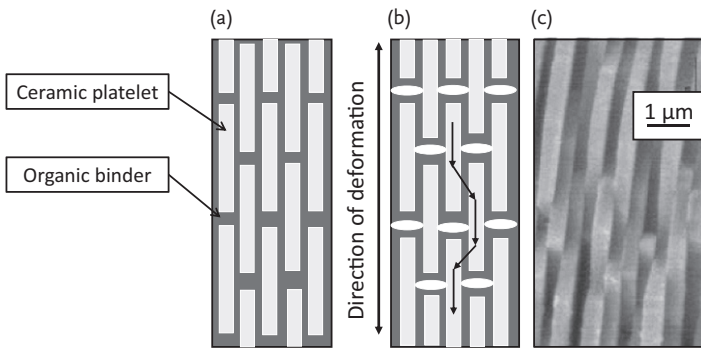
Figure 11.22 Structure of an idealized and a natural nanocomposite consisting of a platelet-shaped filler bond together with a polymer. (a) Idealized arrangement of the ceramic building blocks and the polymer filler. (b) Flow of the stress in a composite according to Figure 11.22a. In this graph, it was assumed that the stress was so high that the soft binder in-between the ceramic platelets is already broken. The part itself is not broken, as the bonding between ceramic platelet and binder remains intact. (c) Electron micrograph of nacre [17] (mother-of-pearl) a natural high-strength nanocomposite that comes close to an idealized structure as displayed in Figure 11.22a.

ordered inorganic platelets are bonded together with proteins, a design leading to high-strength material. To a large extent, these composites are insensitive to flaws [17]. Schematically, this type of materials without and under load is shown in Figure 11.22.

The type of composite as depicted in Figure 11.22 is preferred in nature. The archetype of this structure is found in nacre, consisting of crystallized mineral platelets (aragonite) with a thickness of a few nanometers bonded together with collagen as matrix. This "brick and mortar" structure combines two materials with quite low strength to a high-strength composite. This structure is to a large extent resistant against disastrous cracks. The crack resistance can be understood looking

at Figure 11.22b, where the flow of stresses is marked. It was assumed that the stress was so high that the soft binder in-between the ceramic platelets is broken. However, the bonding between polymer and ceramic remains intact and, therefore, the part itself did not break. The simplified model shows the ceramic structure carrying most of the load, which is transferred via the high-shear zones between the ceramic platelets. The part will break when the stress reaches a level where either the ceramic platelets will break or, more probably, the shear stress between the organic binder and the ceramic filler leads to debonding [17]. The electron micrograph of nacre depicted in Figure 11.22c shows that there is not too much idealization in the model structure. It can be shown theoretically that there exists an optimum aspect ratio of the ceramic bricks corresponding to the condition that protein and mineral fail at the same load [17]. Certainly, such an idealized structure has disadvantages, too. It is important to note that the good properties of the structure depicted in Figure 11.22 are not observed in the direction perpendicular to the platelets. This fact must be considered when designing optimal structures of composites with platelet-shaped fillers.

11.5.2
Particle-Filled Polymers

Polymers filled with ceramic particles show some improvement of their mechanical properties. Therefore, based on theoretical considerations, the expectations towards polymers filled with nanoparticles were high. However, as already mentioned in the previous section, manufacturing of these composites is quite difficult; therefore, the experimental results were widely scattering. Figure 11.23 displays stress–strain diagrams of composites based on a polyamide-6 (nylon-6) as material for the matrix. As the filler, silica nanoparticles were selected with a diameter of 17 and 80 nm, respectively. Analyzing this graph, two features are
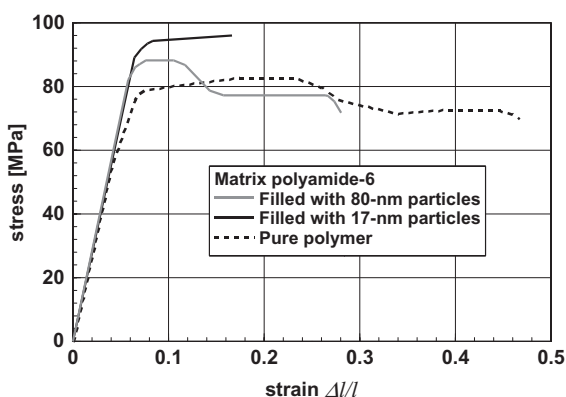
Figure 11.23 Stress–strain diagram of pure and nanoparticulate-silica-filled polyamide-6 (nylon-6) nanocomposite. The composite shows improved strength connected to reduced ductility. This effect is extremal for the smallest particles [18].
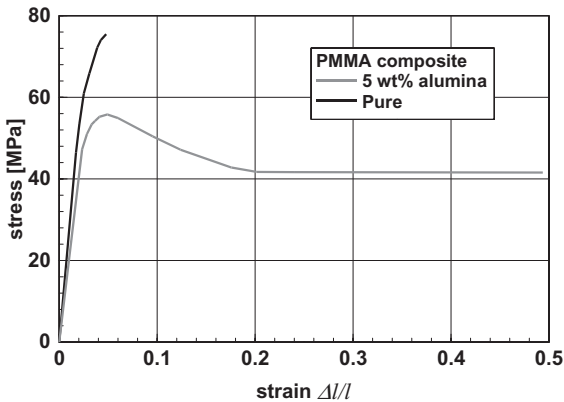
Figure 11.24 Stress–strain diagram of PMMA, pure and filled with 5 wt% alumina particles. The particle size was 40 nm. Contrary to expectations, the pure polymer exhibits the highest strength and the least strain at rupture as compared with the filled material [14].

striking: The filled polymer shows an, up to 15%, improved fracture stress, where the better improvement is obtained with the smallest particles. Having Figure 11.21 with its related explanations in mind, this result was as expected. Certainly, there is no advantage without disadvantages; for both composites, the strain at rupture is reduced significantly. However, this does not necessarily reduce the fields of applications, as a strain at fracture of 0.17 (=17%) is sufficient for nearly all possible applications. In spite of all the problems connected to production and applications, one must bear in mind that an increase of the strength means a reduction in the consumption of materials.

As was explained in the previous section, bonding in-between the ceramic particles and the polymer matrix is essential for the quality and the properties of the composite. If the bonding is insufficient, the filler particles will act as flaws and not as a strengthening element. Such an adverse example is shown in Figure 11.24. This figure displays stress–strain diagrams of pure PMMA and PMMA filled with 5 wt% (which is equivalent to ca. 1.5 vol%) alumina. The size of the alumina particles was in the range of 40 nm. Against expectations, the filled polymer showed, in this special case, reduced strength, and increased ductitility as compared to the pure PMMA specimen. The reduced fracture stress can be explained by insufficient binding inbetween the polymer matrix and the filler particles; however, the improved ductility remains without explanation. The reduced *Young*'s modulus is explainable by the fact that the particles act like pores (see Eq. (11.6)).

11.5.3
Polymer-Based Nanocomposites Filled with Silicate Platelets

Nanocomposites with a polymer matrix filled with silicate platelets exhibit very special properties. They have high strength and, most importantly, a significantly

(a) (b) (c)
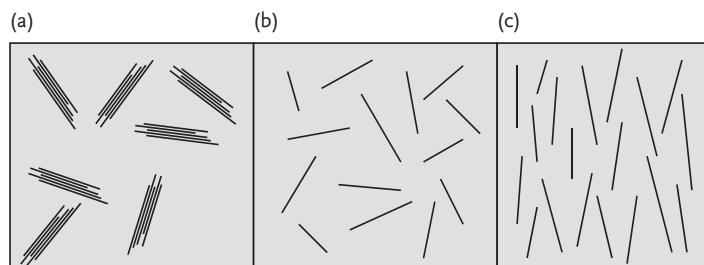
Figure 11.25 Possible arrangements of platelets as filler particles in a polymer matrix. (a) Conventional composite. Particles consisting of stacks of layers are distributed in random in the matrix. (b) Randomly oriented defoliated layers. (c) Defoliated layers as shown in Figure 11.25b; however, more or less parallel oriented. This structure resembles that of nacre.

reduced inflammability. The latter property makes this composite material important for the automobile and aerospace industry. Lastly, because of these special properties, polymers filled with silicate platelets, are a billion-dollar business. Originally, these composites were developed by Toyota in 1989, intended for use in the automotive industry.

As silicate platelets, defoliated (also called delaminated) layered silicates (phyllosilicates), such as montmorillonite, are in use. Such layered silicates can be split by mechanical methods and defoliated to single layers by chemical processes. Before looking at processes for the production, first it is necessary to understand which is the optimal structure for a certain application. Figure 11.25 displays, in a simplified way, the three most important types of structures, possible for layered silicates in a polymer matrix.

The composites depicted in Figure 11.25 are typical for different states of material development. In Figure 11.25a, there are stacks of silicate layers randomly embedded in the polymer matrix. One may expect improved properties if the stacks of silicate layers are delaminated (singularized). After delamination, one may obtain two different structures: One with arbitrarily oriented platelets or one with parallel-oriented platelets. The structure with parallel-oriented platelets resembles that of nacre, which shows high strength; however, the strength of this structure is not isotropic, there are directions with higher and directions with lower strength. If this anisotropy is not intended, the structure, as is depicted in Figure 11.25b with randomly oriented platelets must be selected, even when the maximal strength is lower. In any case, the optimal structures need singularized plates, which means that the particles are split up into individual layers. Figure 11.26 displays a typical electron micrographs of such a composite according to Figure 11.25c.

Figure 11.26 shows mostly defoliated sheets of 5.6 wt% montmorillonite in a polystyrene matrix [19]. Besides the nearly perfect defoliation, the individual sheets are more or less oriented in parallel.

From its basic idea, composites consisting of a polymer matrix and defoliated phyllosilicates should exhibit excellent mechanical properties. As shown in Figure 11.27, exactly these expectations were fulfilled. In this graph, stress–strain diagrams of composites consisting of nylon-6 as matrix material and additions of montmorillonite [20]. The depicted results were determined at room temperature and 350 K.

Figure 11.27 shows that the addition of only 3 wt% montmorillonite to nylon-6 nearly doubles the strength of the material. This statement is valid at room temperature and at slightly elevated temperature (350 K), too. In particular, at the
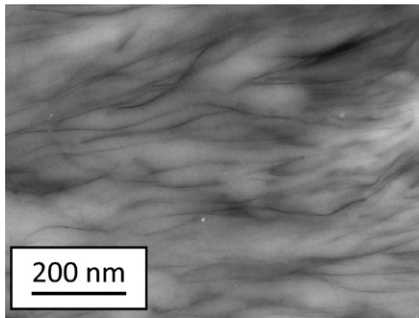
Figure 11.26 Electron micrograph of a typical composite consisting of a layered silicate, 5.6 wt% montmorillonite in a polystyrene matrix. To obtain optimal properties, the defoliated layers are aligned almost parallel [19]. (Reproduced with permission by Elsevier.)
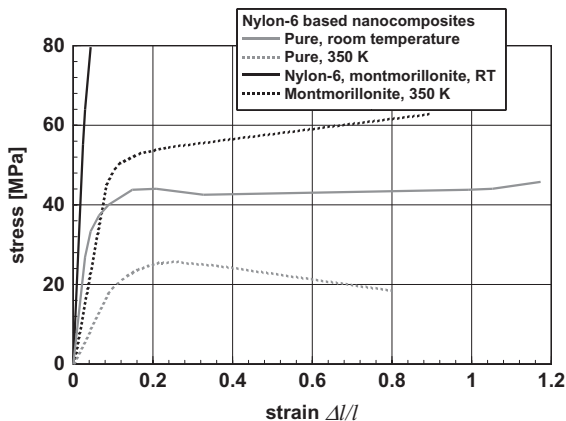
Figure 11.27 Stress–strain diagrams of nanocomposites consisting of a nylon-6 matrix and 3 wt% montmorillonite [20]. In comparison to the pure polymer, the strength of the composite is significantly improved. Additionally, the *Young*'s modulus of the composite is higher.
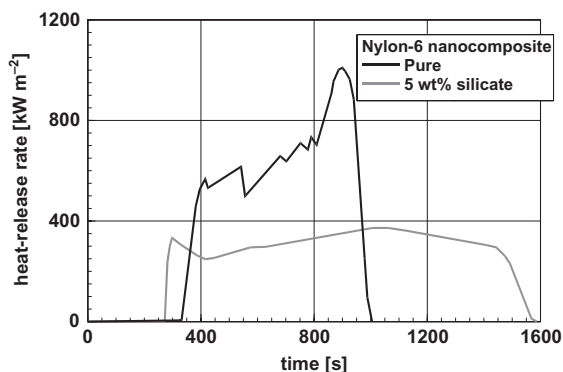
Figure 11.28 Heat release of pure nylon-6 and a composite of nylon-6 filled with 5 wt% silicate under a heat flux of 35 kW m^{-2} [21]. The reduction of the maximum heat-release rate to nearly a third is remarkable, and an important safety feature, for example, in the automotive industry.

higher temperature, the strength of the composite remains higher than that of the pure polymer at room temperature. In spite of the significant improvement of the strength, the strain at rupture remained in a range that does not create problems in technical applications. The higher *Young*'s modulus of the composite, in comparison with the pure polymer, is notable; this increase is, possibly, caused by the stiffer silicate platelets in the polymer matrix. Besides the improved strength, the reduced inflammabilty, the flame-retardant properties, are of equal, or possibly higher, importance. Advantages in this direction are observed in the released heat and the maximum temperature of flames during burning. Figure 11.28 displays the heat release during heating the material with 35 kW m^{-2} [21]. During this experiment, the specimen starts burning.

The results presented in Figure 11.28 make clear the silicate filling of polymers reduces the flammability significantly. The maximum energy that is released during this experiment is approximately one third of the heat released from the pure polymer during the same experiment. Interpretation of the results with respect to the reduced heat release is given by the following considerations: When the specimen is heated from one side, the polymer evaporates and starts burning. The silicate filler does not burn; it remains as a layer at the surface. This surface layer acts as a thermal insulator; therefore, the heat supply to the residual material is reduced, the evaporation rate is reduced, the amount of inflammable gas is reduced; hence, the amount of heat produced at the surface is reduced. Translated to technical applications, one can say that the propagation of flames is at least reduced, if not stopped altogether.

The polymer polypropylene has many advantages in processing; however, polypropylene burns quite well. Therefore, one may ask if a phyllosilicate filler could improve the properties of this polymer in a way that leads to broader applications. The improvement of the mechanical properties is not as significant as for nylon-6

as matrix material. Figures 11.29a,b display *Young*'s modulus and tensile strength of a composite with polypropylene matrix filled with different amounts of montmorillonite [22]. It is obvious that at a silicate content of about 7 wt% saturation is observed. One observes an increase of the *Young*'s modulus of ca. 40% and an increase of the tensile strength of less than 30%. Even these values are not as spectacular as those of the nylon-6 based composite, with respect to the application also these values are important.

More important than the improvement of the mechanical properties is the reduction of the inflammability of polypropylene by additions of layered silicates. Figure 11.30 displays the heat-release rate of these composites [23]. In this example, the reduction of the heat-release rate is even more dramatic than that for the
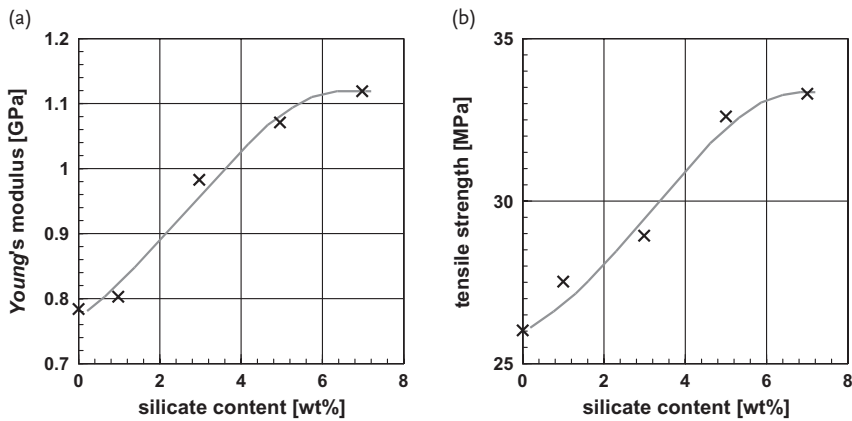
Figure 11.29 *Young*'s modulus (a) and tensile strength (b) of polypropylene filled with different amounts of montmorillonite. The improvement of these properties is remarkable [22].
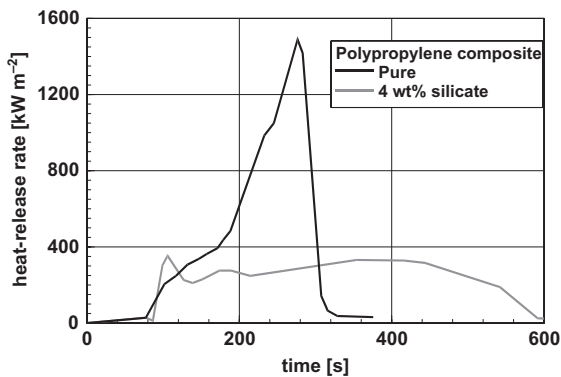
Figure 11.30 Heat-release rate of a polypropylene 4 wt% silicate nanocomposite under a heat flux of 35 kW m^{-2}. The reduction of the maximal heat release rate from nearly 1500 to 330 kW m^{-2} is remarkable [23].

composite with nylon-6 as matrix material. Lastly, it is reduced to the same value as was found with the nylon-6 based composite. Even when the strength of the polypropylene matrix composites is significantly lower, the reduction of the inflammability expands the variety of materials for technical applications.

11.5.4
Carbon-Nanotube- and Graphene-Filled Composites

Nanocomposites with carbon nanotubes or graphene as filler are very promising, as both materials are extremely stiff; the *Young*'s modulus is around 1 TPa. Additionally, carbon nanotubes exhibit a maximum tensile strength close to 30 GPa [24] and graphene 130 GPa [25]. However, these values are in dispute, other authors report *Young*'s moduli for carbon nanotubes in the range from 0.64 to 1.8 TPa. In any case, whatever the correct values are, carbon nanotubes and graphene are stiffer and exhibit higher strength than any other material available in large quantities for reasonable prices. Additionally, it is not too difficult to distribute carbon nanotubes or graphene in a polymer matrix. This makes these composites a highly promising class of materials. Interestingly, to some extent predetermined, the shape of the specimen is oriented on the habit of the filling material; this means, carbon nanotubes are primarily tested as fibers, whereas graphene-filled specimens are, in general, films. In the case of carbon nanotubes, the technical application goes in two different directions: Composites with relatively small additions of nanotubes and materials where the binding polymer is the minor phase and the fibers are the majority phase.

As examples of the technological direction applying a small amount of carbon nanotubes in a polymer matrix, Figure 11.31 is shown [26]. This figure displays
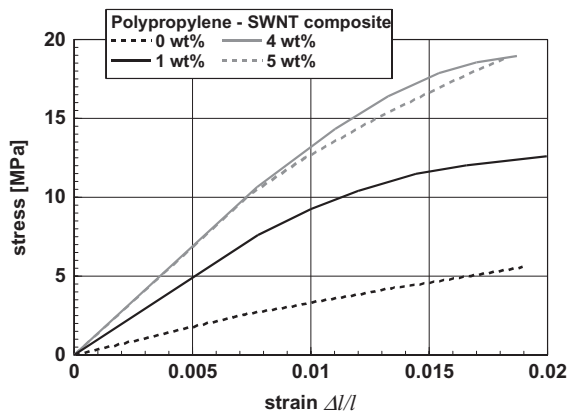
Figure 11.31 Stress–strain diagram of fibers with a thickness of 1.6 mm consisting of polypropylene as matrix filled with different amounts of single-wall carbon nanotubes [26]. It is remarkable that even the addition of only 1 wt% carbon nanotubes improves the strength by a factor of two, without a significant reduction of the strain at rupture. The *Young*'s modulus increases with increasing number of carbon nanotubes.

the stress–strain diagrams of a series of specimen with different contents of single-wall carbon-nanotube-containing composites. These specimen were fibers with a diameter of 1.6 mm. Polypropylene was selected as matrix material.

Figure 11.31 shows a series of important facts: Even additions of only 1 wt% (which is equivalent to ca. 0.75 vol%) carbon nanotubes lead to a doubling of the strength, without losing the ability for plastic deformation. With the production method applied by these authors, a maximum strength is obtained with 4 wt% carbon nanotubes. Larger additions are without advantage. Additions of 4 wt% carbon nanotubes increase the strength by a factor of 3.4; a remarkable success. The *Young*'s modulus also increases with increasing content of carbon nanotubes. This is understandable, as the *Young*'s modulus of carbon nanotubes is a few orders of magnitude higher than that of polypropylene.

As mentioned above, there is a second group of fibers based on carbon nanotubes, where the fibers are the majority phase. As a first example, Figure 11.32 displays an electron micrograph of a binderless fiber. In this fiber, double-walled carbon nanotubes were aligned near perfectly in parallel. These fibers were produced in lengths up to a few centimeters; the diameters were in the range between 3 to 20 μm [26].

The binderless fibers consisting of double-walled carbon nanotubes show remarkable mechanical properties. Figure 11.33 displays a stress–strain diagram of a fiber according to Figure 11.33. The specimen had a length of 5 mm and a diameter of 5 μm.

The stress–strain diagram depicted in Figure 11.33 reveals a significantly higher strength, as compared to the material with polymer binder and lower content of carbon nanotubes (see Figure 11.31). The strength increases by a factor of nearly 60. Certainly, as the content of carbon nanotubes is higher, also the *Young*'s modulus is higher, here the factor is six. However, compared to the *Young*'s
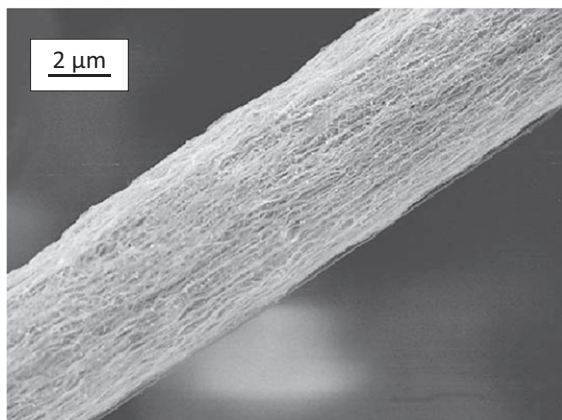
Figure 11.32 Fiber consisting of double-walled carbon nanotubes [26]. These fibers were produced in lengths up to a few centimeters in a diameter range from 3 to 20 nm. This fiber does not contain any binder. The nearly perfect parallel alignment of the fibers is remarkable. (Reproduced with permission by Elsevier.)
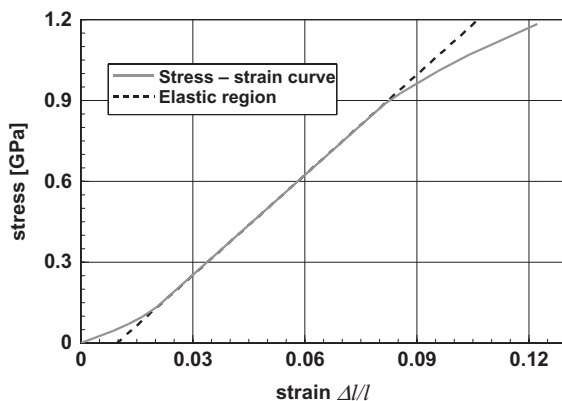
Figure 11.33 Stress–strain diagram of a fiber made of double-walled carbon nanotubes without any binder [26]. The specimen had a length of 5 mm and a diameter of 5 μm. The first region with a reduced stress–strain ratio is caused by settling phenomena; either at the interaction of the specimen with the testing apparatus or, respectively, additionally, within the fiber. To calculate the *Young*'s modulus, only the dotted line should be used.

modulus of roughly 1 TPa of a single carbon nanotube, the value of 16 GPa found in this specimen is comparatively low. The yield stress seems to be around 0.9 GPa, where a decrease of the slope of the stress–strain curve is observed. This decrease may be caused by nonlinear elastic behavior of the nanotubes, or, more probably, by slippage between aligned nanotubes, and, possibly, by fracture of a small number of nanotubes. Scanning electron micrographs support such a mechanism.

The second example of material with a high content of carbon nanotubes shows properties of a specimen, exhibiting the highest strength of a material produced. In this example, single-walled carbon nanotubes were bonded together with 40 wt% polyvinyl alcohol. The carbon nanotubes were coated with the binder. The diameter of the fibers were around 50 μm; the authors, Dalton et al [27], claim that they are able to produce fibers in a length up to 100 m. A stress–strain diagram, obtained from these fibers is shown in Figure 11.34. In this graph, one sees strength of 1.8 GPa, a strain at rupture of more than 100% after reaching the yield stress of 0.7 GPa. This huge deformation, resembling superplasticity, is possible because these fibers do not develop any necking. Possibly, slippage between individual nanotubes within the fiber might facilitate this large plastic deformation. These are really remarkable values for the mechanical properties, exceeding even the strength of the material with the highest strength known until now, spider silk. A stress–strain diagram of spider silk is plotted for comparison in this figure. Please note, the strength of quality steels is, generally, below 0.5 GPa, the best high-strength steels are in the range of less than 1.5 GPa.

Composites using graphene as filler are even more promising, as graphene shows a more than four-fold higher strength as compared to carbon nanotubes.
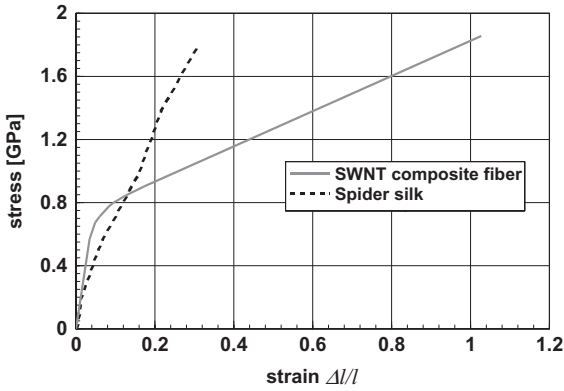
Figure 11.34 Stress–strain diagram of a composite fiber consisting of 60 wt% single wall carbon nanotubes coated with polyvinyl alcohol. The specimen had a diameter of 50 μm. For comparison, a stress–diagram of spider silk, the natural material with the highest strength is given [27].
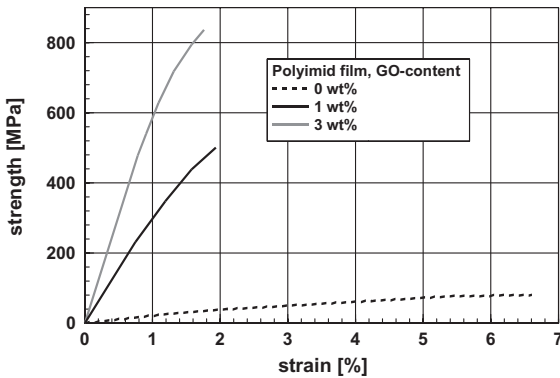
Figure 11.35 Stress–strain diagrams of polyimide films with a thickness of 0.1 mm filled with different amounts of graphene oxide (GO) flakes [28].

The composits with the highest strength are produced by *in situ* polymerization; graphene is used as graphene oxide (GO). In most cases, graphene oxide consists of a single sheet of covalently bond carbon, connected at the double bonds (see Chapter 5) to oxygen functional groups, such as hydroxyl, epoxide, or carbonyl groups.

Graphene oxide synthesized by functionalization of the surface to make the sheets hydrophilic was incorporated into a polyimide polymer film by *in situ* polymerization. The resulting film has a thickness of 0.1 mm. The amount of graphene oxide was varied up to 4 wt%. Figure 11.35 displays the stress–strain diagrams obtained from these films, in comparison with an unfilled pure polymer film [28].

The addition of graphene oxide to polyimide to obtain composites led to a material of high strength. The highest strength was obtained by adding 3 wt%; higher additions reduced the strength. This is a similar phenomenon as was found for carbon nanotubes (see Figure 11.31). The maximal strength of about 800 MPa is about 40 times higher than the best values obtained with additions of comparable amounts of carbon nanotubes to a polymer. Compared with the unfilled polyimide, the increase of the strength is ten-fold; an even higher increase is observed for the *Young*'s modulus. These first results are extremely promising.

References

1 Karch, J., Birringer, R., and Gleiter, H. (1987) *Nature*, **330**, 556.

2 Valiev, R.Z., Islamgaliev, R.K., and Alexandrov, I.V. (2000) *Prog. Mater. Sci.*, **45**, 103–189.

3 Nieman, G.W., Weertman, R.W., and Siegel, R.W. (1990) *Scr. Met. Mater.*, **24**, 145–150.

4 Meyers, M.A., Mishra, A., and Benson, D.J. (2006) *Prog. Mater. Sci.*, **51**, 427–556.

5 Youngdahl, J., Sanders, P.G., and Eastman, J.R. (1997) *Scr. Mater.*, **37**, 809–813.

6 MacKenzie, J.K. (1950) *Proc. Phys. Soc.*, **63**, 2–11.

7 Sanders, P.G., Eastman, J.A., and Weertmann, J.R. (1997) *Acta Mater.*, **45**, 4019–4025.

8 Chokshi, A.H., Rosen, A., Karch, J., and Gleiter, H. (1989) *Scr. Mater.*, **23**, 1679–1684.

9 Chang, H., Altstetter, C.J., and Averback, R.S. (1992) *J. Mater. Res.*, **7**, 2962–2979.

10 Siegel, R., and Fougere, G.E. (1995) *NanoStructured Mater.*, **6**, 205–216.

11 Kim, H.S., Estrin, Y., and Bush, M.B. (2000) *Acta Mater.*, **48**, 493–504.

12 Ashby, M.F., and Verall, R.A. (1973) *Acta Mater.*, **21**, 149–163.

13 McFadden, S.X., Valiev, R.Z., and Mukherjee, A.K. (2001) *Mater. Sci. Eng.*, **A319–321**, 849–853.

14 Mishra, R.S., Stolyarov, V.V., Echer, C., Valiev, R.Z., and Mukherjee, A.K. (2001) *Mater. Sci. Eng.*, **A298**, 44–50.

15 Betz, U., Padmanabhan, K.A., and Hahn, H. (2001) *J. Mater. Sci.*, **36**, 5811–5821.

16 Jordan, J., Jacob, K.I., Tannenbaum, R., Sharaf, M.A., and Jasiuk, I. (2005) *Mater. Sci. Eng. A*, **393**, 1–11.

17 Gao, H., Ji, B., Jäger, I.L., Arzt, E., and Fratzl, P. (2003) *PNAS*, **100**, 5597–5600.

18 Reynaud, E., Jouen, T., Gautheir, C., and Vigier, G. (2001) *Polymer*, **42**, 8759–8768.

19 Fu, X., and Qutubuddin, S. (2001) *Polymer*, **42**, 807–813.

20 Gloaguen, J.M., and Lefebvre, J.M. (2001) *Polymer*, **42**, 5841–5847.

21 Alexandre, M., and Dubois, P. (2000) *Mater. Sci. Eng.*, **28**, 1–63.

22 Liu, X., and Wu, Q. (2001) *Polymer*, **42**, 10013–10019.

23 Gilman, J.W., Jackson, C.L., Morgan, A.B., Harris, R., Jr., Manias, E., Giannelis, E.P., Wuthenow, M., Hilton, D., and Phillips, S.H. (2000) *Chem. Mater.*, **12**, 1866–1873. Figure 5.

24 Yu, M.-F., Files, B.S., Arepalle, S., and Ruoff, R.S. (2000) *Phys. Rev. Lett.*, **84**, 5552–5555.

25 Lee, C., Wei, X., Kysar, J.W., and Hone, J. (2008) *Science*, **321**, 385–388.

26 Li, Y., Wang, K., Wei, J., Gu, Z., Wang, Z., Luo, J., and Wu, D. (2005) *Carbon*, **43**, 31–35.

27 Dalton, A.B., Collins, S., Muñoz, E., Razal, J.M., Ebron, V.H., Ferraris, J.P., Coleman, J.N., Kim, B.G., and Baughman, R.H. (2003) *Nature*, **423**, 703–703.

28 Wang, J.Y., Yang, S.Y., Huang, Y.L., Tien, H.W., Chin, W.K., and Ma, C.C. (2011) *J. Mater. Chem.*, **21**, 13569–13575.

12
Characterization of Nanomaterials

Considering characterization methods, one has to distinguish methods delivering information averaged over a large ensemble of particles, the global properties, and those informing about one single or a limited number of particles, the local properties. The overall behavior of nanomaterials is controlled by their global properties, whereas the local properties help to understand why a material behaves in a specific way. For a complete characterization of a batch of nanoparticles, both types of methods are indispensable.

12.1
Specific Surface Area

The surface of an ensemble of nanoparticles, which is accessible from outside bears a lot of information. Looking at the surface of perfectly separated particles it is easy to calculate the surface of a given quantity. For the sake of comparison, the surface A of an ensemble is given in square meters per gram ($m^2\ g^{-1}$). (Even though this is a non-SI unit, it will be used in this book, because this unit is internationally accepted for comparison of powders.) Assuming spherical particles with a diameter d, the specific surface A is given by:

$$A = \frac{6}{\pi d^3 \rho} \pi d^2 = \frac{6}{d\rho} \quad \text{in} \left[m^2\ kg^{-1} \right], \tag{12.1a}$$

$$A = \frac{6}{\pi d^3 \rho} \pi d^2 \frac{1}{1000} = \frac{6}{d\rho} \frac{1}{1000} \quad \text{in} \left[m^2\ g^{-1} \right]. \tag{12.1b}$$

In Eq. (12.1), the quantity ρ stands for the material density. Assuming separated spherical particles; Figure 12.1 displays the specific surface for alumina using density of $3.5 \times 10^3\,kg\ m^{-3}$. The assumption of a constant density for all particle sizes is, possibly, not correct; however, to show the basic properties, these differences are not essential.

Looking at the huge specific surface areas that are expected from separated nanoparticles and knowing that the largest specific surface areas determined experimentally are in the range of a few hundred square meters per gram, one
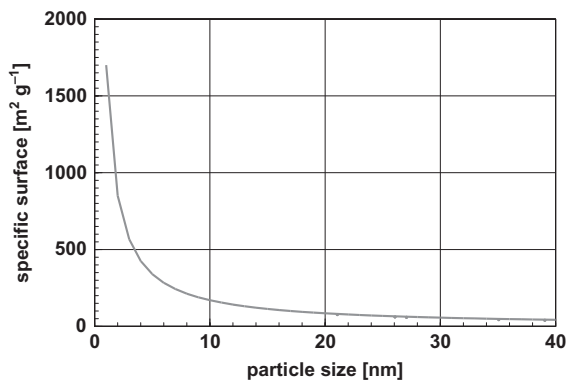
Figure 12.1 Specific surface of separated spherical alumina particles as a function of the particle size.

sees that there are a few more parameters influencing this characteristic quantity. First, one must take care of the degree of agglomeration. Each area, where two or more particles are in contact with each other, does not contribute to the specific surface; this leads to a reduction of the specific surface. The assumption of spherical particles is, certainly, much too simplified. Particles that are not compact solids, but rather cloudy arrangements of molecules, as is quite often found in silica, alumina, or carbon black, show, even when these particles touch each other, specific surfaces of $1000\,m^2\,g^{-1}$ and more.

The specific surface is measured by adsorption of a nonreactive gas, for example, nitrogen. Assuming a complete coverage of the surface with a monolayer of N gas molecules, each one covering an area a_M, the surface A of a specimen is given by:

$$A = Na_M. \tag{12.2}$$

Equation (12.2) assumes that between the particle surface and the gas molecules there are attractive, *van-der-Waals*, forces overcoming disordering effects of thermal motion. This process is called physisorption; when chemical interaction between surface and adsorbate is observed, the process is called chemisorption. In a somewhat arbitrary way, the limit between physisorption and chemisorption is defined, at an enthalpy of interaction of approximately $50\,kJ\,mol^{-1}$. The assumption of a perfect monolayer leads to the *Langmuir* adsorption isotherm, assuming that there is a fixed number of possible sites for gas adsorption at the surface, and further layers of gas molecules are not allowed until all possible site for the previous layers are occupied. This assumption is not realistic; *Brunauer et al.* [1] expanded *Langmuir*'s model allowing incompletely filled layers. Figure 12.2 displays the surface coverage according to Brunnauer *et al.*

Brunnauer et al. assumed, similar to *Langmuir*, there is no interaction between the layers of adsorbed molecules; therefore, *Langmuir's* theory is applicable to each layer. These assumptions made this theory successful und widely applicable. Based on this theory, a procedure to measure specific surfaces was developed. This
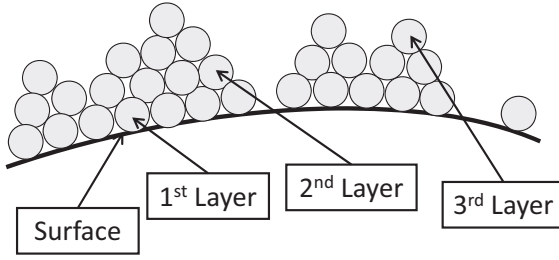
Figure 12.2 Assumption of *Brunauer et al.* about the adsorbed layers at a surface. Basically, they assume a multilayer system, not necessarily forming completely filled layers.

method, called the BET method, (According to the first letters of the inventors (*Brunauer*, *Emmett*, and *Teller*) is now the standard method to measure specific surfaces, which are called BET surfaces. The specific surface is calculated using the BET function

$$\text{BET function} = \frac{\dfrac{p}{p_0}}{V_{\text{ads}}\left(1 - \dfrac{p}{p_0}\right)} = \frac{1}{V_{\text{ads}}\left(\dfrac{p_0}{p} - 1\right)} = \frac{p}{p_0}\frac{1}{cV_{\text{mono}}} + \frac{1}{V_{\text{mono}}}. \qquad (12.3)$$

In Eq. (12.3) the quantity p stands for the gas pressure during the measurement and p_0 for the saturation pressure of the adsorbate at the measuring temperature, V_{ads} stands for the volume of the adsorbed gas determined experimentally; V_{mono} stands for the volume of one monolayer at the specimen and c, the BET constant, is a material-dependent constant value, depending on the ratio between the enthalpy of adsorption and the enthalpy of vaporization of the adsorbate. (For details of the lengthy derivation of this formula, please consult a textbook on physical chemistry.) To evaluate BET experiments, one plots the BET function versus $\frac{p}{p_0}$. This plot gives a straight line. Figure 12.3 demonstrates this.

The intercept of the straight line defined by Eq. (12.3) with the abscissa $\frac{p}{p_0} = 0$, gives $\frac{1}{V_{\text{mono}}}$, the amount of gas adsorbed at the surface, the slope $\frac{1}{cV_{\text{mono}}}$ may be used to calculate the missing BET constant c.

The BET experiment delivers the amount of gas adsorbed at the surface. The surface area of the material is calculated from the number of gas molecules in a monolayer at the surface

$$N_{\text{S}} = \frac{V_{\text{S}}}{V_{\text{M}}} N_{\text{A}}, \qquad (12.4)$$

where V_{S} is the gas volume adsorbed at the surface and V_{M} the volume of one mol of gas, both under standard temperature and pressure conditions, and N_{A}
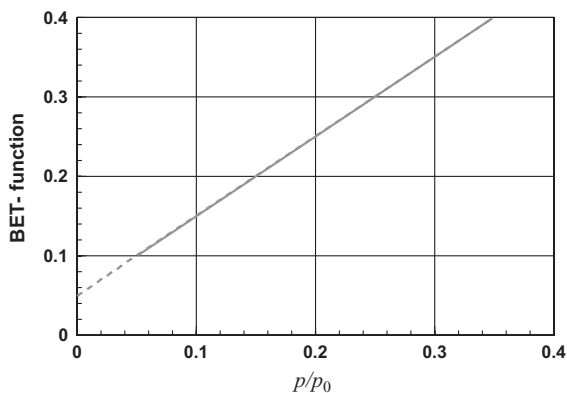
Figure 12.3 Plot of the BET function determined at different pressures plotted versus $\frac{p}{p_0}$. The experimental values are extrapolated to $\frac{p}{p_0} = 0$.

Avogadro's number. The specific surface of a specimen A with the weight m is then given by:

$$A = \frac{N_S a_M}{m}. \tag{12.5}$$

The quantity a_M is the area covered by one molecule. In the case of nitrogen, this value is $a_M = 0.158\,\text{nm}^2$.

As already mentioned, the surface areas of technical nanopowders are in most examples in the range between 50 and $100\,\text{m}^2\,\text{g}^{-1}$. Only in special cases, where the material does form compact particles, can the specific surface area exceed even $1000\,\text{m}^2\,\text{g}^{-1}$.

12.2
Analysis of the Crystalline Structure

Analyzing the crystalline structure of nanoparticles, or nanomaterials in general, is of great importance, as these small particles often have different structures to their bulk counterpart (see Chapter 7). However, as the particles are small, analysis of the structure faces a series of problems. In general, diffraction techniques using X-rays or electrons are applied. These methods of analysis provide information on the crystallographic structure and, additionally, some information on the particle size. The physical background of diffraction is found in the wave nature of electrons and X-rays. Provided these waves are in an appropriate range of wavelength relative to the lattice structure of the specimen, one obtains a diffraction pattern that is typical of the structure of the particles. With decreasing particle size, the lines in the diffraction patterns are broadened; therefore, sometimes an unequivocal assignment of a structure is difficult or even impossible. A typical example is
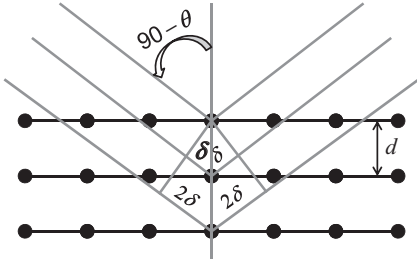
Figure 12.4 Basic geometry of diffraction on lattice elements using X-rays or electrons. The waves incoming under an angle of θ against the surface are "reflected" under the same angle. Between two consecutive lattice planes, the "reflected" waves obtain twice the path difference of δ.; in total 2δ.

the differentiation between the cubic and the tetragonal structure, where, because of the line broadening, the typical splitting of the lines is no longer observable.

Diffraction experiments using X-rays are performed, generally, in reflection, whereas electron diffraction is performed nearly exclusively in transmission. The physics background of diffraction experiments for lattice analysis is depicted in Figure 12.4.

The incoming waves arriving at the specimen under an angle of Θ are scattered at each atom and leave the specimen at the same angle. The scattered waves leaving the specimen interfere. In-between two consecutive lattice planes the waves get, because of a different path length δ, a phase difference, in total they leave the specimen with the path difference of 2δ per lattice plane. In other words, the difference in the path length between the wave scattered in the plane directly at the surface, and the wave scattered in the first plane is 2δ. The same value is added in-between the first and the second plane, then, in total, the path difference will be 4δ. This difference in the path length of the incoming and the outgoing wave is a function of the distance between two consecutive lattice planes d and the angle θ between the direction of the waves and the lattice planes.

$$\delta = 2d\sin\theta. \tag{12.6}$$

As mentioned above, the waves leaving the specimen interfere. A diffraction line is observed at a maximum of the interference pattern. Assuming a wavelength λ, the condition for an interference maximum of the order n is

$$n\lambda = 2d\sin\theta \quad n = 1,2,3,\dots. \tag{12.7}$$

The distance d between two directly adjacent lattice planes depends on the lattice structure and the orientation in the lattice. The orientation in the lattice, strictly speaking, the lattice planes are described by the *Miller* indices, (see Chapter 5) which are the reciprocal values of the intercept of the lattice planes with the axes of the coordinate system. The coordinate system is normalized in a way that it obtains the value 1 at the lattice constant a. Generally; one uses the letters h for the value in the x direction, k in the y direction, and l in the z direction.

In the simplest case, the cubic lattice, the spacing of two lattice planes with the indices (h,k,l) and the lattice constant *a* is given by:

$$d_{(h,k,l)} = \frac{a}{\left(h^2 + k^2 + l^2\right)^{0.5}}. \tag{12.8}$$

Using Eq. (12.7) the interference condition in a cubic lattice is

$$n\lambda = 2\frac{a}{\left(h^2 + k^2 + l^2\right)^{0.5}}\sin\theta. \tag{12.9}$$

To avoid too large numbers for the *Miller* indices, conventionally, one incorporates the order of diffraction into the *Miller* indices:

$$\lambda = \frac{2a}{\left(n^2h^2 + n^2k^2 + n^2l^2\right)^{0.5}}\sin\theta = \frac{2a}{n\left(h^2 + k^2 + l^2\right)^{0.5}}\sin\theta. \tag{12.10}$$

Using Eq. (12.10), it is possible to evaluate a diffraction pattern to calculate the lattice constant a and the *Miller* indices. Doing this by hand is a very tedious job, which is better done by specialized programs.

It was already mentioned that the width of the diffraction lines increases with decreasing particle size. The first and, in spite of many simplifications in the theoretical derivation, most applied formula was derived by Scherrer [2].

$$D_c = \frac{\kappa\lambda}{b\cos\theta}, \tag{12.11a}$$

$$b = \frac{\kappa\lambda}{D_c\cos\theta}. \tag{12.11b}$$

In Eq. (12.11a,b) D_c stands for the crystallite size vertical to the analyzed lattice plane with the *Miller* indices (h,k,l), θ is the diffraction angle and b the width of the diffraction line at half-intensity (in a 2θ–intensity plot), the quantity κ is a constant factor depending on the crystal structure and habit. It is found to be in the range between 0.89 and 1.39. For cubic materials, a value of 0.94 is often selected. λ is the wavelength of the X-rays or electrons applied in the experiment. For small nanoparticles, the line width b may be taken directly from the diffraction plot. For particle sizes of 100 nm and more, the instrumental influences on the line width must be taken into account, which is determined using perfectly crystallized coarse-grained material. Comparing results obtained using the *Scherrer* equation with micrographs, one must take into account the fact that this formula gives the size of the crystallites and not the particle size. Because of agglomeration, there may be significant differences.

Analyzing Eq. (12.11b) one sees the fact that the line width increases with decreasing particle size and increasing wavelength. Therefore, in the case of X-rays, one should try to use wavelengths as short as possible. However, this is thus limited as the energy of the X-rays should not be sufficient to excite X-ray fluorescence, as this makes any structural analysis nearly impossible by conventional means. The situation is better in the case of electron diffraction. In this

case, the wavelength of the electrons is always sufficiently short to obtain useful diffraction patterns. This difference between X-ray and electron diffraction is also the reason for the sometimes-disturbing finding that one does not find an X-ray diffraction pattern, but a relatively good electron diffraction pattern. The reason is found in the different wavelengths: X-ray diffraction is usually done with Cu Kα radiation having a wavelength of 0.154 nm, for electron diffraction, in most cases, an energy around 100 keV, equivalent to a wavelength of 3.7×10^{-3} nm, is selected.

A typical example of the difference in the ability of showing interference pattern of very small particles is depicted in Figure 12.5. This figure displays the X-ray and electron diffraction diagrams of anatase particles with sizes in the range of ca. 2 nm. Additionally, an electron micrograph is depicted where a few single particles are indicated. The X-ray diffraction diagram in Figure 12.5a does
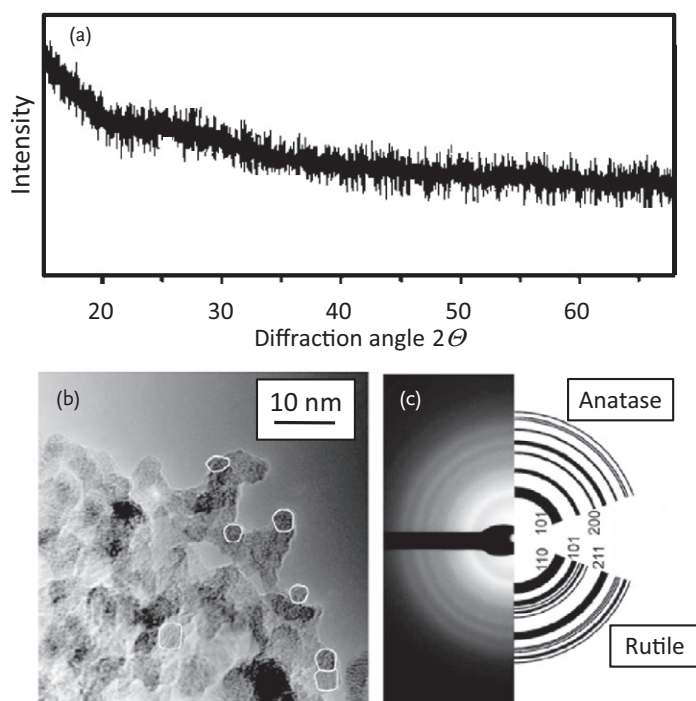
Figure 12.5 Characterization of titania, TiO_2 particles, crystallized in the anatas structure, with a diameter of ca. 2 nm by different methods [3]. The X-ray diffraction pattern (a) of this specimen does not show any diffraction peaks; this suggests that the specimen is amorphous [3]. In the electron micrograph displayed in (b) are some of the grains are highlighted to show their real dimensions. In contrast to (a) the electron diffraction pattern (c) of the material show very broad and weak lines that are typical of small grain sizes. Besides the experimental diffraction pattern (c) displays the theoretically expected pattern. Based on this diffraction pattern the specimen was identified as anatase. (Reproduced with permission by the American Institute of Physics.)
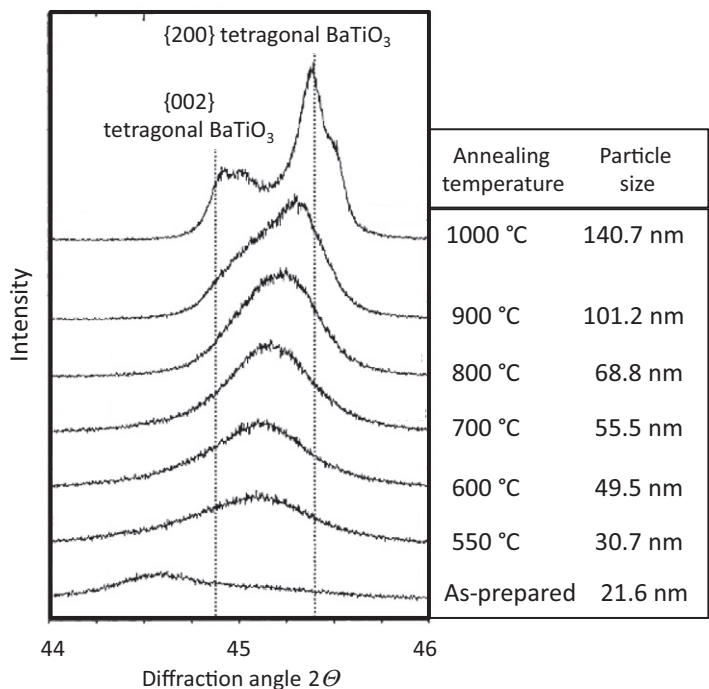
Figure 12.6 Bariun titanate of different grain sizes obtained by annealing at different temperatures. Range of diffraction angles of the {200} and the {002} diffraction lines of tetragonal BaTiO₃. These two diffraction lines are separated at particle sizes significantly above 100 nm. At smaller particle sizes it is impossible to decide if the specimen consisted of the tetragonal, the cubic phase, or a mixture of both [4]. (Reproduced with permission by Elsevier.)

not show any diffraction line, just a very small broad peak around 25 to 30 degrees. This diffraction pattern suggests that the specimen is amorphous. This is different in Figure 12.5c, where the electron diffraction pattern is depicted. Even when the diffraction lines are weak, the material is unequivocally identified as anatase.

A further problem connected to line broadening due to small particle size is the insufficient separation of directly adjacent lines, how they appear, for example, in tetragonal structures. Figure 12.6 displays a series of diffraction pattern obtained from barium titanate, BaTiO₃ with different grain size caused by different annealing temperatures [4]. In this temperature range, a mixture of the cubic and the tetragonal phase is expected.

Figure 12.6 displays the {200} and the {002} diffraction lines of tetragonal BaTiO₃ as a function of the particle size, obtained at different annealing temperatures. In the case of the largest particles the two diffraction peaks of the tetragonal phase are readily visible. With decreasing particle size, the separation of the two lines gets poorer, caused by the increasing width of the diffraction lines. For all
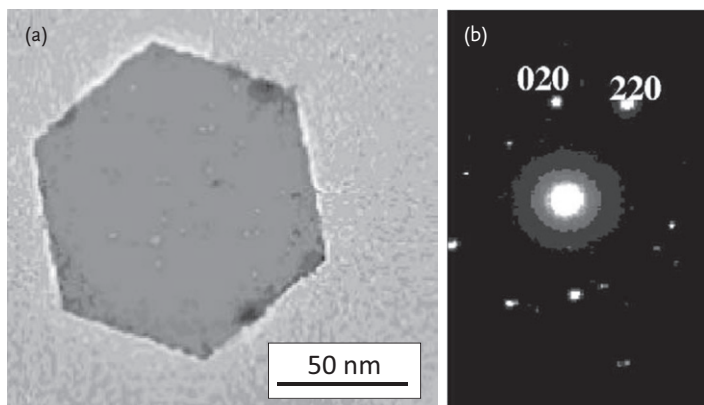
Figure 12.7 Single-crystal platelet of a CuFe$_2$O$_4$ and its electron micrograph (a) and the electron diffraction pattern (b) [5]. The numbers in the diffraction pattern indicate the lattice plane belonging to the diffraction signal. (Reproduced with permission by Elsevier.)

specimens with particle sizes below ca. 140 nm, it is impossible to decide if the specimen consists of the tetragonal, the cubic phase, or a mixture of both.

A very special technique for electron diffraction is the selected-area diffraction (SAD), a technique that is already in transition to the local methods. In this case, the electron beam is focused to a very small spot, enabling the operator to make electron diffraction of only one particle. Figure 12.7 displays an example. The specimen was a small platelet of CuFe$_2$O$_4$ [5]. This copper ferrite crystallizes in the cubic spinel structure. In plate (a) an electron micrograph displays the platelet, which shows a perfect hexagonal shape, indicating quite a perfect crystallization. Plate (b) displays the electron diffraction pattern, which consists, typical for a single crystal, only of a few isolated diffraction points. These points are the basis for a structure determination.

12.3
Electron Microscopy

12.3.1
General Considerations

To convey a visual impression of shape, size and structure of nanoparticles, nowadays, electron microscopy is the only means of sufficient technical maturity. However, electron microscopy is a broad science of its own, a job for specialists. This chapter outlines a few basic facts, which should help to understand the explanations of the specialists.

The possibility to see two particles separated in an image depends on the resolution power of the system. The resolution of an optical (this is valid for any optical
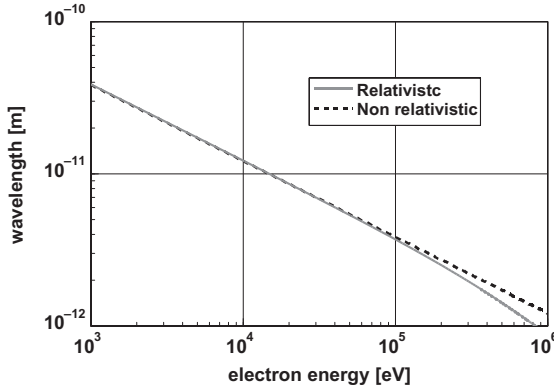
Figure 12.8 Wavelength of electrons as a function of the acceleration voltage. The wavelength is plotted with and without the relativistic correction of the electron mass.

system, independently if it is based on light or electrons) system is given by the *Abbe* criterion

$$x_{min} \approx \frac{\lambda}{N_A}. \tag{12.12}$$

In Eq. (12.12) the quantity x_{min} stands for the minimal distance of two points, which can be seen separated in an optical system working with the wavelength λ and the numerical aperture N_A. In a good light optical microscopes, the numerical aperture is for objectives with high magnification in generally around 1 or more. Equation (12.12) makes it clear that the larger the numerical aperture is, the better is the resolution power of the instrument. Knowing that the range of the visible light ends at 400 nm, one learns that the smallest distance that could be resolved is around 400 nm. Hence, smaller distances are not separable. This is why electron microscopes are necessary. Figure 12.8 displays a graph showing the wavelength of electrons in an electron microscope as a function of the operating voltage. As the velocity of the electrons in an electron microscope is close to that of the light, due to the relativistic increase of the particle mass, a correction of the wavelength is necessary. Therefore, Figure 12.8 displays the "classical" wavelength and the one after applying the relativistic correction.

Looking at Figure 12.8 and having Eq. (12.12) in mind, one could think that an acceleration voltage of 10^3 V is sufficient to obtain atomic resolution. However, this is not correct for two reasons: First, the numerical aperture of an electron microscope is, classically, in the range of less than 10^{-2}. Secondly, electrons of such a low energy are unable to pass through a specimen. The tiny value of the numerical aperture is necessary as rotational symmetric electron lenses cannot be corrected against spherical and chromatic aberration. Reducing the numerical aperture minimized this problem. By applying electron energies up to 200 keV, lattice resolution was possible. Using cold field emission cathodes, perhaps combined with an electron energy filter, the problem of chromatic aberration was

bypassed. The problem of spherical aberration was solved by the development of correction elements, which are not circularly symmetric. New electron microscopes equipped with both types of correction elements are able to depict, for example, the position of every atom in a graphene layer at an electron energy of only 80 keV (see Figure 12.17).

Box 12.1   Wavelength of Accelerated Electrons

Electrons have, like many other elementary particles, a two-fold nature: They can act as particles or as waves. In electron microscopy, both natures are essential. Looking at the wave nature: The wavelength of electrons is controlled by the acceleration voltage. According to *de Broglie* the wavelength λ associated to a particle with the mass m is given by

$$\lambda = \frac{h}{mv}. \tag{12.13}$$

In Eq. (12.13), the quantity h is *Planck*'s constant ($h = 6.63 \times 10^{-34}$ J s) and v the velocity of the electrons. From the energy balance

$$U = eV = \frac{mv^2}{2} \Rightarrow v = \left(\frac{2eV}{m}\right)^{\frac{1}{2}}, \tag{12.14}$$

the velocity of the electrons may be calculated. In Eq. (12.14), e is the electrical charge ($e = 1.602$ C), and m the rest mass of the electrons and V the acceleration voltage of the system. In electron microscopy, voltages above 100 kV are applied. At these high energies, the velocity of the electrons come into a range where mass is increased by relativistic phenomena. Using the *Lorentz* transformation, the mass m of a particle (in this case an electron) traveling with the speed v and the mass $m_0 = 9.11 \times 10^{-31}$ kg at $v = 0$ ("rest mass"), is calculated by

$$m = \frac{m_0}{\left[1 - \left(\frac{v}{c}\right)^2\right]^{\frac{1}{2}}}, \tag{12.15}$$

where c is the speed of light ($c = 2.998 \times 10^8$ m s^{-1}). After inserting in Eq. (12.14), one obtains

$$\lambda = \frac{h}{\left[2m_0eV\left(1 + \frac{eV}{2m_0c^2}\right)\right]^{\frac{1}{2}}}. \tag{12.16}$$

The relativistic increase of the electron mass reduces the wavelength of the electrons. Figure 12.8 was calculated using this formula.

Now, one can estimate the necessary voltage for electron microscopes. If one wants to see points at a distance of 0.5 nm apart and the numerical aperture of

the electron microscope is 5×10^{-3}, a reasonable value for electron microscopes, an electron energy of at least 10^5 eV is needed. To compensate for other problems, electron microscopes for materials science apply voltages in the range from 150 to 300 kV. For very special purposes, instruments with acceleration voltages up to 1 MV have been built. However, it must be noted that the resolution power of these instruments is not significantly better.

More recent instruments working with systems to obtain monochromatic electrons (monoenergetic) and correction of the spherical aberration have a larger aperture, hence, they no longer need such high electron energies, as they have a larger numerical aperture.

12.3.2
Setup of Electron Microscopes

Lenses for electron microscopes nowadays apply magnetic fields. These magnetic lenses show rotational symmetry. When the first electron microscopes were built, instruments using electrostatic lenses were also on the market.

To understand the design principles of an electron microscope, one has to understand the interaction of the electrons with the specimen. Electrons passing a specimen are scattered

- elastically – the energy of the electrons is retained, or
- inelastically – electrons lose energy.

Electron optical systems are adjusted for exactly one energy of the electrons; therefore, in contrast to light optical systems; the electron lenses must be readjusted when the energy of the electrons is changed. As a consequence, the illumination (condensor) systems must deliver electrons of only one energy. A modern field emission system for the electrons has an inherent energy spread of typically 0.7 eV. Even this is too much to obtain maximum resolution. Therefore, this energy spread must be reduced to values smaller than 0.2 eV applying an electron monochromator in the illumination system. This is depicted in Figure 12.9.

As mentioned above, a certain number of the electrons are scattered inelastically. To avoid image blurring, these electrons, scattered in a larger angle, are caught by a diaphragm. Inelastically scattered electrons going in the direction of the axis of the electron microscope are removed by a second electron monochromator. (Even when the inelastic scattered electrons blur the image, using special devices, they are a precious tool for detailed analysis of the specimen.) Besides chromatic aberration, spherical aberration, caused by the different focal length of rays close to the axis of the microscope as compared to those with larger distance from the optical axis, is the most important limitation for image resolution. Minimizing the numerical aperture reduces image blurring by spherical aberration. Limited by chromatic and spherical aberration the resolution of electron microscopes is in the range of 0.15 to 0.2 nm.

Correction of the spherical aberration is impossible in electron optical systems with rotational symmetry. The problem of spherical aberration was overcome by
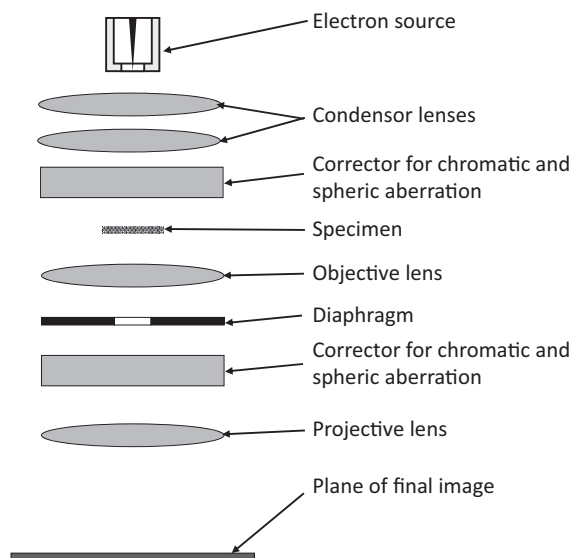
Figure 12.9 General setup of a high-performance electron microscope The magnetic lenses were – for better perception – drawn like light optical lenses.

a design of Rose [6], who combined conventional electron lenses with multipole elements. This design reduced the spherical aberration by a few orders of magnitude. Since these correctors are applied, the resolution power of electron microscopes is practically no longer limited. Nowadays, "sub-*Ångström*" resolution electron microscopy (an *Ångström* is a non-SI length unit. $1\,\text{Å} = 0.1\,\text{nm}$) is technically no longer a problem.

The setup displayed in Figure 12.9 shows an electron source, where the electrons, emitted from the tip of a field emitter (needle-shaped point source) are accelerated to the demanded energy, in most cases in the range between 100 and 300 keV. The corrector for chromatical and spherical aberration consists of a monochromator and a correction element according to *Rose*. The condensor system (*Köhler* illumination system) focuses the electrons at the specimen. To improve visual perception, the magnetic lenses are depicted like light optical lenses. After passing the specimen, the image of the specimen, formed by elastic and inelastic scattering of electrons in the specimen is enlarged with the objective lens. Next, the electron beam is limited by a diaphragm to remove inelastically scattered electrons. Furthermore, this diaphragm is applied to adjust contrast and resolution within certain limits and to change between bright- and dark-field microscopy. The possibility to switch between bright- and dark-field microscopy is depicted in Figure 12.10.

For dark-field imaging, the diaphragm is shifted out of the optical axis; a measure blocking the direct beam (in the language of optics designers, the information connected to the 0th diffraction order is blocked). The same result is obtained – significantly better – by tilting the illumination system. In recent instru-
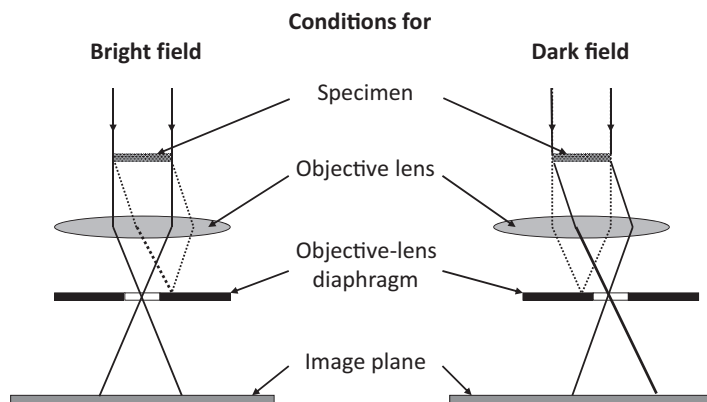
Figure 12.10 Positioning of the diaphragm for bright-field and dark-field electron microscopy. For dark-field imaging, the 0th diffraction order (direct beam) is blocked; therefore, it does not contribute to image formation. Comparing bright- and dark-field micrographs of the same spot of the specimen may be important for correct interpretation of electron micrographs.

ments, this is not a mechanical tilting, rather tilting by bending the electron beam using a magneto-optical element, which facilitates variations in tilting angle and rotation.

Before the image is magnified to its final size, the electrons pass a correction system, to minimize spherical and chromatic aberration. Finally, the magnified image of the specimen is visible on the fluorescence screen. It may be recorded using photographic or electronic means.

12.3.3
Interaction of the Electron Beam with the Specimen

For transmission electron microscopy, the specimens are very thin foils or individual particles. Generally, the thickness of specimens is limited to 100 nm or less. The thicker the specimen, the higher the energy (voltage) of the electrons needed for penetration. In contrast, scanning electron microscopes may work in transmission and; additionally, may give information on the surface interaction of the electrons. The specimen scatters and absorbs the electrons. Only the elastically scattered electrons are usable for imaging. However, the inelastic scattered electrons and those having lost some of their energy by absorption processes also carry important information about the specimen; and in special devices, they are used for special types of imaging. Figure 12.11 displays a specimen exposed to the electron beam together with the information obtainable with different devices.

Inelastic scattered electrons have lost parts of their energy in the specimen. This energy is, primarily, converted to X-rays. Two processes are observed:
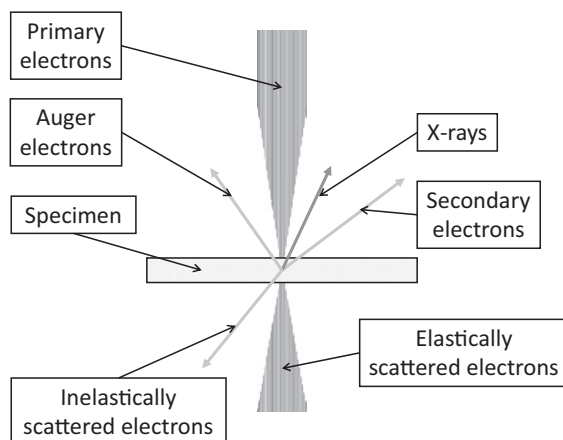
Figure 12.11 Electrons and photons leaving the specimen after passage of energy-rich electrons for image formation. Each one of these signals carries specific information about the specimen and its composition.

- Deceleration of the electrons in the electric field of the atomic nucleus, leading to the emission of "bremsstrahlung" (radiation of deceleration). Bremsstrahlung is characteristic of the deceleration process; however, it is not characteristic of the specimen. Bremsstahlung has a continuous spectrum with a maximum energy equal to the energy of the incoming electrons.

- Ionization of inner shells of the atoms. This process leads to the emission of characteristic X-rays. This emission is characteristic of the elements in the specimen and is used for qualitative and quantitative analysis of the specimen.

Ionization of an inner shell leads an electron vacancy in an inner shell; which is filled by transfer of an electron from a more outer-lying shell. This process is connected to an emission of the excess energy as an X-ray photon, which is characteristic of the emitting atom. Depending on the shell from where the electron was expelled, and the one delivering the electron to fill this vacancy, characteristic X-rays are grouped into different series. Figure 12.12 displays the system graphically.

Complementing Figure 12.12, Table 12.1 gives a compilation of some of the X-ray emission series for elements, where the largest principal quantum number $n = 4$. In the periodic system of the elements, this system of emission series is continued up to a maximum principal quantum number $n = 7$.

The emitted characteristic X-rays allows unequivocal identification of the atoms in the specimen. The wavelength of the emitted X-rays follows *Moseley*'s law:

$$v = \alpha(Z - \beta)^2. \tag{12.17}$$

In Eq. (12.17) v is the frequency of the emitted X-ray line, Z the atomic number of the emitting element and the quantities α and β are constants depending on
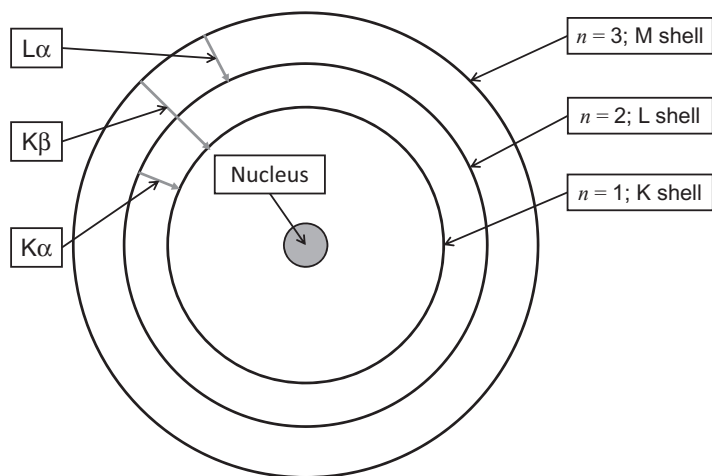
Figure 12.12 Simplified structure of an atom. This graph indicates the different electron shells, their names, and the most important electron transitions leading to the emission of X-rays. The denomination of the emitted X-rays is also indicated.

Table 12.1 Denomination and main quantum numbers of electron shells of atoms and the most important transitions leading to X-ray emission. The notation of the emitted X-ray lines is also given.

Shell of the initial electron vacancy		Shell donating the electron to fill the vacancy		Notation of the emission lines series	Difference of principal quantum numbers
Designation	Principal quantum number	Designation	Principal quantum number		
K	1	L	2	Kα	1
K	1	M	3	Kβ	2
K	1	N	4	Kγ	3
. . ..					
L	2	M	3	Lα	1
L	2	N	4	Lβ	2
. . ..					
M	3	N	4	Mα	1

the line system. *Moseley*'s law lastly says that the energy (which is proportional to the frequency) of the emitted X-rays increases quadratically with the atomic number. From Table 12.1 it is obvious that there is a sequence in the energy of the emitted X-ray lines.

$$E_K > E_L > E_M, \tag{12.18}$$

where E_K, E_L, and E_M are the energies of the *K, L,* and *M* emission lines. Besides information about the element, the emitted X-rays carry information about the
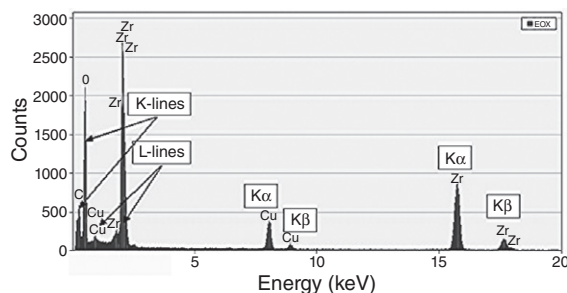
Figure 12.13 X-ray spectrum acquired with an energy-dispersive system of a specimen consisting of zirconia, ZrO_2, particles (Szabó, D.V., KIT, Karlsruhe, private communication (2007).

valency state of the atoms. However, this is a quantity of minor influence. Technically, an evaluation of this phenomenon is possible only in an energy range of the emitted X-rays of less that 1 keV.

The emitted X-rays are analyzed either in a wavelength- or an energy-dispersive system. Even though the resolution of wavelength-dispersive systems is better, the application of energy-dispersive systems is more or less standard in connection with electron microscopes, as these systems are faster and easier to operate.

Figure 12.13 displays a typical emission spectrum of a specimen taken in an energy-dispersive system. The specimen consisted of zirconia particles.

The X-ray spectrum displayed in Figure 12.13 shows, as expected, the K lines of zirconium and oxygen and the L lines of zircon. Additionally, there is a relatively strong signal of copper and carbon. These are artifacts! The copper lines stem from the copper mesh used as specimen carrier and the carbon signal from the carbon film used as electron-transparent substrate for the zirconia particles.

In connection with inelastic scattering of electrons, when exciting an atom, the electrons loose energy. This energy loss is, lastly in the same way as the excited X-ray emission, characteristic of the specimen and its composition. Consequently, this consideration leads to electron energy loss spectroscopy (EELS). Figure 12.14 displays a typical EELS spectrum. Certainly, at the maximum is at the energy loss zero, this is the elastically scattered part of the electron beam. Next, especially in the case of metals, one finds the plasmon peak, which is typically found in a range of less than 10 eV. Subsequently, the element-specific absorption edges with their fine structure are observed.

Generally, the EELS spectra are not applied for quantitative elemental analysis, they are used, rather, to analyze the plasmons and, if possible, to obtain information on the binding in the specimen. The latter is possible only in the range of small energy losses, perhaps below 1 keV, which is, in most cases, characteristic of L and M X-ray lines. As an example, Figure 12.15 displays the section of the energy loss in the range of the L absorption edge of vanadium and the K edge of oxygen [7].

Figure 12.15 displays the L absorption spectrum of vanadium and the K absorption of oxygen, measured by EELS, of three different vanadium oxides. In each
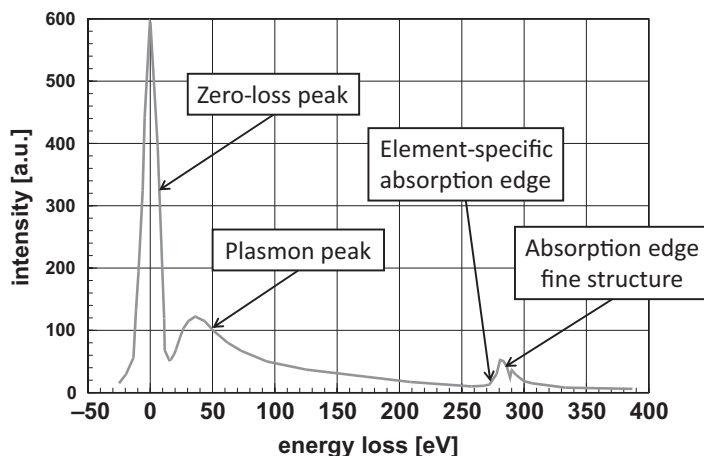
Figure 12.14 Typical EELS spectrum. Besides the primary electrons, characterized by zero energy losses, one finds traces of the interaction with the plasmons and, at larger energy losses, the interaction peaks, which are typical of the elements in the specimen.
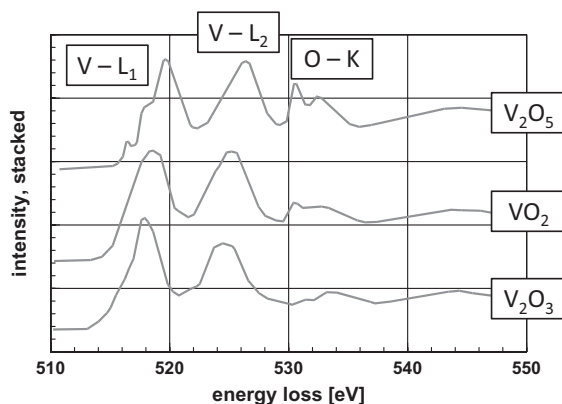
Figure 12.15 EELS spectrum in the range of the L absorption edge of vanadium and the K edge of oxygen [7]. To demonstrate the power of this technique, the spectra of three different vanadium oxides are shown; they represent V^{3+}, V^{4+}, and V^{5+}. The different coordination in these three oxides has an influence on the shape of the oxygen K absorption edge and the position of the L absorption edge, too. It is obvious that EELS spectra allow very far-reaching statements.

one of these oxides, vanadium is in a different valency (V^{3+}, V^{4+}, and V^{5+}) and the oxygen ions in a different environment. The significant differences between these three spectra allow quite a good interpretation about valency and coordination of unknown spectra, as the position of the K absorption edge and the position of the L edge depend on the valency of the metal ion.

12.3.4
Some Examples of Transmission Electron Microscopy

As mentioned above, only the elastically scattered electrons carry information about the image. Elastic electron scattering depends on the energy of the electrons V and the number of electrons of the atoms in the specimen, described by the atomic number Z, is essentially proportional to $\left(\dfrac{Z}{V}\right)^2$. This has important consequences on the contrast within an image. Assuming zirconia, ZrO_2 as specimen; for zirconium $Z = 40$ and therefore $Z^2 = 1600$; for oxygen $Z = 8$ and $Z^2 = 64$ one sees that the scattering power of zirconium is 25 times higher than that of oxygen; hence, there is no chance to get a picture showing the positions of the zirconium and the oxygen atoms. The probability for inelastic scattering is, to a first approximation, proportional to the atomic number. Therefore, methods of analysis measuring the energy loss of inelastic scattered electrons (such as EELS = electron energy loss spectrometry) work better with elements of high Z. However, as there is a linear proportionality, one has a chance to see, for example, the oxygen signal besides that of a metal of higher atomic number. Lastly, the same considerations are valid with respect to the emitted X-rays. This means, X-ray analysis works better with heavy elements as compared to light ones.

Image formation in optical microscopy depends primarily on contrast due to absorption. In high-resolution electron microscopy, differences in absorption play a negligible role. High-resolution images are formed by interference of the elastic scattered electrons leading to a distribution of intensities depending on the orientation of the lattice planes in a crystal relative to the electron beam (diffraction contrast). Therefore, at certain angles the electron beam is diffracted strongly off the axis of the incoming beam, while at others, the beam is nearly completely transmitted, allowing deductions as to the arrangement of atoms within a crystal lattice. Certainly, in the case of a noncrystallized specimen, absorption plays a distinctive role in image formation.

Figure 12.16 displays a high-resolution electron micrograph of a zirconia specimen coated with alumina. This figure displays all the advantages and problems connected to electron microscopy. The core of this composite particle is crystallized. One sees the regular arrangement of the columns of zirconium ions. Because of its low atomic number, the oxygen ions are not visible. The zirconia core is surrounded by amorphous alumina. As the atomic numbers of aluminum ($Z = 13$) is very low, the visibility of the coating layer is poor. Furthermore, as the coating is amorphous, this layer does not show any structure.

Figure 12.16 displays a high-resolution electron micrograph of crystallized zirconia, shows a "picture" of the lattice. Micrographs like this are obtained if the electron beam is exactly in the direction of a crystallographic orientation. The observers "sees" columns of atoms in their crystallographic exact neighborhood. (As mentioned above, these high-resolution images are due to the diffraction contrast. Changing the focus adjustment may change the contrast. In particular, this point makes the interpretation of high-resolution electron micrographs very
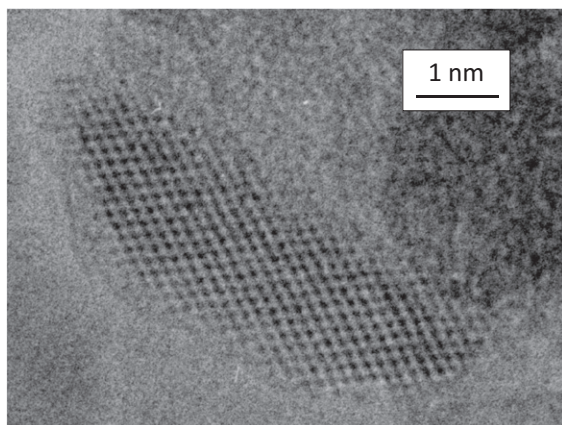
Figure 12.16 Zirconia particle coated with alumina. As the zirconia core is crystallized, one sees a well-ordered arrangement of the zirconium ions; whereas the oxygen ions are, because of their low atomic number invisible [8]. The alumina coating is structureless, because it is amorphous. This electron micrograph was taken with an electron energy of 200 kV.

difficult.) This is useful, provided the crystallographic orientation is characterized by low *Mille*r indices, to determine the crystallographic structure of the specimen. By tilting the specimen, changing the orientation of the specimen with respect to the electron beam, it is possible to obtain additional structural information.

Electron microscopes using a system to correct spherical aberration do not need extremely high voltages to obtain atomic resolution. Figure 12.17 displays an example. This micrograph, taken at 80 kV acceleration voltage displays a sheet of graphene. One sees the hexagons, which are structuring elements of graphene. This is exactly the image that is expected from the theoretical considerations and depicted as sketched in Figure 5.11. One of these hexagons, placed in a white circle, is highlighted by dark points. The distance between two of these points is 0.14 nm.

When analyzing a specimen in an electron microscope, sometimes it is advised to change between the bright-field and the dark-field mode. By varying tilting angle and rotation, one sees quite rapidly if a material contains crystalline grains or not. In dark field electron microscopy, those crystallized particles that are in the proper orientation to the electron beam appear bright. A typical example is displayed in Figure 12.18.

The specimen used for Figure 12.18 consisted of amorphous alumina with small zirconia precipitates. The bright spots visible in the dark-field micrograph, plate (b), indicate that the specimen contains crystallized particles. Changing the tilting angle and the rotation of the incident electron beam produces other bright spots, depending in the crystallographic orientation with respect to the electron beam.
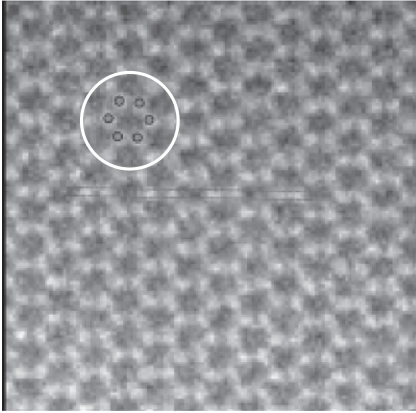
Figure 12.17 High-resolution electron micrograph of a graphene sheet. This micrograph was taken with an electron energy of 80 keV [9]. One sees the elementary structure of graphene, the hexagons, which are highlighted in one example in the white circle. The distance between two of these points is 0.14 nm. (Courtesy by FEI Company, 2012).
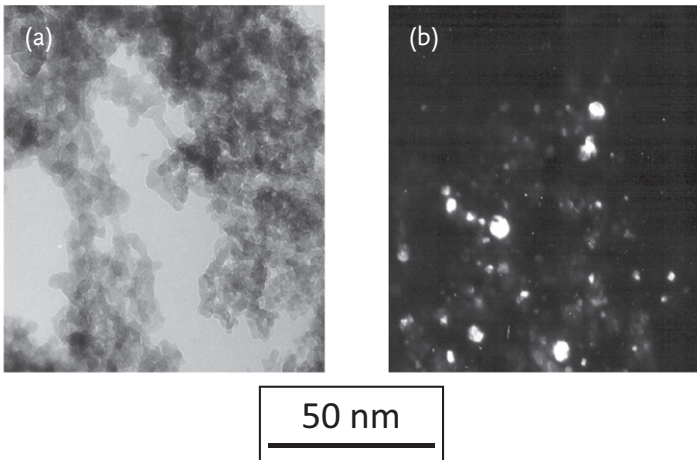
Figure 12.18 Comparison between a bright-field (a) and dark-field (b) electron micrograph of a specimen consisting of amorphous alumina particles with small crystallized zirconia precipitates. (D: Vollath and K. Sickafus, Los Alamos National Laboratory, USA (1992), unpublished results.)
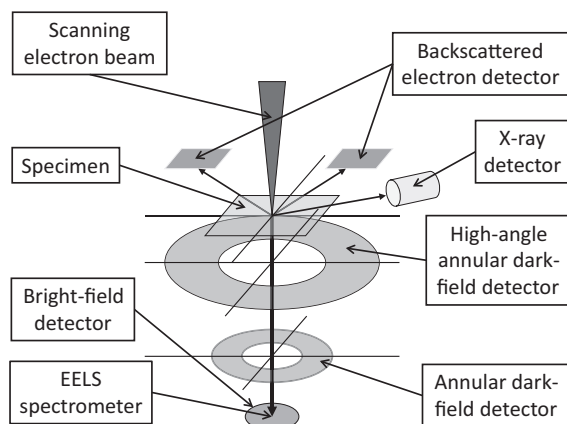
Figure 12.19 Possible information obtainable from a scanning electron system.

12.3.5
High-Resolution Scanning Electron Microscopy

Until the development of correcting elements for chromatic and spherical aberration, scanning electron microscopes were hampered by relatively poor spatial resolution. At this time, scanning systems were used primarily for elemental analysis using the characteristic X-rays excited in the specimen. This has changed, nowadays; scanning systems have the same possibilities for high resolution as transmission electron microscopes; now atomic resolution is attainable. Additionally, there is much additional information extractable from the scanning signal. Figure 12.19 gives an overview of the new possibilities.

High-resolution scanning electron microscopy is possible, since sufficiently small electron beams are provided using illumination systems with minimized spherical and chromatic aberration. There is a series of possible signals, which may be used to analyze or image the specimen. These systems are:

- Detectors for backscattered electrons.

- X-ray detectors, in most cases energy-dispersive systems (EDX). This system gives localized information about the composition of the specimen.

- Angular detectors, which collect inelastically scattered electrons. As inelastic electron scattering depends on the atomic number Z, such systems deliver images where the difference in the atomic number results in contrast. The best Z-contrast is obtained using the high-angle annular dark-field detector (HAADF).

- Electron energy loss systems give, compared with X-ray spectrometry in a reciprocal way, information about the composition of the specimen in a localized manner.
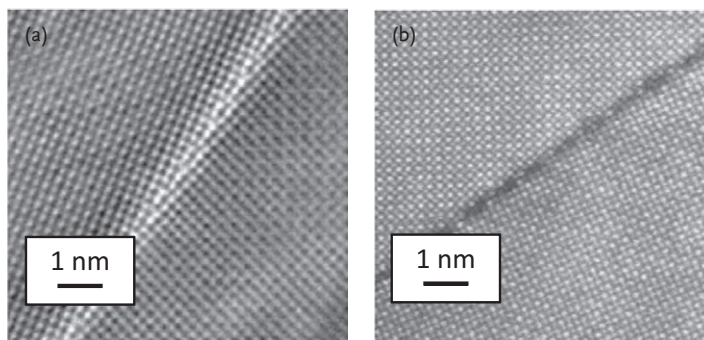
Figure 12.20 SrTiO₃ specimen [10]. Comparison of a transmission electron micrograph (a) with a HAADF micrograph of the same spot of the specimen. The enhanced contrast and the better resolution of the HAADF image due to the different atomic number is clearly visible. (Courtesy by FEI Company, 2012. The micrographs were taken using a Titan G2 with probe Cs-corrector).

In particular, the localized chemical analysis using X-rays or EELS allow the identification of lattice elements or even single atoms.

Figure 12.20 displays two electron micrographs of the same spot of a SrTiO₃ specimen [10].

Figure 12.20 displays a comparison between a transmission electron micrograph (plate a) and a HAADF image (plate b) of the same spot of the specimen. This comparison clearly demonstrates the advantage of the high-angle annular detector with respect to the contrast caused by the different atomic number (Z contrast). Certainly, in this example the difference in Z was relatively large, ($Z_{Sr} = 38$, $Z_{Ti} = 22$) therefore, in the HAADF image the titanium atoms are poorly visible, whereas in the transmission electron micrograph, there is nearly no difference. In both plates the oxygen is, because of its low atomic number ($Z_O = 8$), invisible. Combining the possibilities of EDX and EELS gives, in combination with the possibilities of high-resolution scanning systems images that show and identify the atoms in a lattice exactly on their place. Figure 12.21 displays an example. Again, SrTiO₃ was selected as the specimen [10].

This figure shows that the identification of each atom in the lattice is unequivocally possible. Using some image-processing software, the contours of the atoms can be flattened; the images would become more beautiful. Additional to strontium and titanium, it was shown that it is possible to obtain indications of the positions of the oxygen atoms, too.

In the example displayed in Figure 12.21, columns of atoms in a crystal lattice were identified. However, in special cases, it is also possible to identify single atoms. Such an example is displayed in Figure 12.22. In this case, the specimen was a single layer of graphene. In this layer, one carbon atom is replaced by a silicon atom. Besides the HAADF micrograph, a schematic drawing of the situation around the impurity atom is shown.
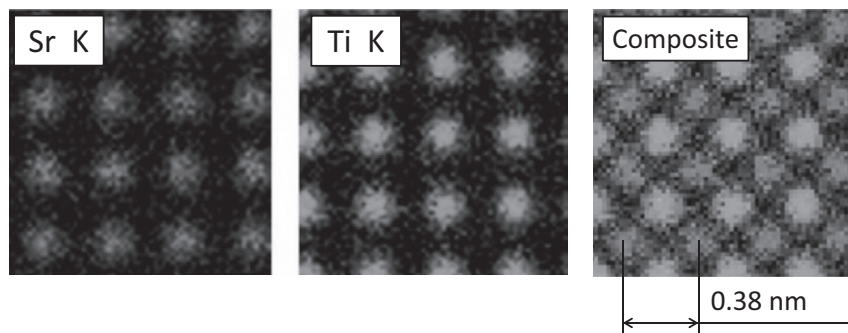
Figure 12.21 Identification of the different atoms in the lattice of a SrTiO₃ specimen by combination of EDX and EELS. One clearly sees that each atom is unequivocally identified [10]. Using some image processing software, the pictures could be prepared more "beautifully". (Courtesy by FEI Company, 2012. The micrographs were taken using a Titan G2 with probe Cs-corrector).
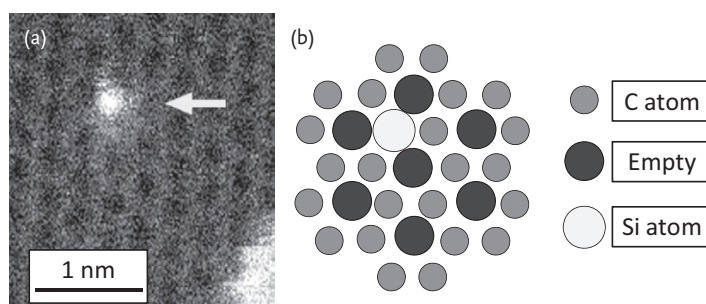
Figure 12.22 HAADF image of a graphene sheet with the inclusion of one silicon atom in the lattice. (plate a) [11] (Reproduced with permission by the American Institute of Physics.) Plate (b) is a schematic drawing of the situation depicted in plate (a). In both plates: the dark spots are the empty space in-between the atoms, because of its higher atomic number, the silicon atom is brighter ($Z_C = 6$, $Z_{Si} = 14$).

For the interpretation of this figure, it is important to realize that the empty space in-between the carbon atoms is dark, whereas the carbon atoms themselves, because of their scattering power, are a little brighter. The impurity silicon atom is, because of its highest atomic number Z ($Z_C = 6$, $Z_{Si} = 14$), the bright spot in the figure. It is interesting to see the hexagonal arrangement of the carbon atoms and of the space in-between them.

Finally, it should be pointed out that using EELS experiments it is possible to depict even surface plasmons of metallic nanorods. A typical picture is given in Chapter 9, Figure 9.18.

References

1 Brunnauer, S., Emmett, P.H., and Teller, E. (1938) *J. Am. Chem. Soc.*, **60**, 309–319.

2 Scherrer, P. (1918) *Göttinger Nachr. Math. Phys.*, 98–100.

3 Schlabach, S., Szabó, D.V., Vollath, D., de la Presa, P., and Forker, M. (2006) *J. Appl. Phys.*, **100**, 024305. Fig. 1, 2.

4 Suzuki, K., and Kijima, K. (2006) *J. Alloys Compd.*, **419**, 234–242.

5 Du, J., Liu, Z., Wu, W., Li, Z., Han, B., and Huang, Y. (2005) *Mater. Res. Bull.*, **40**, 928–935. Fig. 2e,f.

6 Rose, H. (1990) *Optik*, **85**, 19–24.

7 Laffont, L., Wu, M.Y., Chevallier, F., Poizot, P., Morcrette, M., and Tarascon, J.M. (2006) *Micron*, **37**, 459–464.

8 Vollath, D., and Szabó, D.V. (2002) in *Innovative Processing of Films and Nanocrystalline Powders* (ed. K.-L. Choy), Imperial College Press, London, pp. 210–251.

9 FEI AN033 11 11 (2011) The monochromator with X-FEG electron source.

10 FEI AN 0032 10 11 (2011) Titan™ G2 with ChemiSTEM Technology.

11 Lovejoy, T.C., Ramasse, Q.M., Falke, M., Kaeppel, A., Terborg, R., Zan, R., Dellby, N., and Krivanek, O.L. (2012) *Appl. Phys. Lett.*, **100**, 154101 1-4.9.

Index